Universidad del País Vasco
Euskal Herriko Unibertsitatea

Ph.D. Thesis

Friction torque in ball slewing bearings for wind turbines

Presented by:

Iñigo Escanciano García

Thesis Advisors:

Dr. Iker Heras Miguel
Prof. Josu Aguirrebeitia Celaya

Bilbao, January 2023

A Santiago Escanciano

Agradecimientos

Este proyecto representa no solo el resultado de esfuerzos individuales, sino también de experiencia, paciencia y colaboración de diversas personas que han dejado su huella en cada fase de este proceso.

En primer lugar, agradezco a mis directores de tesis, Iker Heras y Josu Aguirrebeitia, por transmitirme sus conocimientos de lo que era algo nuevo para mí y han hecho posible este trabajo. Durante estos años me han ofrecido esa seguridad y buena dirección, además de dedicación y atención al trabajo realizado, que no es poco teniendo en cuenta mi orden dentro del desorden.

En segundo lugar al Grupo ADM con el que me he sentido uno más en todos los aspectos profesionales y personales, en especial a Igor Fdez. de Bustos con el que he adquirido experiencia y compartido andanzas en la competición MotoStudent en paralelo a este trabajo y me ha permitido descansar mentalmente, agotándome físicamente.

Agradecer como no, a todos los compañeros de la sala, tanto actuales como pasajeros que bien han terminado su recorrido en la universidad o épocas como la pandemia los han reubicado. Con estos he compartido horas de café, vivencias, ideas y más café, y han sabido tanto aguantar mis quejas y resuellos en etapas complicadas, así como alegrarse por los logros conseguidos. Igualmente, agradezco el buen trato recibido por todos los miembros del Departamento Ingeniería Mecánica.

It goes without saying that I would like to thank Fraunhofer IWES, with special mention to Matthias Stammler, Florian Schleich, Arne Bartschat and Oliver Menck, for collaborating with the research group, which has offered its expertise and data on wind turbine bearings that have added considerable weight to this thesis. I would also like to express my gratitude as this

collaboration enabled me to stay at Fraunhofer IWES Large Bearing Laboratory, which has been valuable to me both personally and professionally.

Por último, y no menos importante, agradezco a mi familia y amigos por su apoyo e interés constante. En especial a mi madre, Mª Angeles García, por apoyarme en todo momento y desvivirse no solo ahora sino en todo el recorrido hasta este punto, que ha hecho posible que llegue hasta aquí y lograr mis objetivos.

Iñigo

Abstract

In recent years, there has been a significant increase in wind energy, with notable growth in both offshore and onshore installations, according to the IEA. Slewing bearings are large rolling bearings that enable the yaw and pitch rotations of bladed wind turbines. These bearings are designed to support the axial loads, radial loads and tilting moment caused by wind forces. This Doctoral Thesis focuses on the structural modelling and friction torque calculation of four-point and eight-point contact slewing bearings. However, the proposed approaches can be adapted for other types of slewing bearings, such as crossed roller slewing bearings. During this research work, certain hypotheses were considered, which have been key in the decision-making process:

- A bearing subjected to axial load can be modelled with cyclic symmetry. In this case, the load distribution is not significantly affected by the flexibility of the rings. However, in the case of a bearing subjected to radial load or tilting moment, the deformation of the rings affects load distribution. The flexibility of the structures the rings are attached to dictates to a large extent the shape of these deformations. Therefore, a general calculation method can be developed under the rigid ring hypothesis.

- Previous research works have shown that the kinematic of the balls can be affected by the stick regions in the ball-raceway contacts. However, in the case of slewing bearings, where the load distribution problem is made independent from the friction torque problem, other works have shown that these stick regions do not affect the bearing friction torque. Thus, the full sliding contact assumption allows for a faster computation of the friction torque problem.

- The slewing bearings of blade wind turbines are characterised by their small oscillatory movements. The ball-raceway contact lubrication lies

between an EHL and boundary lubrication. An equivalent problem to the first hypothesis arises, where modelling a realistic frictional contact involves a complex model, which can extend the current research work beyond the scope. However, assuming a coefficient of friction that can be experimentally adjusted is a common practice and a more effective solution for this problem. Thus, Coulomb's friction model is used instead, where the friction force is defined by a coefficient of friction multiplied by the normal force.

Based on these hypotheses, current research has made improvements to friction torque calculation and slewing bearing simulation techniques. The following list summarises the process followed and the decisions made for this work:

- Based on the slow speed and large size assumption, the load distribution problem is separated from the friction torque problem. In order to fit the analytical model results to experimental test results, a preload scatter is implemented in the load distribution calculation step, to then calculate the friction torque as the sum of the contribution of each ball to the friction torque. The tuning parameters of the analytical model are varied and by means of multiple calculations, the model adjusts the experimental results. Some discrepancies are observed under tilting moment, for which FE analyses are performed to solve the load distribution problem and obtain better fit results. Finally, a more precise methodology for calculating the friction torque is achieved and some guidelines for its calculation are proposed.

- The rigid ring hypothesis has been proven to delimit the capabilities of the analytical model. Therefore, the effect of the flexibility of the bearing is studied through FEM. A real model of a blade-bearing-hub assembly is used to analyse the load distribution under real boundary conditions. Different combinations of modelling techniques or simplifications are used, such as simplifying the bolted joints or substituting the bearing with an equivalent three-spring model that could be useful in early design stages, or using a different blade material, which could also reduce the bearing testing costs. This work verifies the importance of the boundary conditions on load distribution are, whereby it is concluded that these greatly affect the friction torque results. Some improvements on Daidié's mechanism are performed, which is used to replace the balls and simplify

the ball-raceway contact in FE analysis. The enhanced implementation of the mechanism reduces the error made on the less loaded balls for a bearing with a radial displacement, which is an important contribution since the friction torque is driven by these less-loaded balls.

- An analytical approach to calculate the friction torque in an efficient way is presented that complements the previous methodology, which is precise but computationally expensive. A normalised friction torque expression is obtained, which only depends on the microgeometry of the bearing and the external loads. A Design of Experiments is built around this to obtain an extensive normalised friction torque result database. Finally, a friction torque calculation tool is presented, which relates the normalised friction torque with the normalised external loads in the form of heatmaps. These heatmaps are classified for each combination of microgeometrical parameters. Moreover, the obtained database could be implemented in external calculation software that permits friction torque estimates in early design stages, with more accuracy than the expressions offered in design guidelines.

Resumen

En los últimos años, ha habido un aumento significativo en las instalaciones onshore y offshore de energía eólica, según la IEA. Los rodamientos de vuelco permiten el giro de guiñada y cabeceo en las turbinas eólicas de pala. Se caracterizan por sus grandes dimensiones comparados a los rodamientos convencionales y son diseñados para soportar las grandes cargas axiales, radiales y de momento introducidas por el viento.

Esta tesis doctoral se centra en la modelización estructural y el cálculo de par de fricción de los rodamientos de vuelco de cuatro y ocho puntos de contacto. Sin embargo, las soluciones propuestas en este trabajo pueden ser adaptadas a otros tipos de rodamientos de vuelco, como son los rodamientos de vuelco de rodillos cruzados, entre otros.

En la realización de este trabajo de investigación, se han considerado ciertas hipótesis que han sido clave en la toma de decisiones y han condicionado el flujo de trabajo:

- Anillos rígidos: si bien un rodamiento sujeto a una carga axial puede ser modelado por simetría cíclica, esto no es cierto bajo cargas radiales o momentos de vuelco. Este tipo de cargas provocan unas deformaciones en los anillos que afectan a la distribución de fuerzas en los elementos rodantes, no cumpliendo así con los requisitos para emplear dicha simetría. A su vez, las rigideces de los elementos colindantes al rodamiento dictan en gran medida la forma que toman estas deformaciones y, por tanto, afectan a la distribución de fuerzas.

  Por tanto, una de las principales hipótesis es la consideración de anillos rígidos, que permite el desarrollo de un más general de cálculo.

- Deslizamiento puro: en trabajos de investigación del estado del arte se ha observado que las regiones en adhesión del contacto bola-pista pueden afectar a la cinemática de las bolas. Sin embargo, para el caso de rodamientos de vuelco, donde los modelos de par de fricción permiten independizar el problema de distribución de fuerzas del problema de par de fricción, otros trabajos han demostrado que estas regiones no afectan al par de fricción del rodamiento.

  Por tanto, se considera la hipótesis de deslizamiento puro en los contactos bola-pista, permitiendo así un cálculo más rápido del par de fricción sin perdidas de precisión de cálculo.

- Fricción de Coulomb: los rodamientos de vuelco empleados en turbinas eólicas de pala se caracterizan por los pequeños movimientos oscilatorios que realizan para ajustar el ángulo de ataque de las palas y orientación de la góndola. En estos casos, la lubricación de los contactos bola-pista se encuentra a medio camino entre una elasto-hidrodinámica y una lubricación límite. Modelar este estado de lubricación requiere de un trabajo costoso y aumentaría el coste computacional del modelo. Sin embargo, asumiendo un coeficiente de fricción que puede ajustarse de forma experimental es una solución práctica y a su vez extendida que simplifica el problema y permite abordarlo de una forma más general, solución equivalente a la primera hipótesis.

  Por tanto, se emplea el modelo de fricción de Coulomb, donde la fuerza de fricción se define como el producto de un coeficiente de fricción por las fuerzas normal del contacto.

Teniendo en cuenta las hipótesis anteriores, este trabajo ha realizado unas mejoras en el cálculo del par de fricción y en las técnicas de simulación de rodamientos de vuelco. La imagen de a continuación muestra esquemáticamente las principales aportaciones del este trabajo.

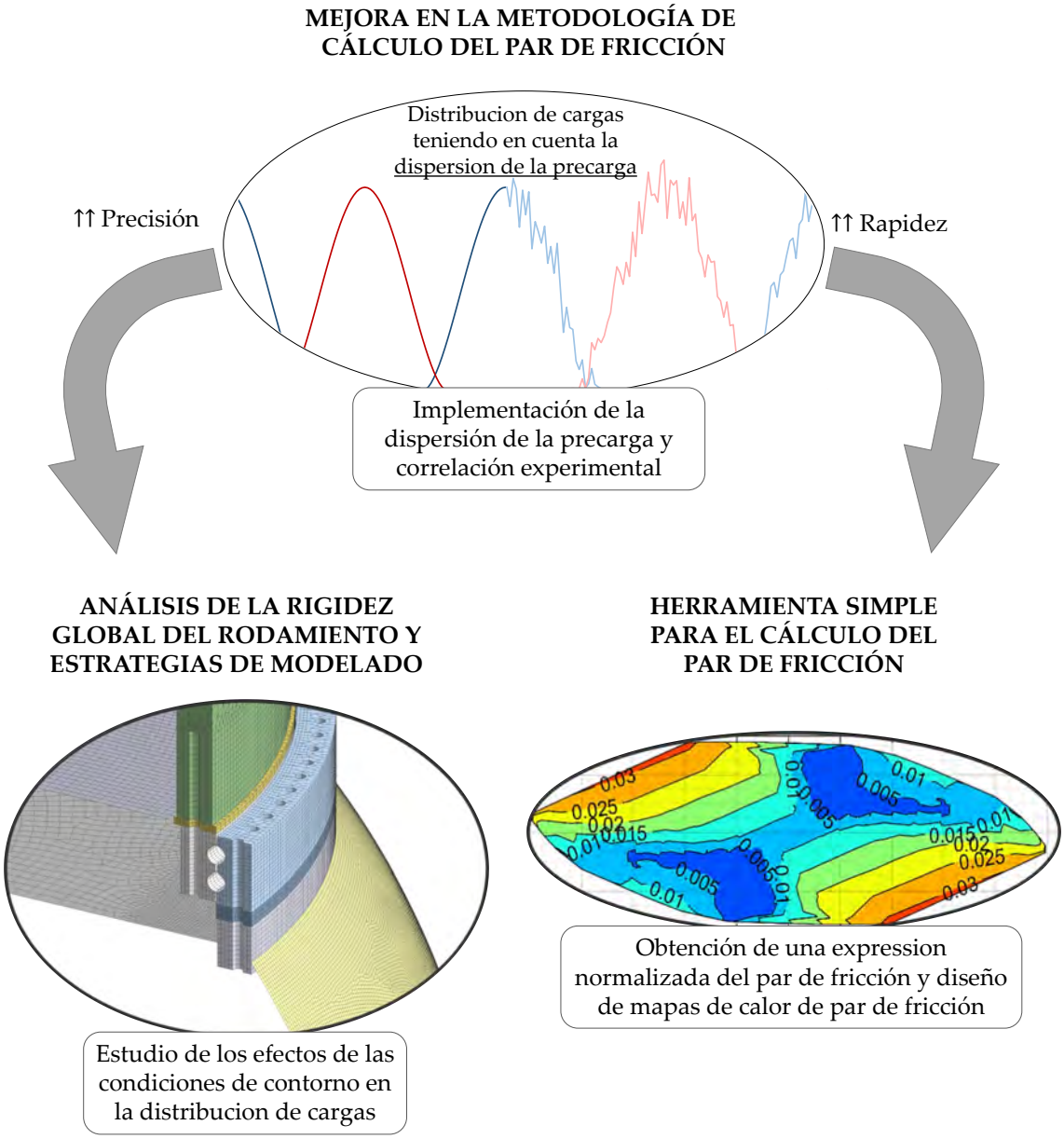

A continuación, se resume el flujo de trabajo, las tomas de decisiones y las conclusiones obtenidas durante la realización de esta tesis doctoral:

- Bajo la suposición de grandes dimensiones y bajas velocidades de rotación, es posible separar el problema de distribución de fuerzas del de par de fricción. De este modo, se implementa una dispersión de precarga en la fase de cálculo de distribución de fuerzas, para posteriormente calcular el par como la suma de la contribución de cada una de las bolas al par de fricción. Se realizan múltiples cálculos variando los parámetros de ajuste del modelo analítico para conseguir ajustar los resultados de par a los medidos experimentalmente. De estos ajustes, se observan ciertas

discrepancias cuando el rodamiento está sometido a momentos de vuelco, en especial para valores altos del mismo.

Por tanto, se realizan unos análisis mediante EF, sin dispersión de la precarga, para resolver el problema de distribución de fuerzas, que son posteriormente introducidos en la herramienta analítica en el paso de cálculo del par de fricción. Estos resultados de par ajustan mejor los ensayos experimentales, con lo que se demuestra que es necesario tener en cuenta la flexibilidad del rodamiento y os componentes que lo rodean para un buen cálculo del par de fricción.

Finalmente, se logra una nueva metodología que permite calcular el par de fricción de forma más precisa, y se proponen unas guías para el cálculo del par de fricción en función de los datos que se conozcan.

- Queda demostrado que la hipótesis de anillos rígidos es un delimitante en el modelo analítico. Por tanto, se decide ahondar en el estudio de la flexibilidad de los rodamientos mediante elementos finitos. Para ello, se emplea un modelo de un ensamblaje real de pala-rodamiento-buje de turbina eólica, lo cual permite analizar el rodamiento bajo condiciones de contorno reales. Se emplean y comparan diferentes técnicas de modelización y simplificación de elementos, como la sustitución de las uniones atornilladas por elementos más simples y su simplificación, la simplificación del modelo del rodamiento por tres muelles que caracterizan su rigidez o el estudio de un material diferente de pala que no solo podría simplificar su modelado sino permitir reducir los costes de ensayar los rodamientos. Los resultados de los análisis muestran la importancia de los elementos colindantes y la buena modelización de las condiciones de contorno a la hora de calcular la distribución de fuerzas en el rodamiento, lo cual afecta en gran medida al par de fricción, como se mencionaba en el apartado anterior.

  En este trabajo, también se han realizado avances en el mecanismo de Daidié, el cual permite sustituir las bolas de los rodamientos mediante muelles de rigidez no lineal. La mejora obtenida permite que el error cometido en el cálculo de distribución de fuerzas se vea reducido cuando el rodamiento está bajo una carga radial, en especial en las bolas menos cargadas. Si bien esto no afecta en gran medida a la rigidez global del

rodamiento, es un avance importante ya que el par de fricción se ve afectado principalmente por estas bolas.

- Se presenta una nueva metodología más eficiente para el cálculo del par de fricción que complementa a la presentada en el primer apartado, la cual era más precisa pero computacionalmente costosa. Se obtiene una expresión normalizada del par de fricción, que depende únicamente de la microgreometría del rodamiento y de las fuerzas externas aplicadas al mismo. Se crea un diseño de experimentos (DoE) a partir de esta formulación que, mediante una extensiva campaña de simulaciones, se obtiene una base de datos de resultados de par de fricción normalizados.

  Finalmente, se presenta una nueva herramienta de cálculo del par de fricción que relaciona el par de fricción normalizado con las cargas externas normalizadas, en forma de mapas de calor. Estos mapas de calor son generados y clasificados para cada una de las combinaciones de microgeometría analizadas. Además, la base de datos de par de fricción obtenida puede ser implementada en un software de cálculo externa, de forma que permita estimar el par de fricción de los rodamientos en etapas tempranas de diseño, con mayor precisión que las expresiones que se proponen en catálogos y guías de diseño actuales.

Contents

List of Figures

List of Tables

List of Symbols and Acronyms

Symbol	Description
C	Constant parameter for the friction torque
C_{0a}	Axial load-carrying capacity
C_{0r}	Radial load-carrying capacity
C_{0m}	Tilting moment load-carrying capacity
D_{ext}	External diameter of the bearing
D_{int}	Internal diameter of the bearing
D_w	Ball diameter
D_{pw}	Pitch diameter of the ball set
E	Young modulus
F_a	Bearing axial force
F_a^n	Normalised bearing axial force
F_r	Bearing radial force
F_r^n	Normalised bearing radial force
H	Bearing height
K	Contact stiffness constant
m	Mean effective preload
M	Bearing tilting moment
M^n	Normalised bearing tilting moment
n	Number of ball rows
p	Preload level

$\boldsymbol{Q_{i,\psi}}$	Ball load in contact diagonal i with angular position ψ
$\boldsymbol{r^{ap}}$	Distance between the friction force differential and the axis of the bearing
$\boldsymbol{R_c}$	Radius of the raceway
$\boldsymbol{s}$	Osculation ratio
$\boldsymbol{SD}$	Standard deviation of the effective preload
$\boldsymbol{seed\ no.}$	Seed number to generate the random numbers
$\boldsymbol{T_i}$	Contribution of ball number i to the bearing friction torque
$\boldsymbol{T}$	Bearing friction torque
$\boldsymbol{T^n}$	Normalised bearing friction torque
$\boldsymbol{Z}$	Number of balls per row
$\boldsymbol{\alpha_0}$	Ball-raceway initial contact angle
$\boldsymbol{\alpha_{i,\psi}}$	Ball-raceway contact angle in contact diagonal i with angular position ψ
$\boldsymbol{\beta}$	Ball rotation angle
$\boldsymbol{\gamma}$	Angular direction of the shear stress
$\boldsymbol{\Delta_\alpha}$	Contact angle variation
$\boldsymbol{\Delta_a}$	Initial axial distance between raceway curvature centres
$\boldsymbol{\Delta_a^n}$	Normalised initial axial distance between raceway curvature centres
$\boldsymbol{\Delta_r}$	Initial radial distance between raceway curvature centres
$\boldsymbol{\Delta_r^n}$	Normalised initial radial distance between raceway curvature centres
$\boldsymbol{\delta_a}$	Bearing axial displacement
$\boldsymbol{\delta_a^n}$	Normalised bearing axial displacement
$\boldsymbol{\delta_r}$	Bearing radial displacement
$\boldsymbol{\delta_r^n}$	Normalised bearing radial displacement
$\boldsymbol{\delta_\theta}$	Bearing angular displacement
$\boldsymbol{\delta_\theta^n}$	Normalised bearing angular displacement
$\boldsymbol{\delta_p}$	Ball-raceway interference due to preload
$\boldsymbol{\delta_{lim}}$	Ball-raceway contact deformation limit

$\boldsymbol{\delta_{i,\psi}}$	Ball-raceway contact deformation in contact diagonal *i* with angular position ψ
$\boldsymbol{\rho, \theta}$	Cylindrical coordinates for shear stress integration in contact ellipses
$\boldsymbol{\mu}$	Coefficient of friction
$\boldsymbol{\mu_a}$	Apparent coefficient of friction
$\boldsymbol{\psi}$	Ball angular position

Acronym	Description
ADM	Análisis y Diseño Mecánico
BEAT	Bearing Endurance and Acceptance Test rig
BEM	Boundary Element Method
CEM	Contact Element Method
DoF	Degrees of Freedom
DoE	Design of Experiments
FE	Finite Element
FEM	Finite Element Method
GWEC	Global Wind Energy Council
HAWT	Horizontal Axis Wind Turbine
IEA	International Energy Agency
INSA	Institut National des Sciences Appliquées
ISO	International Organization for Standardization
IWES	Institute for Wind Energy Systems
LaMCoS	Laboratoire de Mécanique des Contacts et des Structures
MSE	Mean Relative Error
no.	Number
NREL	National Renewable Energy Laboratory

RCF	Rolling Contact Fatigue
RMSE	Root Mean Square Error
SE	SuperElement
TS	Technical Specification

1 Introduction

1.1 Context and motivation

The use of renewable energies is growing around the world, especially wind and solar energy. According to the International Energy Agency (IEA), the global renewable energy capacity has increased by 113% from 2015 to 2021, reaching 2408.5 GW by the end of 2021 [1,2], which is approximately 28% of the worldwide-generated electricity. The forecast is to reach 4500 GW of world renewable energy capacity by 2024 [3]. The evolution of the energy capacity produced by each technology can be seen in Figure 1.1. In 2022, the Global Wind Energy Council (GWEC) reported [4] a 9% increase of new wind power capacity since 2021, reaching a total capacity of 906 GW. The forecast according to IEA [1] is for onshore wind additions to increase from 74 GW in 2021 to 109 GW in 2027. In addition, global annual offshore wind installations are expected to increase 50% to over 30 GW in 2027. Moreover, the European Commission countries stated their long-term goal of installing 317 GW [5] of offshore renewable energy by 2050.

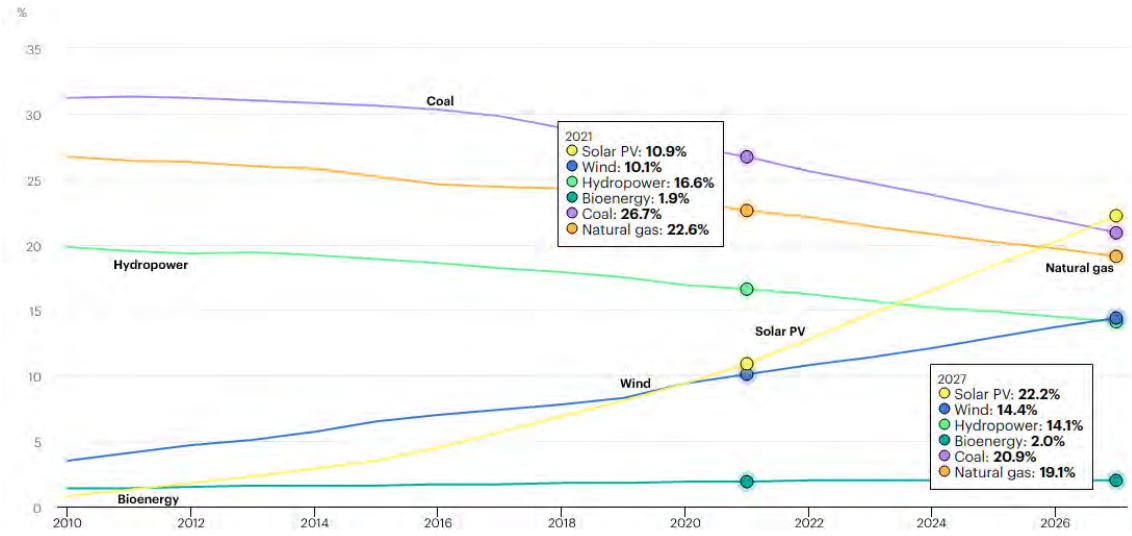

Figure 1.1. Share of cumulative power capacity by technology [6].

In the wind energy sector, three-bladed horizontal-axis wind turbines (HAWTs) are the most common type of turbines. They range from small turbines for residential use to large turbines in commercial wind farms. These wind turbines consist of several main parts, including the blades, rotor hub, nacelle and tower. The nacelle, located on top of the tower, rotates to adjust the orientation (yaw) of the turbine to the wind direction. The hub is attached to the nacelle, which rotates to generate electrical energy. The blades rotate (pitch) around their axis relative to the hub to maximise performance and regulate electrical energy generation. Pitch and yaw rotations are possible thanks to the slewing bearings that this research work focuses on. Figure 1.2 below shows the location of these bearings on a bladed wind turbine.

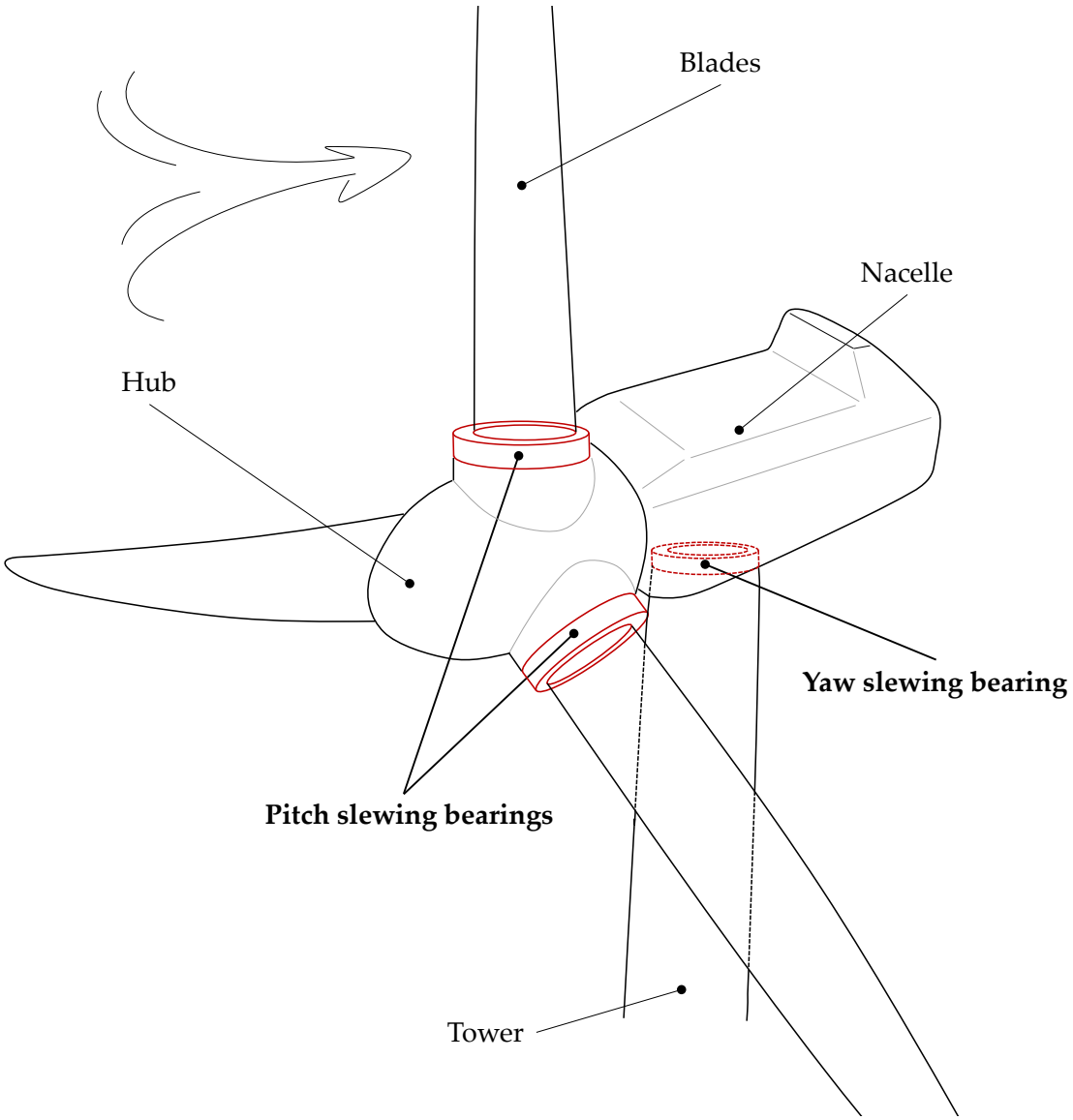

Figure 1.2. Pitch and yaw bearings of a blade wind turbine.

These bearings bear the loads generated by the wind forces, the weight of the components and the centrifugal forces due to the rotation of the blades (see Figure 1.3). These variable high loads make it necessary to design and manufacture the bearings with specific materials and technologies that allow them to withstand prolonged operating conditions over time. In addition, they must also meet safety, reliability and durability requirements to avoid turbine operation failures. Therefore, proper selection of slewing bearings and their regular maintenance is critical to ensure the efficiency and lifetime of bladed wind turbines. This has resulted in significant interest in the research and development of slewing bearings in the industry, which has led to the development of mathematical models to simulate the mechanical behaviour of these bearings under different operating conditions.

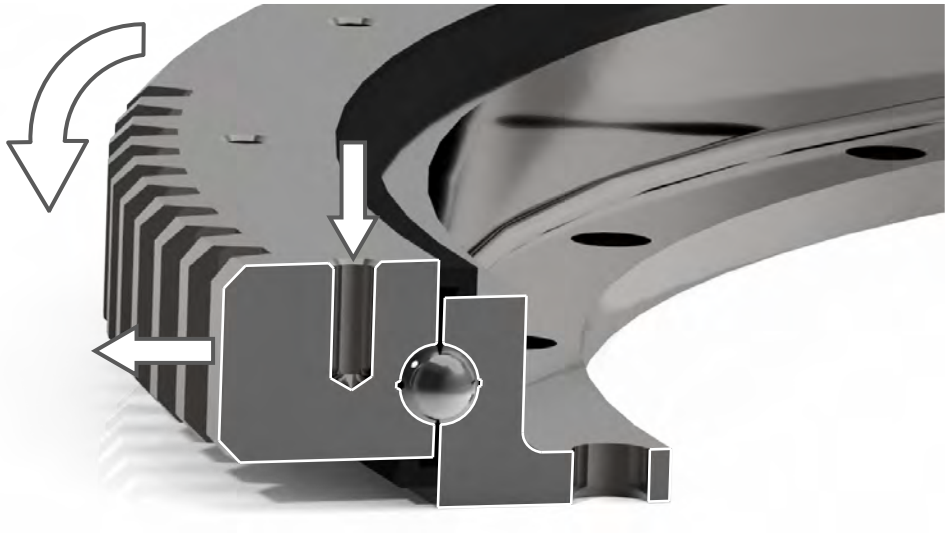

Figure 1.3. Four-point contact slewing bearing model and acting loads.

This can be seen not only in the research field but also in the large number of slewing bearing manufacturers of this type found around the word, as shown in Figure 1.4. Indeed, slewing bearings are not only used in the renewables energy sector (bladed wind turbines and solar tracking systems), but also in a variety of industries, such as construction (tower cranes and concrete pumps), mining (bucket-wheel excavators and conveyor systems), space (radio telescopes) and robotics (robotic arms), among others (Figure 1.5). Given the wide variety of applications, their dimensions can vary enormously. However, due to their orientation-focused use, all of these applications share the same design requirements: they rotate or oscillate at slow speeds and support axial, radial and moment loads simultaneously, as shown in Figure 1.3.

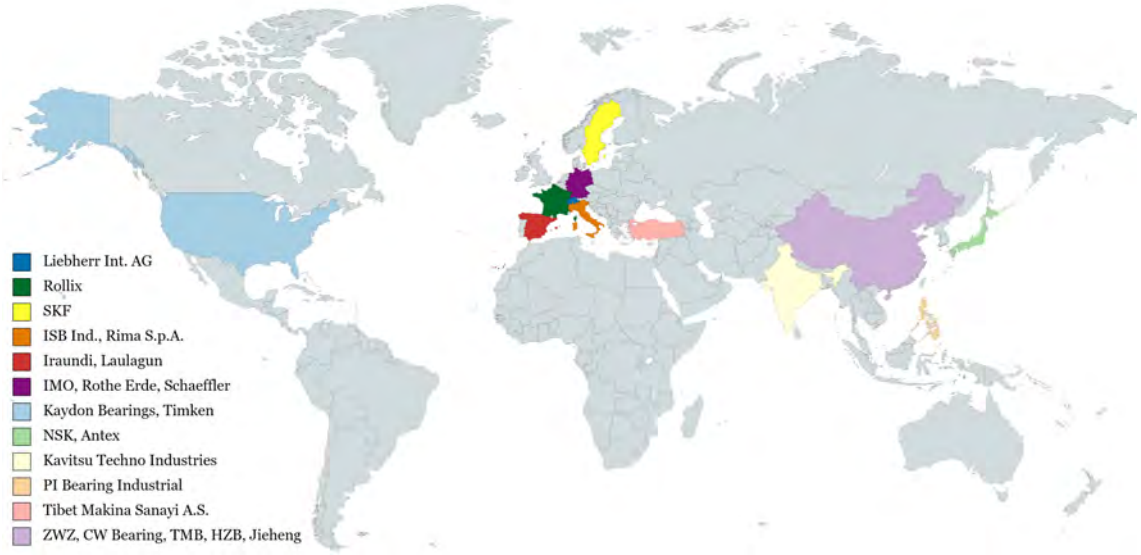

Figure 1.4. Showcase of worldwide slewing bearing manufacturers.

Due to the importance of slewing bearings, the Mechanical Analysis and Design (ADM [7]) research group, from the Faculty of Engineering of Bilbao at the University of the Basque Country (UPV/EHU), has conducted extensive research in the field during the recent years. The group has collaborated with manufacturing companies such as Iraundi S.A. and NBI Bearings; international research entities such as Fraunhofer IWES, NREL and LaMCoS; and research laboratories such as INSA Lyon, leading to numerous significant contributions to the scientific community in the form publications [8–25] and many national and international conferences [26–34]. Their work has led to progress in the mechanical modelling of slewing bearings, particularly in wind energy applications. The group's close relationship with the industry has allowed for a better understanding of current industry demands, ensuring their research remains both relevant and impactful. This Doctoral Thesis is based on the most recent progress made by the ADM group in this field, more specifically for four-point and eight-point contact slewing bearings, which the following section focuses on.

Figure 1.5. Slewing bearing applications.

1.2 Slewing bearings description

1.2.1 Slewing bearing parts

This section provides a general description of these bearings, explaining the different parts (see Figure 1.6) and their characteristics. As there are different types of slewing bearings, the main differences between these are described later in Section 1.2.2.

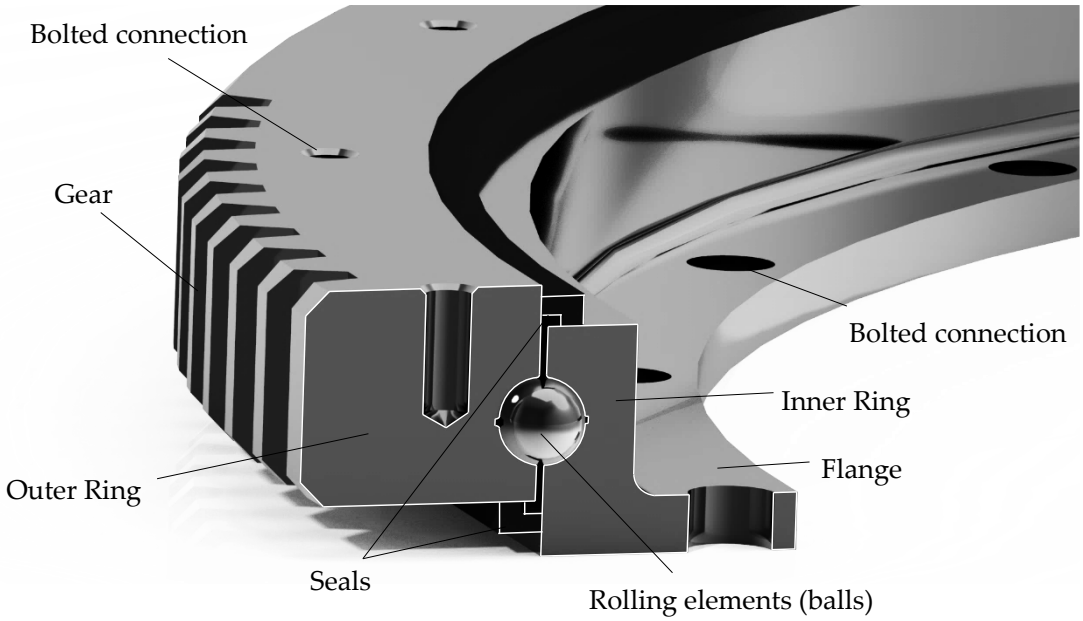

Figure 1.6. Representation of the parts of a four-point contact slewing bearing.

The general parts of slewing bearings are as follows:

- Rings: slewing bearing rings consist of an inner ring and an outer ring. These are typically made of carbon steel, but in some types of bearings, such as wire-race bearings, rings are also made of aluminium alloys, or even polymers or composite materials. The raceways are machined in the rings, which are usually case-hardened to ensure a surface with good wear properties. The rolling elements are in contact with the raceways of both of these rings.

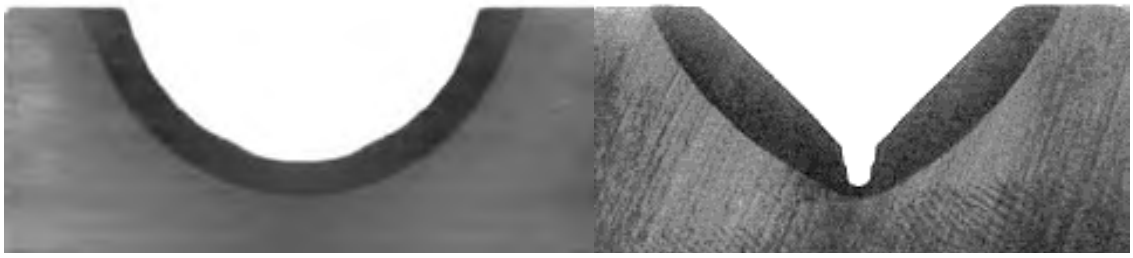

Figure 1.7. Hardened pattern and detail of the raceway of a ball-raceway (left) and a roller-raceway (right) [35].

The main macrogeometric parameters used to define a bearing are: the height (H), the internal diameter (D_{int}), the external diameter (D_{ext}) and the mean diameter (D_{pw}), as shown in Figure 1.8. This last one, also called the pitch diameter of the rolling set, is most commonly used to indicate the bearing size. In slewing bearings, the mean diameter is characterised by being much larger than the rolling element size (D_w). Because of this, these bearings are known for being more slender, and usually larger, than general purpose bearings, and thus, the rings are more flexible.

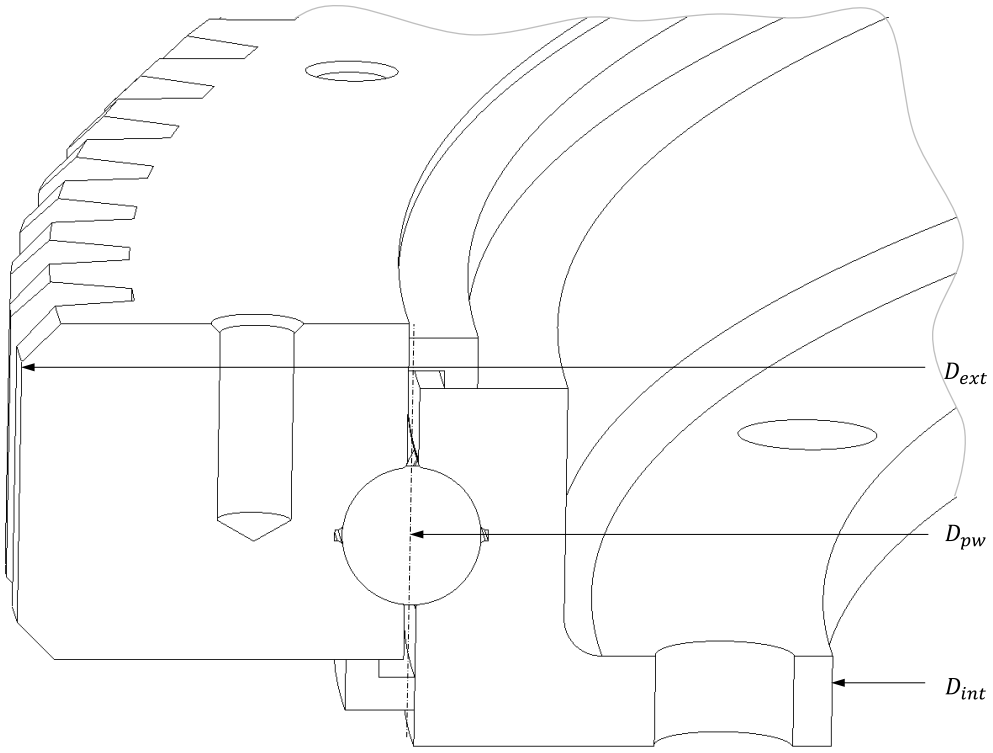

Figure 1.8. Representation of a slewing bearing and its main macrogeometric parameters.

- Rolling elements: depending on the design requirements, the rolling elements can be either balls or rollers. Both of them are mostly

manufactured with chromium alloy steel. The type of contact they make with the races is what differentiates them.

The ball-raceway contact (Figure 1.9a), usually named "point contact", takes an elliptical shape under load. The load is transmitted from the races to the balls, at a certain contact angle (α, α_0 when the bearing is unloaded, see Figure 1.9), which varies depending on the acting loads. Also, depending on the ball diameter compared to the curvature of the races (R_c), the contact ellipse becomes bigger with the load. The relationship between the raceway diameter and the rolling element diameter is known as osculation ratio ($s = D_w/2R_c$). These parameters are shown in Figure 1.10.

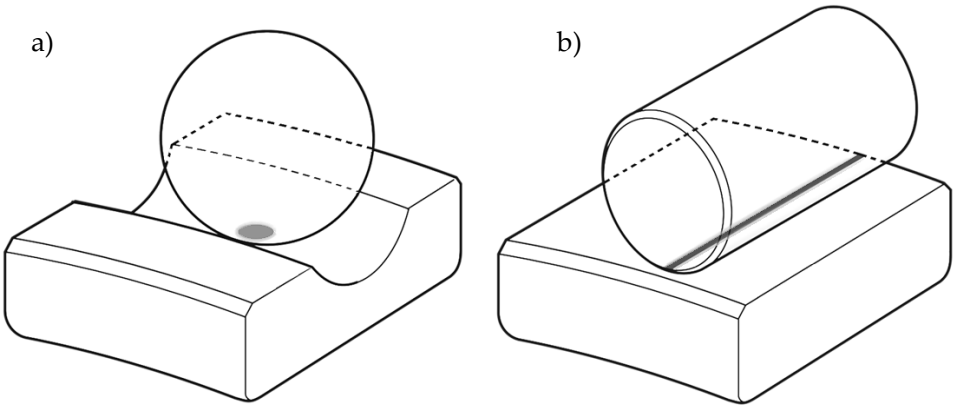

Figure 1.9. Ball-raceway point contact (a); roller-raceway line contact (b).

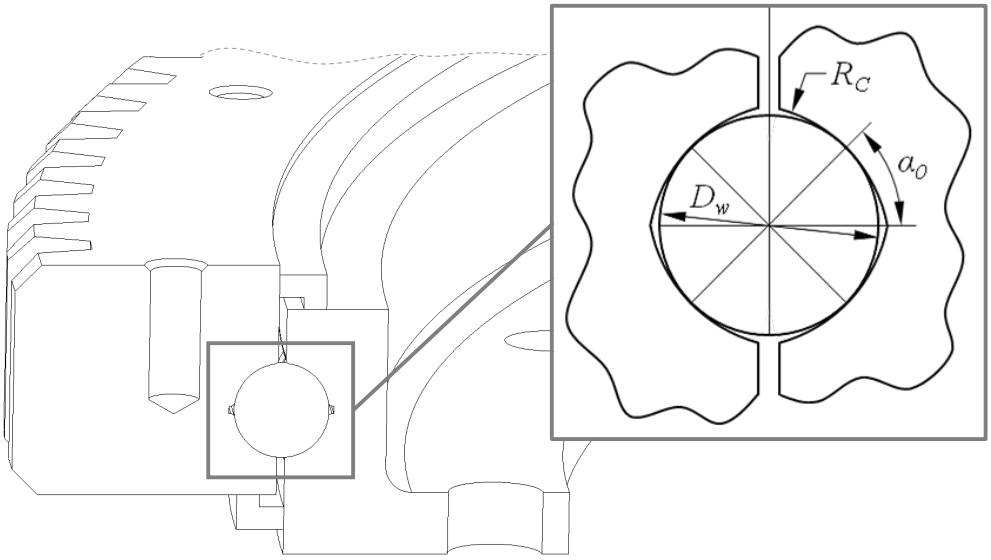

Figure 1.10. Four-point contact slewing bearing section detail.

On the other hand, the roller-raceway contact is called a "line contact", and the patch is rectangular for straight roller bearings (Figure 1.9b). There are numerous roller profiles (spherical, crowned, logarithmic and so on, see Figure 1.11), each one with its benefits and drawbacks.

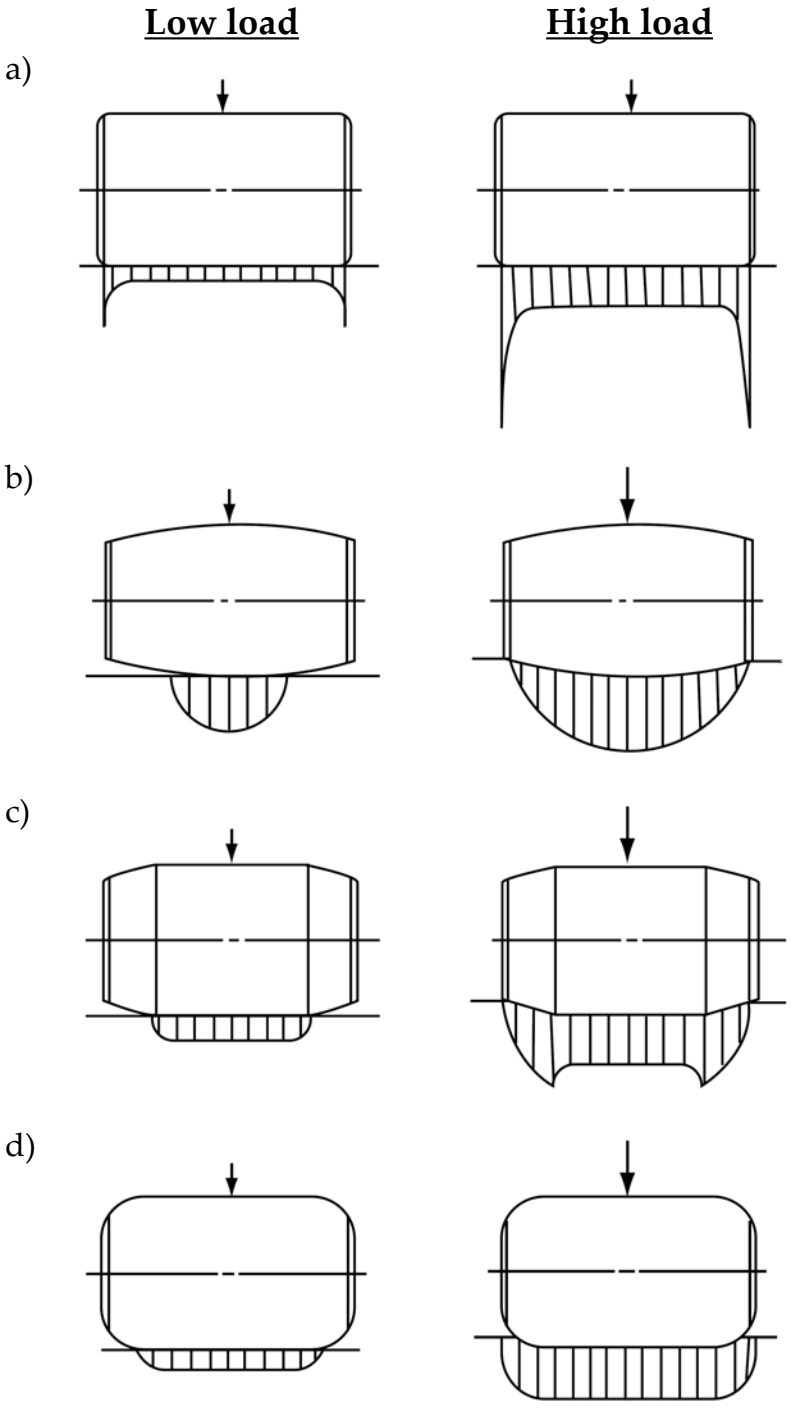

Figure 1.11. Roller-raceway contact load shape for different roller profiles: straight (a), crowned (b), partially crowned (c) and logarithmic (d) [36].

The main difference between balls and rollers lies in the higher static capacity of roller bearings due to the increased roller-raceway contact area. However, this leads to roller bearings exhibiting higher frictional forces. In addition, while the manufacturing of roller bearings is simpler, the mounting process for ball bearings is much easier.

It is common for slightly oversized rolling elements to be mounted on both roller and ball bearings. This means that the diameter of the assembled rolling element is higher than the space left between the races. This is commonly called the preload of the rolling elements (δ_p), and it usually consists of a few microns of deviation from the nominal diameter. This preload can also be affected by the manufacturing errors of the races or the assembly process of the bearing to the structures. The preload is used to remove any vibration caused by clearances between the rolling elements and the raceways. Also, the preload causes an increase in the stiffness of the bearing, which implies an increase in the bearing movement accuracy [20]. However, high preloads could lead to less room to load the balls before failure, a substantial increase in the friction torque and high wear rates. In practice, the preload level can be estimated by measuring the idling friction torque [25], since larger preloads involve larger friction torques when the bearing is unloaded.

- Separating elements: these can be spacers or cages. Both of these elements have the same purpose: to separate the rolling elements and avoid any contact between them during the bearing operation. These elements ensure their correct arrangement and, without them, the rolling elements would end up interfering with each other, which could result in a reduction in the capabilities of the bearing. The performance of the spacers or the cages is similar, and both are manufactured in plastic or metal. Spacers are sometimes replaced with slightly smaller balls.

- Bolted connections: there are two main types of bolt holes that can be machined in the bearing rings or the bearing flanges. One type consists of mounting holes (Figure 1.12), which are used to connect the bearing to the surrounding structures. These are uniformly and usually evenly arranged in the outer and inner rings. However, sometimes the inner ring has more holes as it withstands higher tilting moments compared to the outer ring.

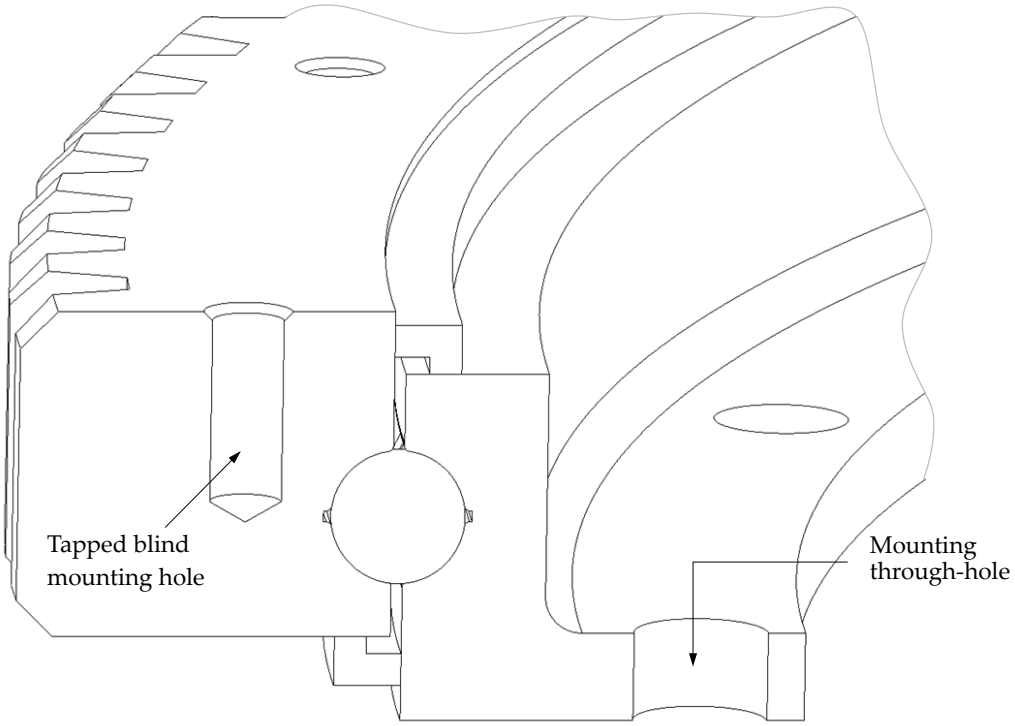

Figure 1.12. Representation of mounting holes of a slewing bearing.

The second type of hole is the assembly hole (Figure 1.13), which is used in the case of slewing rings separated into two parts. The purpose of this separation is to fill and assemble the bearing, and only one of the rings (outer or inner) is separated, and thus, the assembly holes are only present in one of the rings.

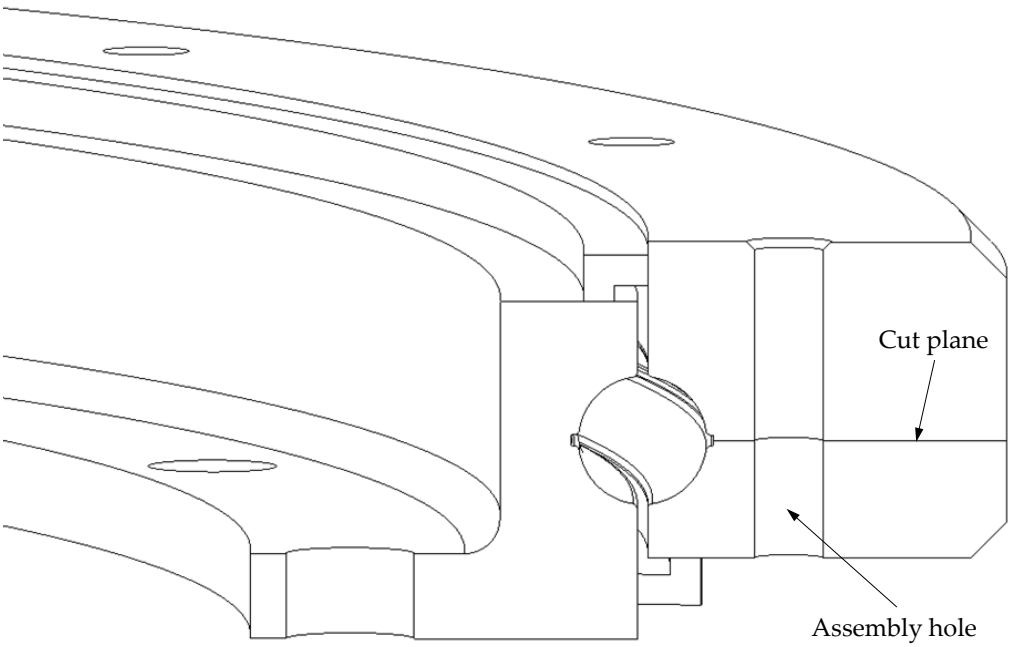

Figure 1.13. Representation of the assembly hole and cut plane of a slewing bearing.

- Load plug: the machining of assembly holes and halving the bearing race can be avoided by using a load plug. This consists of a radial hole in one of the rings, which allows the rolling elements to be inserted into the raceways. After that, the load plug is inserted into the hole, which has the raceway machined into it, providing a continuous raceway. This was a solution patented by INA-Schaeffler for wire-race bearings [37], but it is more commonly used for four-point contact slewing bearings. An example of the load plug on a bearing is shown in Figure 1.14.

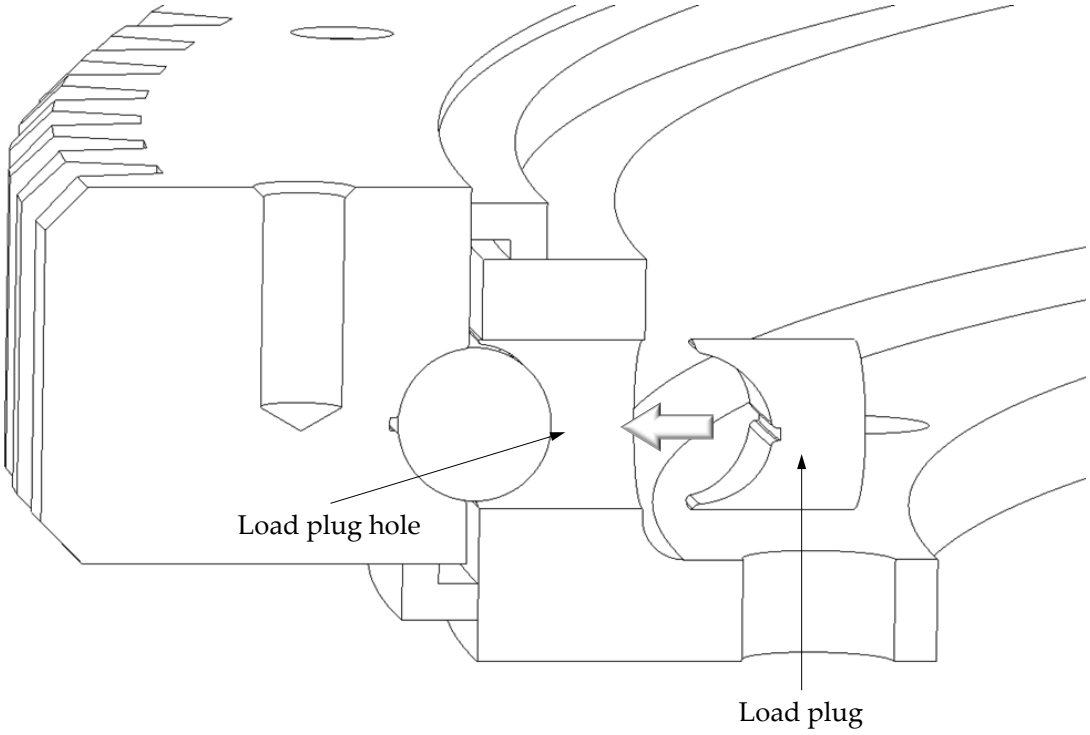

Figure 1.14. Representation of a load plug in a slewing bearing.

- Lubricant: there is at least one lubricating hole on each of the bearing rings. These holes allow the raceways to be fed with grease and are normally in the radial direction of the bearing. Advanced bearing technologies ensure the bearing is properly lubricated by an automated system that regularly replenishes the lubricant, providing the bearing with this maintenance task.

- Seals: these elements are located between the rings (see Figure 1.15), preventing dust, water and other undesired elements from entering the bearing. They also minimize leakages, reducing the maintenance required regarding lubrication. Seals are more relevant when the bearings are working in adverse environments with substances that could impair the

performance of the bearing, such as seawater in offshore platforms, or sand particles from deserts in onshore platforms. The seals are typically made of NBR.

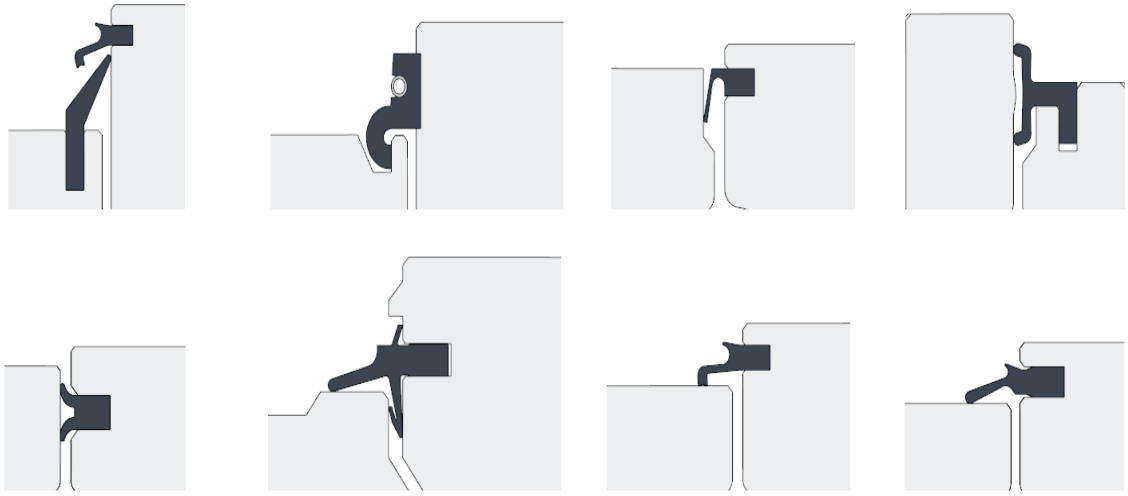

Figure 1.15. Bearing sealing examples [38].

- Gear: the gears of these bearings are driven by an electric motor, which performs the relative movement of one ring with respect to the other. They can be machined on the inner or outer ring, depending on the application. These gears are mainly spur gears, but they can also be helical and worm gears. There are cases when the gear is machined on a different element connected to the bearing, reducing the cost and complexity of the bearing design. The gear teeth are usually case-hardened.

1.2.2 Slewing bearing types

Slewing bearings can be classified based on the rolling element type, the number of contacts and the number of rows. This has affected how different literature works and how manufacturers refer to the same bearings.

Table 1.1 provides a list of the different types of slewing bearings arranged in an appropriate order, which are then described.

Table 1.1. Breakdown of the most common slewing bearings.

	One row	**Two rows**	**Three rows**
Balls	Four-point contact slewing bearing	Eight-point contact slewing bearing / Two-row four-point contact slewing bearing Double-row angular contact slewing bearing	-
Rollers	Crossed-roller slewing bearing	Double-row angular contact roller slewing bearing	Triple-row roller slewing bearing
Mixed	-	Double-row roller-ball slewing bearing	Triple-row roller-ball slewing bearing

Four-point contact slewing bearings and crossed-roller slewing bearings (Figure 1.16) are single-row slewing bearings with their races machined directly on the rings. The former contains balls as rolling elements, while the latter usually has cylindrical rollers. Four-point contact slewing bearings are so called because the balls have four points of contact, i.e. two contact diagonals, which provide the bearing with the ability to withstand axial forces, radial forces and tilting moments.

In contrast, the rollers of crossed-roller slewing bearings have only two contact lines, which again means one contact diagonal per rolling element. This is why the rollers are assembled alternating their orientation so that each roller diagonal has the contact angle opposite to the previous one. In this way, each pair of crossed rollers is topologically equivalent to a four-point contact ball.

These two bearings differ precisely because of this composition of rolling elements, which, as mentioned in the previous section, gives the crossed-roller slewing bearings a higher load capacity, while the four-point contact slewing bearings have a lower friction torque, in the case of an equivalent size of rolling elements and bearing mean diameter.

Figure 1.16. Four-point contact slewing bearing (left) and crossed-roller slewing bearing (right) [39].

The eight-point contact slewing bearings, also called two-row four-point contact slewing bearings, are basically the same as four-point contact slewing bearings, but with a second row of balls exactly the same as the first, with almost the same bearing dimensions. This results in a bearing with a higher capacity than the previous ones while maintaining the advantage of low friction torque values. This type of bearings should not be confused with double-row angular contact ball slewing bearings, as the latter are characterised by having two rows of balls, each of which has two-point angular contact balls (see Figure 1.17).

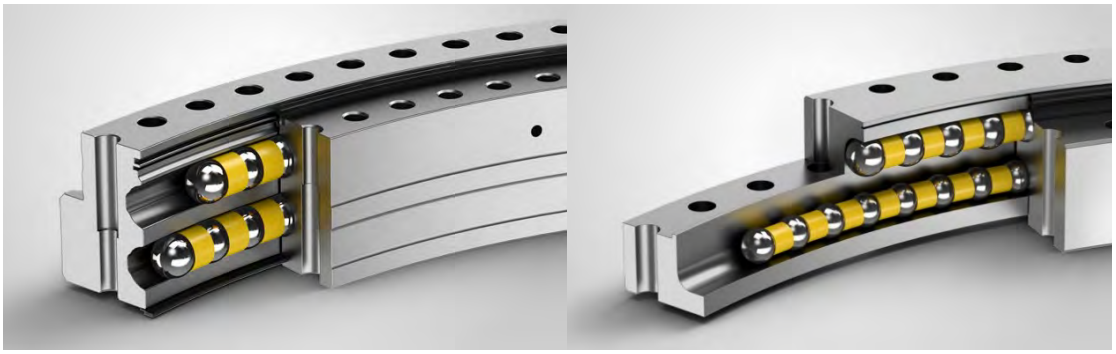

Figure 1.17. Two-row four-point contact wire race slewing bearing (left) and double-row angular contact slewing bearing (right) [39].

When it comes to double-row slewing bearings designs, the crossed-rollers arrangement is not commonly used. Instead, there are double-row angular contact roller bearings (see left image of Figure 1.18), consisting of two rows of rollers, where the contact angle of one row is rotated by 90° with respect to the other row. This arrangement allows each row to bear the loads the other row is unable to. In addition, triple-row roller slewing bearings, as the name suggests, also use rollers as rolling elements, with the advantage of an additional row of rollers. This way its capacity is increased with its size, making these bearings more suitable for large-scale applications, with the drawback of their increased

cost and friction torque. On these bearings (see right image of Figure 1.18), the two rows of parallel rollers withstand the axial and tilting moments, while the perpendicular one bears the radial forces.

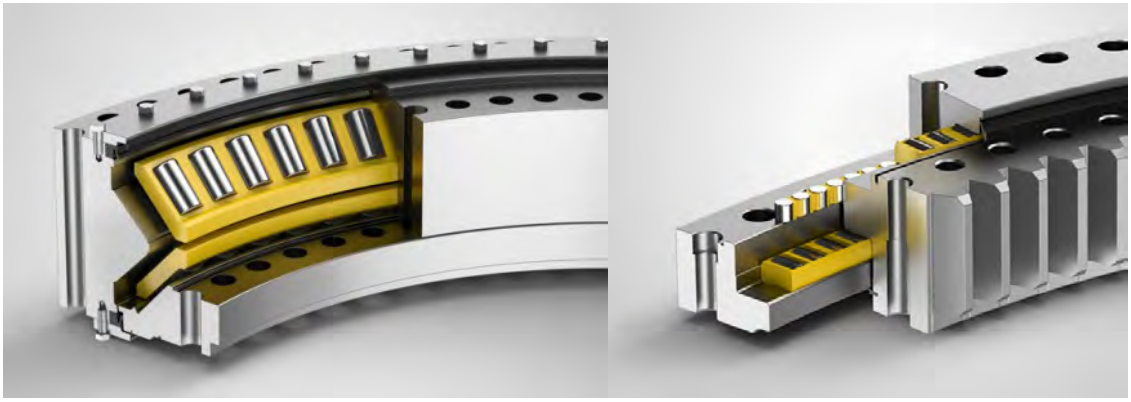

Figure 1.18. Double row angular contact roller slewing bearing (left) and triple row roller slewing bearing (right) [39].

Some bearings use both types of rolling elements, such as double-row roller-ball slewing bearings (see the left image of Figure 1.19). These are characterised by having a row of rollers, arranged in a similar way to thrust roller bearings, and another row of two-point angular contact balls. As these bearings are designed to support high axial loads in one direction, the rollers are sized to support most of the axial load, while both rollers and balls support the radial load and tilting moment. The same mixed use of rolling elements is seen in triple-row roller-ball slewing bearings (see right image of Figure 1.19). This design is similar to triple row roller slewing bearing with balls as main rolling elements, and rollers as auxiliary rolling elements placed in the middle row, to support radial forces.

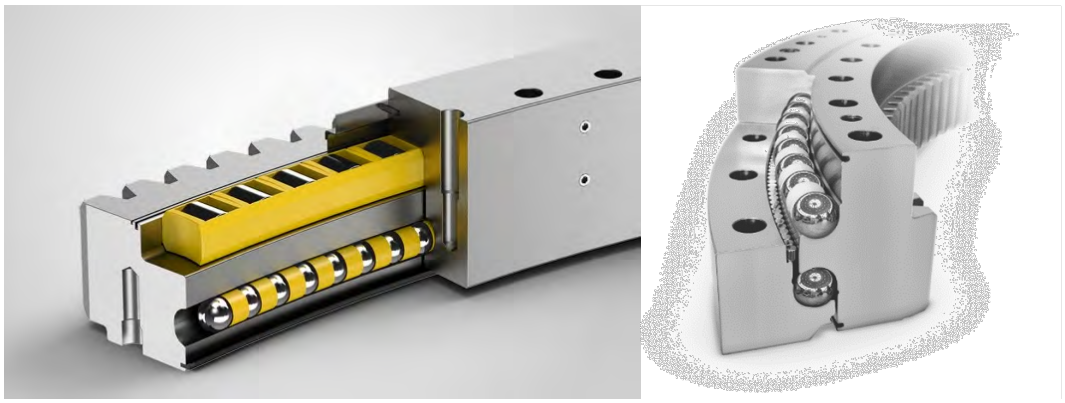

Figure 1.19. Double row roller-ball slewing bearing (left) [39] and triple row roller-ball slewing bearing (right) [40].

All of these variants have their advantages and disadvantages; however, the type of slewing bearing most used in modern and large wind turbine applications is the two-row four-point contact slewing bearing.

Besides the aforementioned bearing types, others use wires between the ring and the rolling elements. The four-point contact wire race slewing bearings and crossed-roller wire race slewing bearings (Figure 1.20) share the same properties and differences with their equivalent slewing bearings without wires. The installation of the wires allows a compact form factor to be maintained while reducing the weight of the bearing due to the by using lighter alloys in the rings.

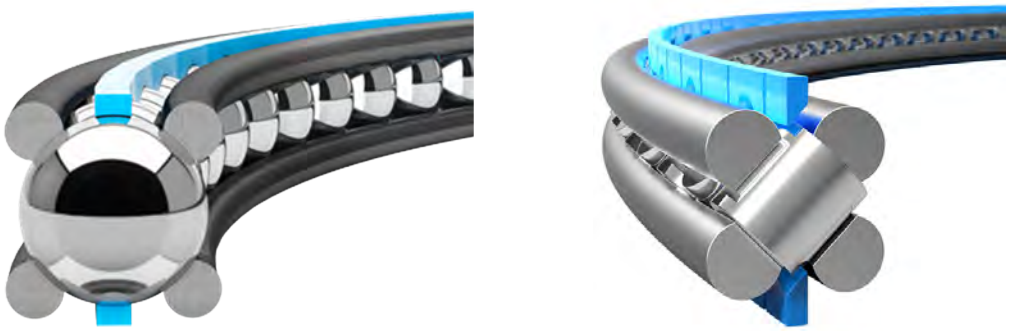

Figure 1.20. Four-point contact wire race slewing bearing (left) and crossed-roller wire race slewing bearing (right) [41].

These other mentioned bearings can also be seen with wire races: double-row angular and triple-row wire race roller slewing bearings, as shown in Figure 1.21.

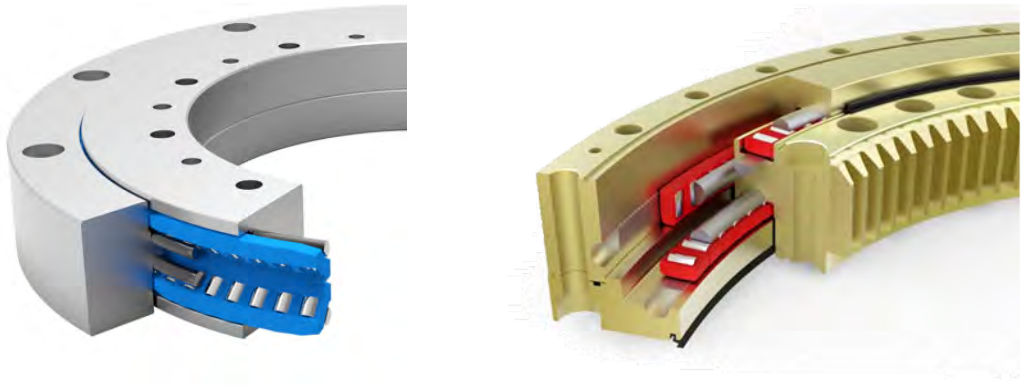

Figure 1.21. Double-row angular wire race contact roller slewing bearing [41] and triple-row wire race roller slewing bearing.

1.2.3 Failure modes

Just like conventional bearings, slewing bearings can fail due to various factors. ISO 15243:2017 [42] describes various failure mechanisms and modes for any type of bearings; however, many of them are related to high angular velocities or other factors that do not concern slewing bearings. In this section, the failure modes related to slewing bearings are classified depending on the bearing parts involved:

- Outer/inner ring: one of the failure modes of the rings is caused by tooth breakage and its crack propagation. The high load conditions under which these bearings operate can cause static fatigue failure on the gear teeth whose crack propagates through the bearing rings. Additionally, dust and other environmental contaminants can cause tooth abrasion, pitting, or corrosion, hastening gear failure. Furthermore, the rings can fail due to crack propagation through the mounting holes. Loads are transmitted through them from the surrounding structures, which can lead to fatigue cracking. Aside from that, the rings are prone to failure due to structural fatigue caused by the large deformations of the bearings.

- Raceways: Since the operating mode for these bearings is at low speeds, they can be equated to quasi-static cases and therefore certain faults can be grouped together and referred to as static faults. One of these failure modes occurs when the static load carrying capacity is exceeded, due to extreme loads leading to high contact loads, resulting in permanent deformation of the raceways, i.e. indentations. In addition to this, under extreme loads the ring deformations can be excessive, which together with a suboptimal bearing design, leads to the ball-raceway contact patch reaching the edges of the races, generating stress peaks and permanent deformations (Figure 1.22). On top of that, core crushing is another type of static damage that can occur as a result of the hardness difference between the hardened surface and the core of the ring.

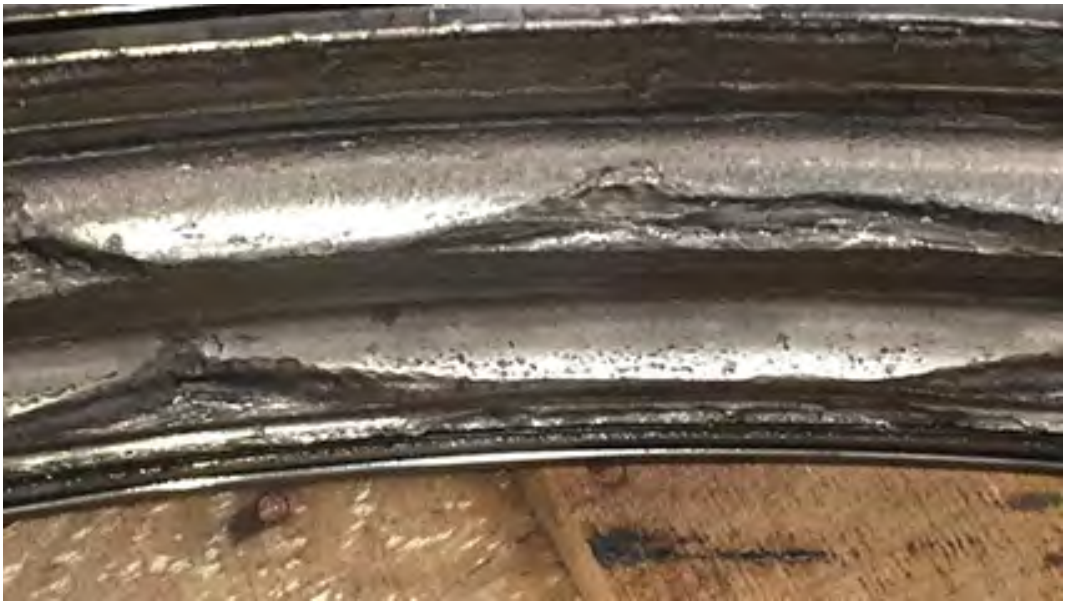

Figure 1.22. Edge loading (contact truncation) failure [43].

Another type of failure that races may experience is related to Rolling Contact Fatigue (RCF) where core crushing can also occur. However, this type of failure is more typical in conventional bearings due to their high rotational speeds. Meanwhile, slewing bearings rotate in an oscillating and non-continuous manner, so the fatigue life calculation specified in the standards is not applicable and needs to be adapted. Nevertheless, a non-static failure that is related to these bearings is wear and false brinelling. The term false brinelling exists to define the failure mode of a bearing under lubricated contact conditions, where adhesive wear occurs. This failure mode is very similar to fretting corrosion, which is excessive wear occurring under dry contact conditions. Both of these failures can be seen in Figure 1.23.

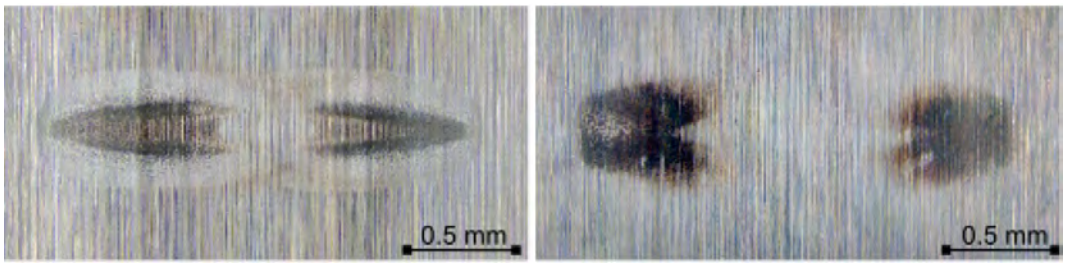

Figure 1.23. False brinelling (left) and fretting corrosion (right) [44].

In addition, pitting and wear are two factors that increase the probability of this phenomenon. Proper quality control of the manufacturing, correct heat treatment of the raceways, as well as proper design and analysis of

the bearing under operating load conditions can prevent or reduce these damages.

In general, these types of raceway failures are very important in conventional bearings that rotate at full speed, as they induce vibrations and noises that lead to poor performance. By contrast, in the case of slewing bearings, they involve greater rotation problems, such as an increased friction torque, which are inconvenient but do not result in the bearing having to be replaced, as long as it can continue rotating.

- Cage: high ring deformations can cause large deformations and increased wear on the cages, as well as fatigue fracture due to alternating loads. This causes improper ball-raceway contact, resulting in increased wear of these components and, as a result, bearing malfunction. A crack or the complete breakage of the cage could cause the bearing to stop rotating, which could involve the bearing being replaced.

Figure 1.24. Cage fracture [43].

- Lubricant: the presence of debris, lubricant degradation due to poor maintenance, or incorrect lubricant selection can all result in incorrect viscosity, preventing the bearing from functioning properly. Incorrect

lubricant quantity can also cause the lubricant to cause additional failures that affect the performance of the bearing. These failure modes can include increased wear, pitting, rust and even indentation of the debris.

- Seals: adverse environmental conditions cause increased wear and accelerated material ageing, which, combined with large deformations, can result in lubricant loss and contamination.

The following table summarises the damage modes mentioned above due to various possible causes:

Table 1.2. Ball slewing bearing failure modes.

Rings	Raceways	Cage	Seals	Lubricant
Structural fatigue	Indentation	High deformations	High deformations	Incorrect viscosity
Gear contact fatigue	Edge loading	Wear	Abrasion/ Wear	Debris and contamination
	Core crushing	Fracture	Material ageing	Degradation of the properties
	Rolling contact fatigue			Incorrect amount
	Pitting			
	Wear			
	False brinelling			

1.3 Slewing bearing selection criteria

As this work focuses on one and two-row four-point contact slewing bearings, the following section will focus on the aspects of these when it comes to design or selection criteria. However, most of the bearings share similar aspects, so these should be applicable to all types of slewing bearings, with their corresponding standards or equivalent guidelines.

1.3.1 Static load-carrying capacity

While the dimensions of the bearings are mostly imposed by the elements they are connected to, they must be able to perform correctly under operating load conditions. To this end, there is the static load carrying capacity, which indicates the maximum load that a bearing can support. However, although this load is defined as the maximum permissible axial force (or axial load-carrying capacity C_{0a}), radial force (or radial load-carrying capacity C_{0r}) or tilting moment (or tilting moment carrying capacity C_{0m}) of the bearing, it is actually related to the maximum permissible contact deformation between rolling elements and raceways. Standard ISO-76 [45,46] proposes that the maximum acceptable deformation of a bearing is 0.0001 times the diameter of the rolling elements. This value is defined in such a way that it is acceptable in all bearing applications, taking into account the most heavily loaded rolling element or raceway contact. This ensures the proper operation of any bearing so it does not generate unforeseen noises or vibrations, as well as premature fatigue failures under low lubricated conditions. This same standard also indicates that, as an approximate way of avoiding such permanent deformation, the rolling elements should not reach a maximum contact pressure, which varies depending on the rolling elements, as indicated in Table 1.3.

Table 1.3. Maximum pressure allowed for each type of rolling element [45].

	Self-aligning ball bearings	***Other ball bearings***	***Roller bearings***
Maximum pressure [MPa]	4600	4200	4000

Because of this, the corresponding value of maximum ball-raceway contact pressure for four-point contact slewing bearings is 4200 MPa. The external load that generates this maximum permissible pressure at the most heavily loaded ball-raceway contact is called the static load capacity. The standard provides formulae that allow the load capacity to be calculated under certain assumptions, such as, for example, the invariance of the ball-raceway contact angle and the neglection of the flexibility of the rings or the surrounding structures. Moreover, as mentioned above, three acting loads can be applied to a bearing and thus, there are three load-carrying capacities, whereas ISO-76 standard only proposes

formulae that allow calculating two of them: the axial load carrying capacity (1.1) and the radial load carrying capacity (1.2).

$$C_{0a} = f_0 \, Z \, D_w^2 \sin \alpha_0 \tag{1.1}$$

$$C_{0r} = f_0 \, i \, Z \, D_w^2 \cos \alpha_0 \tag{1.2}$$

The works of Aguirrebeitia et al. [8,20] introduce the concept of general static load capacity, which not only allows the static load capacity of a tilting moment to be calculated, but also defines an acceptance surface that takes into account any combination of the three acting loads. Furthermore, this method takes into account the effects of the contact angle variation and the preload. However, a disadvantage is that it does not account for the flexibility of the rings, as well as the standard, for which the FEM is still the preferred choice.

Continuing with the ISO-76 standard, this follows calculation criteria that are devised for conventional bearings, which normally have through-hardened rings and small dimensions, and the adjacent elements usually provide high stiffness. However, when it comes to slewing bearings, due to their large dimensions, the raceways are case-hardened by procedures such as induction, which does not harden the entire ring body but rather only a depth of millimetres, depending on the process. In addition, these bearings are thinner, which means that they are partially affected by the stiffness of the elements they are connected to. In fact, the standard does not consider failure modes affecting bearings with case-hardened raceways, as was studied by Lai et al. [47] and Gönz et al. [48], where, due to differences in material properties after the hardening process of the races, in addition to residual stresses from the process, the bearings could fail as a result of sub-surface fracture nucleation, also known as core crushing. In these studies, they also observed that indentation failure was more common in bearings where the thickness of the hardened layer was not deep enough.

In addition, the standard does not cover another failure mode, which affects all types of ball bearings: the truncation of the contact ellipse. This is because as a load is applied to the bearing, the contact angle of the ball-raceway changes. This can lead to the contact patch reaching the limits of the raceway as shown in Figure 1.25, resulting in stress concentrations that can exceed the pressure and deformation limits mentioned above. This tends to occur on the most heavily loaded balls since, in addition to the variation of the contact angle, the load on

the balls tends to increase, so the contact ellipse size also increases, which accelerates the aforementioned effect.

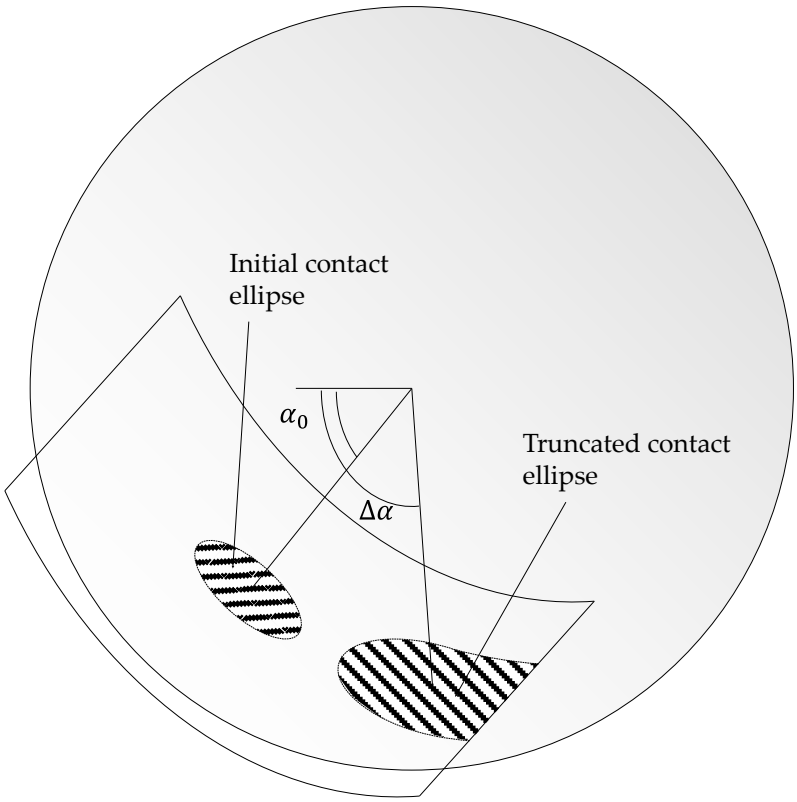

Figure 1.25. Outline of the contact ellipse truncation due to a high contact angle and the lengthening of the ellipse area.

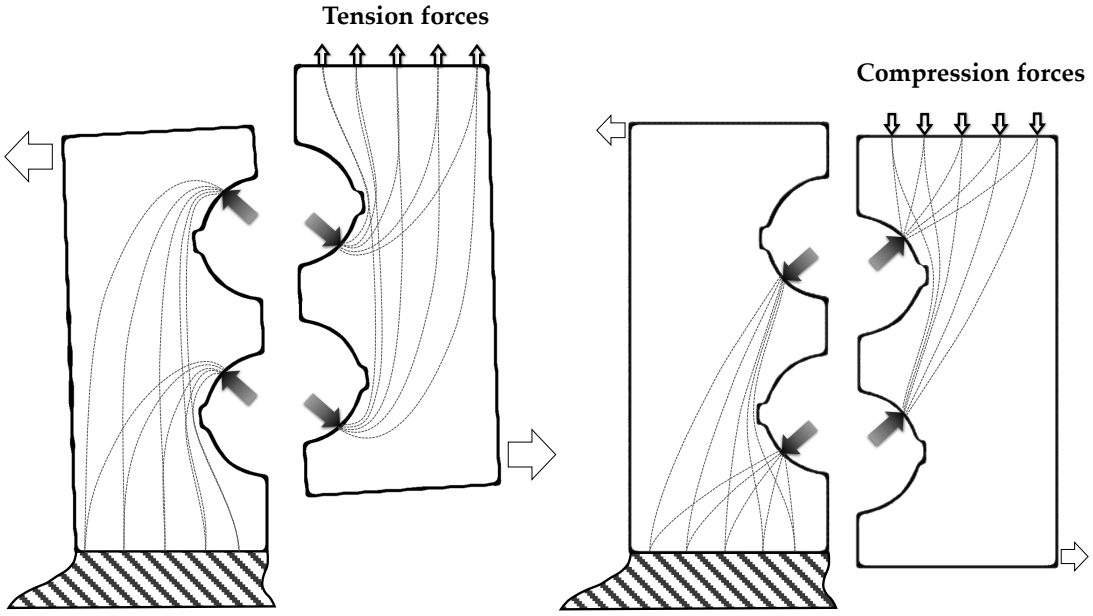

Figure 1.26. Force lines and deformation of the rings for tension and compression forces.

However, this can also occur because of the flexibility of the rings. For example, four-point contact slewing bearings tend to show greater flexibility at the furthest edges from the bolted connection (see Figure 1.26). Therefore, when a slewing bearing zone is subjected to tension, a more rapid change in contact angle ($\Delta\alpha$) is observed, and truncation is more likely to occur. Figure 1.26 shows the bearing deformations subjected to tension and compression forces, as well as the force lines, which lead to greater ring deformations.

1.3.2 Stiffness

Another parameter that determines bearing behaviour is its stiffness, which can be defined as the relationship between the displacement of one ring relative to the other and the applied load. The aforementioned standard does not specify anything about the design criteria for bearings considering their stiffness. In this sense, as a general rule, the greatest stiffness is sought, while complying with other design criteria, such as static load capacity, weight and friction torque.

Four-point contact slewing bearings are slender bearings whose deformations are highly affected by the surrounding elements. Therefore, when calculating the stiffness of these bearings, the boundary conditions of the model and typical assumptions such as rigid rings have a significant effect on the results. Ignoring the effect of these assumptions can lead to an overestimated stiffness, induced by elements that do not represent reality, underestimating the possible final deformations of the whole structure, as shown above in Figure 1.26.

The current state of the art proposes models where rigid rings are considered as the surrounding elements are often unknown. However, the FEM method is the way forward as models of varying levels of complexity can be modelled. This allows calculations to be performed to measure the stiffness provided by the bearings parts, and also to take into account the flexibility of the surrounding structures.

1.3.3 Friction torque

Friction torque is the action that resists bearing rotation. This action is generated by the friction forces occurring at the contacts in the bearing. In bearings with rolling elements, the friction forces are generated at the contact between the rolling elements and the raceways. Rolling elements usually have a rolling motion with sliding. This means that, in the case of ball bearings, one part

of the contact ellipse is pure rolling (stick) and the other part is sliding (see Figure 1.27). The resulting forces on the contacts oppose the natural motion of the rolling elements, the sum of which produces a resulting moment that opposes the bearing rotation.

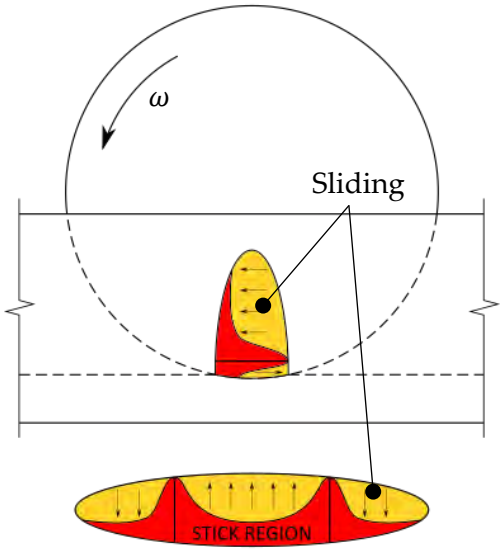

Figure 1.27. Contact ellipse stick and slip regions which produce friction forces [25].

Because of this, the contact patch shape and its forces are the main factors affecting the friction forces of each contact and this is why several factors can influence the friction torque, such as the type of rolling elements, the design of the raceways, their surface quality, the lubrication, the load the bearing is subjected to, among others.

In contrast to bearing stiffness, friction torque should be as low as possible, and this is a key criteria in the selection of a bearing, as it is an indicator of its performance. Low friction torque results in high efficiency as the power required to rotate the bearing decreases. Similarly, in the case of bearings used for power generation, it leads to higher energy efficiency. Conversely, as a result of lubricant deterioration, high friction torque values can be reached, increasing the wear and reducing the performance of the bearing. Optimizing the bearing geometry and the preload of the rolling elements, as well as appropriate lubrication and maintenance systems can help to reduce friction torque and its negative effects.

Since calculations using numerical models such as FEM (Finite Element Method), BEM (Boundary Element Method) or CEM (Contact Element Method) are computationally expensive, several analytical models in the literature allow

for estimating the friction torque by making some simplifications. However, bearing manufacturers often use their own formulae based on their experience. There are also design guidelines, such as the Wind Turbine Design Guideline (DG03) [49] by NREL (National Renewable Energy Laboratory), which offers a very simplified and easy-to-use expression (1.3) to obtain a rough estimate of the friction torque (T) as a function of the external loads, bearing mean diameter and an apparent coefficient of friction (μ_a).

$$T = \mu_a \frac{D_{pw}}{2}\left(\frac{4.4M}{D_{pw}} + 2.2F_r + F_a\right) \tag{1.3}$$

Slewing bearings are designed to withstand external forces, to be rigid enough to not deform or interfere with other elements, and to have enough preload - and thus precision - to avoid erroneous operation. All of this affects the final friction torque of the bearing, which must be overcome when rotating it. Calculating the friction torque is therefore critical to avoid selecting the incorrect drive motor. A correct estimation of the friction torque allows for an equilibrium to be reached between the load-carrying capacity and its performance. In addition, friction torque can be used as a quality control indicator, where a big difference from the reference value may indicate a problem during the manufacturing and assembly process. The present Doctoral Thesis focuses its main research line on friction torque.

1.3.4 Dynamic load-carrying capacity and fatigue

Although the static capacity of a bearing has been discussed above, the fact is that most bearings are subjected to variable loads. Even if the loads were stationary, the rotation of the bearing would cause varying loads on the rolling elements. It is therefore necessary to set the dynamic capacity parameter of a bearing and its fatigue life. Again, standard ISO 281:2007 [50] and its expanded modification ISO/TS 16281:2008 [51] propose a simplified procedure that allows for it to be calculated. Some manufacturer catalogues also provide some guides that allow for the calculation of the bearing lifetime, accounting for the surface finish, geometrical parameters, acting loads and lubrication among others, but focus mainly on conventional bearings.

However, slewing bearings do not reach the same high rotating speeds as conventional bearings. These bearings operate by oscillating from a reference

point at different speeds in order to direct the component in the right direction and withstand very high loads, such as wind forces in the case of bladed wind turbines. Therefore, given the specifics of these bearings, no fatigue criterion has yet been established in the current standards that take into account all the possible operating conditions in which they can be used.

All these intricacies have aroused a great deal of interest in the research community, from offering methods to calculate the lifetime of these bearings to monitoring the bearings to predict their forthcoming failures, i.e. Houpert et al. [52], a research work that proposes an alternative method to calculate the bearing life in oscillating components by implementing corrective coefficients to the standard formulae. However, while this Doctoral Thesis will not deal with dynamic bearing design, many of the concepts used and conclusions drawn from this work will provide, albeit less significantly, certain insights that will enable a better bearing life calculation.

1.4 Literature review of slewing bearings

There is an extensive list of ISO standards [53] relating to rolling bearings. However, these standards are intended for general bearings and are difficult to apply to slewing bearings because they have very specific characteristics that do not share with ordinary bearings. Despite this, there is an extensive list of research works that are widely used in the design, manufacturing and testing of ball slewing bearings. This section compiles a list of these research works classified according to the topics involved in this Doctoral Thesis. Nonetheless, some of these deserve to be mentioned first, as although they are related to conventional bearings, they cover a wide range of topics and are recognised, used and referenced in most research and design works, such as the study by Harris and Kotzalas [36,54]. These works are so extensively detailed that they can be used for all types of bearings. In addition, the National Renewable Energy Laboratory (NREL) published a guideline (DG03) [49] for wind turbine bearings, which Harris also took part in, along with Rumbarger and Butterfield, which is worth mentioning because of its specialized focus on slewing bearings. Recent research works by Stammler et al. [55,56] outlines the major differences and updates that the new version of DG03 will cover as "the DG03 does not reflect today's state of the art, yet it is referred to…". These works discuss some topics

such as the minimum requirements for FE modelling and inaccuracies in the friction torque formula.

The table below contains a summary of the research papers that will be explained descriptively in the following sections in a structured manner, to not only provide the necessary knowledge for this work, but also to illustrate the evolution of literature as a function of the interaction between different studies focused on different topics and the resources available at the time. The most relevant works related to this Doctoral Thesis will be described in more detail in the relevant chapters.

Table 1.4. Categorisation of the research work references.

Symbols: Analytical (A) – Finite Elements (FE) – Experimental (E)

Research interest	Description	*Method*	References
Load distribution problem	Normal contact theory	*A*	[57–61]
		FE + A	[62]
	Load-carrying capacity and load distribution models	*A+E*	[63–66]
		A	[8,9,19,67–73]
		A+FE	[12,20,23,27,74]
		FE	[21,75–78]
	Ball-raceway normal contact models	*FE*	[79–82]
	Experimental testing and validation	*FE + E*	[83–85]
		E	[86–88]
Friction torque problem	Simple formulae	*A+E*	[89,90]
		A	[40,49,91,92]
	Formulae with multiple friction sources	*A*	[93–101]
	Tangential contact theory	*A*	[102–119]

	Ball-raceway frictional contact models	*A*	[25,88,120–126]
		FE+A	[12,23–25]
	Experimental testing and validation	*E*	[84,90,127–134]
Bearing Global Stiffness	Rigid boundary models	*A*	[71,135–138]
	Flexible boundary models	*A*	[139–141]
		A+FE	[10,12,23,74,142]
Fatigue life	Standards and guidelines	-	[49–51]
	Contact fatigue	*FE*	[143–145]
		E	[146–152]
Lubrication and wear	False brinelling and fretting corrosion	*E*	[44,153–157]
	Coefficient of friction	*E*	[31,99,100,124]
Condition monitoring	Failure prediction and monitoring techniques	*E*	[87,158–163]
	Experimental testing and sensorisation	*E*	[84,127–134]

1.4.1 Load distribution model

The load distribution problem tries to obtain the balance between the external forces or displacements applied to the rings of a bearing with the contact forces generated on the rolling elements. For this purpose, it is necessary to solve the contact problem between the rolling elements and the raceways must be solved first.

The first remarkable approach to solve the point contact problem was done by Hertz [57,58], who solved it by assuming small elastic deformations compared with the curvature radius of the contacting bodies, which is also known as the Hertz theory. Furthermore, he assumed that the surfaces were non-conformal, without any imperfections and any friction forces, so that the contact problem

was only taking normal forces into account. The Hertz theory is partially applicable to ball slewing bearings, as the contact is non-conformal in the circumferential direction due to the large size of these bearings, leading to the small size of the contact area in that direction. However, it is highly conformal in the radial direction, as could be seen in the contact patch shown in Figure 1.28, where the size of the contact patch in that direction is larger. Aside from that, the friction loads can be significant on these bearings.

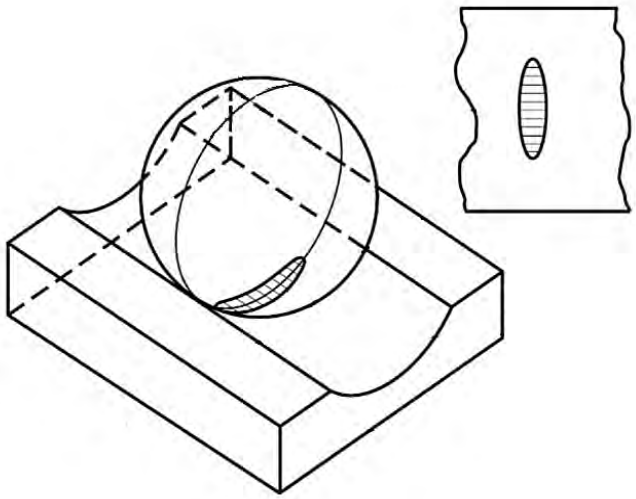

Figure 1.28. Ball-raceway contact ellipse detail [164].

Brewe and Hamrock [59] would later offer a simplified approach to solve the contact problem, which avoids solving the elliptic integrals of the Hertz theory. Their research work proposed explicit equations to calculate the major and minor semi-axes and the normal contact deformation of the contact ellipse. Later, Houpert would also develop a different approach to avoid the same elliptical integrals for both hertzian [60] and non-hertzian contacts [61]. His alternative offered some expressions based on tabulated constants, of which there were fewer and which simpler to understand and apply. Later, Pandiyarajan et al. [62] would show that the formulae from the Hertz theory would approximate the Finite Element (FE) calculations for large bearings quite well. His work compared the results obtained using the analytical formulae from the Hertz theory with the results obtained using the Finite Element Method (FEM) for an angular contact thrust bearing, obtaining a high degree of correlation between them.

When it comes to the load distribution of the applied loads among the rolling elements in a bearing, Stribeck [63–65] solved the problem for conventional ball bearings under various loads. Sjoväll [67] proposed a method to solve the load

distribution for a combination of axial and radial loads for both ball and roller bearings by means of load distribution integrals. Jones [68,69] proposed a model for radial ball and roller bearings under any load combination. However, the resulting equations were highly non-linear, so they needed to be solved using numerical methods. Rumbarger [70] proposed a method for the case of an axial load combined with a tilting moment generated by the eccentricity of the axial load, for a thrust bearing.

Several years later, Zupan and Prebil [165] developed a model for four-point contact slewing bearings to study the load-carrying capacity under combined loads. They also studied the effect of some geometrical parameters and compared the results considering both ideally stiff rings and elastic surrounding structures. An FE model was used to calculate the stiffness matrixes for the analytical model and the computed tangential stresses were compared with the experimental measurements. Meanwhile, Houpert [71] proposed an approach which considered the relative displacements between the rings of a bearing, consisting of three translations and two tilting angles.

Subsequently, Amasorrain et al. [72] adapted Jones' work and proposed a calculation procedure for the load distribution of the rolling elements in a four-point contact slewing bearing considering rigid rings, which was used as a reference for Olave et al. [74] to later implement ring deformations in her analytical model. The later research work, used superelements (SE) to obtain the stiffness matrix of the rings and surrounding structures for the analytical model.

Aguirrebeitia et al. proposed an interference model, based on a generalization of the equations presented by Sjoväll and Rumbarger, for calculating the load combinations that result in static failure for four-point contact slewing bearings [8], crossed-roller slewing bearings [27] and three-row roller bearings [9]. Later, Aguirrebeitia et al. enhanced the models to consider the variation of the ball-raceway contact angle [19] and the ball preload [20], which were based on Houpert's research work [60] to solve the contact problem.

Potočnik et al. [73] proposed a method for taking irregularities, clearances or ring deformations into account when solving the load distribution problem. Starvin and Manisekar [75] and Aithal et al. [76] used Finite Element Analysis (FEA) to calculate the effect of manufacturing errors on load-carrying capacity and load distribution in large-sized angular contact ball bearings, demonstrating

that they can be significant. Heras et al. [12,23] also proposed a methodology to calculate the load distribution problem considering ball preload, manufacturing errors and ring flexibility on four-point contact slewing bearings using analytical methods based on the minimization of potential energy. These research works also used FE calculations to obtain the stiffness matrix of a ring sector to be implemented into the analytical model.

Recent fast and significant advances in computational capabilities have enabled the calculation and validation of many models: numerical, analytical, and experimental. Because of this, a great deal of work has been focused on optimising the bearing FE modelling, which has enabled faster and more accurate load distribution calculations. In the research works mentioned below, different efficient modelling techniques are shown which strive to reduce the computational cost and the convergence problems linked to the non-linearity of the contacts.

In Golbach's research work [80] the balls were replaced with a four-node element (two on each of the raceways) that complied with the goal of simulating the elastic behaviour of the contact as well as the variation of the contact angle. To accomplish this, the centres of the raceways were rigidly connected to two points on the raceway itself. Then, to represent the stiffness of the contacts, both race centres were connected with a non-linear element. This element modelled the ball behaviour of two non-conformal elastic bodies based on the work conducted by Brewe and Hamrock [59] mentioned above.

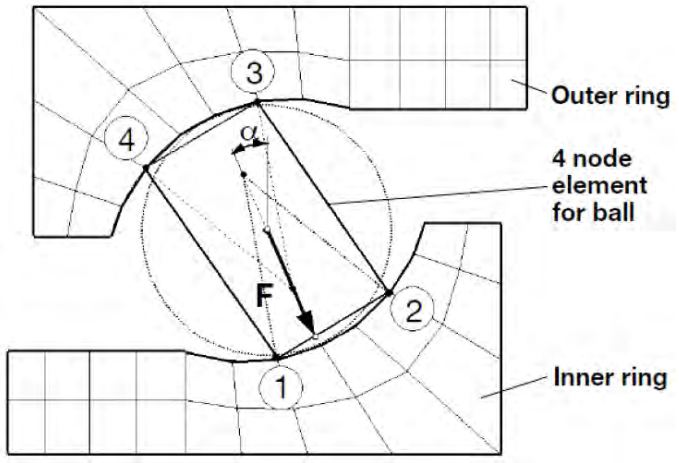

Figure 1.29. Proposed ball-raceway contact model by Golbach [80].

Later, Smolnicki et al. [81,82] proposed a model where the ball was removed and replaced with two rigid beams and one non-linear tension-only elastic

element, which represents the structural behaviour of the contacts. The rigid beams connected the raceways with their curvature centres and the non-linear elements of both of the centres. The load-deformation behaviour of the non-linear elastic element was defined by the potential function (1.4). C and η were parameters determined by FE analyses instead of hertzian contact formulation.

$$\delta = CQ^{\eta} \tag{1.4}$$

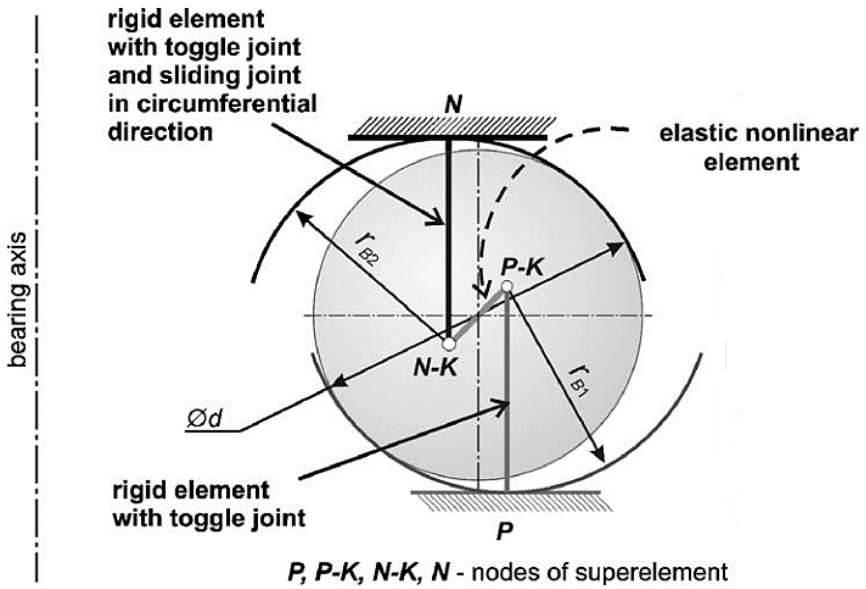

Figure 1.30. Proposed ball-raceway contact model from Smolniki [81,82].

The most remarkable contribution was proposed by Daidié et al. [79], who adapted the work of Golbach to four-point contact slewing bearings, replicating the model for each contact diagonal. In his work, the raceway centres were connected with tension-only spring elements. To represent the ball-raceway load-deformation behaviour with those elements, they applied Houpert's work [60]. The Daidié's mechanism was the best replacement for modelling ball-raceway contact, since it was developed for high osculation ratios. Because the elastic elements considered the contact stiffness, the raceway was stiffened by means of rigid shell elements. The rectangle size was defined by the semi-axes of the hypothetical contact ellipse the ball raceway contact would have. For this, they also used the approach proposed by Houpert [60] mentioned above. Finally, each raceway centre was connected to its corresponding stiffened raceway rectangle using rigid beams (see Figure 1.31). With all of this, the transmitted forces would not deform the raceway and they would be transmitted through the rigid beams to the elastic elements.

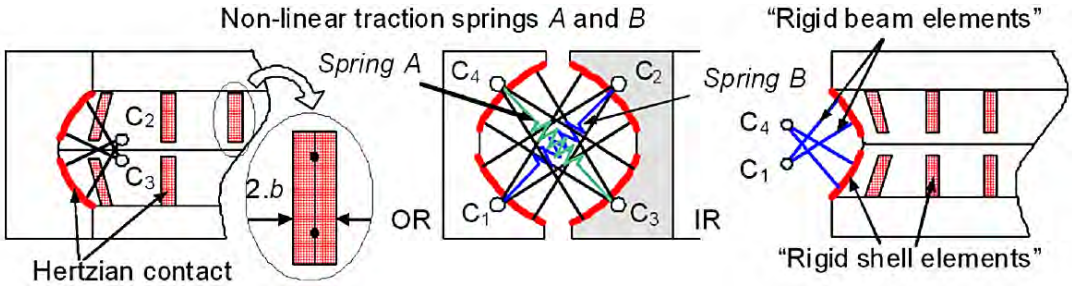

Figure 1.31. Ball-raceway contact model of Daidié [79].

The recent research work from Graßmann et al. [166] presented an alternative which modelled Daidié's mechanism using force distributed constraints instead of rigid beams connected to the whole surface of the raceway for each ball-raceway contact sector. This technique avoids the possible indentation that the original Daidié's mechanism may show, accounting twice for the deformation of the raceways.

These finite element techniques, although still needing to be solved with a non-linear solver, avoid the modelling of the balls. This means that the number of Degrees of Freedom (DoF) of the problem is reduced both by the non-existence of the rolling elements and by not needing to refine the mesh of the ball-raceway contact, reducing the computational cost significantly. Moreover, the use of the previous mechanisms reduces the convergence problems that may arise from the contacts such as chattering (solver convergence issue on the contacts) or rigid body motion from a lost contact. Thus, these techniques are widely used in the research community and in the industry.

These research works have served as a reference for many slewing bearing models, such as Chen and Wen [77,78] who used it to run FE simulations of large-scale rolling bearings. Aguirrebeitia's analytical model [20] was also validated through FE simulations which used Daidié's mechanism. This model considered the ball preload by changing the length of the non-linear spring to apply the preload on the balls. Spiewak [66] also used Daidié's mechanism in a two-row four-point contact slewing bearing to calculate its static carrying capacity. Heras et al. [12] used the superelement method, using the approach by Plaza et al. [21], reducing the rings to the raceway centres and obtaining the stiffness matrix, to then implement Daidié's mechanism to solve the load distribution problem.

Plaza et al. [21] studied the advantages of applying the SE method for FE simulation of a blade-hub assembly, where they reduced the structural behaviour

of the rings and adjacent elements to the contact surfaces of the bearing raceways. With a similar approach, Heras et al. [12] also applied the SE method, but this time to obtain the stiffness matrices of the rings reduced to the centres of the raceways in order to implement them in the analytical load distribution model, which was based on the minimisation of the potential energy described above [12,23] to subsequently calculate the friction torque of the bearing.

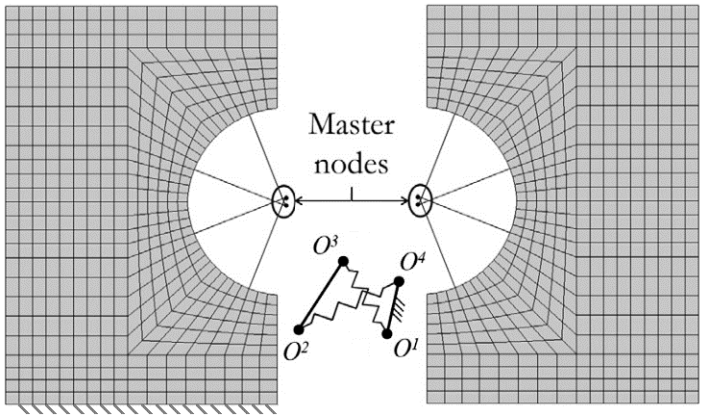

Figure 1.32. SE based ball-raceway contact FE model of Heras [12].

Subsequently, Leupold et al. [83] carried out FE simulations considering surface-to-surface contact for the ball-raceway contact of a two-row four-point contact slewing bearing. This aimed to obtain results that are more accurate and predict the edge loading. He used a test rig to validate the obtained results experimentally, which was also part of the FE model while calculating the load distribution.

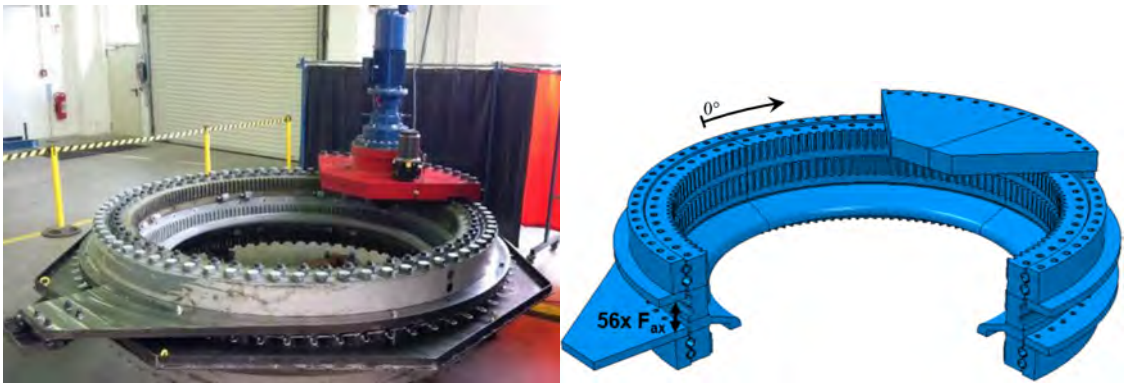

Figure 1.33. Leupold bearing test rig [83].

In addition to the above-mentioned research works that use analytical and numerical methods, others use experimental methods to validate their models as the latter one. Zupan et al. [86,87] made a purpose-built test for the experimental verification of the load-carrying capacity of large-sized rolling bearings. Lacroix

et al. [88] developed an experimental procedure to analyse global displacements by digital image correlation and compared them with the numerical results of a four-point contact slewing bearing. This served to validate the numerical model by assuming both rigid and flexible rings and housing. Seok Nam et al. [84] developed a highly reproducible test rig for pitch and yaw bearings of wind turbines and cross-validated the FE model using strain gauges over the test rig. Liu et al. [85] validated their FE model, based on Daidié's mechanism, of a four-point contact slewing bearing with experimental results under variable axial loads and tilting moments. To do this, they inserted strain gauges inside the circumference of the inner rings, measuring the load distribution indirectly. Graßmann et al. [166] also validated their FE contact model with a more detailed sub-modelling technique and experimental tests of a two-row four-point contact slewing bearing, sensorised with strain gauges on the outer ring.

It is also worth mentioning that most of the manufacturers offering load distribution formulae in their catalogues are based on a mixture of analytical equations and experience from their experimental tests.

1.4.2 Friction torque problem

The friction torque is one of the current hot topics in the field of slewing bearings. By correctly calculating this parameter, the manufacturers obtain a more reliable product, while the end users get a better system performance.

The first relevant research work in this area was done by Palmgren [89] for conventional bearings, who proposed a friction torque model with a load-dependent and a load-independent part. Because of the low rotational speeds of slewing bearings, there is no need to consider the speed dependence, so the expression he presented was as equation (1.5):

$$T = f_0\, 10^{-7} \cdot 160\, D_{pw} + f_1\, P_1\, D_{pw} \tag{1.5}$$

Where f_0 and f_1 are empirical values, P_1 is the equivalent load as a sum of all the absolute contact loads. However, this procedure required solving the load distribution problem and fitting the data with experimental values, so it was not that widely used. It was not until many years later that NREL proposed an equivalent simple way to estimate the friction torque of slewing bearings [49], which was also dependent on an axial load, radial load and tilting moment.

However, it does not consider any combined effect between these loads, so the contribution to the friction torque from each external load is considered independently. Furthermore, this formula includes an apparent coefficient of friction, which is dependent on the separating elements used (cage, spacers or none). This formula can be expressed as a generic expression for the friction torque, which also considers the friction torque contribution of the assembly without any load applied, as shown in (1.6):

$$T = \mu_a \frac{D_{pw}}{2}\left(A\frac{M}{D_{pw}} + B\,F_r + C\,F_a\right) + T_0 \tag{1.6}$$

Where T is the friction torque value, M, F_r and F_a are the external loads, tilting moment, radial force and axial force, respectively; A, B and C are constant coefficients; μ_a is the apparent coefficient of friction; and T_0 is the idle friction torque. The generic expression (1.6) is sometimes provided by different manufacturers in their catalogues, and each one modifies the coefficients of each load based on their experience and bearings. While the manufacturers tend to define $A = 4.4$, $B = 3.8$ and $C = 1$ [40,91,92], the NREL proposes $B = 2.2$ [49], leading to the most extended formula for slewing bearings, which was shown above in (1.3).

However, these formulations are approximate functions that do not consider the effect of some common aspects of slewing bearings such as the ball preload, the contact angle variation or the osculation ratio, among others.

On the other hand, some manufacturers, such as SKF [93], offer a friction torque estimation expression as a modification of the one proposed by Palmgren [89], where the friction torque is divided into various sources as expression (1.7):

$$T = T_{rr} + T_{sl} + T_{seal} + T_{drag} \tag{1.7}$$

Where T_{rr} is the friction torque caused by the rolling contacts, T_{sl} is the friction torque contribution from the sliding contacts, T_{seal} is the friction torque contribution caused by the sealing parts and T_{drag} is the friction torque caused by the drag of the lubricant. This manufacturer offers analytical expressions to calculate the effect of each part based on their bearing models and experience with their bearings.

Todd and Johnson [94] proposed an approach for angular contact ball bearings to consider the effects of the spin, microslip and hysteresis on the friction torque, together with the contact angle variation. Other research works [95–97] separately calculated the effect of different components on the friction torque, providing simple but powerful formulae for the friction torque calculations. Olaru [98] and Bălan [99,100] also proposed new models for ball bearings with two contact points, as well as Chi Zhang [101] for tapered roller bearings, which considered roller skewing.

There are various sources of friction torque that affect all bearings depending on the interactions between components considered in the model (ball-raceway, ball-cage/separators and seals-rings, among others). However, due to the low rotational speeds at which slewing bearings usually operate, they lack some of these sources of friction or they can be simplified, e.g. the effect of the lubricant drag, which can be substituted by an effective coefficient of friction. The contribution of some of these contacts, such as the seals-rings contact or the separating elements, can be assumed as independent from the external loads. Given the high loads the slewing bearings support, the shear stresses of the ball-raceway contacts are the main contributors to the friction torque.

Carter [102] formulated the distribution of the shear stresses for a roller-raceway contact, showing how the maximum surface shear stresses were occurring on the edge of the contact. Mindlin [112] studied the tangential loads between two sliding elastic bodies. He found that the tangential tractions became infinite at the edges of the contact patch, resulting in slip. Thus, he showed that on a circular contact surface, the tangential force should not exceed the product of the normal pressure and the coefficient of friction. Poritsky [113] solved the contact problem in two dimensions also assuming hertzian contact, for both normal and tangential loads. Smith and Liu [114] agreed with Poritsky and showed how the maximum shear stress may be at the contact surface. Finally, Johnson [115–119] studied and expanded the theoretical formulation of tangential forces and micro-slip in rolling contact.

The rolling contact problem has not only been a problem for the bearing sector. In fact, the railway sector has tried to solve the same problem, where the Hertz theory has also been widely used. As a result, various studies conducted in the railway sector have made major contributions that apply to the bearing sector. One of the most widely known contributions in this sector was by Kalker,

who first studied the rolling contacts in full adhesion [105]. This theory assumed continuous traction distribution at the edge of the contact, which is known as Kalker's creep force *linear theory*, and the table of longitudinal creepage and spin coefficients he presented are known as *Kalker's coefficients*. He extended Haines and Ollerton [106] strip theory to add lateral and spin creepage, where the wheel-raceway contact patch is assumed to be elliptical. In his research works [104,105] he separated the contact area into parallel slices along the longitudinal axis. He later defined the relation between the longitudinal and lateral creepages and the total creep force in the *empirical theory* [107]. Subsequently, he simplified this linear theory [108] and developed the FASTSIM [109] computational algorithm. In this *simplified theory*, he approximated the relation between the tangential surface traction and displacement by using flexibility parameters, dependent on the aforementioned creepage and spin coefficients. This algorithm, valid only for hertzian contacts, is widely used in the study of wheel-track contacts since it allows for the dynamic study of these with a low computational cost. Kalker then developed the *exact contact theory* [110], which he implemented in the CONTACT computational algorithm. This was a generalization of the principle of virtual work for solving the contact problem. However, although this was much more accurate and valid for non-hertzian contacts, it was 1000 times slower than FASTSIM [111].

As previously stated, the shear stresses of the contacts between the raceways and rolling elements are the main contributors to the friction torque in slewing bearings, which rotate at low speeds. In this regard, Jones [120] proposed an approach where the bearing kinematics were solved by solving the equilibrium of the external forces on the ball. He assumed full sliding on the contacts (Figure 1.34a), so the friction forces were computed as a product of the normal forces and coefficient of friction of Coulomb. Hamrock [121] used Jones' approach and adapted it to three-point contact ball bearings. Leblanc and Nélias [122,123] later adapted this model to four-point contact ball bearings under any load combination. However, these models assumed rigid rings, so Lacroix et al. [88] subsequently proposed a method to account for the flexibility, based on Leblanc and Nélias' work.

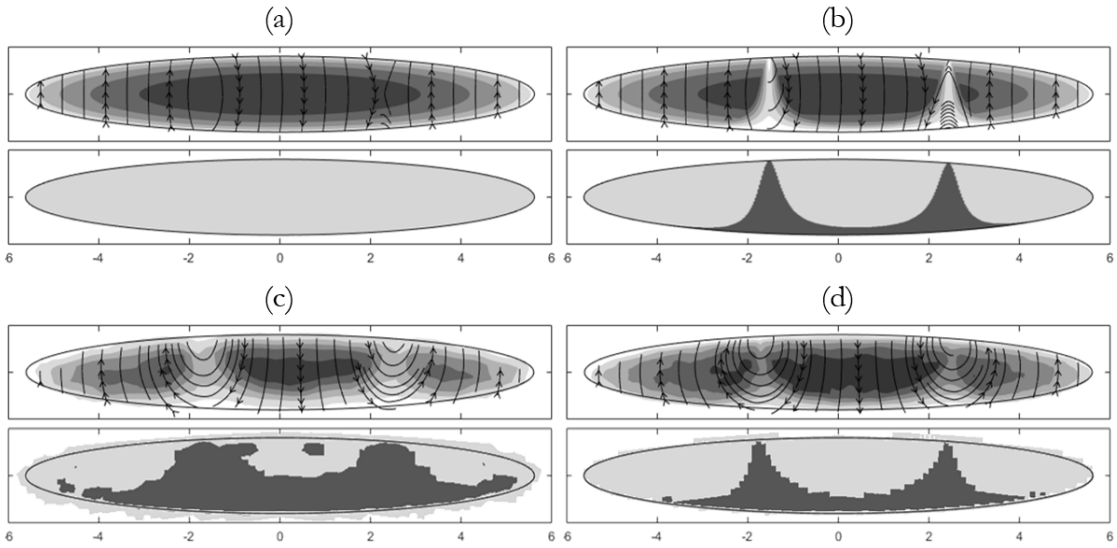

Figure 1.34. Shear stress (up) and contact stick-slip status (down) for a ball-raceway contact: (a) Leblanc and Nélias model; (b) FRANC model; (c) FE global model; (d) FE submodelling [25].

In addition to all of this, ball slewing bearings are large-sized bearing, used for orientation purposes, their operational rotational speeds are low, and the inertial effects could be neglected. Taking this into account, Joshi et al. [124] adapted Leblanc and Nélias' work. Consequently, the load distribution problem and the kinematics were solved separately. Joshi validated his model with friction torque experimental results. However, he studied the four-point contact and the two-point contact state of the balls separately. Based on this, Heras [25] implemented Joshi's previous approach, enhancing the algorithm to avoid the model convergence problems. In the case of slewing bearings for wind turbines, under regular working loads, which imply high tilting moments, most of the balls are in the two-point contact state. These balls behave in the same way as typical angular contact balls. Consequently, stick regions will exist in the contact area according to the Heathcote slip [125], even if in high-conformity contacts the slip is dominant in most of the contact region [126]. This effect could be seen in Figure 1.34b, c and d. The contact patch shear stresses and stick-slip regions for four-point contact slewing bearings using the aforementioned analytical methods are shown in Figure 1.34.

However, Heras et al. [12,23–25] studied the stick-slip regions using FE (Figure 1.34c) for a ball-raceway contact, even using submodelling (Figure 1.34d) to obtain more precise results, from which he concluded that the full sliding hypothesis (Figure 1.34a) was acceptable for these bearings to compute the

friction torque. Stammler et al. [90] also compared different friction torque models with experimental results, concluding that none of the models could completely predict the friction torque. Later, Menck et al. [127] obtained new experimental results and offered an empirical equation to model the friction torque, which requires previous experimental testing.

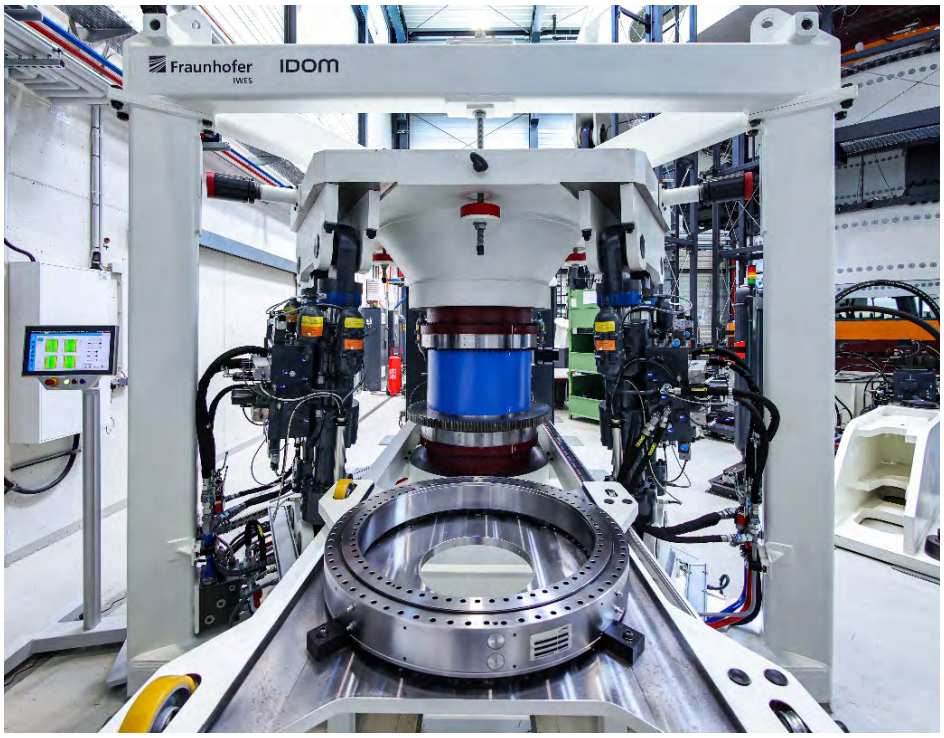

Figure 1.35. IWES BEAT1.1 multiaxial bearing test rig (©Fraunhofer IWES/Ulrich Perrey) [127].

The experimental results obtained by Menck and Stammler were performed at the Fraunhofer IWES Large Bearing Laboratory (Figure 1.35) test rig for full-scale medium-sized slewing bearings. This test bench is one of the most advanced available today, which can be used to apply static loads and perform fatigue tests, as well as monitor ring deformations, friction torque, wear, etc. This laboratory is known for its research on large bearings for wind turbines, which has various test benches [128] for large-sized bearings. The BEAT 6.1 test bench was completed in 2019, which could be used to validate FE models and contact calculation models, and to perform accelerated tests of true slewing bearings of 20 years in 6 months. This test rig is capable of introducing static loads up to 50 MNm, and dynamic tilting moments of 25 MNm in all directions and monitors all types of data due to the incorporated advanced data acquisition system. The test rig applies the loads into the structure by means of six hydraulic cylinders, transmitted to the top bearing. These loads are then transmitted to the lower

bearing via a connector part, which emulates the stiffness of a wind turbine blade. The working principle of the BEAT 1.1 (Figure 1.35) is the same but for smaller bearings, but considers stiffer boundary conditions for the bearings.

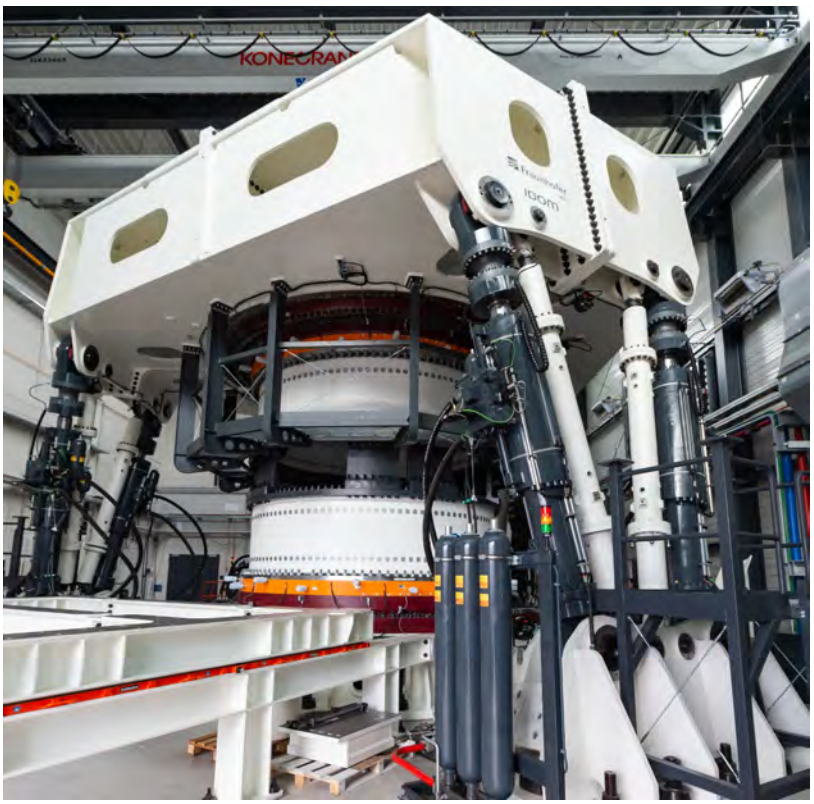

Figure 1.36. IWES BEAT6.1 multiaxial bearing test rig (©Fraunhofer IWES/Ulrich Perrey) [128].

Previously, other test rigs enabled experimental bearing measurements, which could also be used for slewing bearings. However, due to the large dimensions of these bearings compared to conventional bearings, small-sized bearings were commonly used to analyse the behaviour and obtain scaled results of these, such as the one used by Joshi et al. [124], which applied an axial load by tightening six load screws. Paleu et al. [129] also developed a test rig for high-speed rolling bearings that applied axial force into the tested bearings by means of loaded springs.

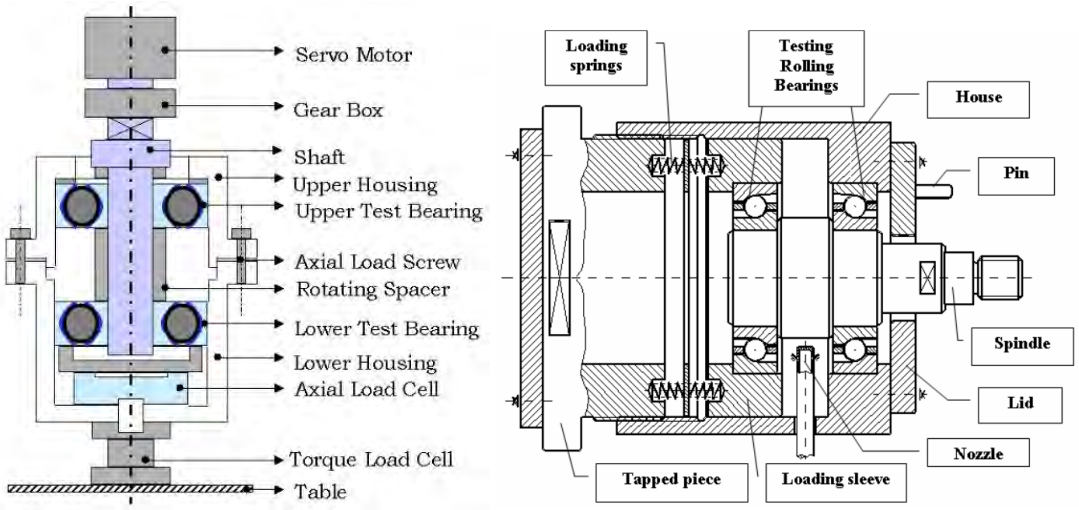

Figure 1.37. Axial test rigs used by Joshi [124] (left) and Paleu [129] (right).

A more complete test rig can be seen in the Korea Institute of Machinery and Materials (KIMM) [84,130]. This test rig tests the bearings in pairs, while the top bearing rotates and the lower one remains fixed. The working principle is the same as the aforementioned BEAT 1.1 and BEAT 6.1 from Fraunhofer IWES, where the acting loads are generated by six hydraulic cylinders and a force transmitting element is placed between the bearings.

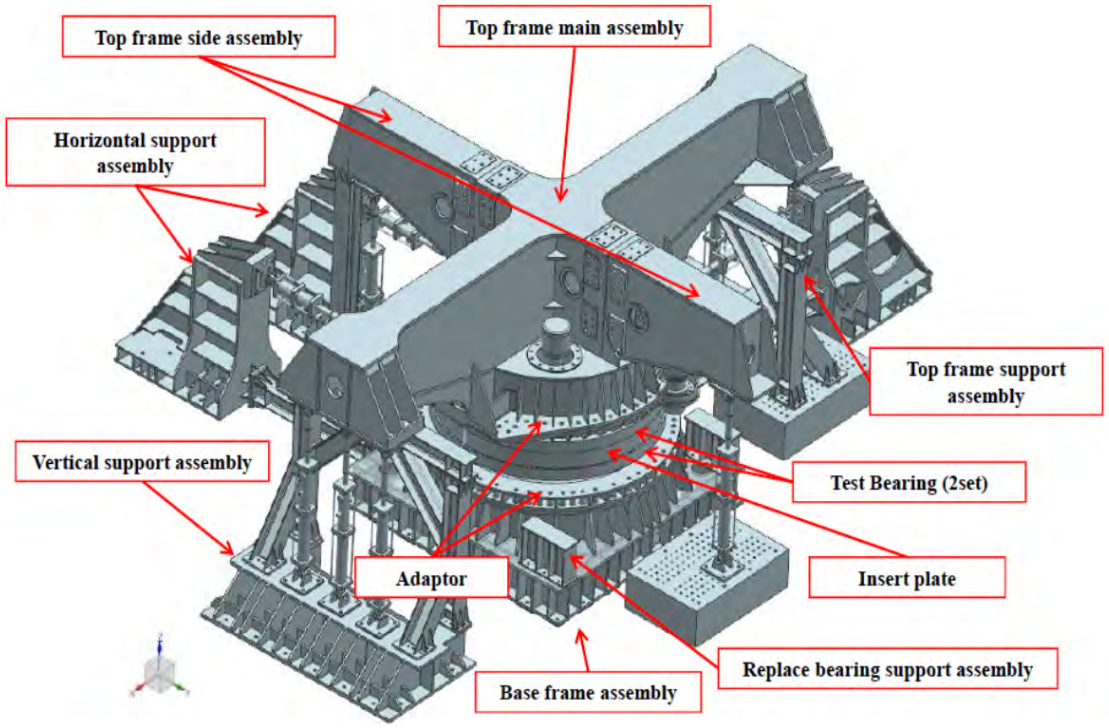

Figure 1.38. KIMM bearing test rig [84].

Windbox is an energy cluster composed of Antec, Erreka, Glual, Grupo Wec, Hine, LauLagun and Siemens Gamesa located in the Basque Country, Spain that also owns a full-scale test rig including all the bearing interfaces on it: hub, blades, pitch drives and so on. The Windbox test rig was developed to test the pitch and yaw bearings and main shaft bearings of wind turbines. This test rig [131] (Figure 1.39) applies the loads on the blades and is capable of testing three slewing bearings at the same time, up to 55 MNm static loads and 35 MNm dynamic loads, monitoring deformations, temperatures, and vibrations, among others. Fraunhofer IWES also developed the BEAT 2.1 test bench [128] that enabled the testing of the entire hub-blade and bearing-rotor groups, consisting of a hub and three blades (two blade roots and one full blade), but it can only test one slewing bearing.

Figure 1.39. WINDBOX test rig [131].

Naturally, bearing manufacturers are the other main users and developers of these real-scale test rigs, for example, the one owned by Schaeffler [132], called Astraios (see Figure 1.40), which enables the testing of wind turbine main shaft bearings statically and dynamically. The axial load and tilting moments of this test rig are applied to the bearing by the four axial hydraulic cylinders, and the four radial ones simulate the weight of the hub and the blades. Other manufacturers, such as Liebher [133] and Rothe Erde [134] also own their own true-scale test rigs.

Figure 1.40. "Astraios" test rig from Schaeffler [132].

However, the availability of experimental results for friction torque in slewing bearings is scarce, as most of the available test rig results belong to manufacturers who use these data to adjust the formulae they provide in their catalogues. Thus, the number of research papers that publish friction torque test data for slewing bearings is minimal, and therefore those that are published, such as those of Menck et al. [127] are of extremely relevance.

1.4.3 Bearing global stiffness

As could be seen in the previous sections, many manuscripts consider their model bearings with rigid rings or surrounding structures. However, it has also been shown that implementing the flexibility of these components can be useful when calculating the load distribution of bearings. In addition, bearings have another key feature during bearing design and selection, namely the overall bearing stiffness, which can be affected depending on the boundary conditions of the model.

Compared to other parameters and calculation methods, the global stiffness of bearings has no standardised calculation process, which has led to manufacturers providing bearing stiffness curves without much detail about the calculation process or the assumptions made in the calculation.

Indeed, load distribution calculation methods also allow for bearing capacity and stiffness to be calculated, such as Houpert [71], Lim and Singh [135], Hernot et al. [136], Liew and Lim [137] and Noel [138] research works. However, these works consider rigid rings, so they only assume the deformation of the ball-raceway contact.

The models proposed by Jones and Harris [139], Harris and Broschard [140] and Mignot et al. [141] for planetary gear-transmission bearings consider the stiffness of the structures. However, those were viable because these bearings are always subjected to the same boundary conditions and loads. In contrast, this is not applicable for slewing bearings due to their varying load condition, so an analytical approach is not feasible in a simple manner.

Some of the analytical approaches described in section 1.4.1, such as the semi-analytical methodology shown by Olave et al. [74] can be used to consider global deformations. Also, the work performed by Guo and Parker [142] considered ring deformations via FEM. Heras et al. [12,23] also proposed a methodology to calculate the load distribution problem considering ring flexibility obtaining the stiffness matrix of the rings by means of FE sector models. However, when it comes to obtaining a simple formulation for calculating the bearing stiffness while accounting for flexibility, the difficulty lies in requiring numerical methods. However, Heras [10] proposed a simple engineering formulation to calculate stiffness in four-point contact slewing bearings, considering ring deformations, which were calculated using FEM. These approximated formulae gave a maximum relative error of 7.5% when compared to FE results.

1.4.4 Fatigue life

The fatigue life of slewing bearings, considering rolling fatigue as the failure mode, only relies on ISO 281:2007 [50] and its extension ISO/TS 16281:2008 [51] as accepted standards, which were developed for conventional bearings. These standards are based on the life estimation proposed by Lundberg and Palmgren [167,168]. The NREL [49] provides a simplified version of the life calculation methods for yaw and pitch slewing bearings. However, all these procedures have their limitations, which have sparked an interest in researching and providing specific calculation methodologies for these bearings.

Sawiki et al. [143] provided the mathematical model for calculating the fatigue life of large-diameter slewing bearings and developed an FE model to determine the actual bearing loads due to housing distortions. Potočnik et al. [144] also used an FE analysis to calculate the bearing loads considering the manufacturing errors in a double-row four-point contact slewing bearing. Portugal et al. [145] established a methodology to estimate the multiaxial fatigue damage under random loads. It was more generalist and intended for machine components lacking a fatigue life calculation procedure, so it matched slewing bearing characteristics. Later, Menck et al. [127] compared two methods proposed by NREL, one of which requires less computational effort, and the ISO/TS 16281:2008 method for calculating the bearing loads and the lifetime of slewing bearings. Here a higher lifetime result for the fastest and least computationally intensive method was found. Meanwhile, the other two provided very similar results and thus, they proposed an adjustment to increase the accuracy of the first method.

When it comes to analysing the contact fatigue in more detail, Poplawski et al. [146] started to evaluate the lifetime of different roller profiles using different calculation methods. Göncz and Glodež [147] used FE to assess the rolling contact fatigue considering an induction-hardened layer in the raceways. Schwack et al. [148] compared four different approaches to calculate the fatigue life of a blade bearing. Later, Londhe et al. [149] studied the subsurface stresses in the case of ball-raceway contact, also considering the raceway induction hardened layer in the raceways and its implications. He et al. [150,151] also studied the effect of the hardened raceway layer on a triple-row roller bearing.

Overall, no rigorous and exact procedure currently defines the fatigue calculation of slewing bearings. The most similar approach was proposed by Houpert et al. [52], who proposed an alternative method to calculate the bearing life in oscillating components by implementing corrective coefficients to the bearing life calculation formulae from ISO 281:2007. This is also related to the wide variety of failure modes of these bearings due to their varying dimensions and operating conditions.

1.4.5 Lubrication and wear

The lubrication conditions are particularly important as they are directly related to the efficiency of the bearing. The increasing use of wind turbines and the subsequent increase in the number of slewing bearings make the lubrication condition of the bearings a critical aspect.

The lubrication conditions also affect different bearing failure modes, predominantly those related to wear. Godfrey [153] extensively reviewed the differences between these false brinelling and fretting corrosion failure modes, and Schwack et al. [44] later used his work as a reference stating that when the contact is lubricated, the predominant failure would be false brinelling; although, fretting corrosion would prevail in dry contact. The latter used finite element analysis (FEA) to predict wear in the experimental tests. With all this, the work analysed the main characteristics of these two types of wear marks.

Other research works [154,155] do not focus as much on differentiating between these two types of failures and call them both "standstill marks". This name comes from the situation these marks appear in, as they occur in stationary or vibrating conditions with small-amplitude relative movements between the bodies in contact. It is precisely this movement that is most common between the raceways and rolling elements of slewing bearings, which rotate to orientate the objects and remain stationary supporting the loads, or making small orientation adjustments of just a few degrees. The research works that focus on the lubrication conditions under these movements are scarce [156,157], and they place greater emphasis on analysing the lubricant and the contact. Other research works [99,100] analyse the coefficient of friction but in other types of bearings. The slewing bearings case is equivalent to quasi-static cases due to the slow and small oscillatory movements they make and their lubrication conditions usually lie between the boundary lubrication and an incipient EHL. Instead of implementing these lubrication models, it is far more effective and useful in most cases to assume a friction coefficient that can be experimentally adjusted, which is a common practice when modelling this type of bearings. Examples of this are the works performed by Joshi et al. [124] and Heras [31], who focus on comparing the performance of these bearings with different greases, measuring the coefficient of friction or the friction torque by means of experimental tests.

1.4.6 Condition monitoring

As with lubrication, condition monitoring and failure detection in slewing bearings during operation have become particularly important. The fact that their behaviour is highly conditioned by their surrounding structures and varying load cases depending on their application makes it essential for them to be monitored during operation in order to detect possible unexpected premature failures.

Of works focused on condition monitoring, worthy of mention is that work carried out by Zupan [87] that enabled the monitoring of the rotational resistance, load stress distribution and microdeformations of the bearing raceways. In combination with the simulation of real running conditions, any damage occurring in the bearings or early signs of damage can be detected. Bai et al. [158] provided a way to evaluate the wear conditions of slewing bearings using ferrography and spectrometric analysis of the oil, which provide insights into the wear process. There are some alternate monitoring approaches that enable the detection of failures and make maintenance decisions based on monitoring vibrations, acoustics or temperatures [159–163].

On the other hand, friction torque related work, such as that mentioned in Section 1.4.2 is useful for monitoring bearing conditions. Due to the strong relationship between friction torque, rolling element or raceway wear, and lubricant, any abnormality occurring in the bearing can be detected by a change in the estimated value of the friction torque. Due to the difficulty of performing full-scale bearing tests for these types of bearings, research works involving experimental tests such as [84,90,127,130] become extremely important in this context, given the number of results they are able to obtain.

The full-scale test rigs provide a wide range of results thanks to their large amount of sensors, which enable the evaluation of other failure-inducing factors, such as load distribution or ring deformations, in addition to the fatigue tests that can be performed. This information can be used to track the sensor results during operation and implement a predictive maintenance strategy or to serve as reference during the bearing design stage.

1.5 General overview of the research work

The following section provides an overview of the work carried out in the Doctoral Thesis to meet some initial objectives established in the initial stages of it. Before going into the details of each chapter, the goal of this section is to summarise and provide an understanding of the reasoning that has led to the final objectives, which have undergone certain changes compared to the initial ones. The relevance of each chapter is clarified in this way, so linking each chapter requires no extra effort during reading.

1.5.1 Initial objectives

Considering the limitations of state-of-the-art simulation methods and techniques for characterizing the behaviour of four-point and eight-point contact slewing bearings, the following initial objectives were established for this research work:

1. Improving the accuracy of state-of-the-art approaches to calculate the friction torque of ball slewing bearings.
2. Validating the friction torque models through experimental testing.
3. Developing an easy-to-use tool to assess the friction torque, so it can be useful for bearing customers and manufacturers:
    3.1. Obtaining an engineering formulation for the load distribution problem based on the external loads.
    3.2. Obtaining an engineering formulation for the friction torque problem based on the load distribution of the balls.

1.5.2 Initial hypotheses

To reach the previous objectives, the following hypotheses were initially considered:

1. Rigid rings: under axial load, the bearings can be modelled with cyclic symmetry, where the flexibility of the rings does not significantly affect load distribution. Contrarily, in the case of radial and tilting moment loads, the deformation of the rings is known to affect load distribution. However, because these deformations are dependent on the flexibility of

the structures the rings are attached to, the hypothesis of rigid rings allows a general calculation method to be developed that is valid for early design stages while also being more precise than existing ones.

2. Sliding ball-raceway contacts: previous results obtained by the research group concluded that considering stick regions to solve the friction torque problem has no effect on the end result. As a result, the hypothesis of a full sliding contact model is assumed.

3. Constant coefficient of friction: the small oscillatory movements of slewing bearings and their lubrication condition, usually between the boundary lubrication and an incipient EHL, allow for the assumption of a friction coefficient that can be experimentally adjusted; something which is a common practice when modelling this type of bearings as it is far more effective, useful and easier to implement. For this, the Coulomb friction model is used, which is defined as a friction coefficient constant multiplied by the normal force.

1.5.3 Summary of the research work

Chapter 2 presents a friction torque calculation method, focused on first and second objectives. According to the research work by Joshi et al. [124], the load distribution problem is separated from the friction torque problem.

First, the load distribution is computed, and then the bearing friction torque is calculated as the sum of the friction torque contribution of all the balls. The research work in this chapter attempts to fit an analytical model of friction torque to the experimental results obtained by Fraunhofer IWES in [127]. Since initially a large discrepancy between the analytical model and the experimental results is observed, the model is fitted during the calculation of the load distribution problem by simulating a scatter of the ball preload. As mentioned in the hypotheses, this model assumes rigid rings for this calculation step.

The next calculation step, which consists of the friction torque calculation, works under the assumption of full sliding at the balls-raceway contact. By means of multiple calculations of the fitting parameters, the analytical model is able to fit the results of the friction torque to the experimental ones. However, as important discrepancies in the results are observed under a tilting moment, the decision was made to feed the model with load distribution results obtained

using FE. The first calculations show how the flexibility provided by the FE model obtains closer results to the experimental ones, so this calculation procedure appears to be the best one to use in future research works.

In this regard, as a result of the work carried out during the time spent at the Fraunhofer IWES, the preload scatter is going to be implemented in an FE bearing model. This bearing model is also part of the test bench FE model that can be simplified using SE. The same procedure can be used to obtain more precise results of load distribution and, as a result, of friction torque.

Based on the results obtained in Chapter 2, the rigid ring hypothesis is proven to be delimiting the capabilities of the analytical model. It was subsequently decided to investigate the flexibility of the bearings by means of FE, although this is not one of the initial objectives. In this regard, Chapter 3 focuses on analysing various FE modelling techniques and their effect on bearing flexibility are examined.

FE modelling of slewing bearings is not new, but there is no standardised procedure for it. This chapter will investigate the effect of various factors affecting the load and contact angles of rolling elements, as well as ring deformations. The main goal is to model a real-dimensioned blade-bearing-hub assembly provided by Fraunhofer IWES, so that the simulations are as close to a bearing used in the wind industry as possible. With this model, it is possible to analyse the load distribution shape of the rolling elements when considering the real boundary conditions of a bearing. To assess this, the results are compared for different modelling strategy combinations, such as the effect of simplifying the bolted joints by rigid joints between solids, as well as the effect of using a different material blade model, such as steel. These strategies could be useful in the early stages of bearing design and during their testing, given the ease and cheapness of manufacturing and testing steel blades rather than composite ones. Based on this, the conclusion is reached that the boundary conditions of the bearings affect the load distribution results, and hence the friction torque results.

This creates a future line of work that coincides with the one in the previous chapter: the need to use finite elements to evaluate the load distribution in order to obtain precise results, which is then incorporated into the friction torque calculation. On top of that, a model with real boundary conditions in the final stages of the wind turbine design should be used.

Finally, Chapter 4 presents a normalisation of the friction torque. The state-of-the-art friction torque models depend on the coefficient of friction, three macrogeometric parameters, three microgeometric parameters and three external loads. After analysing the relationship between the external loads and the load distribution (contact loads and angles), it is found that the external loads cannot be further extracted from the analytical expression, which corresponds to objective 3.1. This implies modifying the path to reach objective 3.2, from obtaining a formulation of the friction torque problem based on the load distribution of the balls to obtaining a direct formulation based on the external loads related to the friction torque.

Finally, the effect of the three macrogeometric parameters and the coefficient of friction is successfully extracted. By means of this implementation, a friction torque model with fewer variables is achieved, which, from a computational cost point of view, allows a Design of Experiments (DoE) to be performed. With the results of this DoE, a normalised friction torque tool is created, where the normalising parameters are the three microgeometric parameters and the external loads. Although the flexibility of the rings is not taken into account, this procedure allows for the friction torque to be calculated in the early design stages, with the same simplicity provided in the design guidelines and with more accuracy.

The obtained results have identified a future line of work where a similar DoE can be performed by mapping all combinations of loads and contact angles in which a ball can be found. This would allow the linking of the load distribution solution by means of FE together with the friction torque contributed by each ball that would be found in this database. In conjunction with the above future line, a tool could be created that considers the flexibility of the rings together with the preload scatter and a fast and accurate tool to calculate the friction torque.

Figure 1.41 schematically identifies all of the various work steps, conclusions, and identified future lines to provide a visual representation of the work.

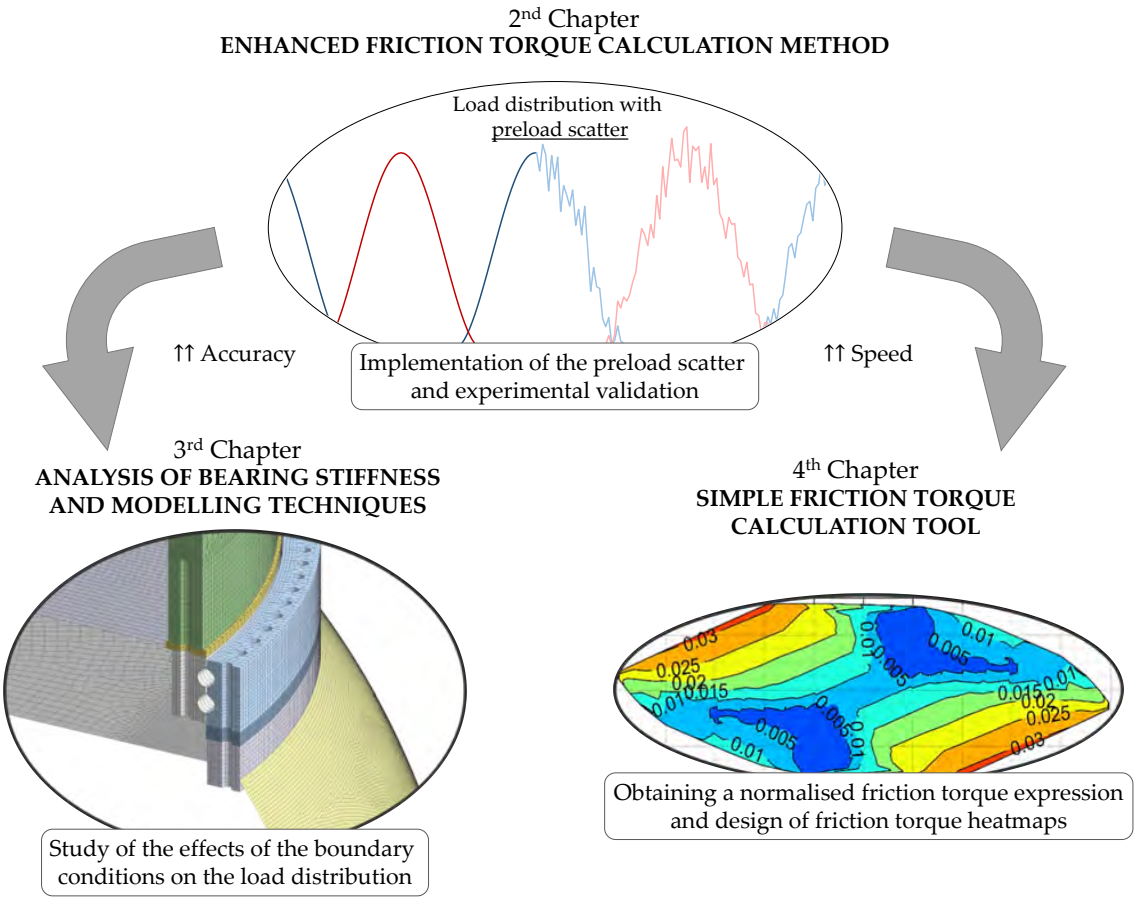

Figure 1.41. Schematic representation of the research work and future lines.

1.5.4 Achievements and future lines

Some of the initial objectives were modified as a result of decisions made during the research process. As a result, the objectives achieved are identified below as a modification of the initial ones:

1. Improving the available analytical tool for the calculation of the friction torque of ball slewing bearings: this objective is achieved in Chapter 2 through the implementation of a preload scatter in the load distribution problem and combined with FE analysis. The findings in the preceding chapter create a need for further research on slewing bearing modelling techniques, which is covered in Chapter 3.

2. Validating the friction torque models through experimental testing: this objective is achieved during the validation of the analytical friction torque model fitting the experimental test results, which are in Chapter 2, as a means to achieve objective 1.

3. Developing a simple tool to assess friction torque: previous objectives 3.1 and 3.2 are replaced by an engineering formulation for the friction torque problem based on the external loads and bearing microgeometry, which is developed in Chapter 4. A normalised expression for the friction torque is obtained to achieve this. Moreover, a DoE is developed around this formulation to obtain a database that relates these parameters with their normalised friction torque results. The obtained data is interpolated and a series of heatmaps (normalised friction torque maps) are created that relate the friction torque with the microgeometry and the external loads.

Finally, the future lines defined as a consequence of the results of the thesis are as follows:

- Implementing the preload scatter in an SE based FE model, which enables load distribution to be calculated in a fast and precise way.
- Using the FE load distribution results considering a preload scatter, to feed the friction torque model and fit the experimental results.
- Obtaining friction torque maps for different ball geometries to develop a faster way to compute the friction torque of a bearing.
- Developing a more precise tool for the friction torque calculation capable of accounting for ring flexibility and preload scatter.
- Studying the effect of different boundary conditions, such as different blade sizes or materials, and obtaining an engineering formulation that approximates the load distribution based on them.

2 Effect of ball preload scatter on friction torque

2.1 Introduction

This chapter proposes an improved methodology by which to calculate the friction torque of slewing bearings.

In order to calculate the friction torque in two-point angular contact bearings, there are approaches such as the one proposed by Houpert [97], where the contribution of different sources of friction are calculated separately and they are added together to obtain the total torque. Manufacturers also provide similar formulae for their conventional (not slewing) bearings [93,169]. More advanced approaches have also been proposed for angular contact ball bearings, like the recent one by Zhao et al. [170]. These formulae can be applied to four-point contact bearings if they only bear axial forces, since in this case, they work like two-point angular contact bearings. However, these are not valid for ball slewing bearings, either for those with one row (four-point contact bearings) or with two rows (eight-point contact bearings). In slewing bearings, the rolling elements are usually assembled with preload (negative clearance) and bear not only axial loads, but also bending moments and radial forces. This fact has a significant effect on ball kinematics and the friction torque, meaning that the approaches in [93,97,169] are not applicable. With this in mind, and on the basis of Jones's work [120] for angular contact ball bearings, Leblanc and Nelias [122,123] proposed a model to solve the load distribution and ball kinematics in four-point contact bearings subjected to any load combination, either assembled with clearances or preloaded. These approaches [120,122,123] assumed rigid rings and full sliding on the ball-raceway contacts. Once the load distribution and ball kinematics are known, the friction torque can be computed. Later, Joshi et al. [124] refined the previous approach specifically for slow speed applications, which is mostly the case of slewing bearings. Moreover, the approach was also validated, obtaining

a good correlation with the experimental results of the friction torque. Regardless of the capabilities of the approach, there are some convergence issues, which can be overcome as proposed by Heras [25]. Besides that, the friction torque of slewing bearings can also be calculated using the Finite Element Method (FEM) [12,23,24], although this involves a high computational cost. Nevertheless, this method allowed Heras et al. [24,25] to study the stick-slip regions in ball-raceway contacts. These works concluded that, even if the stick regions affect the shear stresses on the contacts, their effect on the friction torque is almost negligible. For this reason, it was concluded that the full-sliding hypothesis in [122–124] is acceptable when calculating the friction torque in ball slewing bearings. It is worth mentioning that, in [23], the effect of manufacturing errors on friction torque was studied using the FEM. This research work showed that, when friction torque is conditioned by the preload, manufacturing errors can significantly affect it.

As stated before, the load distribution and ball kinematics must be known in order to make a reliable estimate of the friction torque. According to [124], assuming low speeds allows decoupling the load distribution problem and the solution of the kinematics. Therefore, the former can be solved independently, for which there are various approaches. In this regard, analytical approaches based on contact geometrical interferences can be used, like the one proposed by Aguirrebeitia et al. [8,20], where rigid rings are assumed. Other authors [12,23,74] considered the flexibility of the rings and the surrounding structures in their models. Nevertheless, given its versatility, using the FEM is the common practice to consider the flexibility of the system, regardless of the high computational cost [18,77,79,85,171–174]. In this sense, there are various techniques to make FE models more efficient by substituting the balls with non-linear springs that simulate the flexibility of the contacts. From research works which consider the flexibility of the system, the conclusion was drawn that it has a high impact on the load distribution. Regarding the manufacturing errors, it must be noted that these affect the friction torque insofar as the load distribution is affected by them. Some works simulate manufacturing errors by means of analytical approaches [12,23], while others used FE techniques [75,76].

Regarding friction torque experimental data in literature, there are many works that perform tests with radial, axial or angular contact bearings [96,97,175–177]. However, there is no extensive literature on friction torque tests with ball

slewing bearings. Long et al. [178] studied the effect of the contact angle for a four-point contact bearing with clearance and under axial load, but under these load conditions it behaves like a regular angular contact bearing. Joshi et al. [124] conducted some experimental tests for an axially loaded small-sized four-point contact bearing, considering both preload and clearances. Yet, in the preloaded case, they considered loads where the balls always had four points in contact, thus not representing what happens when the load is increased and a transition happens, where the balls switch from four to two contact points. Later, Heras et al. [31] performed experimental tests to study this transition on a small-sized ball slewing bearing. Additionally, the experimental tests were compared with the analytical results obtained using Joshi's approach [124]. That same year, Stammler et al. [90], from the Fraunhofer IWES, published research with normalised friction torque results obtained experimentally. Since the results were normalized, they could not be used for comparison purposes with data from other sources. The latest and more complete experimental results for ball slewing bearings were performed and published by Menck et al. [127], also from the Fraunhofer IWES. For this research, friction torque tests were performed for three different sizes of ball slewing bearings (blade bearings), working under axial forces and bending moments.

The main goal of this chapter is to propose an innovative methodology by which to predict friction torque in ball slewing bearings. In particular, this work focuses on the transition of the contact state of the balls from four to two contact points. This transition has been observed in experimental tests [31,127] and reproduced using FE simulations [24]. Nonetheless, using current analytical formulations [124], the transition occurs abruptly for axial loads [31] and is not consistent with experimental tests. Thus, to smooth the transition, the author proposes considering of a scatter in the preload of the balls when calculating the friction torque analytically, instead of assuming the same preload in all the balls. After proving the versatility of this proposal by means of a sensitivity analysis, the parameters of the model are tuned for a particular case, in order to fit experimental test results for axial load and bending moment [127]. Additionally, the effect of the flexibility of the rings and the surrounding structures on the friction torque is also studied. To conclude, different strategies are suggested to implement the proposed methodology in different case scenarios, in order to achieve the most accurate friction torque estimation model in each case.

2.2 Preload scatter implementation

The implementation of a preload scatter in the friction torque model is explained in this section. First, the evolution of the friction torque and the ball kinematics are examined for the no preload scatter case and compared for some preliminary experimental results. This analysis is the basis for the need for a model that predicts friction torque considering a preload scatter. Following that, the impact of the new variables added to the model is analysed.

2.2.1 Analysing the friction torque problem

The analytical model was based on the work of Leblanc and Nelias [122,123] for calculating friction torque, which could be separated from the load distribution problem under the assumption of low velocities as proposed by Joshi et al. [124], as mentioned above. For the load distribution problem, the ball-raceway interference-based model from Aguirrebeitia's work [8,20] was used.

When considering a bearing with no manufacturing errors and rigid rings, all of the preloaded balls are subject to the same stress under the axial loading of the bearing. The preload is the only parameter that affects the loading in the unloaded case, implying that it affects the initial friction torque. The effect of this was analysed by varying the preload values while keeping all the other parameters the same. Figure 2.1 shows the different friction torque values obtained for the unloaded case (0 kN of axial force) by simply varying the preload. These results are a sample of some analyses obtained using the same bearing as in [31], which were obtained in the subsequent studies described below.

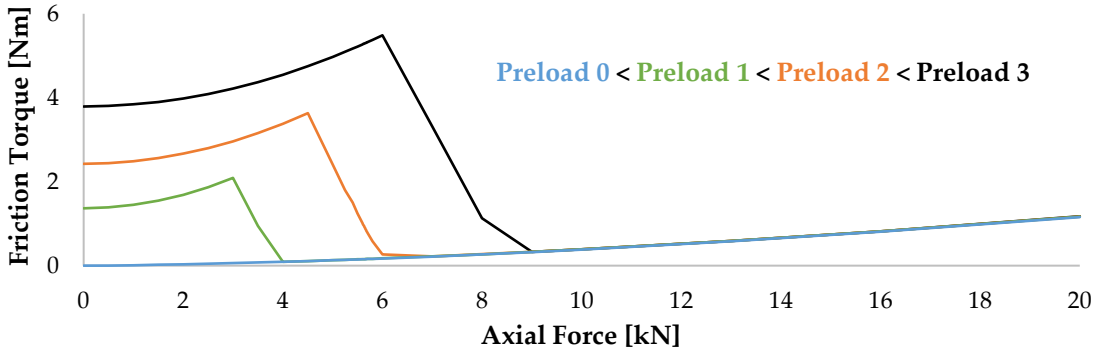

Figure 2.1. Analysis of the effect of different preload values in the original analytical model.

The preload value of the analytical model was varied for an unloaded bearing case (0 kN) to fit the experimental results obtained in [31]. Then, the analysis for the whole range of the axial load was computed. Figure 2.2 shows the results of the evolution of the friction torque under axial load for both experimental and analytical results.

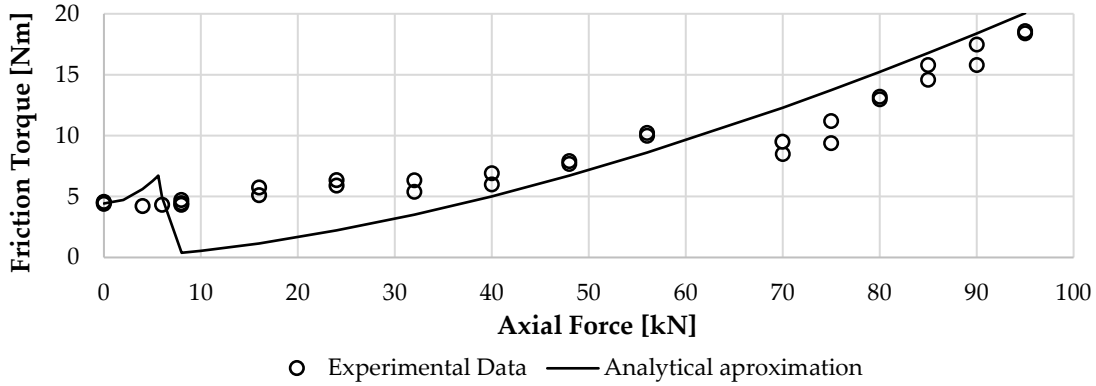

Figure 2.2. Comparison of the analytical model and experimental friction torque results [31] adjusted for the unloaded bearing case.

Figure 2.2 shows that the analytical results do not adequately correspond to the experiments in [31]. The behaviour of the analytical model can be separated into three stages for a better understanding:

- For the first range from 0 kN to 5.6 kN, friction torque increases. The loads are distributed among all the balls uniformly and these are on four contact points with the raceways. In this situation, with the increase of the axial load, the load at two of the four contact points (one diagonal) increases, while it decreases at the other two points (second diagonal).

- After a certain axial load, depending on the bearing, the load difference between the two contact diagonals is high enough that the ball kinematics change and the friction torque decreases drastically. This can be seen in the range from 5.6 kN to 8 kN for this bearing in Figure 2.2.

- Once the contact status of the balls changes from four points to two points, which means that the contact on one of the diagonals is lost, the axial load increase leads to a friction torque increase. This is shown in Figure 2.2 starting at 8 kN axial load.

In practice, all the balls never have exactly the same ball-raceway contact force in an idling state; in other words, the actual ball preload is not the same on all the

balls after the bearing is assembled and before applying any load. Therefore, this initial increase in friction torque followed by an abrupt drop does not occur in practice, as the experimental test results show in Figure 2.2. For a better understanding of this phenomenon, the changes in the kinematics of a ball for an increasing axial load were analysed.

Figure 2.3a shows the displacements of a four-point contact slewing bearing ball under an axial load and the aforementioned three stages or zones the ball goes through. Figure 2.3b shows the evolution of the friction torque of a preloaded ball together with the variation of the angle of the rotation axis of the ball (β). This figure corresponds to a more detailed analysis of the friction torque in Figure 2.2 with more load steps from 0 kN to 20 kN axial force. However, in this case, only the contribution of one ball to the friction torque was analysed. Together with the explanations below, this figure contributes to better understanding the phenomenon.

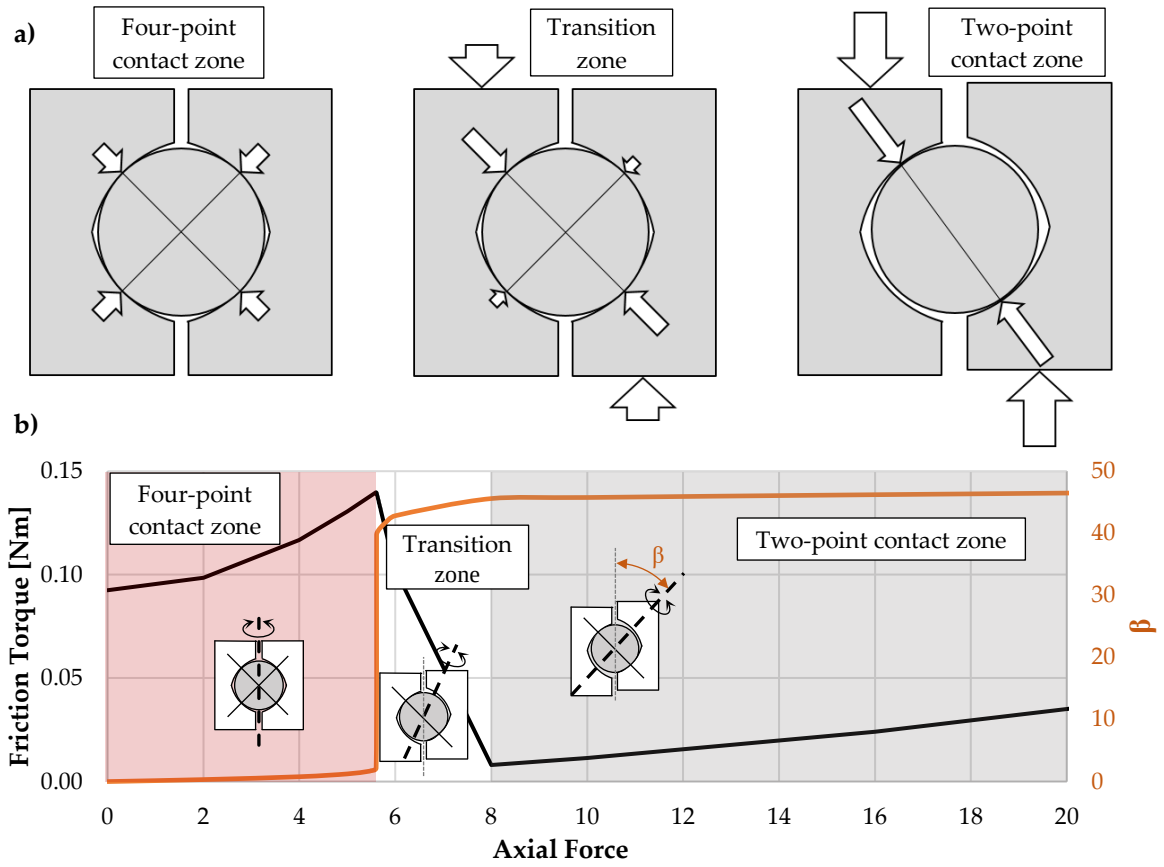

Figure 2.3. Three-phase schema (a) and friction torque evolution and ball rotation angle β change (b) of a four-point contact slewing bearing ball under axial load.

Three zones were established based on the evolution of the contribution of one ball to the total friction torque of a bearing subjected to an axial load (see Figure 2.3b). These zones were established according to the contact status of the balls and are easily identifiable.

In the first zone, referred to as the *four-point contact zone*, the axis of rotation of the ball is parallel to the axis of rotation of the bearing, so both rolling and spinning occur on ball-raceway contacts. This can be seen in Figure 2.3b, where the axis of rotation of the ball is depicted. In the idling state, the ball has four equally loaded contact points due to the preload, which corresponds to the point with 0 kN axial load.

When the axial load increases, not only does the load at two of the contact points increase as stated before but also affects the ball-raceway contact angle. This fact causes the angle of rotation of the ball β to change slightly in this first zone, as shown in Figure 2.3b. The increase of the normal contact forces at these two points involves higher frictional forces, thus increasing the friction torque. At the same time, the load at the other two contact points decreases, together with the rolling component at these points, and increases the spinning component, which also affects the friction torque increase. The overall friction torque increase can be seen in Figure 2.3b from 0 kN to 5.6 kN axial load.

In the second zone, called the *transition zone*, two of the contacts have already lost a large portion of their load. This makes the two most loaded contact points switch to a rolling state without almost any spinning so that the axis of rotation of the ball is almost perpendicular to the most loaded contact diagonal. This change in the kinematics causes a drop in the ball's contribution to the friction torque of the bearing (see Figure 2.3b from 5.6 kN to 8 kN).

Finally, in the area referred to as the *two-point contact zone*, the previously less loaded contacts become completely unloaded, leaving the other two to support the entire applied load. In this area, the ball's contribution to the bearing friction torque increases with the axial load as shown in Figure 2.3b from 8 kN and onwards.

After analysing the kinematics of one ball, it is possible to justify the friction torque drop in the analytical approximation for the entire bearing (solid line in Figure 2.2). If all of the balls in the bearing are subjected to the same conditions, they will all experience the same behaviour shown in Figure 2.3b. As a result, the

drop that occurs for one ball is replicated in all of the balls and the bearing behaves in the same way.

Contrarily, the experimental results (see experimental results in Figure 2.2) show a smooth evolution of the friction torque with the applied axial load. This can be explained under the hypothesis that, instead of all balls changing kinematics at the same time, a gradual transition from four to two points of contact is assumed. This gradual transition can be caused because, in practice, the actual preload is not the same for all balls. Figure 2.1 presented above shows how different ball preloads cause the transition to occur at different points, according to the analytical approach. Therefore, having different preloads on each ball will cause the transition of each one to occur at a different axial load, thus smoothening the drop observed in the bearing's friction torque.

Menck et al. [127] published the most recent and precise experimental results for ball slewing bearings, also from Fraunhofer IWES, which were provided for this work to be analysed in the same manner. The main difference between these bearings and previous ones is their larger diameter, which is closer to the dimensions of the bearings commonly used in wind turbines.

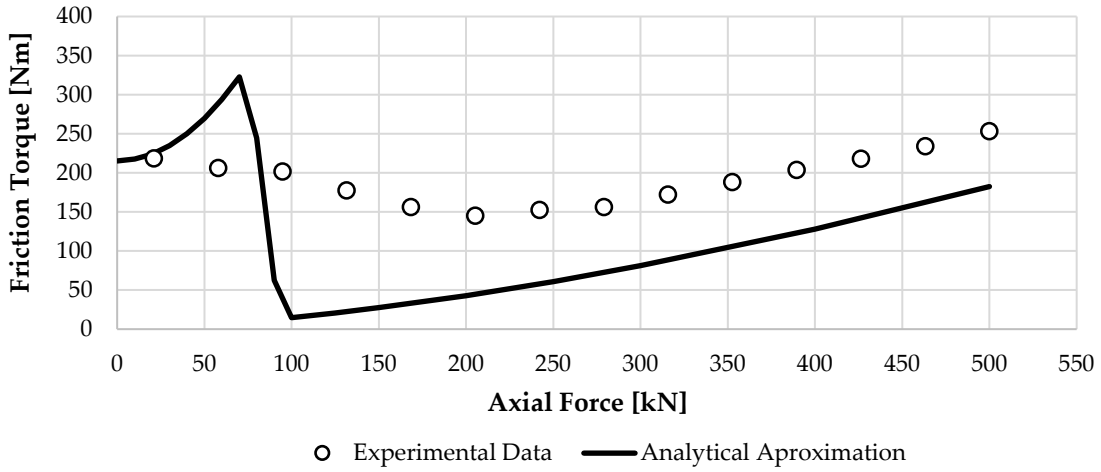

Figure 2.4. Comparison of the analytical model and experimental friction torque results [127] adjusted for the unloaded bearing case.

After adjusting the analytical model to the above-mentioned experimental results for the unloaded bearing case (see Figure 2.4), the same behaviour was observed: a sudden drop of the friction torque after exceeding an axial load value (80 kN). Afterwards, the friction torque kept increasing with the axial load (from 100 kN onwards). In addition, for these results, a difference in the friction torque

in the *two-point contact zone* (from 200 kN to 500 kN in Figure 2.4) was identified. This could be due to the effect of different elements, such as the seals or the cage, acting as a constant source of friction torque.

In short, the difference in the actual preload of the balls can justify the discrepancy between the analytical and experimental results. Therefore, this was adopted as the main hypothesis the method presented in this study was based on. In this regard, two main factors may account for the difference in the actual preload of the balls: the manufacturing errors of the raceways and the assembly process of the bearing to the surrounding structures.

On the one hand, manufacturing errors of the raceways alter the expected preload of the balls, causing some of them to be more or less loaded (or even have clearances). Meanwhile, the manufacturing errors of the balls are almost negligible, as they are measured and classified accordingly.

On the other hand, due to the flexibility of the rings, the preload level of the balls may vary as a result of the bolt-tightening process [171], when the bearing is assembled to the surrounding structures. Besides this, the load distribution can be affected by the lack of axisymmetry of those structures. In the case of a bearing under an axial load attached to a non-axisymmetric structure, each sector of the bearing will deform differently, resulting in a non-uniform load distribution.

2.2.2 Proposed approach

Considering the facts presented above, which explained the insufficient accuracy of the analytical approach, it is proposed to include scattering of the preload in the model by means of a statistical distribution in order to overcome the limitations of the analytical model. The details regarding the proposed analytical approach and the implementation of the preload scatter are given in this section.

As introduced in Section 2.1, calculating friction torque for ball slewing bearings involves solving two problems. The first problem involves estimating the distribution of the contact loads and angles on each ball-raceway contact (load distribution problem). The second problem involves calculating the friction torque as the sum of the friction torque contribution of each ball under the previously calculated load state (friction torque problem).

The model used for the load distribution problem only considers local deformations on the contact areas and does not account for the global deformations of the rings; i.e. rigid rings are assumed. Since the stiffness of the bearing rings and the adjacent elements differs from one application to another, this assumption was adopted not only for simplicity but also for the generality of the approach. Thus, the contact interference model in [20] was used, which accounts for the contact angle variation and the ball preload.

The preload used for this analysis must consider the final load state of the balls after the bearing assembly process. The term preload refers to the intended interference between the balls and the raceways caused by an assembly of an oversized ball. To distinguish this theoretical ball preload term from the preload value used in this work, the latter will be referred to as "effective preload" from now on. Thus, this “effective preload” accounts for manufacturing errors and ring deformations during the assembly process, in concordance with [31].

For the implementation of the preload scatter, the model was provided with the capability of defining the effective preload of each ball independently. A normal distribution was chosen as the method by which to implement the different values of the preload. This normal distribution was defined by two parameters, the mean value (m) and the standard deviation (SD) of the effective preload.

In addition, the statistical distribution requires an input of random numbers to generate the standard deviation. This was accomplished by using the MATLAB (version 2019a) software functions *rng*, which stands for Random Number Generation (RNG), and *randn*. The first function “seeds” the random number generation function, *randn*, so it produces a predictable sequence of numbers. Because this method relies on an initial number to generate a series of numbers, it is also known as PseudoRandom Number Generator (PRNG). The second function generates the normally distributed random numbers depending on the given seed number ($seed\ no.$). The decision was made to keep the seed no. constant for traceability purposes.

For this stage, the inputs needed to solve the load distribution problem consisted of the geometrical parameters, the statistical parameters that define the effective preload (m, SD and $seed\ no.$) and the applied external loads. The geometrical parameters involve the ball diameter (D_w), the bearing mean

diameter (D_{pw}), the osculation ratio of the contact (s), the initial contact angle (α_0), the number of balls per row (Z) and the number of rows (n). The outputs of the load distribution problem are the contact loads (Q) and contact angles (α) for each ball-raceway contact point.

On the other hand, the friction torque problem depends on the aforementioned outputs from the load distribution model, with the exception of some geometrical parameters. The model used for this purpose in this work was based on the approach presented by Joshi et al. [124]. Once the problem is solved, the kinematics are known and the shear stresses in each contact can be computed, which allows for the calculation of friction forces and the contribution of each ball to the friction torque independently. The model used in the current work also implemented the strategies proposed by Heras [25] to solve the convergence problems of the latter work. In addition, according to Heras' work, and as a part of the hypotheses accepted for this research, full sliding was considered in the current model, since considering regions in adhesion gives almost identical results regarding friction torque and has a higher computational cost.

The model also included an independent constant parameter (C) that was directly added to the friction torque result. This constant allows for friction torque curve adjustment when the shape of the analytical results fits the experimental data, but there is an offset, as shown in Figure 2.4, to which the effect of the seals or any separating element on the friction torque is attributed.

The experimental results obtained in [31] used a bearing with none of those elements. By adjusting the friction torque with the new analytical tool by varying the preload, it is possible to evaluate the effect of these elements. If the analytical results fit the experimental data in the *two-point contact zone*, the constant contribution of these components could be verified.

The experimental measurements in [31] were carried out with two different axial force sensors, which implies a discrepancy in the evolution of the friction torque, as shown in Figure 2.5 (from 56 kN to 70 kN).

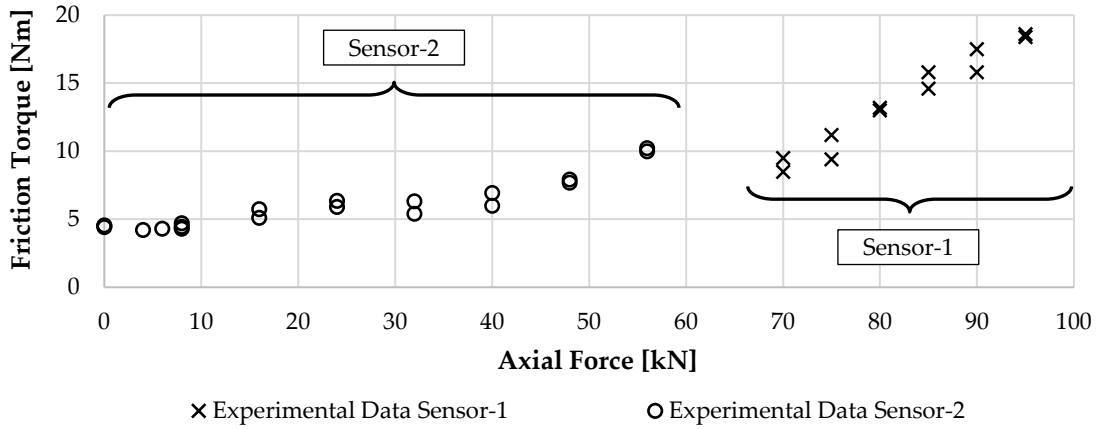

Figure 2.5. Experimental results of an axial test rig for a smaller size slewing bearing with no seals or separating elements [31].

Therefore, in order to adjust the analytical model to the experimental results, only those obtained with the same axial force sensor, in this case, Sensor-2, were used. However, these result points are enough to evaluate both the *two-point* and *four-point contact zones*. Nonetheless, when the results are shown, all the experimental results will be maintained in order to qualitatively observe the shape of the friction torque evolution.

Figure 2.6 shows the analytical approximation to the friction torque results, based on the Leblanc and Nelias model [122,123]. The analytical model was adjusted to match the friction torque of the experimental results for the unloaded case ($F_a = 0$ kN).

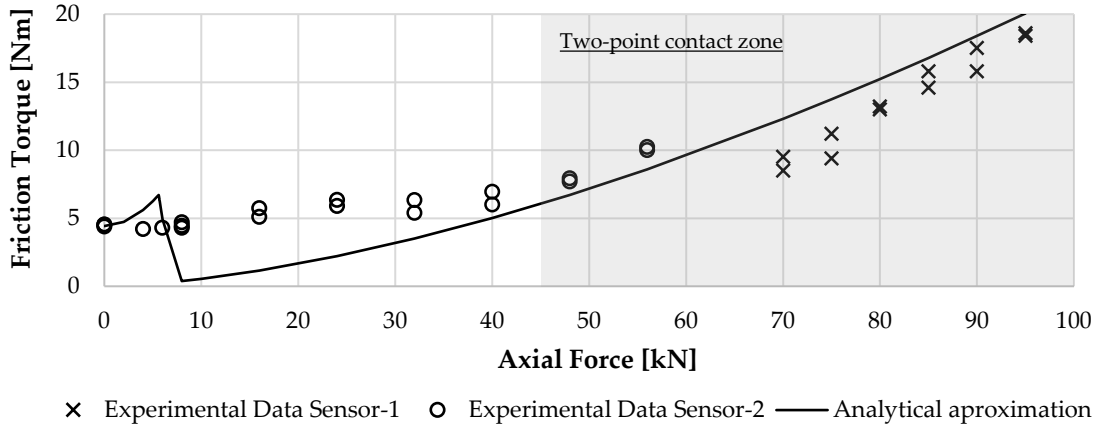

Figure 2.6. Analytical approximation to experimental results of a slewing bearing with no seals or separating elements.

First conclusions could be established based on the obtained fitting of the analytical model to the experimental results, with a focus on the *two-point contact*

zone (see Figure 2.6, F_a > 45 kN). It can be appreciated that as the axial force on the bearing increases, the analytical tool is capable of adjusting the friction torque in this zone.

On the one hand, this confirms that friction torque in the *two-point contact zone* is hardly affected by a preload scatter under compressive axial load. It must be noted that the bearing tested has a smaller mean diameter compared to the ones tested in [127], so the stiffness of the bearing races is higher.

On the other hand, it is found that without the constant C parameter, the analytical approximation yields results in the order of magnitude of the experimental results in the *two-point contact zone*. This confirms the hypothesis that there is no need for such a parameter if there are no seals or separating elements; or in other words, the effect of these components is captured correctly in the C parameter.

Therefore, to solve the friction torque problem, the input parameters required mainly consist of the contact loads and contact angles for each ball-raceway contact point (which are the outputs after solving the load distribution problem), the coefficient of friction (μ) and also some geometrical data (D_w, D_{pw}, s), with the friction torque (T) being the output of this stage. Figure 2.7 summarises the calculation stages and their inputs to obtain the bearing friction torque for the analytical model. The figure shows a flowchart for the calculation stages of the analytical model with their respective inputs and outputs to obtain the friction torque.

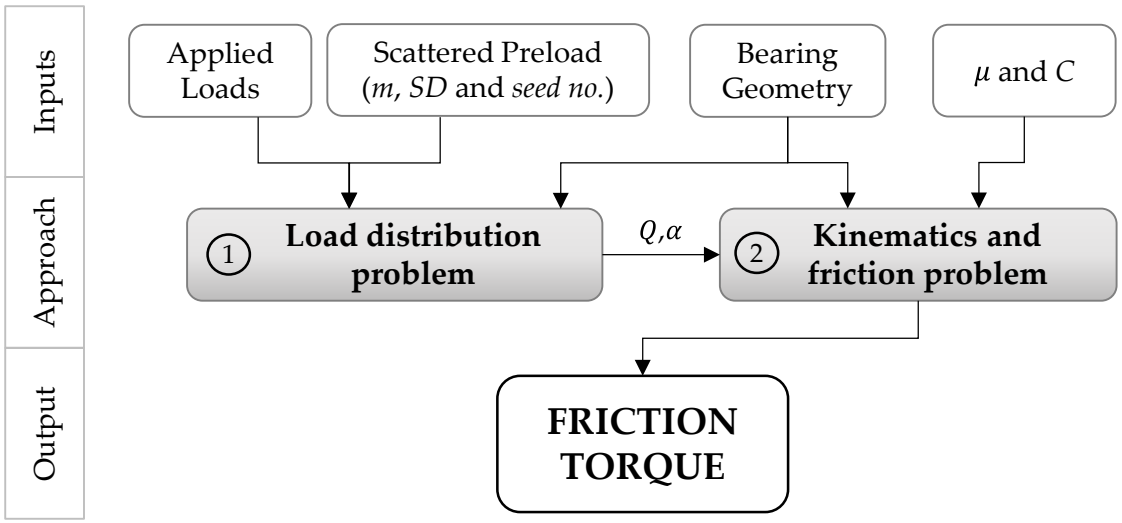

Figure 2.7. Calculation stages of the analytical model

2.2.3 Case study

As explained in Section 2.2.2, the analytical model was tuned to fit already existing experimental data from [127] in order to check the capabilities of the proposed approach to reproduce the real evolution of the friction torque, especially in the *transition zone*. Because of this, the bearing used to study the effect of the tuning parameters (Section 2.2.4) was the same as the one later used to fit the experimental results (Section 2.3).

The bearing geometry details were provided by Fraunhofer IWES and are the ones reported in [127] for the BEAT1.1 test rig, summarized in Table 2.1.

Table 2.1. Nominal dimensions of the measured bearing.

Bearing mean diameter (D_{pw})	**Ball diameter (D_w)**	**Osculation ratio (s)**	**Initial contact angle (α_0)**	**Number of balls (Z)**	**Number of rows (n)**
673 mm	25.4 mm	0.94	45°	69	2

The tuning parameters that were used to fit the analytical model to the experimental results were chosen based on known data (macrogeometry, microgeometry) for this case study, and are listed below:

- The statistical distribution parameters that define the effective preload (m and SD): manufacturing errors are unknown and the effect of the assembly process on the effective preload cannot be calculated directly.
- The coefficient of friction (μ): reference values are known from literature [124,127,177], but it is unknown for each specific case. The considered values when tuning the model must be close to the ones in the references.
- The independent constant (C): the effect of the phenomena related to this parameter (seals, cage, etc.) cannot be estimated directly.

Therefore, according to the established tuning parameters, the friction torque can be defined as follows, based on the analytical approach described in this section:

$$T = f(m, SD, \mu) + C \tag{2.1}$$

2.2.4 Study of the parameters

The effect of the chosen tuning parameters on the friction torque is studied in this section. First, the effect of m and SD is shown, which are the parameters that define the statistical distribution of the preload. Figure 2.8 shows the effect of the SD parameter, which is a direct comparison sample of the effect of the preload scatter with the non-modified analytical model (see Figure 2.8 line m = 7.5 SD = 0 μ = 0.1, all preload values in μm).

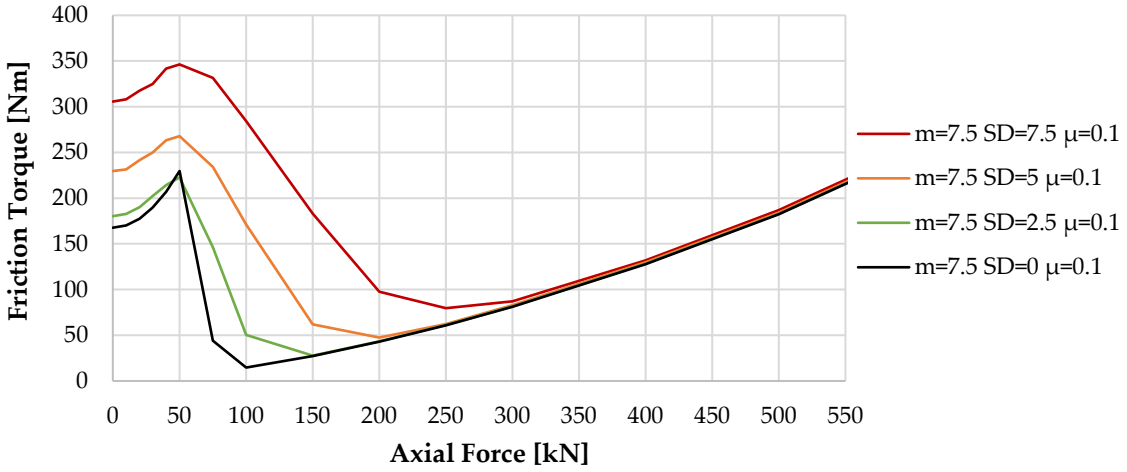

Figure 2.8. Effect on the friction torque of the standard deviation of the effective preload for a constant mean preload m = 7.5μm.

First, as the standard deviation increases, the idling friction torque becomes higher. This result is the expected one, as there are more balls with a higher preload.

Following that, focusing on the *transition zone* (50 kN – 100 kN), the case where there is no deviation of the effective preload (SD = 0 μm) shows a sharp decrease in the friction torque. The plot shows how this sharp variation is smoothened by introducing a deviation into the effective preload distribution.

Finally, due to the smoothened behaviour achieved for the *transition zone*, the *two-point contact zone* starts at higher axial loads. Within the case with zero standard deviation, this occurs for an axial force of 100 kN; for higher values of the standard deviation (SD from 2.5 μm to 7.5 μm), the *two-point contact zone* starts for axial forces in the range of 150 kN to 300 kN, for the considered cases. However, once the *two-point contact zone* is reached in all cases, the friction torque does not vary significantly with the standard deviation.

If the effect of m is analysed, as shown in Figure 2.9, a similar effect is observed. Hence, the higher m is, the higher the idling friction torque becomes. In addition, the friction torque requires a higher axial load to reach the *two-point contact zone*. Finally, as was the case with SD, m does not affect the friction torque once the *two-point contact zone* is reached.

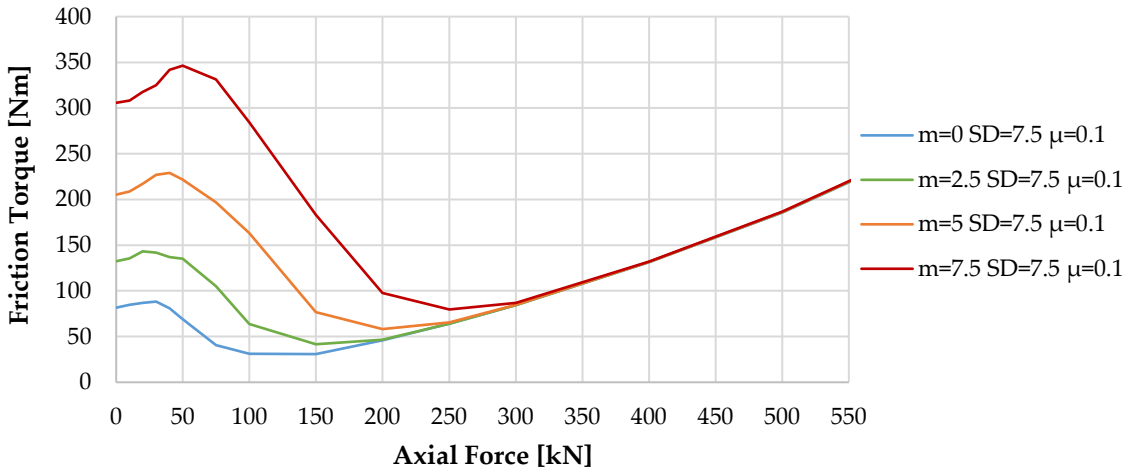

Figure 2.9. Effect on the friction torque of the mean of the effective preload for a constant standard deviation of the preload SD = 7.5 μm.

The effect of different seeds on the statistical distribution of the effective preload is analysed below. Even though the *seed no.* is not considered as a tuning parameter, as it will be kept constant, it affects the effective preload scatter. This is because it affects where the most and least preloaded balls are placed. This can be understood by analysing the bearing load distribution under axial force and tilting moment.

When a bearing is subjected to a pure axial load, the azimuthal position of the balls does not affect the load each ball has to bear, regardless of its preload. Therefore, the seed no. does not affect the friction torque in this load condition. However, this is not so for load cases involving a radial force or a tilting moment, as these external loads do not result in an evenly distributed load on the balls. With this in mind, the effect of the seed no. is only analysed for tilting moment cases, as shown in Figure 2.10.

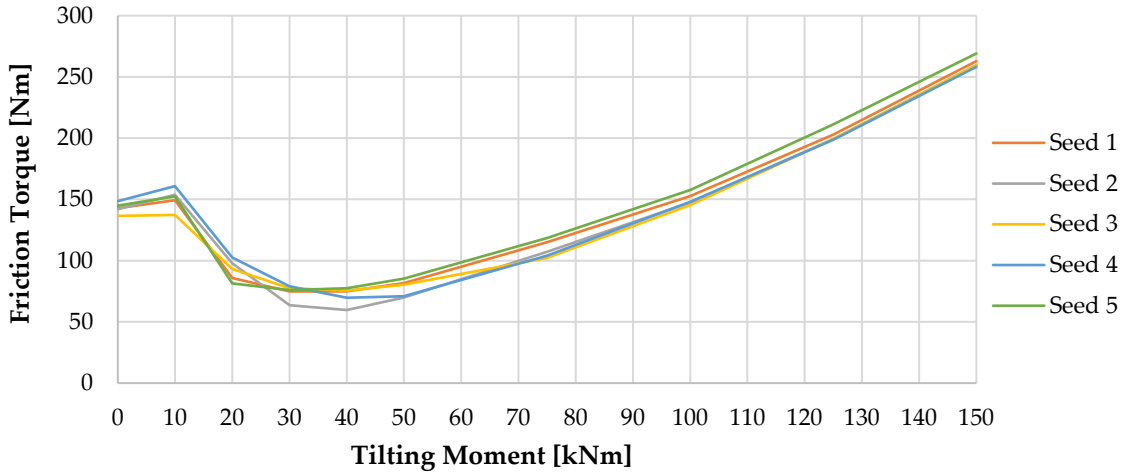

Figure 2.10. Analysis of the *seed no*. selection for random number generation of the friction torque tool.

The result of varying the *seed no*. causes a minor change in the absolute value of the friction torque, with almost no variation in the shape of the curve. However, there could be a greater effect for a different *seed no*. than the one shown in this example for a different geometry or load combination. Considering the case of a bearing with a greater mean diameter and low tilting moments for its size, the number of balls next to the axis of the tilting moment will be greater. With this in mind, these balls will be subjected to a small fraction of the applied load and will remain in the four-point status. Therefore, if these balls are highly preloaded, their contribution to the friction torque will be also high and the friction torque curve will be more uniform.

Therefore, after analysing the effect of the statistical distribution parameters, it can be said that the preload scatter implies noticeable changes in the evolution of the friction torque of a ball slewing bearing. Moreover, the effect smooths the four-point to two-point contact transition, in line with what is found in the available experimental results. Therefore, it is fair to expect a better correlation between the analytical model calculations and the experimental data by considering this preload scatter.

When it comes to analysing the effect of the coefficient of friction (μ), Figure 2.11 shows the effect of varying it on the friction torque. As expected, the coefficient of friction affects the friction torque in a proportional manner. Accordingly, the axial force required to reach the *two-point contact zone* remains the same as the coefficient of friction changes (150 kN for m = 5 μm, 60 kN for

m = 0 μm, see Figure 2.11). Furthermore, it is seen how the *two-point contact zone* remains unaltered for different values of m with the same coefficient of friction.

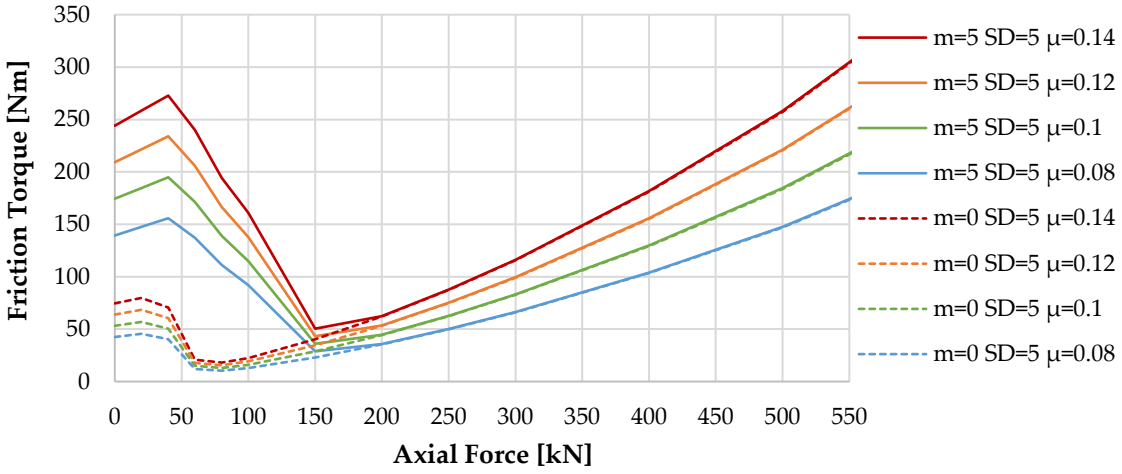

Figure 2.11. Effect of the coefficient of friction μ on the friction torque analysis.

Lastly, constant parameter C introduces an offset to the friction torque, as shown in Figure 2.12.

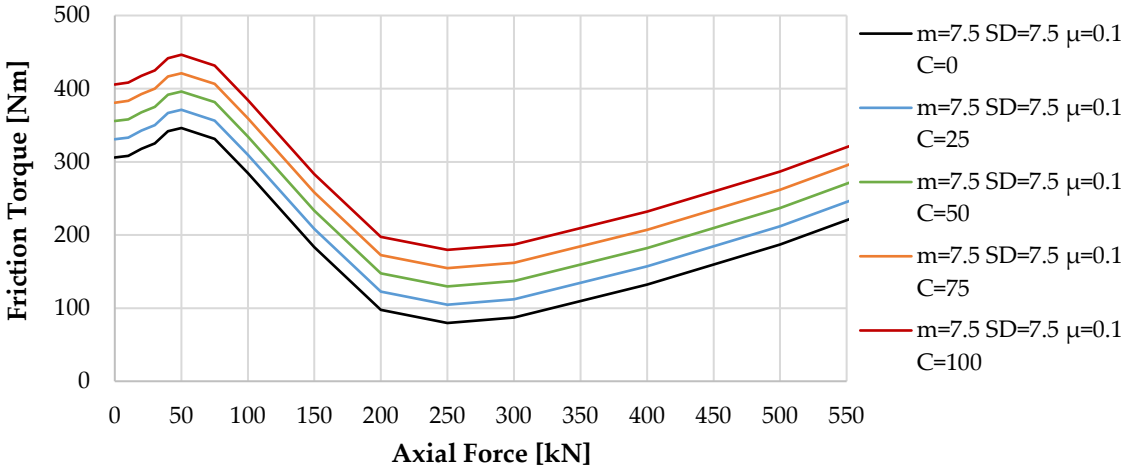

Figure 2.12. Effect of the constant C parameter on the friction torque analysis.

From these analyses, it is concluded that, of the studied parameters, only two of them affect the friction torque on the *two-point contact zone*: μ and C. The first one affects the slope of the curve in this region, while the second one only introduces an offset to the curve. On the other hand, m and SD have been proven to greatly affect the *four-point contact zone* and the *transition zone*, smoothening the drop of the original approach by [124]. Therefore, introducing the ball preload scatter allows the analytical model to obtain a better fit of the experimental

results, which is the goal of this research and which is described Section 2.3 below.

2.3 Correlation with experimental results

From the results of the previous section, a procedure is presented to tune the analytical model in order to fit the experimental data obtained by Menck et al. [127]. This section explains the procedure and its results, which some guidelines for calculating the friction torque under different case scenarios are based on and presented in Section 2.5.

2.3.1 Experimental setup

The experimental friction torque results used for the model correlation in this work were obtained using the Fraunhofer IWES test rig BEAT1.1 (Bearing Endurance and Acceptance Test rig) shown in Figure 2.13.

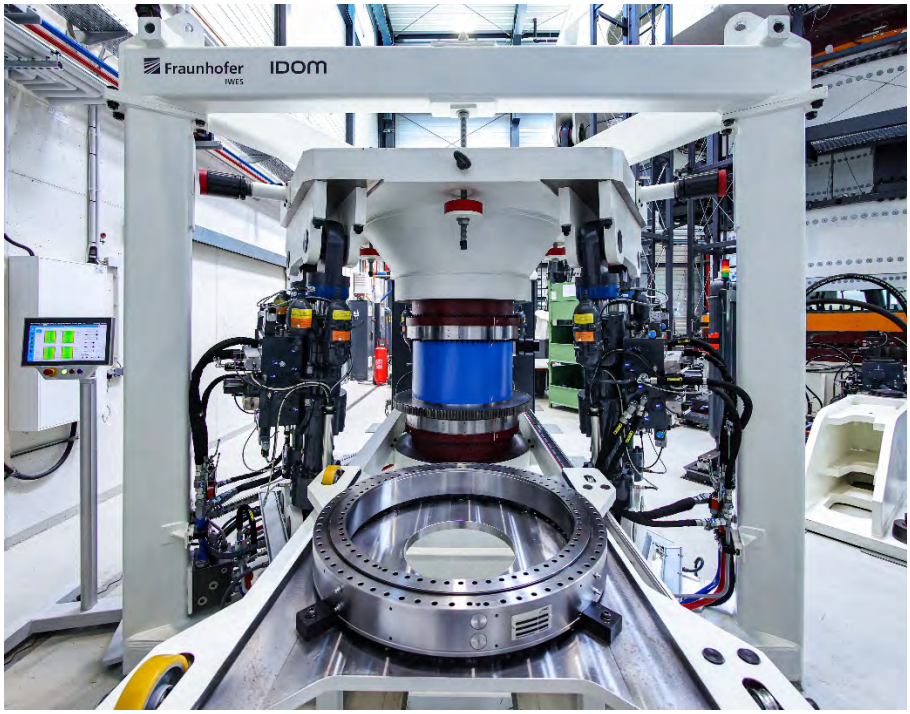

Figure 2.13. BEAT 1.1 test rig with a tested bearing sample. (©Fraunhofer IWES/Ulrich Perrey)

The test rig consists of six hydraulic actuators in a hexapod configuration, connected to a load platform located at the top. This configuration permits a complex load application with six degrees of freedom for any bearing. The test

rig can be separated into three sections: the outer structure, the bearings and the connecting element.

The outer structure consists of two rigid bodies, the top plate and the lower plate or the base, which are connected via the hydraulic actuators as explained above. The actuators impose a relative displacement between the plates, which is subsequently translated into an applied load. Two eight-point contact ball bearings (i.e. two double row four-point contact bearings) with the properties in Table 2.1 are connected to each of the plates, in this case, by means of the bolted connections of the outer rings. Lastly, the connecting element is attached to the inner ring of each bearing, connecting the bearings and serving as the elements from which the applied loads will be transmitted to the bearings.

A geared ring is connected between this element and the inner ring of the lower bearing, which makes contact with a gearbox so that the inner part of the test rig can rotate. This allows the bearings to rotate while the loads are being applied. An electric pitch drive introduces the pitch movements via the gear connection. The friction torque is measured for both bearings together by a calibrated torque meter located between the gearbox and the electrical drive. Due to this position for the measurement, the gearbox torque needs to be subtracted, which is done by means of an empirical function developed by IWES [127]. Later, after obtaining the experimental results, a torque meter was installed directly to the gear ring of the test rig and the previous empirical function was completely validated.

The friction torque results used for the following model approximation procedure were obtained with pure axial force and pure tilting moment tests. The measurements were made for 30 different load levels in the ranges of -200 kN (tension) to +500 kN (compression) for the axial load, and -125 kNm to +125 kNm for the tilting moment. Due to the limited capacity from the bolted connection of the bearing, the maximum tension force is lower than the compressive force for the axial load tests.

2.3.2 Model tuning procedure

Several analyses were performed considering different combinations of the tuning parameters to achieve a good correlation with the available experimental

data [127]. The procedure in this section was repeated for every experimental data set, the results of which are analysed in Section 2.3.3.

It must be noted that because the bearings were tested in pairs in [127], the measured friction torque was divided by two when the plots were presented. Conversely, in the current work, the total friction torque corresponding to both bearings is represented when studying the results, so the experimental results shown below are the same as the previous work multiplied by two. Moreover, the names of the experimental results used in this thesis were renamed according to Table 2.2 to keep a clearer schema of the results.

Table 2.2. Experimental dataset names corresponding to the bearing pairs used for the experimental tests.

Bearing pair in [127]	New experimental dataset name
143 and 144	Experimental data 1
172 and 173	Experimental data 2
162 and 163	Experimental data 3
174 and 175	Experimental data 4

Although all bearing pairs have the same geometric parameters, their friction torque varies. Since the bearings are manufactured to meet the requirements of a maximum unloaded friction torque, the manufacturer is obliged to vary the preload by changing the ball size to adjust the unloaded friction torque, due to the variations introduced by the manufacturing and ring flexibility after the assembly process. Accordingly, the bearing idling friction torque is less than a certain value (requested from Fraunhofer IWES). As a result, even though the bearing pairs are identical and the preload is very similar between them, manufacturing errors can cause the effective preload to vary more than expected, leading to the friction torque variations seen in the experimental results [127].

The analytical model adjustment procedure consisted of searching for a set of values of the tuning parameters that are best fitted to the experimental data. First, this was done for the axial load case, since the different contact state zones (see Figure 2.3b) can be identified more clearly under these working conditions. As explained above, when a pure axial force is applied, the load is distributed almost evenly among the balls, excluding the variation introduced due to the preload

scatter. In this case, there is an axial force value from which the *two-point contact zone* is reached for every ball. Therefore, the best-fit values of the tuning parameters with the axial experimental results were established in the first place. The obtained tuning parameter values were then used to check the correlation with the tilting moment case.

First of all, from the study of the coefficient of friction, it was concluded that it is the only parameter that affects the slope of the friction torque curve in the *two-point contact zone* (see Figure 2.11). Accordingly, it was selected as the first parameter to be tuned for simplicity. In order to isolate the *two-point contact zone* points from the rest of the experimental data points, the slope of the friction torque curve was analysed. When the friction torque starts to increase steadily, it can be assumed that the bearing is in the *two-point contact zone*. Figure 2.14 shows a visual representation of the selection procedure for the coefficient of friction μ. The adjustment procedure of this parameter focused on the slope of the curve in this zone. Given that with the variation of this parameter the slope in this zone changes, the best-fit coefficient of friction for the slope of the experimental results was therefore selected, using the Root Mean Square Error (RMSE).

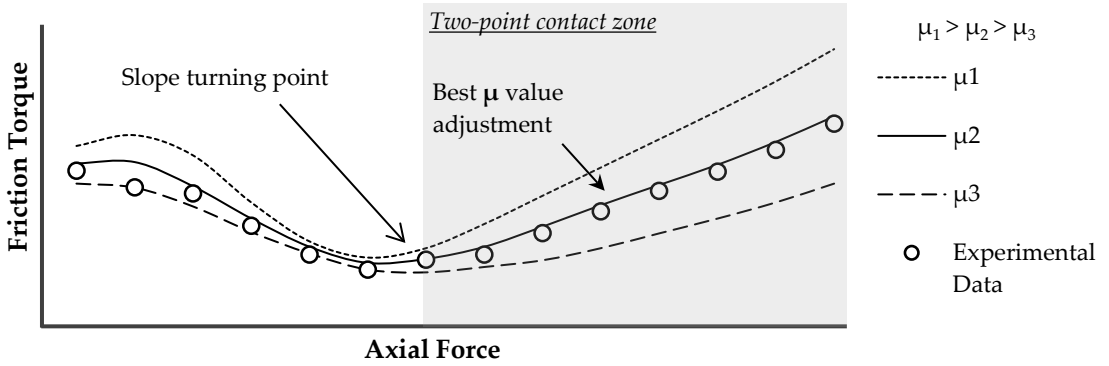

Figure 2.14. Example schema of the selection procedure for the coefficient of friction.

Subsequently, multiple analyses were performed varying m and SD. Different friction torque curves were obtained with these analyses. For each curve, C was adjusted to minimise the RMSE in the *two-point contact zone* (see Figure 2.15).

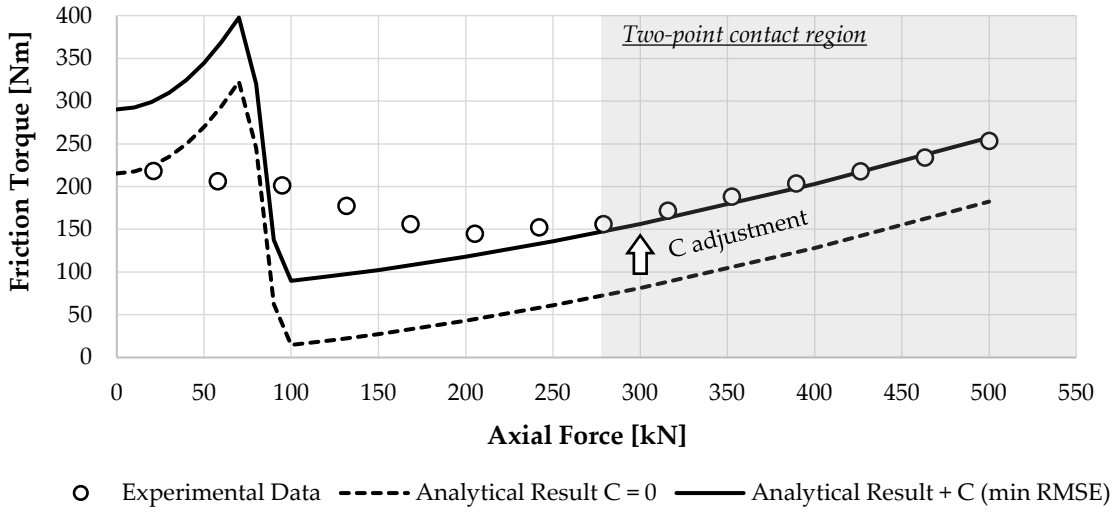

Figure 2.15. Example of a curve adjusted by the C parameter and the visual representation of the absolute error of each point.

Finally, the curves with the lowest mean relative error (which will be presented as a heatmap) for all the axial force values with respect to the experimental results were chosen, as were the tuning parameter value combinations associated with them.

2.3.3 Obtained results

The results in this section are analysed in detail for the *Experimental Data 1* dataset, which is also separated into two sub-sections: axial load case and tilting moment case. The results are then analysed for the rest of the cases.

Following the described procedure, the slope of the compression side of *Experimental Data 1* is analysed. This way the *two-point contact zone* is defined (see Figure 2.16 from 315 kN to 500 kN).

Then, an arbitrary value of the preload is considered to solve the friction torque problem for different coefficient of friction values. Figure 2.16 shows the calculated cases with a constant value given to visually match the experimental data. A coefficient of friction of 0.085 was found to best fit *Experimental Data 1* results, with an RMSE value of 0.991. A detailed view of the *two-point contact zone* and RMSE results can be seen in Figure 2.17.

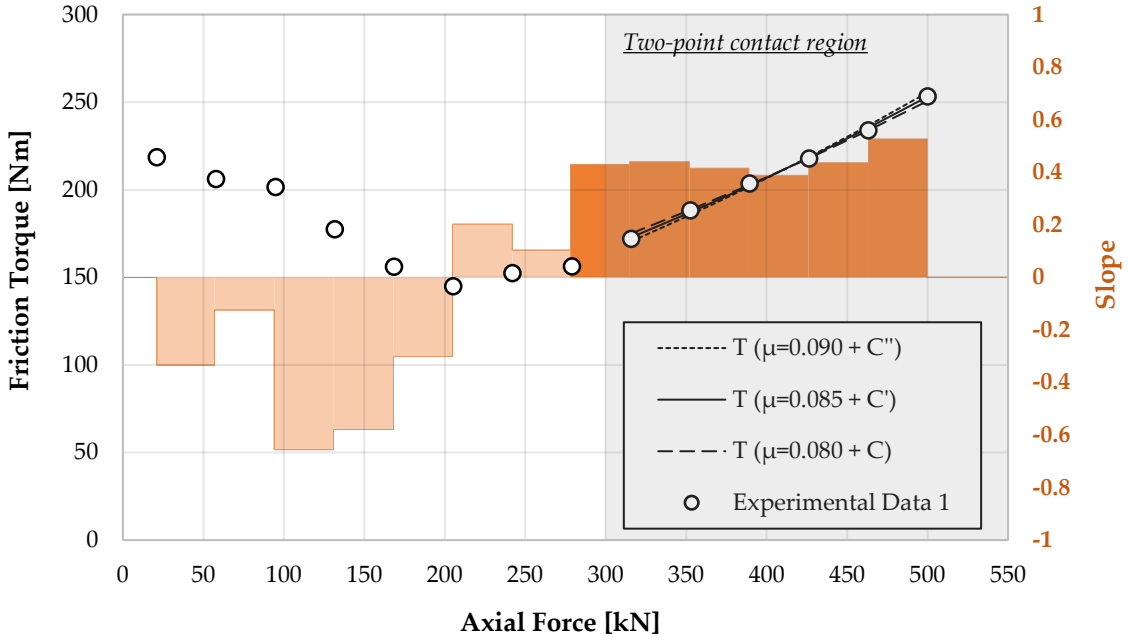

Figure 2.16. *Experimental Data 1* slope and different coefficient of friction results.

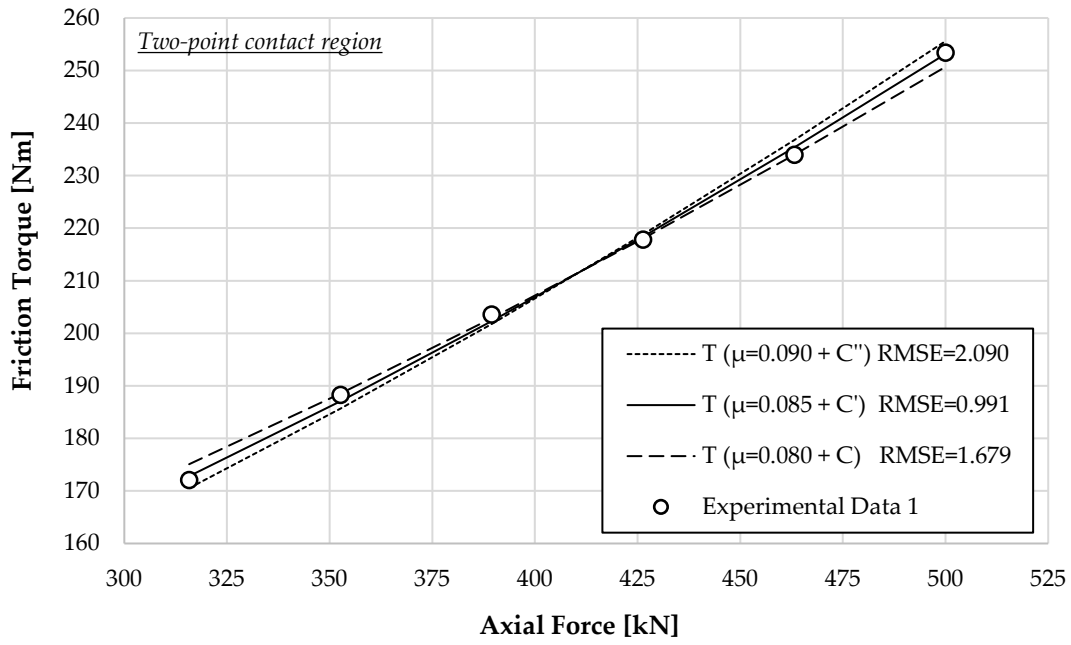

Figure 2.17. *Experimental Data 1* coefficient of friction results detail and RMSE values.

Given the lack of experimental results on the tension zone, the decision was made to adjust the results for the compression side, considering the procedure requirements for some data to evaluate the *two-point contact zone* first.

Afterwards, multiple combinations of m and SD are evaluated with this μ, adjusting each calculated curve with C to minimise the RMSE, matching the *two-point contact zone* with the least possible error (see Figure 2.18). Because the

analytical model considers rigid rings, the friction results obtained for the compression side will be identical for the tension side.

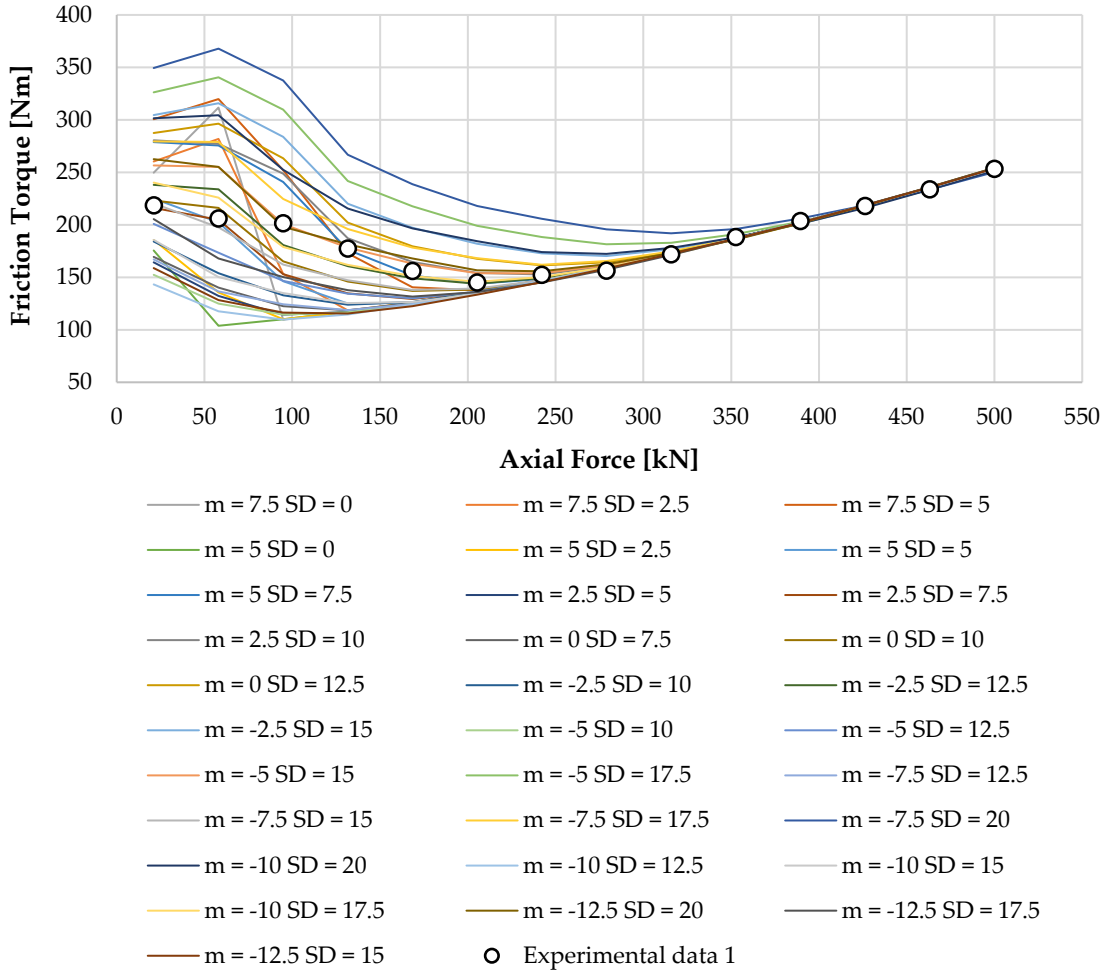

Figure 2.18. Computed combinations of m and SD to fit *Experimental Data 1*.

From this point, all the relative errors for each combination of m and SD are computed to find the preload values with the least relative error with respect to the experimental results. The computed relative errors are expressed as a heatmap in Figure 2.19, which shows that the greater m is, the lower the value of SD that yields a lower error. In Section 2.2.4 above, it was seen how the effect of both parameters, m and SD, was very similar. In this sense, the results in Figure 2.19 are coherent with this, as the cases with the lowest errors are arranged in a band. Therefore, there is no single combination of these m and SD values that best fits the experimental results but rather a set of them.

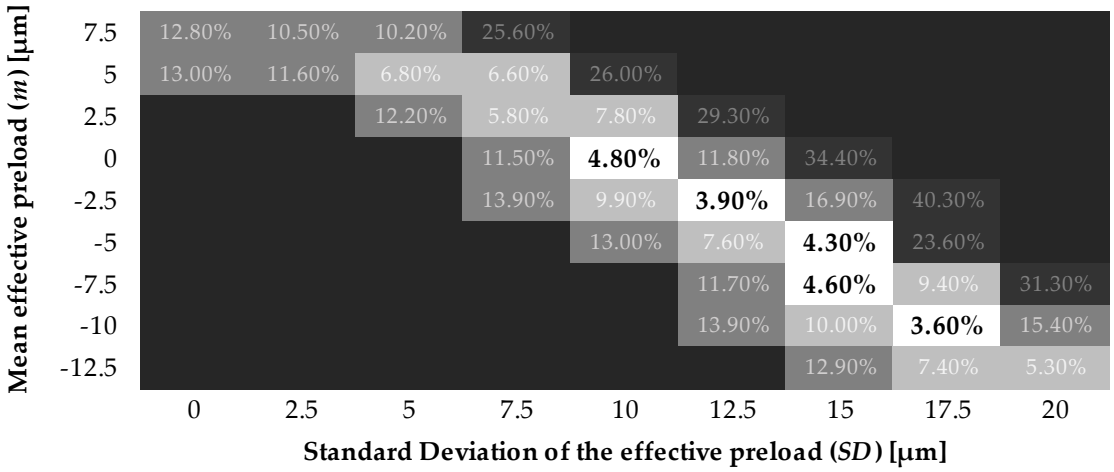

Figure 2.19. Heatmap of mean relative errors for all the computed combinations of *m* and *SD* for *Experimental Data 1*.

Figure 2.20 shows the extracted friction torque curves corresponding to the computed combinations of *m* and *SD* (from Figure 2.18) that yielded a mean relative error lower than 5%, according to Figure 2.19. Both compression and tension load cases are represented in this figure, corresponding to negative and positive values of the axial load, respectively.

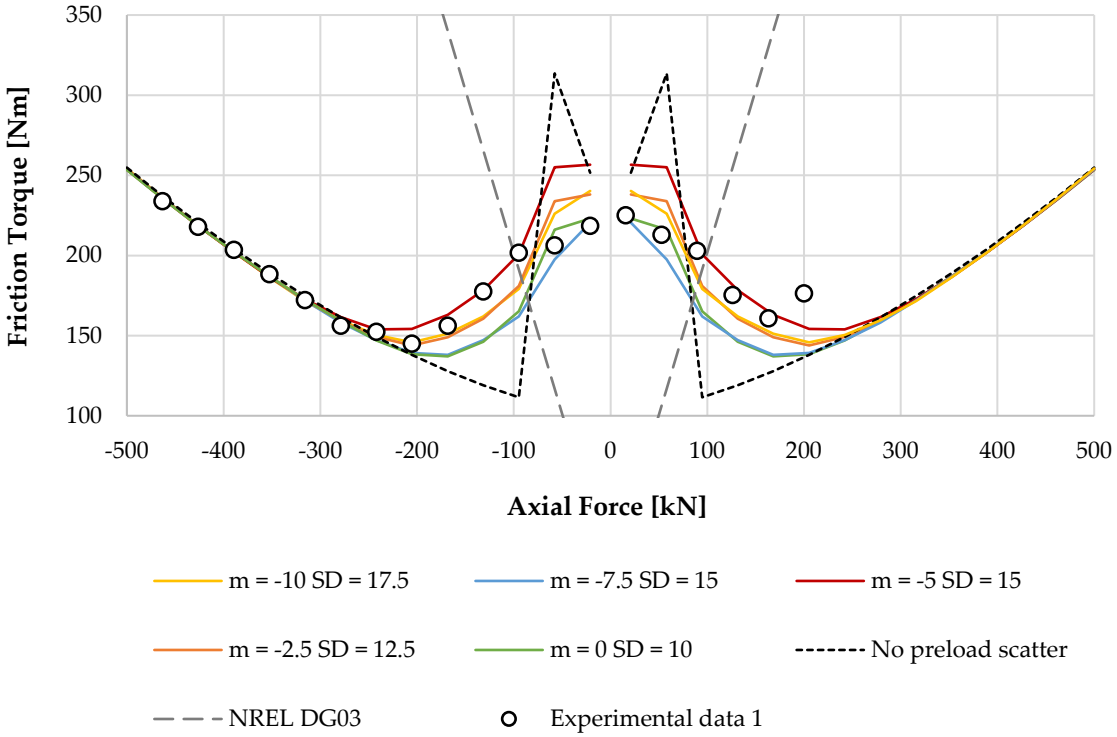

Figure 2.20. Analytical results selection adjusted to *Experimental Data 1* results under axial load.

On the compression side, analytical results show a good match with the experimental data. The analytical results match the experimental data for all the cases once all the balls are in the *two-point contact zone* (see Figure 2.20, approximately from -275 kN to -500 kN). This validates the fact that the effect of the preload is negligible, which was seen in Section 2.2.4.

With regards to tension side, analytical results are symmetrical because, as stated above, under the rigid rings assumption, the load distribution is the same, thus leading to the same friction torque. The results also indicate a good correlation for tension side, except for one experimental data point. The lack of experimental results for higher tension loads prevents any further conclusions being drawn in this regard.

Figure 2.20 also includes the results according to the formula proposed by the NREL in their design guideline [49]. It can be seen how, in line with the guideline, the estimated friction torque is overestimated for high axial loads. Nonetheless, for light loads (see Figure 2.20, approximately from 0 kN to ±200 kN), this formula greatly underestimates the friction torque. In this regard, the proposed method is proven to be far more accurate than the NREL formula. Moreover, the results for the previous analytical model are included in Figure 2.20, where an improvement in the accuracy of the friction torque estimation for low loads, which includes the *four-point contact zone* and the *transition zone*, can be seen.

Once the values for the parameters μ, m, SD and C that give the lowest mean relative error for the axial load case are obtained, they are used to perform calculations for tilting moment. The results of these are shown in Figure 2.21.

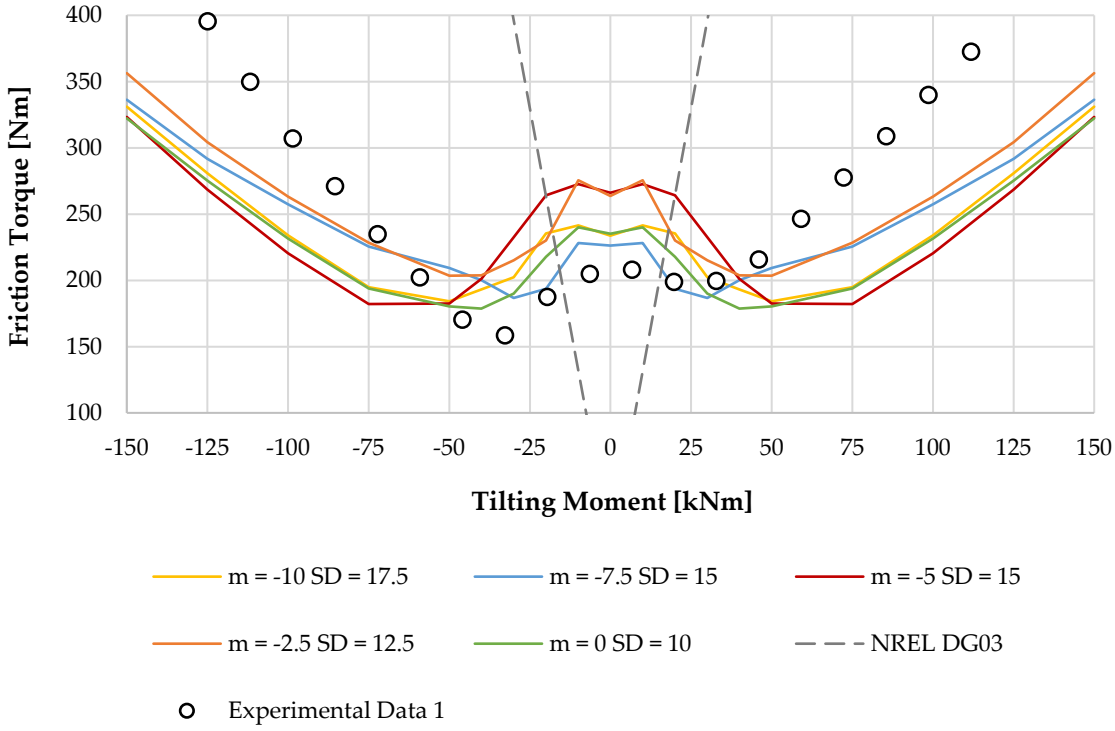

Figure 2.21. Analytical results selection adjusted to *Experimental Data 1* results under tilting moment.

The sign of the tilting moment defines the direction of the applied load. As was the case for axial load, due to the rigid ring assumption, the analytical approach yields the same results for both positive and negative tilting moments. This symmetry is not found in the experimental results, which can be explained by the ring deformation behaviour of the test bearings. If the flexibility of the rings and the structures of the test bench affect the load distribution, it will also affect the friction torque, which would explain not only the lack of symmetry of the test results, but also the poor correlation between the analytical approach and the experimental results. Therefore, even if the current approach is far more accurate than the formula from the NREL [49], it cannot be considered a satisfactory match. This fact leads to the following section (Section 2.4), which considers the effect of the flexibility of the rings and the structures.

However, before analysing the effect of the flexibility, the other experimental cases are presented and briefly analysed below. First, the *Experimental Data 2* test results are shown in Figure 2.22. The results show the same behaviour of the friction torque as for *Experimental Data 1*, where the analytical results offer a perfect fit with the experimental results on the compression side. However, with regards to the tension sides there is a considerable discrepancy with the

experimental results. In fact, the experimental friction torque results show a lack of symmetry, which can be justified because the rings deform more under tension than under compression, which the analytical model does not consider. It should also be noted that *m* has a positive value in this case, while in the previous case, it was negative.

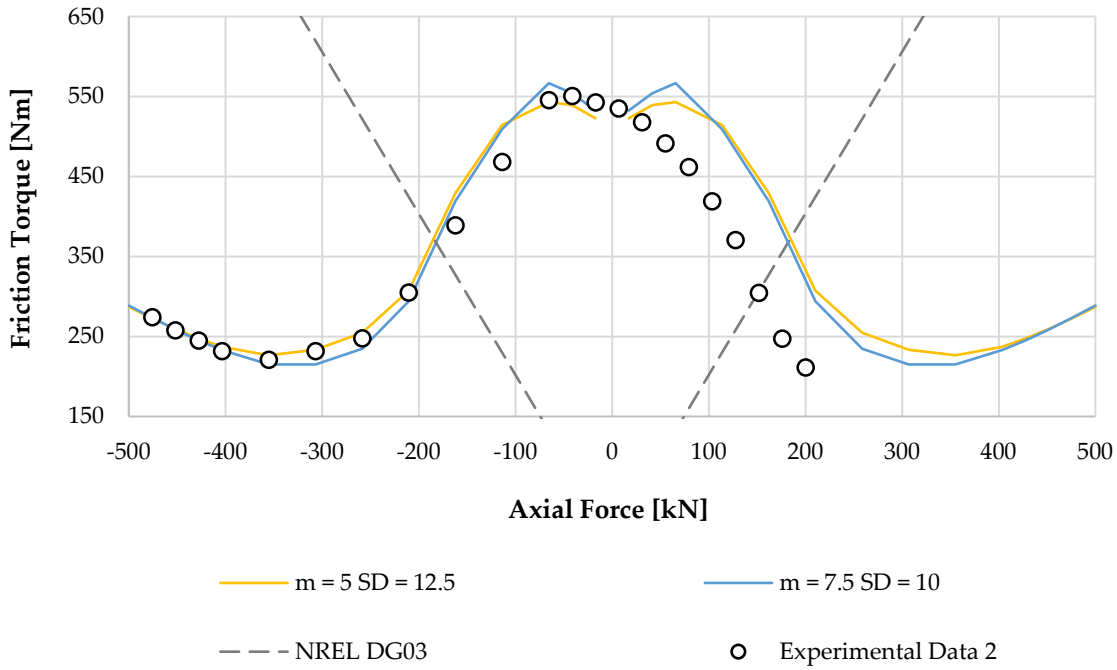

Figure 2.22. Analytical results selection adjusted to *Experimental Data 2* results under axial load.

Meanwhile, in this particular case, there is a big discrepancy between the compression and tension side of the experimental results. Manufacturing errors should have no effect on generating these differences in the case of an axially loaded bearing because the experimental test requires the bearing to turn, varying the manufacturing errors each ball-raceway is subjected to. However, this can be understood if the effect of the flexibility of the rings is considered, as these bearings are more flexible under tension than compression.

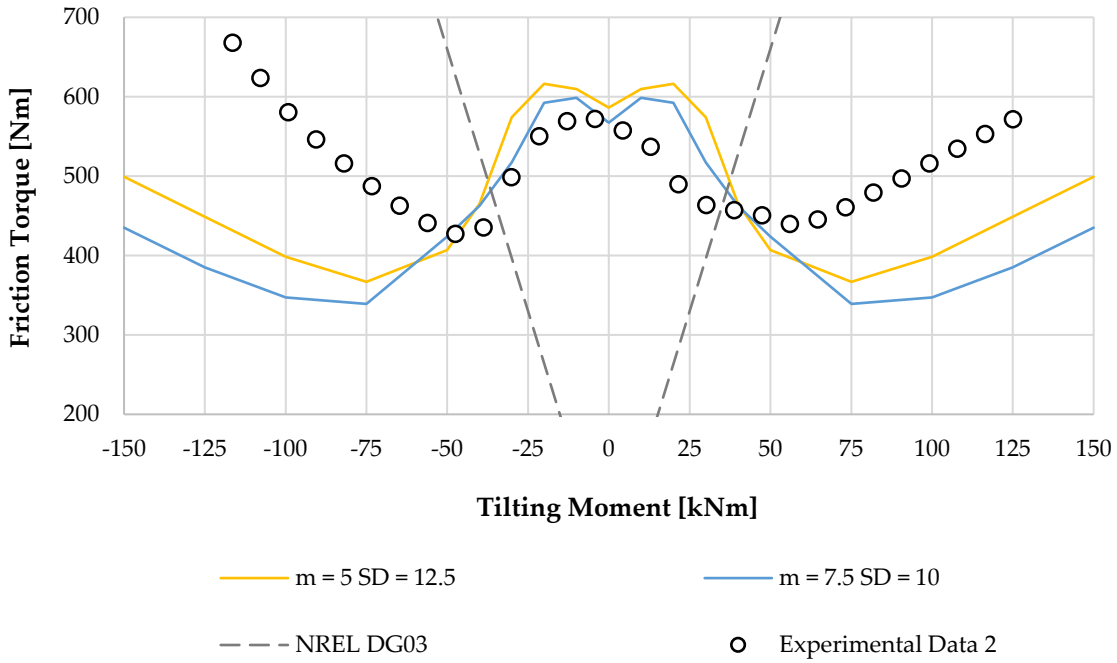

Figure 2.23. Analytical results selection adjusted to *Experimental Data 2* results under tilting moment.

The results for *Experimental Data 2* for a tilting moment are shown in Figure 2.23. Again, the *m* and *SD* combinations obtained prove to be a good fit for light loads (see Figure 2.23, approximately from 0 kNm to ±50 kNm), whilst the NREL formula greatly underestimates the friction torque.

Continuing with *Experimental Data 3* results, these are shown in Figure 2.24. The experimental results are very similar to the *Experimental Data 1* results, which are almost symmetric comparing the tension and compression sides. Two tests were performed with this pair of bearings, which distinguishes these results from previous ones. The results labelled *Exp. Data 3 dis- and reassembled* in Figure 2.24 correspond to the same pair of bearings tested after the bearings were disassembled and reassembled. However, the latter results are not symmetric, which may imply that the assembly process greatly affects the friction torque and therefore is a process that should be controlled.

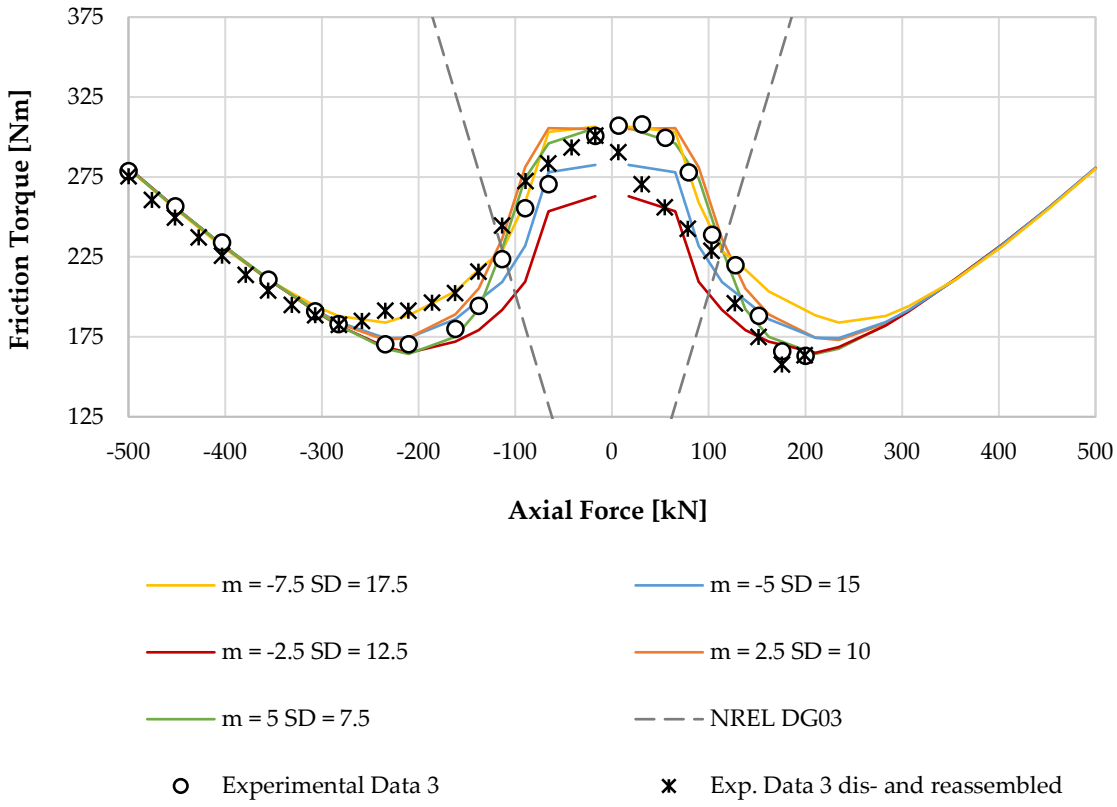

Figure 2.24. Analytical results selection adjusted to *Experimental Data 3* results under axial load.

The analytical results show great consistency with both experimental datasets, even for the tension side. In addition, both experimental results are correctly adjusted in the *two-point contact zone* (from -280 kN to -500 kN), reaffirming the previous conclusion that the preload has a negligible effect in this zone. Furthermore, the existence of two experimental results, which is translated as a comparison between two assembly processes, means it can be concluded that the model is capable of adjusting the results for an axial case while accounting for the deviations introduced by this process.

Figure 2.25 shows the same dataset under a tilting moment, however, it lacks results of the second assembly process. Once more, the *m* and *SD* combinations obtained indicate a poor correlation with the experimental results, while the NREL formula greatly underestimates the friction torque.

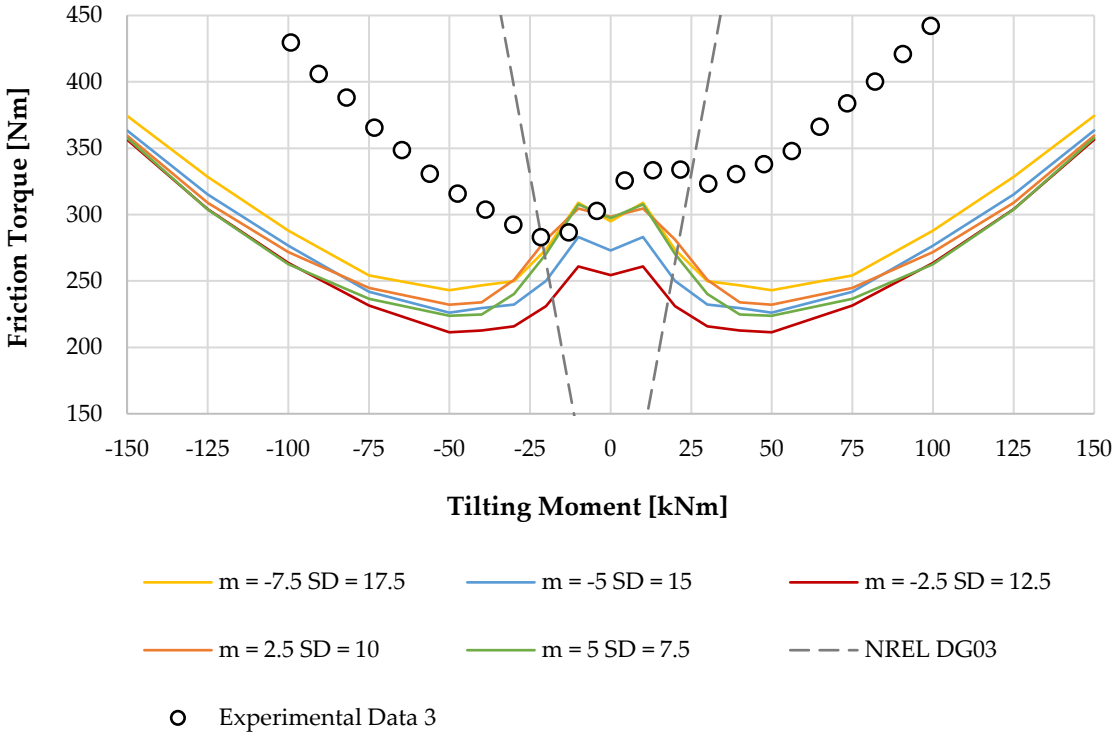

Figure 2.25. Analytical results selection adjusted to *Experimental Data 3* results under tilting moment.

Finally, the *Experimental Data 4* results are shown in Figure 2.26. The analytical results are a great fit with the experimental results regarding compression side, being more accurate than the formula from the NREL. Similar to the results of *Experimental Data 2*, there is a big discrepancy between the compression and tension of the experimental results, so the analytical result cannot match the experimental ones. Again, given the lack of results on the tension side, a separate adjustment for tension side is not feasible.

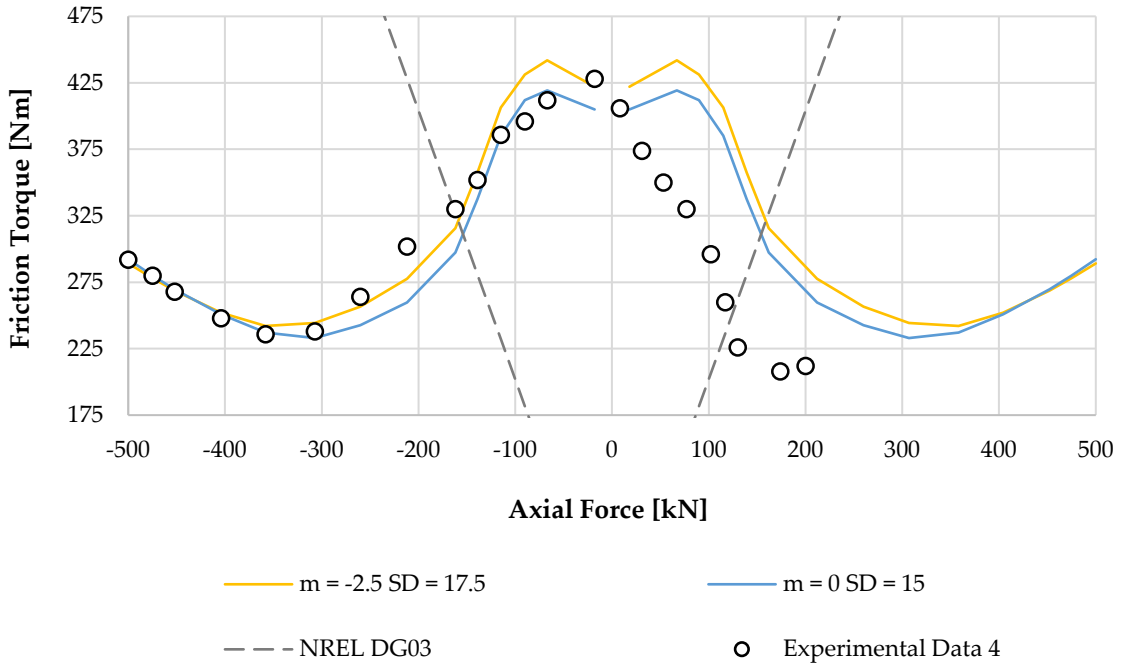

Figure 2.26. Analytical results selection adjusted to *Experimental Data 4* results under axial load.

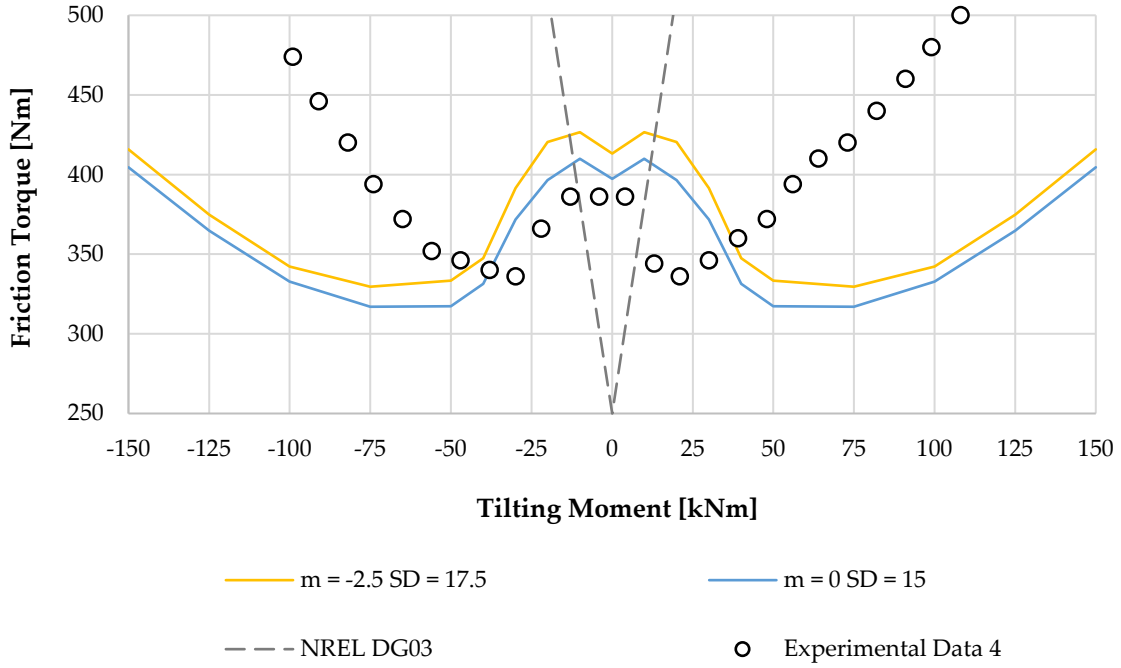

Figure 2.27. Analytical results selection adjusted to *Experimental Data 4* results under tilting moment.

Figure 2.27 shows the *Experimental Data 4* results under tilting moment for the previous m and SD combinations. The analytical results yield far more accurate friction torque values for the low-loaded zone (from 0 kNm to 50 kNm in Figure 2.27). However, the poor correlation between the analytical approach and the

experimental results confirms the need for additional factors, particularly the flexibility of the rings and surrounding structures.

Broadly speaking, the preload scatter hypothesis explains how friction torque varies with the applied load. The model is applicable when the bearing behaves according to the rigid ring hypothesis, i.e. under compressive loads, and yields more accurate results than the model by Joshi et al. [124] and the NREL formula. However, in the event of significant ring deformation, such as when some ring regions are subjected to tension, the model is not capable of fitting the experimental results. These results suggest that the model based on the preload scatter hypothesis can yield accurate results, although rigid ring hypothesis is not applicable in all cases.

The range of the tuning parameters values that best fit the experimental results in each case, offering a mean relative error of less than 5%, are summarised in Table 2.3.

Table 2.3. Experimental dataset names corresponding to the bearing pairs used for the experimental tests.

New experimental dataset name	$\boldsymbol{\mu}$	$\boldsymbol{m}$ **[μm]**	$\boldsymbol{SD}$ **[μm]**	$\boldsymbol{C}$ **[Nm]**
Experimental Data 1	0.085	[-10 , 0]	[10 , 17.5]	[81 , 92]
Experimental Data 2	0.11	[5 , 7.5]	[10 , 12.5]	[73 , 79]
Experimental Data 3	0.09	[-7.5 , 5]	[7.5 , 17.5]	[96 , 113]
Experimental Data 4	0.085	[-2.5 , 0]	[15 , 17.5]	[114 , 123]
Overall	**[0.085 , 0.11]**	**[-10, 7.5]**	**[7.5 , 17.5]**	**[73 , 123]**

The coefficient of friction is always within a range of 0.085 and 0.11, which is coherent with the references [31,124,176,177,179–181]. Since each experimental data corresponds to different bearings, mounted with balls of slightly different sizes, the mean effective preload m is different in each case. Nonetheless, all the bearings were supplied by the same manufacturer, so the manufacturing errors are expected to be similar in every case. Moreover, they were mounted on the same test bench and assembled following the same procedure. Accordingly, the standard deviation of the effective preload SD is very similar in every case, and

always within a range of 7.5 μm and 17.5 μm, which confirms the previous statement. A good fit could be achieved with negative m values, which means that some balls will have clearance (not preloaded after the assembly process). Finally, the value of the constant parameter C is within a range of 73 Nm and 123 Nm, meaning that this parameter has a significant effect on the friction torque for this size of bearings, which is expected to come from the contribution of the seals and the cage.

2.4 Effect of ring deformations

According to the reasons discussed in the previous section, the ring deformations could be the reason for the poor correlation of the friction torque between the analytical approach estimations and the experimental results, for a bearing under a tilting moment. Previous works [12,23,74,77] showed that, for this load case, the rigid rings assumption can lead to fewer balls in the *four-point contact zone*, compared with the results when the flexibility of the rings and the structures are considered. The higher contribution of each ball to the friction torque in the *four-point contact zone* than in the *two-point contact zone* (see Figure 2.3b) reveals a possible cause of the unsatisfactory analytical-experimental correlation under tilting moment (see Figure 2.21, Figure 2.23, Figure 2.25 and Figure 2.27). In addition, the observed differences for some cases under axial force could be reasoned as being due to the behaviour of the bearing under tension (see positive values of axial force in Figure 2.22 and Figure 2.26) and its relationship with the bearing stiffness together with the preload variation.

An FE analysis is performed in this section to examine the effect of the flexibility of the rings and surrounding structures on the resulting load distribution and, as a result, the friction torque for a bearing under a tilting moment. The results are compared to those obtained using the analytical approach, which takes the rigid rings assumption into account.

2.4.1 FE model description

FE structural simulations including the test bench were performed to analyse the deformation behaviour of the bearing rings when a tilting moment is applied. For this purpose, an FE model of the BEAT1.1 assembly, including the two mounted bearings, was developed in ANSYS Workbench [127]. A cross-sectional

view of the FE model of the BEAT1.1 with implemented bearings is shown in Figure 2.28.

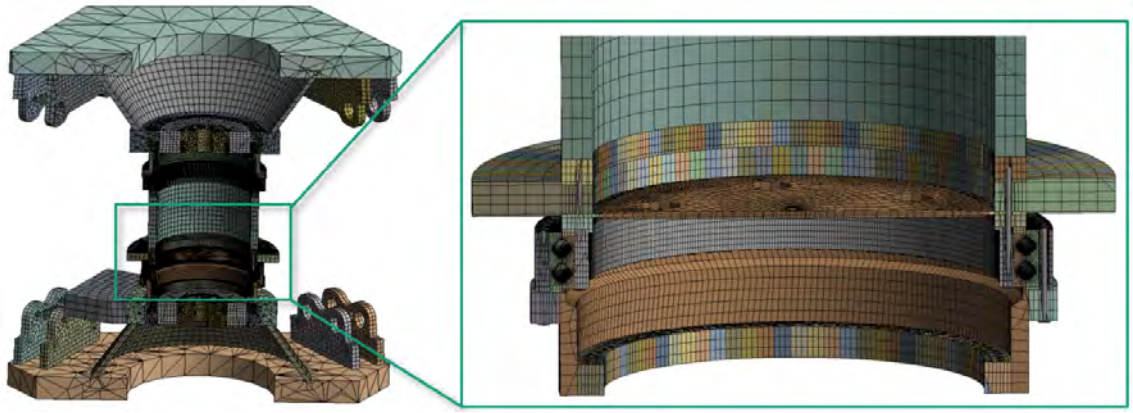

Figure 2.28. Cross-sectional view of the BEAT1.1 test rig FE model [127].

The two identical bearing models are generated using a extension called "Rolling Bearing inside ANSYS" created by CADFEM. The tool, created for the ANSYS workbench environment, implements nonlinear spring elements between the bearing rings to represent the nonlinear contact behaviour between the ball and raceway and generates a highly efficient global FE model (similar to the approach in [79]).

As the test bearings are manufactured with a preload to ensure every ball is in contact in a non-loaded condition, a constant initial ball oversize of 35 µm is considered in the model, with no preload scatter. Bolts and frictional contacts at the flange surfaces are implemented to represent the bolted connections and to enable a realistic deformation behaviour of the structure. The different kinds of loads to achieve the desired load level of the bearing are applied in a certain sequence, which is shown in Figure 2.29.

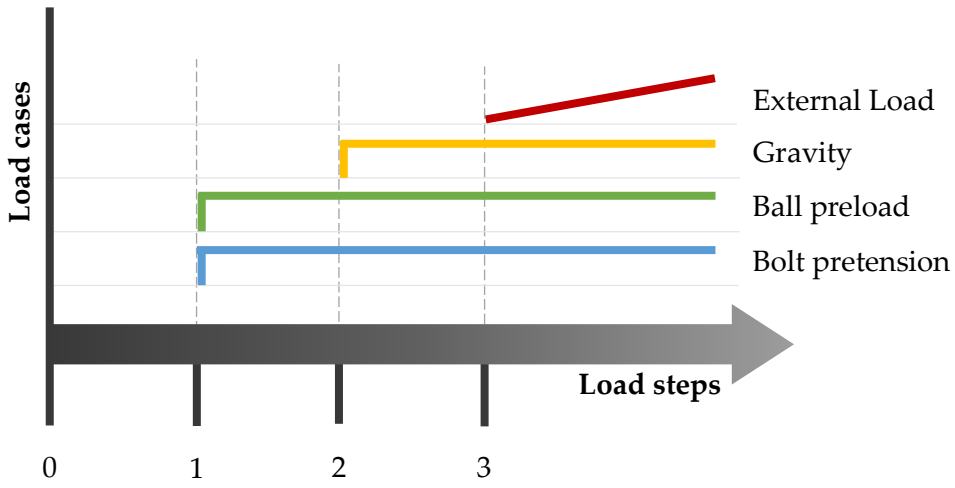

Figure 2.29. Loading sequence for BEAT1.1 FE simulations.

The procedure used to apply the loads on the FE model corresponds to the assembly and testing procedure. In a real assembly, the balls are preloaded due to the manufacturing errors during production. However, the FE model considers the same preload on all the balls. Furthermore, in order to overcome the elastic interaction, the bolts are tightened in a specific sequence, whereas the FE model applies the bolt pretension to all of the bolts at the same time. Thus, because of how the first load step is implemented, manufacturing errors are not considered and all the bolts are evenly preloaded at the same time, resulting in both load cases being implemented in the same load step (Figure 2.29 Step 1, green and blue lines).

In order to understand the reason for applying the gravity load (Figure 2.29 Step 2, yellow line) in the model, the experimental testing procedure must be understood. During the experimental test, the test rig applies a small axial force to overcome the effects of gravity. The applied axial force corresponds to the weight of the components on the lower bearing, so the lower bearing is in an unloaded state.

Following that, the specified load conditions are applied while the bearings rotate to measure the friction torque. Given that intermediate substeps are required to solve the FE non-linear problem, the third load step (Figure 2.29 Step 3, red line) applies the external loads incrementally. This enables calculating all the tilting moment cases in one solution run while obtaining the results for various loading cases.

Therefore, the FE model accounts for the flexibility of the structures, but does not simulate the main sources that cause the ball preload scatter. Nonetheless, even if these effects are not simulated, the contact deformations before applying the external load, which were defined as effective preload, will not be exactly the same on every ball, as the structures will deform after the first load step. As a result, this model allows for the effect of flexibility on friction torque to be isolated.

A tilting moment of 125 kNm is applied on the model as external load. Figure 2.30 shows cross-sectional views of the deformed rings of the lower bearing under this load. Even if the structure surrounding the bearings is cyclically symmetric, the bearing deforms differently on the tension (right) and

compression (left) sides. It could be argued that the frame of the test rig is not cyclically symmetric (see Figure 2.28). However, the FE model's plane of symmetry is perpendicular to the axis where the tilting moment is applied, so it does not justify the lack of symmetry on the load distribution results observed for both negative and positive values of tilting moment.

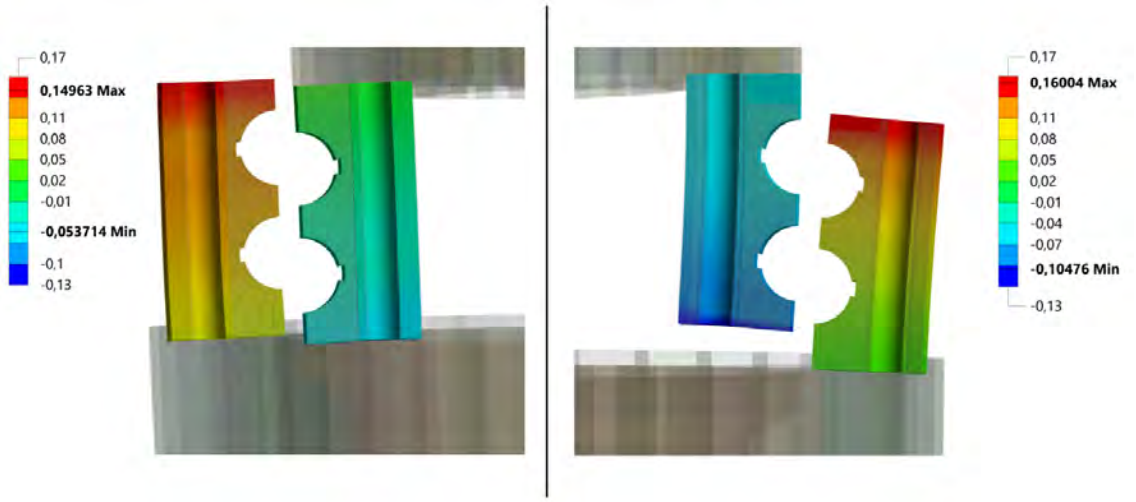

Figure 2.30. Radial nodal displacements of the rings in mm for M = 125 kNm, compression side (left) and tension side (right) in the lower bearing, Scale 50.

It can be seen that the radial displacements on the tension side are significantly higher than on the compression side. In turn, this characteristic ring deformation behaviour leads to different contact forces and angles on both sides. The load distribution shape on the compression side more closely resembles the one obtained with the analytical model considering rigid rings, which does not occur for the tension side.

This confirms that the rigid ring assumption is acceptable when a pure compression load is applied or in the compressed region when subjected to a tilting moment. In the case of axial tensile force, however, the raceways are more flexible, and thus they will "open" (see Figure 2.30, right), affecting the load distribution, so the rigid rings assumption will not provide accurate results. This different behaviour under compression and tension loads also explains the lack of symmetry in the experimental results of the friction torque shown in Figure 2.22 and Figure 2.26 for a bearing under axial load, even if more measurements would be required on the tension side to further confirm this observation.

Furthermore, the FE simulations reveal that both test bearings are not exactly loaded in the same way. This is caused by minor differences in the surrounding

structures for both bearings and shows the sensitivity of the bearing's internal load distribution towards the stiffness of the surrounding structures. As the experimental friction torque is measured for both test bearings, it is also important to consider the load distribution and contact angle evolution of both bearings for the approximation procedure. The FE simulations are conducted with a high number of substeps to calculate the resulting load and contact pressure distributions as well as the contact angle evolutions in both bearings for various different load levels. This extensive data set is used for the following calculations.

2.4.2 Friction torque results

To study the effect of the flexibility of the rings and the surrounding structures on friction torque, the load distribution results from the aforementioned FE analysis were extracted for each load substep after the third load step. Then, this data was used to feed the analytical model for the friction torque calculation. In other words, the load distribution results from the analytical approach, which considers rigid rings, were substituted by the FE model results, while the friction torque problem was solved using the same analytical approach.

As stated when describing the FE model, in this way it is possible to account for the flexibility of the system, but not the sources that cause the preload scatter, even if the effective preload is not the same on every ball. The results using FEM for the load distribution problem and the analytical approach for friction torque problem, are represented with a black line in Figure 2.31, named *FEM Analytical*. The results for the positive values of the tilting moment from *Experimental Data 1* are shown in this figure. This dataset was chosen as the reference as it was the set with more satisfactory results for the axial case (Figure 2.20) and more symmetric experimental results for the tilting moment (Figure 2.21).

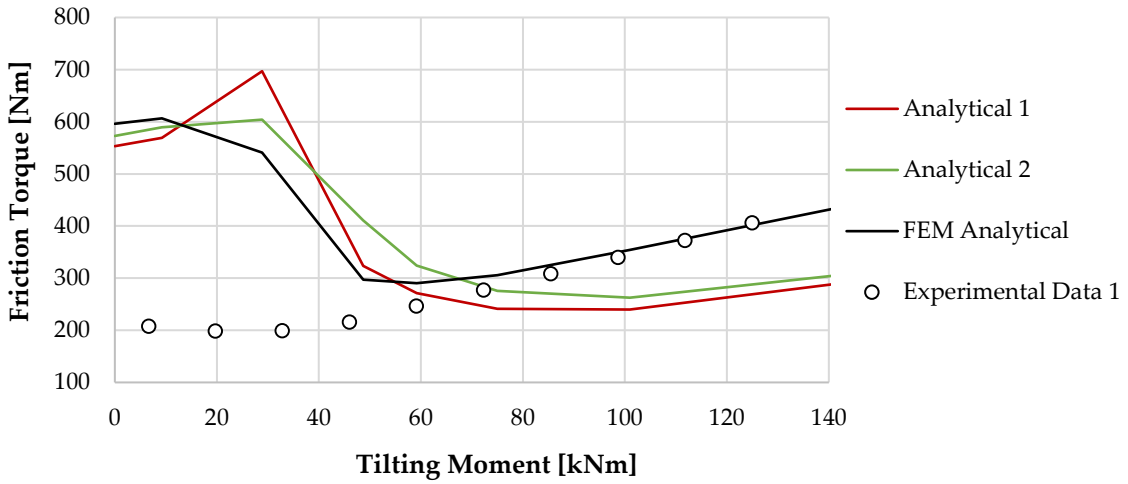

Figure 2.31. Friction torque analysis feeding analytical tool with different stages of FE data.

The results show a very strong correlation with experimental tests for loads from around 60 kNm onwards, while the curve is completely different under 40 kNm. Two major conclusions can be drawn from the results of this first comparison. Firstly, based on the strong correlation for high tilting moments, it can be said that when calculating the load distribution, the flexibility of the structures must be considered in order to achieve accurate estimations of the friction torque. As a result, the analytical approach will yield less accurate results the more flexible the structures are. Secondly, based on the poor correlation for low loads, it can be concluded that the sources of the preload scatter must be considered if accurate friction torque results are required, particularly at low loads where the effect of the preload is significant. In fact, slewing bearings operate under this load condition in many applications, so the effect of the effective preload scatter may be more relevant than the effect of the flexibility of the structures in these cases.

Some other results of the FE model were used to perform a further two analyses to confirm these conclusions and to obtain appropriate references to compare with the new friction torque curve, *FEM Analytical*. In order to provide a comparison of the performed analyses, Table 2.5 shows a summary of the steps taken to solve each problem, in addition to the effective preload calculation, which is further explained hereafter.

Table 2.4. Studied cases to analyse and compare the effect of the flexibility of the rings and surrounding structures on the load distribution and the friction torque.

	Effective preload	**Load distribution problem**	**Friction torque problem**
FEM Analytical	FEM	FEM	Analytical
Analytical 1	FEM average	Analytical	Analytical
Analytical 2	FEM	Analytical	Analytical

In both analyses (named *Analytical 1* and *Analytical 2*), the load distribution problem was solved analytically and consequently based on the rigid ring assumption, i.e. as described in Section 2.2 and 2.3. However, the value for the effective preload was obtained from the FE model after load step 1 (see Figure 2.29). After that, the load distribution problem was solved without considering a preload scatter based on a normal distribution. This way, the analytical approach can be compared with the new *FEM Analytical* results, considering a similar status in the idling conditions (with no applied load). It must be noted that, when the ball preload (ball oversize) is applied in the first step of FE simulations, the rings are deformed so the effective preload, i.e. the actual ball-raceway deformations before applying the external load, will vary from the theoretical preload.

The simulations in *Analytical 1* consist of applying the same effective preload throughout all balls. This preload was calculated as the mean value of all the ball-raceway deformations extracted from the FE analysis after the first load step (see Figure 2.29), i.e. the effective preload according to the FE simulation. With this unique value for the preload, the load distribution and the friction torque were calculated using the analytical approach. Because the preload scatter was not considered in this case, this analysis serves as reference and is depicted with a red line in Figure 2.31. Unlike the case when an axial load is applied (Figure 2.4), the drop in friction torque is not as pronounced when the same value of effective preload is considered for all of the balls. This is explained by the fact that the load is not distributed evenly among the balls when a tilting moment is applied. Even if the effective preload is the same for all balls, the transition from two-point to four-point contact state is more gradual and not simultaneous.

Following this, the second analysis was performed, called *Analytical 2*, in which the applied preload corresponds to the effective preload extracted from the FE analysis after the first load step (see Figure 2.29). This is similar to *Analytical 1*, but without computing the average for all the balls, resulting in a different effective preload for each ball. As a result, this method takes into account the effective preload caused by ring deformations and bolt pretension.

When the results of *Analytical 1* and *Analytical 2* for high loads are compared in Figure 2.29, it is clear that both curves converge to the same results, which are similar to those in Figure 2.21 for the analytical approach. Consequently and because the *FEM Analytical* fits the test results in this load range, it is confirmed that the reason for the poor correlation between the analytical approach and the test results is that the flexibility of the structures is not taken into account in the former model. At low loads, however, the three curves deviate significantly from the test results. This confirms that the ball preload scatter, which is primarily caused by manufacturing errors and not considered in either case, is significant in this load range.

To summarise, there are two options for achieving a good estimation of the friction torque for low tilting moments: (1) the structures are rigid and the analytical approach can be used, so the preload scatter can be considered as proposed in this work; or (2) the structures are so flexible that they affect the friction torque, as is the case, and thus the load distribution must be solved using FEM, taking the preload scatter into account. Since many calculations are required considering different combinations of m and SD, and due to the high computational cost of FE simulations, the second option goes beyond the scope of this research work.

In order to complete the study and justify the effect of the deformations of the rings on friction torque, the results of the load distribution for an applied tilting moment of 150 kNm are shown in Figure 2.32. These results consider both rigid rings, according to the analytical model, and flexible rings, simulated by means of FE analysis. The figure also depicts the contribution of each ball to the total friction torque, which is a function of the load distribution. The contact angle is also shown in the figure for completeness. The results in the figure are for the upper row of the lower bearing of the test rig (see Figure 2.28).

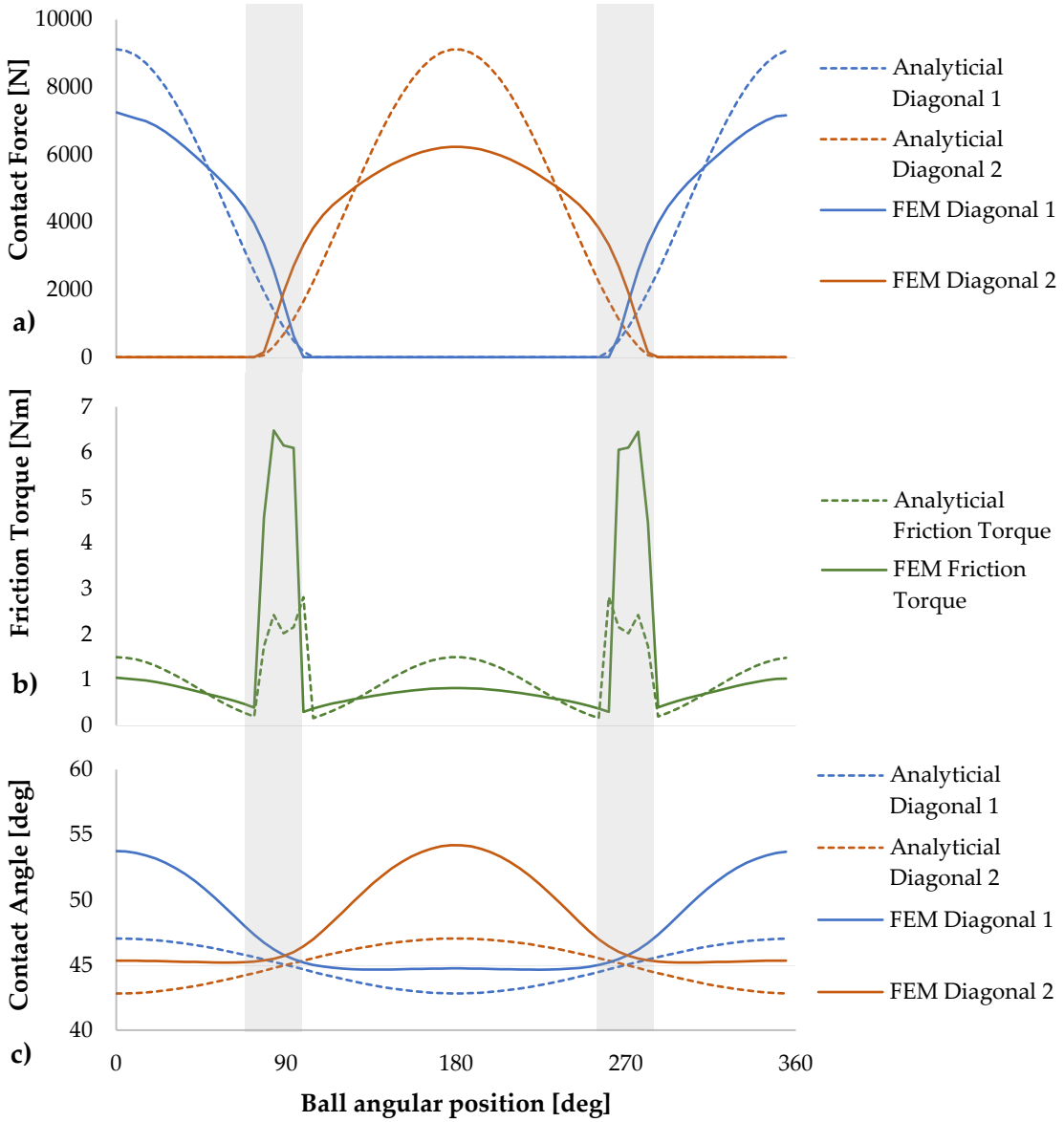

Figure 2.32. Load (a), friction torque (b) and contact angle (c) distribution for the analytical and FE simulations for a tilting moment of 150 kNm.

Focusing on the most loaded region, which occurs at the angular positions 0° and 180° of the balls in Figure 2.32a, the balls are subjected to higher contact forces in the analytical model than in the FE model. This observation is consistent with previous research [12,23,74,77]. These balls are in a two-point contact state, and the higher the load, the greater the contribution to friction torque, as shown in Figure 2.32b.

When looking at the less loaded balls, which are located at the angular positions 90° and 270°, they are in a four-point contact state, which means that both contact diagonals are loaded (see the grey region). In this case, contrary to the observations in [12,23,74,77], considering the flexibility of the structures does

not result in more balls in the *four-point contact zone* for this particular case. Nonetheless, according to the FE model, the balls with four-point contacts are more loaded, leading to a higher contribution to the friction torque. Being consistent with previous explanations based on Figure 2.3b, Figure 2.32b shows how the friction torque of the balls in the *four-point contact zone* is greater even when they are less loaded than those in the *two-point contact zone*. Therefore, and because the load in these balls is lower under the rigid rings assumption, the friction torque is also lower for the analytical model than for the FE model under the considered tilting moment of 150 kNm.

This explains why, for high tilting loads, the proposed analytical approach retrieves lower friction torque estimations than the experimental results in Figure 2.21, Figure 2.23, Figure 2.25, Figure 2.27 and Figure 2.31 for high loads. As previously stated, in the case of low loads, the friction torque is more conditioned by the preload, and therefore by its scatter and the factors that affect it.

2.5 Proposed guidelines

When applying the proposed analytical approach to specific bearings, the user may encounter a variety of case scenarios. The bearing data available will differ depending on whether the user is a bearing manufacturer, a customer with some knowledge of the product or an end user who is unaware of any technical data. Based on that, this section provides instructions on how to use and tune the model to obtain the most reliable friction torque prediction tool possible. Three case scenarios are considered to achieve this goal: the one studied in this thesis (Case 1), the best-case scenario (Case 2), and the worst-case scenario (Case 3). These cases are summarised in Table 2.5.

Different data will be known depending on the case. In this regard, the user has two options for dealing with unknown data: making assumptions (e.g., based on the bibliography or previous experience) or tuning the model for the specific bearing through experimental tests, considering the unknown data as the tuning parameter. This section recommends the minimum number of tests for the second strategy. In this regard, only the most basic tests, such as idling or axial load, are considered.

Table 2.5. Considered case scenarios.

Scenario	Known data		Unknown data	
Case 1	Global geometry:	D_{pw}, i	Coefficient of friction:	μ
	Internal geometry:	D_w, z, α_0, s	Ball preload:	m, SD
			Independent constant:	C
Case 2	Global geometry:	D_{pw}, i	Ball preload (average):	m
	Internal geometry:	D_w, z, α_0, s	Independent constant:	C
	Coefficient of friction:	μ		
	Ball preload (scatter):	SD		
Case 3	Global geometry:	D_{pw}, i	Almost everything	

Of course, in practice, many more intermediate cases than those listed in Table 2.5 may occur. In such cases, the user may modify its strategy in accordance with the case scenarios described below.

2.5.1 Case 1: Studied case

This would be the case for customers with access to the drawings of the bearing. It corresponds to the case studied in this thesis, so all the geometry data was known (see Section 2.3). The procedure by which to tune the model is the one described in Section 2.3.2, where a minimum of four test measurements would be required:

1. Two measurements under high axial load: these points are necessary to determine μ, so they must be in the *two-point contact zone* (see Figure 2.14).

2. Two measurements under low axial load: these points must be located in the *four-point* or the *transition zone*. One of these points may correspond to an unloaded case. With these two points and the previous ones, the parameters m, SD and C can be set.

2.5.2 Case 2: Best-case scenario

This can be the case of a bearing manufacturer, not only with access to the data regarding the particular bearing to be characterized but also to previous experience and extensive knowledge regarding their product, their manufacturing tolerances, previous test campaigns, and so on. With all this

information, the user can have access to reliable values for μ and SD. Of course, for the manufacturer, the geometry is also known. Therefore, the only unknown parameters would be m and C. In this case, the procedure to tune the model is easier, and the minimum number of required tests is lower:

1. One measurement under high axial load to define the C parameter, since m has no effect in the *two-point contact zone* (see Figure 2.3).

2. One measurement in unloaded conditions to define m.

2.5.3 Case 3: Worst-case scenario

This would be the case for an end user whose unique data is D_{pw}, since the geometry of the structure where the bearing is installed must at least be known in order to have an estimation of the friction torque. This is indeed the only data required by the formula proposed by the NREL [49].

In this case, only rough estimations can be made for the friction torque by using the proposed approach. To this end, data from the bibliography can be considered for certain parameters like μ or s, but others can only be estimated, based on conservative assumptions. Having so little information, in this case, the formula from the NREL could be enough to obtain rough estimations for the most loaded case, but the results must be interpreted with caution, since it can yield non-conservative results for low loads.

2.6 Conclusions and additional remarks

The proposed analytical methodology calculates the friction torque in ball slewing bearings considering the ball preload scatter. The obtained results show how the preload scatter justifies the smooth transition from four to two-contact points that the state of the art analytical models show under axial load. Modelling the preload scatter with a normal distribution enables easy correlation of experimental results, while still allowing for the use of alternative distributions or scatter preload sources. Moreover, the model achieves a successful correlation with experimental tests under compressive loads.

Nonetheless, the rigid ring assumption considered in the approach can lead to inaccurate friction torque results when a tilting moment or a tension axial force (less common) is applied. This is mainly caused by the opening of the raceways

and their low stiffness compared to the surrounding structures. Thus, it is concluded that the friction torque depends on the stiffness of the structures the bearing is assembled to.

An important additional conclusion is that, under an applied tilting moment, the less loaded balls determine most of the friction torque of the bearing, which have four points in contact, and not the most loaded ones, which only have two points. This proves how sensitive the friction torque is to the preload (and its scatter) even for high applied tilting moments, since the higher the preload, the more balls will be in the four-point contact state, and therefore the higher the friction torque will be.

The methodology described in this research work is meant to have a practical application, useful for users ranging from a bearing manufacturer with extensive knowledge about their product to a user with more limited information. As a result of the analysis performed, some guidelines for using and tuning the model are proposed, in order to obtain a reliable friction torque prediction tool. In this regard, the presented analytical approach yields considerably more accurate results than the practical formula given by NREL for this type of bearings, even though the latter can still be useful for rough estimations when only the macrogeometry (D_w, D_{pw} and Z) of the bearing is known.

With all of this, it is proven that the preload scatter is capable of taking account of the deviations of the preload coming from the manufacturing errors and bolt pretension, as it is capable of adjusting the friction torque for low loads. Moreover, the constant effect of the seals and the separating elements on the friction torque has been proven. However, in order to develop a more precise tool the flexibility of the rings and surrounding structures must be taken into account.

The FEM has proven to be an effective but inefficient method to account for the flexibility of the rings and the surrounding structures. Furthermore, no simulations have been performed that account for both preload scatter and structure flexibility simultaneously. As a result, the simulations with flexible structures performed in this work show a strong correlation with experimental results for high loads but a poor correlation for low loads, where preload (and its scatter) have a significant effect.

The simulation of structure flexibility and preload scatter can be performed efficiently by incorporating the system stiffness matrices into the analytical procedure. However, for proper implementation the FEM is needed to validate the analytical model for each case. In this regard, an advanced FE model is being developed by Fraunhofer IWES which the preload scatter will be implemented to. On top of that, a superelement based model is considered as an alternative modelling strategy to mitigate the computational cost introduced by FEM, which is important if the same amount of analysis needs to be computed. This way, instead of modelling the entire test bench, only the required bearing geometries must be modelled in the future. In this regard, the next chapter focuses on FE simplification techniques to simulate the flexibility of the bearings and the surrounding structures.

3 FE simulation of pitch bearings

3.1 Introduction

This chapter studies the flexibility of a two-row four-point contact bearing modelled by FE in its working conditions, which involves being assembled between a blade and a hub of a wind turbine subjected to working loads.

Although the most direct way to simulate the flexibility of the bearing rings and the surrounding structures is to use FE with a complete model of the bearing, different research works have focused on simplifying these models to reduce their computational cost. Smolnicki and Rusiński [80–82] proposed an approach to simplify the ball-raceway contact with tension-only springs when performing finite element simulations and compared the effects of simulating the boundary components using different techniques. Daidié et al. [79] enhanced the approach of simulating the ball-raceway contact by proposing a mechanism that considered the variation of the contact angle with the load more accurately. FEM has also been used to obtain data to implement the flexibility of the bearing rings and the surrounding structures in analytical models, such as Olave et al. [74] and Guo and Parker [142], who used superelement (SE) techniques. Some researchers, such as Plaza et al. [21] and Heras et al. [12,23], also considered the effect of ring flexibility using both the SE method and Daidié's mechanism. Heras et al. also used SE with Daidié's mechanism to obtain the stiffness matrices of the rings and implement it into an analytical model [10]. However, this work did not consider the effect of real boundary structures and none of the previous ones showed the effect of the FE modelling techniques used. Regarding experimental testing, IWES BEAT2.1 [90] is a test rig designed to reproduce the real boundary conditions of a bearing mounted on a wind turbine. Even if its FE model considers all the surrounding elements to obtain precise load distribution results, considering bolted connection [182] is not common with these large scale models. However, other research works [166] have shown that the bolt preload variation

may introduce some variations into the load distribution results. This underlines the importance of considering these elements when analysing the bearing.

Although FEM is the most commonly used method for accounting for the flexibility of the components, in wind turbine blade designs, experimental tests provide the most accurate results of their behaviour, with the blade being an expensive component made of composite materials consisting of multiple laminates in different directions.

As a result, in this chapter, the effect of blade material on bearing flexibility and load distribution is analysed in this chapter. In this way, the potential of replacing the blade material with a more common material, such as steel, is assessed for the experimental testing of slewing bearings. Providing the blade material does not have a significant effect on the bearing results, this could be considered at an early stage in the design process, allowing for models that include the blade in the bearing calculations to provide valuable insights that could streamline the design process, as well as enabling cost-effective experimental testing.

When it comes to assessing the effect of the FE techniques used, the simplification of bolted joints by replacing bolts with simple pre-stressed beam elements is the most widely used method [18,21,166]. With this, the model is still non-linear but allows the components to slide or separate from each other. In some cases, the beam elements are suppressed and the components are joined directly using constraints between the contact surfaces [182], which is a common simplification when the interface connection is not the studied region. These constraints consist of constraining both contact faces of the components to achieve the same displacement, referred to as "*bonded contacts*" in FE-based software such as Ansys, allowing for a linear problem. Because of this, the impact of these connections and their cross-effect with the aforementioned material change of the blade is studied. In addition, an alternative way of further simplifying the bearing model is presented and studied, where the bearing is replaced by three non-linear springs that simulate its axial, radial and tilting stiffness.

Similarly, some nuances of Daidié's mechanism are studied, specifically its behaviour under radial load, where the mechanism is forced to operate outside the plane that contains it. Therefore, the impact of this mechanism is assessed

where the degrees of freedom that move it out of the working plane are released and the error introduced by this additional displacement is assessed.

3.2 Reference blade-bearing-hub assembly model

This section focuses on the blade-bearing-hub assembly parts and characteristics. The modelling and simplification techniques used in the reference assembly model are presented below.

3.2.1 Geometry and materials

The geometrical specifications of the components used for the model were provided by Fraunhofer IWES. The model comprises a wind turbine hub, a separator, a two-row four-point contact slewing bearing, a stiffener and a wind turbine blade. Figure 3.1 shows the assembly of these components and their location on a blade wind turbine.

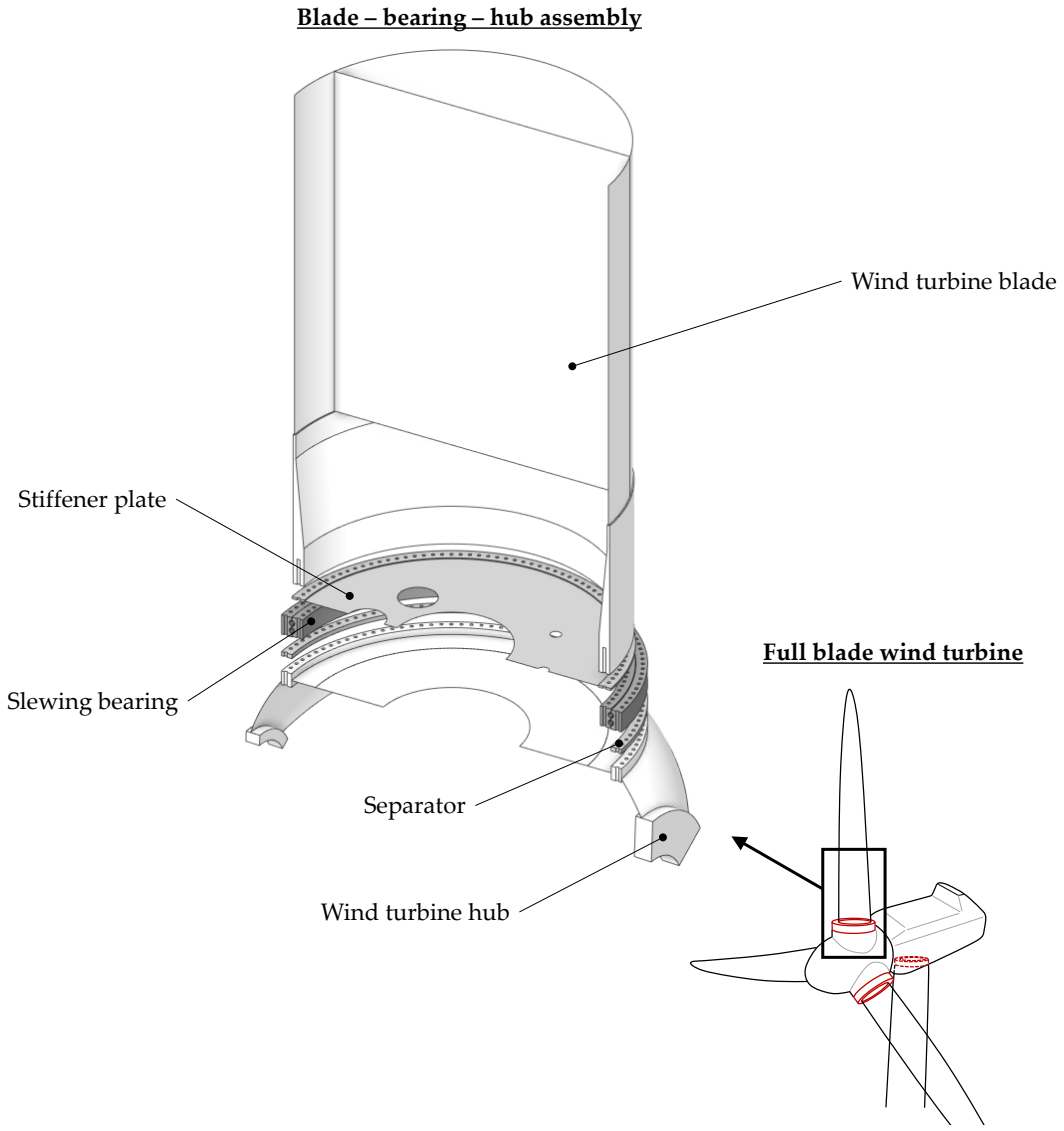

Figure 3.1. Assembly of the model components.

The characteristics of the modelled components of the assembly are described below:

- Wind turbine blade: the blade is the component which is subjected to the wind current forces, and thus, the loads are applied to this component. This element is connected to a stiffener plate and the inner ring of the slewing bearing with bolts that are screwed to its root. The blade is usually made of composite materials which vary depending on the manufacturer, the expected working conditions and turbine size, among other factors. In this case, the composite laminates and their arrangement are provided by Fraunhofer IWES (extracted from IWES Wind Turbine IWT-7.5-164 [183])

so the blade is modelled based on their specifications. Figure 3.2 shows the layout of the composite laminates in the FE model of the blade.

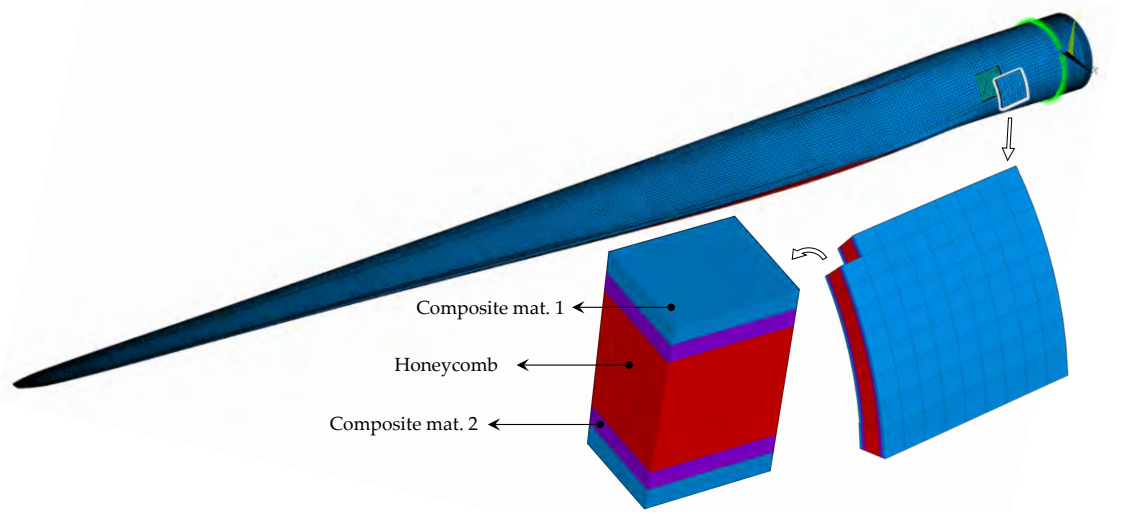

Figure 3.2. FE model of the blade showing the composite material layout.

- Stiffener plate: this plate stiffens the assembly so the wind turbine can withstand the wind forces with less deformations in the radial direction of the bearing. This element allows for large diameter bearings, which prevents their deformation (ovalization) and ensures improved system performance. This element can be divided into two parts: the flange, which is designed to connect the bearing and the root of the blade; and a web that extends from the inner part of the flange to the centre point, which stiffens the assembly to prevent large deformations. This element is modelled with a standard structural steel, with a Young modulus (E) of 200 MPa and a Poissons ratio (ν) of 0.3.

- Slewing bearing: a two-row four-point slewing bearing that withstands the blade loads while enabling blade pitch rotation with respect to the hub. This ensures the blade has a proper pitch angle depending on the wind currents. This is modelled with standard steel material as well.

- Separator: a steel flange that is intended to connect the hub and the bearing.

- Hub: an element that connects the three blade-bearing assemblies with the nacelle and performs the main rotation of the wind turbine. This element, which is made of steel, withstands the loads transmitted from the blades through the bearings.

3.2.2 FE model simplifications

To efficiently analyse the behaviour of the whole model, some modelling simplifications are made. Firstly, only a part of each component is modelled considering its geometrical symmetries. In fact, the external loads also condition these symmetries so these may also be considered.

As the purpose of this work is to study the effect of the bearing and its surroundings, only a portion of the total length of the blade (approximately 7.2 m of the 80 m of the blade) is used, which corresponds to a part known as the blade root. The blade root consists of a cylindrical geometry with two nerves, which permits the modelling of only half of it due to its symmetry planes, further reducing the computational cost. The loads are applied at the top of the blade root, far enough from the bearing ensuring they do not affect its results, which are contained in the symmetry plane of the components. The applied loads are approximate to the real values provided by Fraunhofer IWES, consisting of an axial force in the Z axis direction (F_a = 1000 kN), a radial force in the X axis direction (F_r = 1000 kN) and a tilting moment perpendicular to the Y axis direction (M = 50000 kNm). These loads were extracted from the highest values from multiple load cases, which, when combined, represent an extreme load case. The previous simplifications and symmetries permit a comprehensive consideration and study of the blade flexibility, while significantly reducing the number of nodes of the blade FE model, optimizing the computational efficiency under the worst load case scenario.

The stiffener, the bearing and the separator also have one symmetry plane which coincides with the blade root, so their model can also be halved in the same way. The hub, which originally contained three blades, is modelled to only contain one blade. Because of this, its model is reduced to a third of it, which is enough to study its effect on the bearing and its surroundings. Again, the third part of the hub contains a symmetry plain that coincides with the symmetry plane used in the previous components, so this is also reduced to half of it.

Because of the used symmetry planes used, the reduced models result in a blade-bearing-hub assembly model as shown in Figure 3.3 below. This figure also shows where the loads are applied on the model and its axes.

In addition to this, the symmetries also imply introducing specific boundary conditions. In fact, the boundary conditions applied to the symmetry planes must

consider the deformations in the plane while the elements are always in contact with it. In the software used for these simulations (Ansys 2019 R2), this boundary condition is called *frictionless* boundary condition. Figure 3.3 shows where these frictionless boundaries are applied, shown in orange for the surfaces and yellow for the edges. In addition, a fixed boundary condition is included to represent the joint of the hub with the nacelle, which is indicated in red.

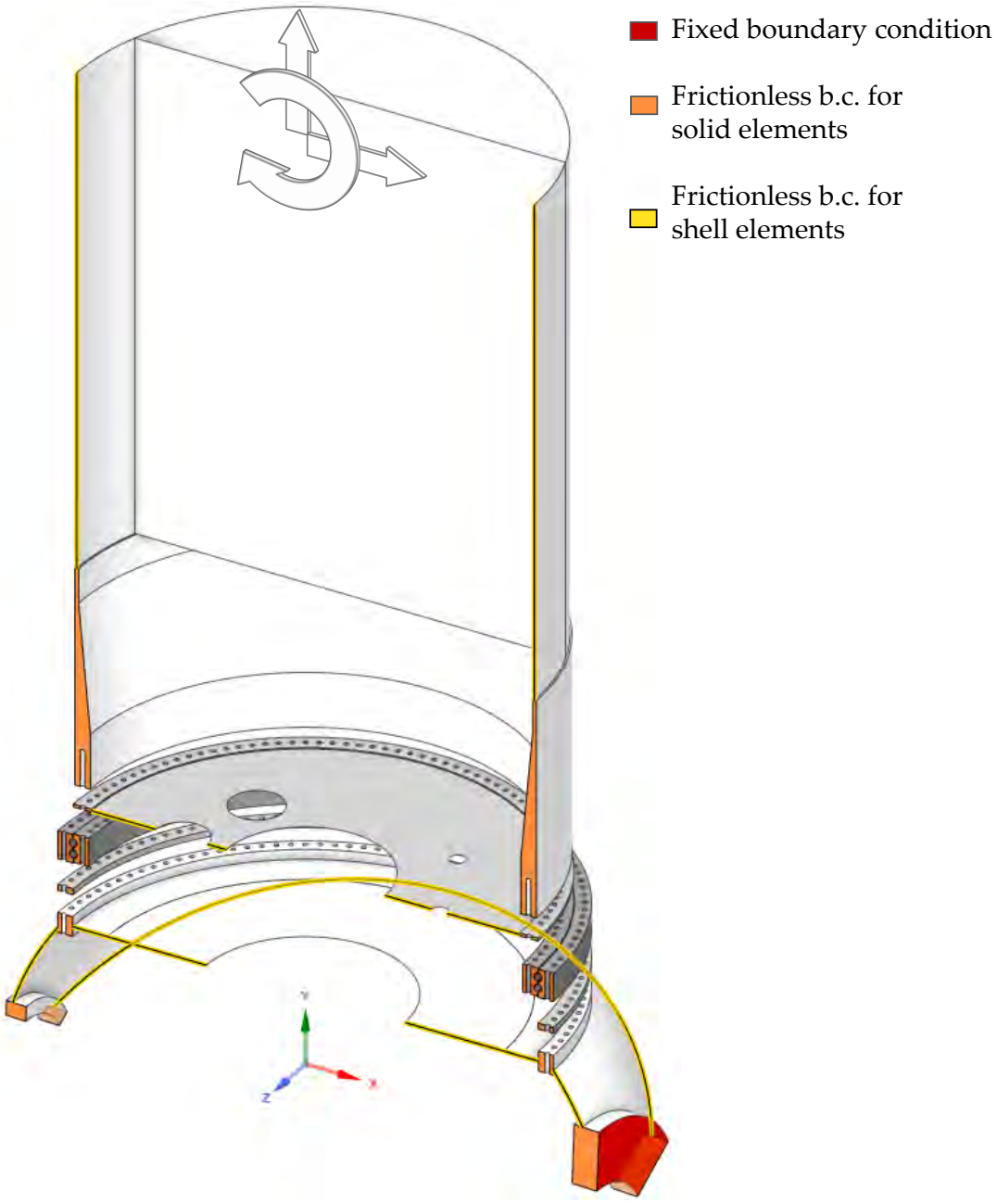

Figure 3.3. Representation of the boundary conditions at the surfaces and the edges of the assembly model and the applied loads.

Furthermore, some component features consist of thin walls, which can be simplified by shell elements. Figure 3.3 shows the frictionless boundary conditions applied to this type of element in yellow, distinguishing them from the surfaces, that are modelled with hexahedrons or tetrahedrons. These thin walls are part of the following components:

- The hub flange that is connected to the nacelle and three additional flanges that connect the blade-bearing assemblies. These flanges are connected with a low thickness geometry that is modelled with shells.
- The stiffener and separator both have webs that stiffen the model. As they are not very thick, these elements are also modelled with shells.

For the elements meshed with shell elements, the frictionless boundary condition cannot be directly applied in Ansys software. However, equivalent boundary conditions are applied by restricting the corresponding degrees of freedom. For the hexahedral mesh, only the displacement out of the plane is restricted when a frictionless boundary condition is applied. For shell elements, however, their rotations whose axes are on the symmetry plane are also restricted, so the shell remains perpendicular to it.

Another way to enhance the model to reduce its computational cost is by reducing the models of the components with equivalent elements with less DoF. In this type of full-scale model, it is common for bolt-modelling techniques to be used that simplify the non-linear problems caused by the contacts of the bolted connections. If a proper model of the bolts was represented, each bolted connection would have a contact between the threaded hole of the nut and the threads of the bolt, requiring a finer mesh in those areas. Additionally, the bolt head and the base of the nut would also require a fine mesh as they make contact with their corresponding components.

The approach taken for this work consists of a simplified bolted connection, allowing frictional contact between the component faces. This widely used technique consists of substituting the bolt model with beams and a pretension element. Besides this, the bolt head and the threaded hole are not represented and constraint equations or rigid elements are used instead to connect the beam with the interfaces. This modelling technique allows the analysis of the model with *frictional* contact (sliding is permitted with a coefficient of friction value of

0.3) between the components while maintaining a simple solution for the bolted connections.

Figure 3.4 represents the modelled bolt pretension element (in blue) with its connections to the corresponding components with rigid elements (in red).

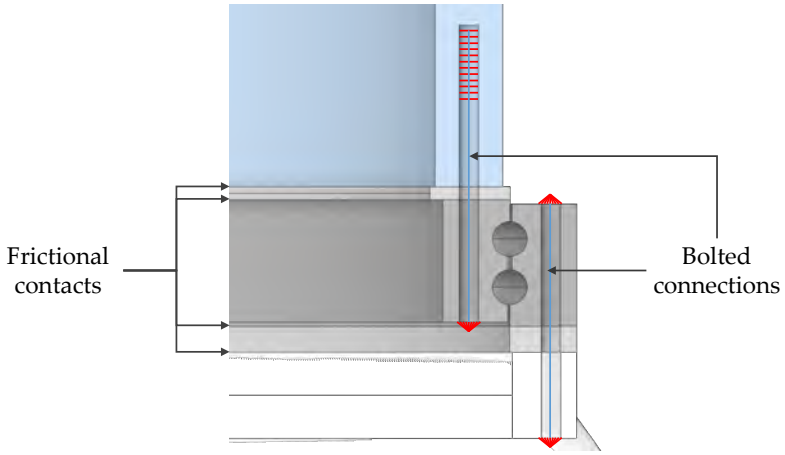

Figure 3.4. Representation of the bolted connection used in the assembly model.

In addition to this, the balls are also replaced with the known and widely used Daidié's mechanism [79] (see Figure 3.5). According to the literature, this mechanism replaces the ball with a mechanism that contains non-linear springs that represent the non-linear deformations that occur in the ball-raceway contact. For the stiffness of the springs, the formulation proposed by Houpert [60] based on Hertz's theory is used. Furthermore, this model takes account of the contact angle change that occurs when a load is exerted on the bearing. Even if this does not convert the non-linear contact problem to a linear one, it does lead to a significant reduction in the number of nodes due to the replacement of the ball models and the finer mesh that the ball-raceway contact implies in the contact elements. Moreover, it helps to reduce the convergence problems that may arise when solving the ball-raceway contact problem.

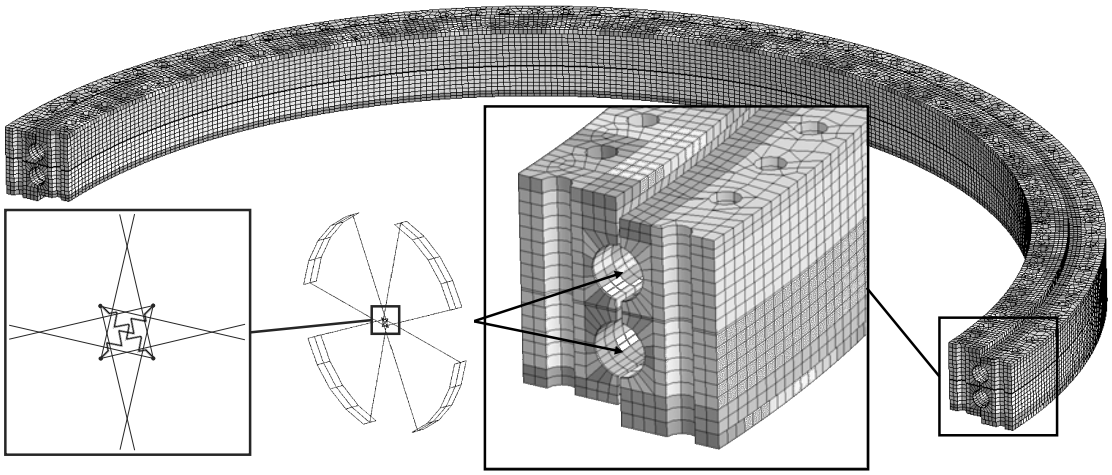

Figure 3.5. Representation of the bearing mesh and ball-raceway contact simplification (Daidié's mechanism) used in the assembly model.

3.3 Studied cases

In this section, the different study cases are analysed by means of the FE.

3.3.1 Blade material

As initially stated, for wind turbine blade designs the components are tested at final design stages, as these tests provide the most accurate results of their behaviour, with the blade being one of the most expensive components. Due to this, substituting the composite blade with a steel one has been considered. If the effect of replacing the blade material is minimal, this would enable experimental testing of the bearing by both manufacturers and users at a significantly lower manufacturing cost, also decreasing any behaviour uncertainty in the final design stages.

In fact, in these stages, the bearings are usually sized and manufactured for a blade that has evolved through the design process, and for reference loads based on the expected wind forces. This means that the requested bearing has to cover the working loads it is sized for with a margin of error, due to possible turbine design changes. Bearing manufacturers are initially unaware of the stiffness of the elements adjacent to the bearing, especially the blade materials. Therefore, they design the bearing under unknown boundary conditions. Finally, both the bearing and the blade are tested with the final materials, with the major variation from the initial design being the blade material and the acting loads.

Furthermore, in the early design stages, knowing the material allows for greater precision in the bearing calculations. If it is found that changing the blade material does not imply major changes in the obtained bearing results, this would make it possible to obtain a bearing design more similar to the one obtained in the final design stages of the turbine. On the other hand, when experimentally testing the behaviour of the bearing, a blade could be used that is made of a material that is simpler and quicker to manufacture and more readily available, which would reduce the experimental test costs.

For all these reasons, the possibility of modelling the blade with a more accessible and easier to model material, such as steel, is proposed. Figure 3.6 depicts the material change made on the model.

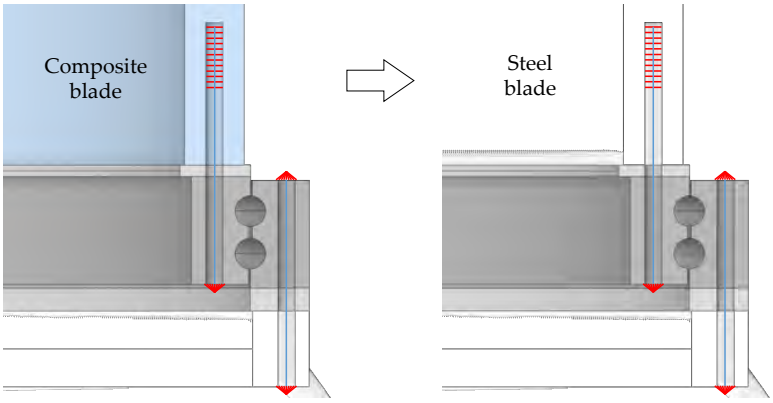

Figure 3.6. Representation of the blade material change in the assembly model.

3.3.2 Bolted connection

The approach taken for this work consists of a simplified bolted connection, but still, the contact problem between the components must be solved. To overcome this problem, and thus reduce the computational cost, the alternative method consists of connecting the interfaces of the components avoiding any frictional contact.

Although there are many different ways to make this simplification, such as implementing constraint equations or creating rigid elements, the Ansys software allows for defining a penalty based contact formulation between the interfaces, which is called a "*bonded connection*". By implementing the *bonded connection* (see Figure 3.7), the bolts do not need to be modelled. This way, the two interface faces of the components are connected so that the joint does not slip and the same deformation is imposed for the nodes of both elements. This type

of connection is widely used in global analyses of large assemblies to avoid adding more small-size elements that are negligible for the analysis.

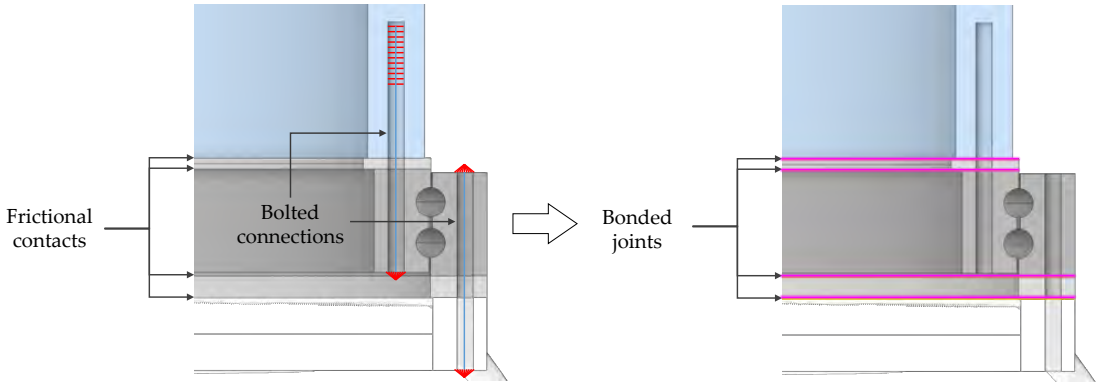

Figure 3.7. Representation of the bonded connection and the omission of the bolts in the assembly model.

3.3.3 Bearing model

Finally, an alternative model that omits the bearing FE model is also studied. This model consists of replacing the bearing with three non-linear springs. Each of these springs is modelled to reproduce the bearing axial, radial and tilting non-linear stiffnesses. The stiffness curves of these are obtained using the same FE modelling technique used in [10]. However, to remain consistent with the methodology, Daidié's mechanism was used to obtain the stiffness values, so no more variables are introduced when comparing the results. Figure 3.8 shows the dimensions of the bearing used to obtain these curves with D_{pw} = 4690 mm, D_w = 80 mm and Z = 147 per row. Figure 3.9 shows a detail of the FE model and meshing, and it can be seen how the bearing rings were attached to stiff flanges that allow opening between components.

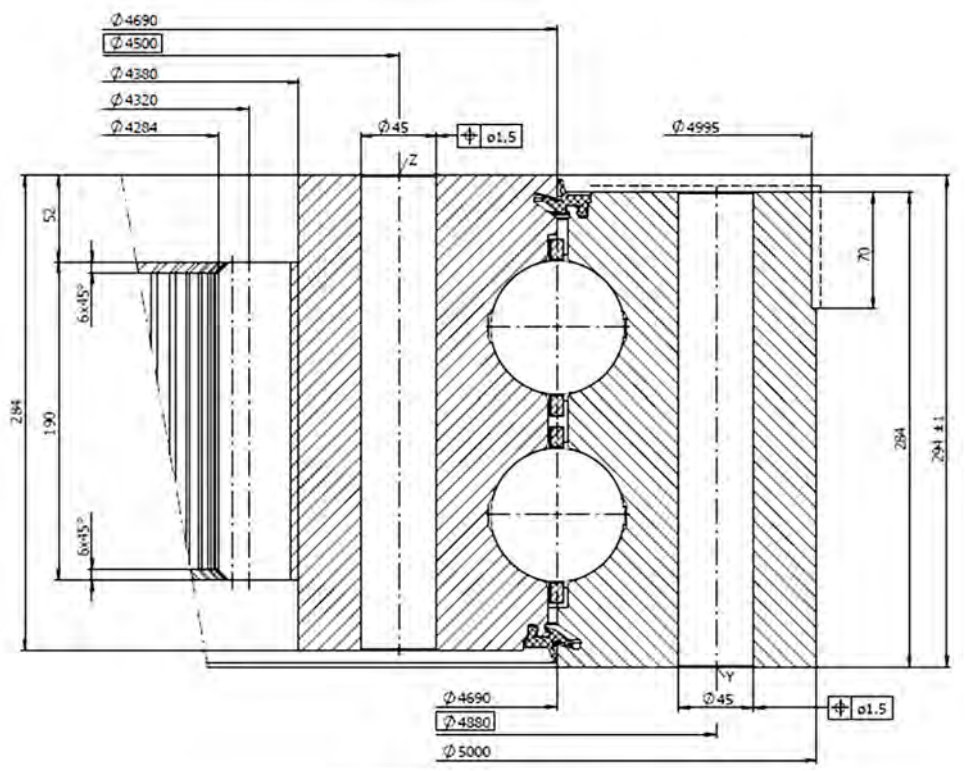

Figure 3.8. Geometrical data of the bearing [184].

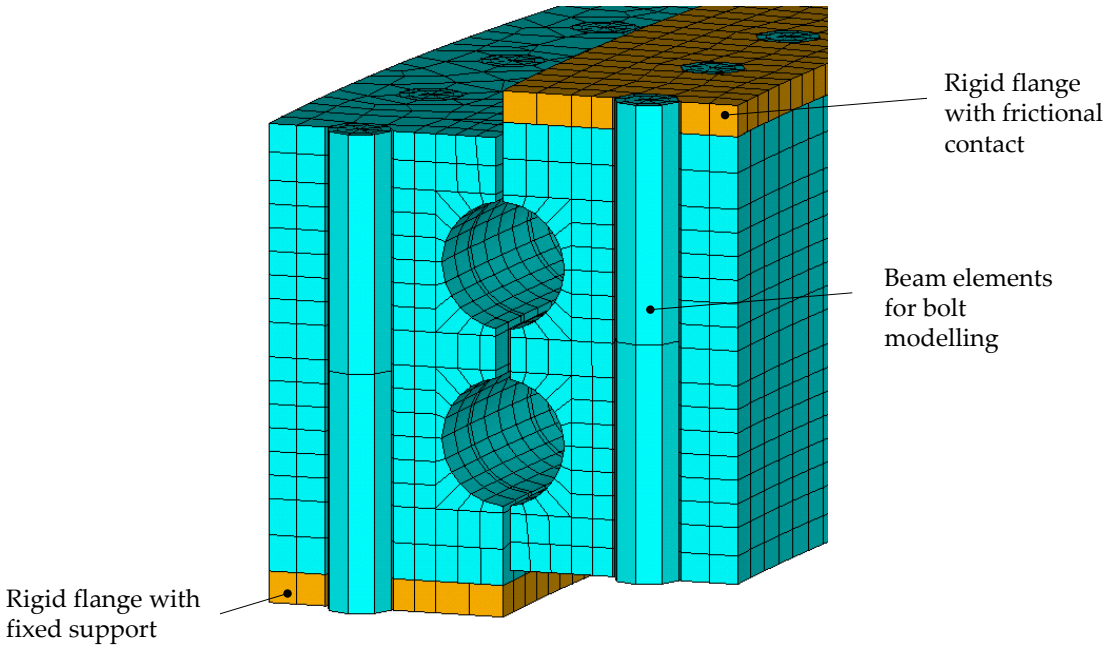

Figure 3.9. FE model of the bearing to obtain the stiffness curves.

The stiffnesses of the springs in the directions where the bearing is replaced are obtained. This is done by adjusting a mathematical expression to the aforementioned bearing model stiffness results. However, for axial stiffness, the behaviour of the bearing differs when subjected to compression or traction, thus

requiring different adjusted expressions as shown in Figure 3.10 and Figure 3.11, respectively.

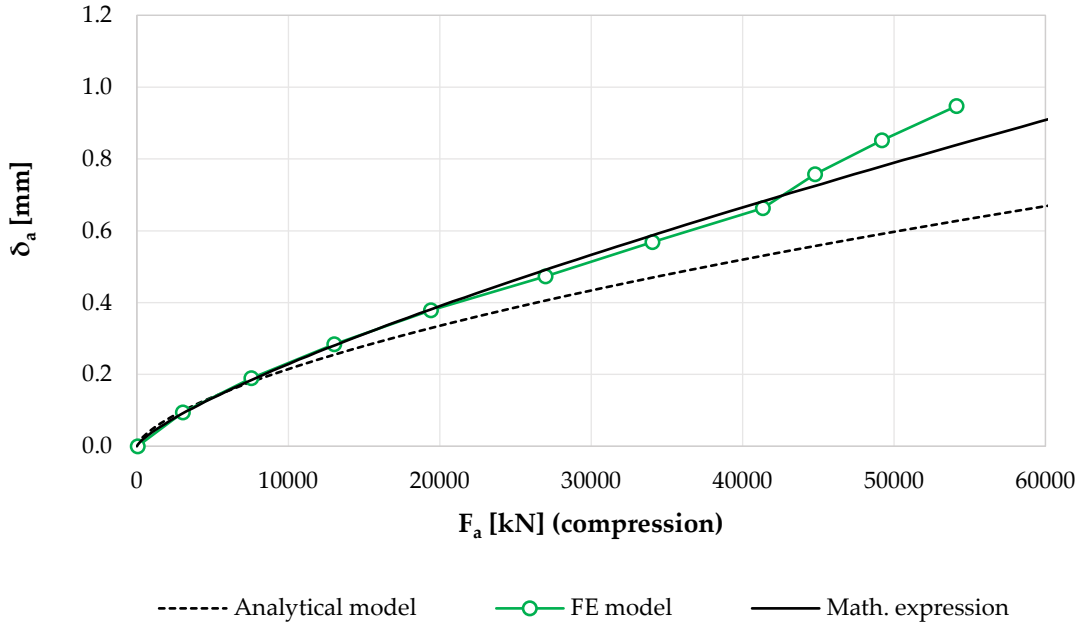

Figure 3.10. Adjusted axial stiffness for compression loads.

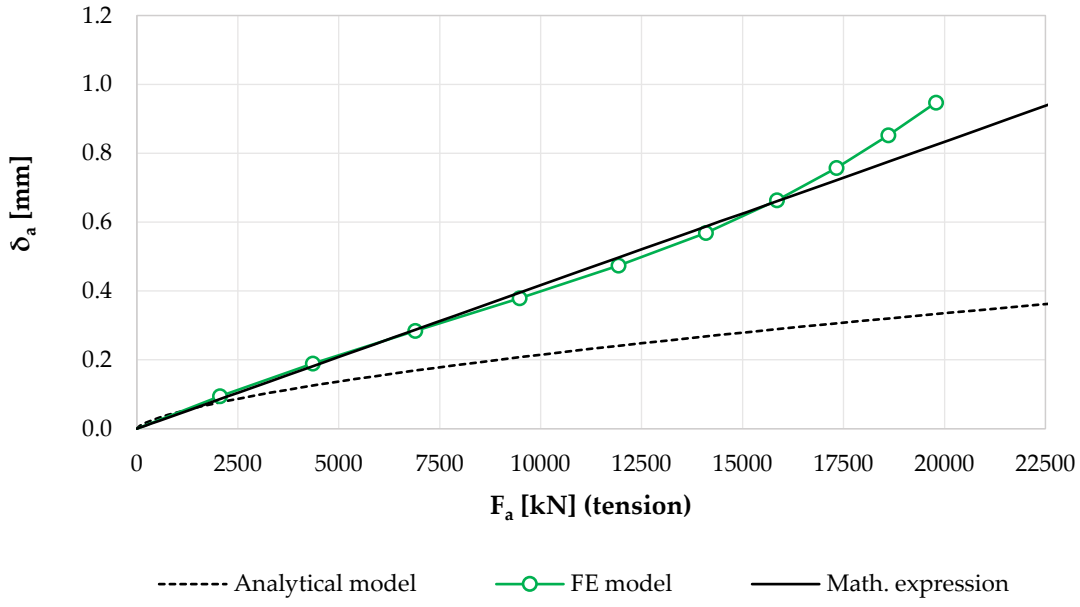

Figure 3.11. Adjusted axial stiffness for tension loads.

In the case of radial and tilting stiffness, only one adjustment procedure is required, and the obtained results are shown in Figure 3.12 and Figure 3.13, respectively.

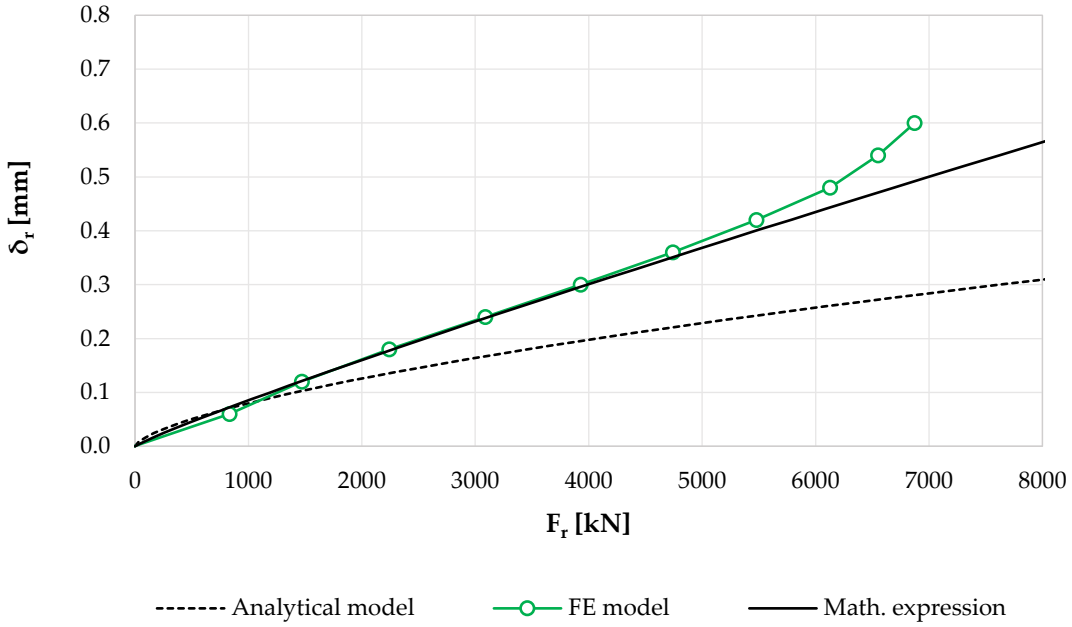

Figure 3.12. Adjusted radial stiffness.

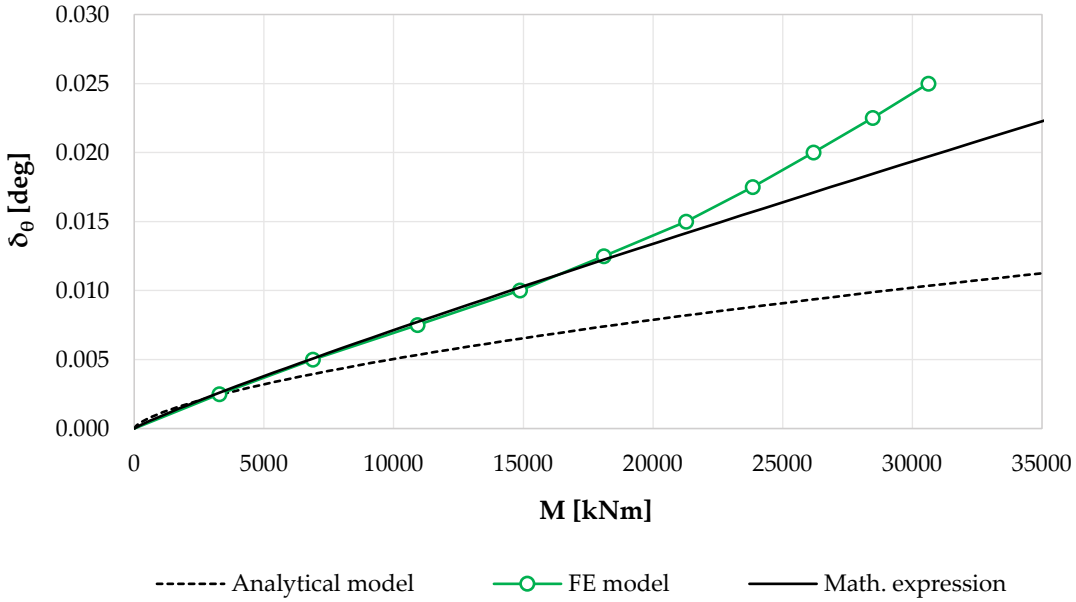

Figure 3.13. Adjusted tilting stiffness.

The bearing stiffness curves have been adjusted so that the mathematical expression simulates each of the stiffnesses. This has been satisfied up to the point where the flanges start to separate from the bearing, where the stiffness alters their behaviour. The adjusting parameters that form the mathematical expression (3.1) are summarised in Table 4.3.

$$F = C \cdot \delta^n \tag{3.1}$$

Table 3.1. Adjusting parameters for the stiffness mathematical expression of the three springs substituting the bearing.

	Axial (compression)	**Axial (compression)**	**Radial**	**Tilting**
$\boldsymbol{C}$	6.8e^4 kN/mm^n	2.4e^4 kN/mm^n	1.5e^4 kN/mm^n	6.8e^6 kN·m/deg^n
$\boldsymbol{n}$	1.3	1.0	1.1	1.1

Figure 3.14 shows the visual representation of the implemented non-linear springs substituting the bearing in the assembly.

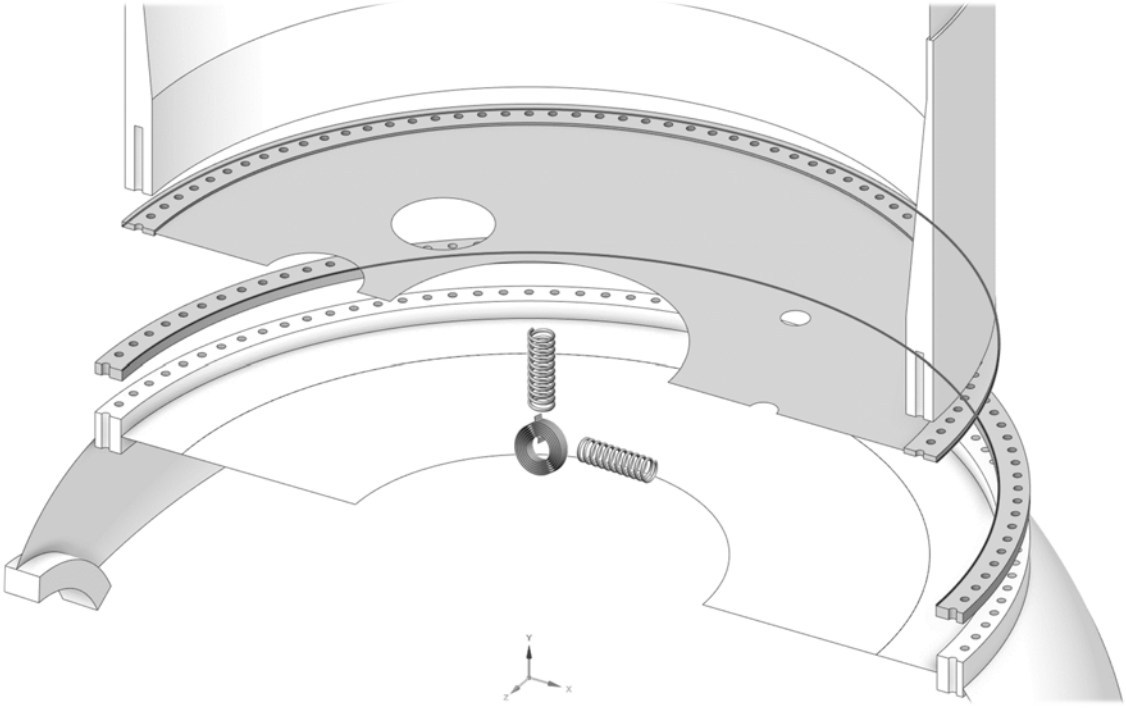

Figure 3.14. Representation of the three springs (axial, radial and tilting stiffnesses) substituting the bearing in the assembly model.

The three springs now replacing the bearing must connect the stiffener plate and extender ring. Thus, two more variants of the model are introduced, depending on the elements used to connect the springs to the surrounding elements:

- MPC184 elements: these elements connect two FE nodes and apply constraints between them. These elements impose the same displacements

or rotations on the nodes, so the element simulates a rigid element between them. Using these elements to connect two components produces a similar effect to a *bonded contact* between components, but allows the connection at a desired distance.

- RBE3 elements: these elements distribute the forces or moments received at the master node to the connecting slave nodes by means of constraint equations. In this model, the spring node is defined as the master node, so it distributes the forces to the surrounding elements, so the elements simulate a more flexible element between them compared with the MPC184 element. The force distribution takes account of the geometry of the slave nodes, so when the distance from the master node to all the slave nodes is the same they are subjected to the same force.

3.3.4 Resulting alternative models

When combining the study of the two types of bolt modelling techniques with the two blade materials, four possible models are obtained (see Figure 3.15), which are as follows:

- **Composite bonded**: a model created by combining the composite blade model with *bonded connections* to connect the components.
- **Composite frictional**: a model created by using the same composite blade as the previous model, but with a simplified bolted connection that allows for frictional contact between the components.
- **Steel bonded**: a model created by using the steel material to model the blade with *bonded connections* to connect the components.
- **Steel frictional**: a model created by using the same steel blade as the previous model, but with a simplified bolted connection and frictional contact between the components.

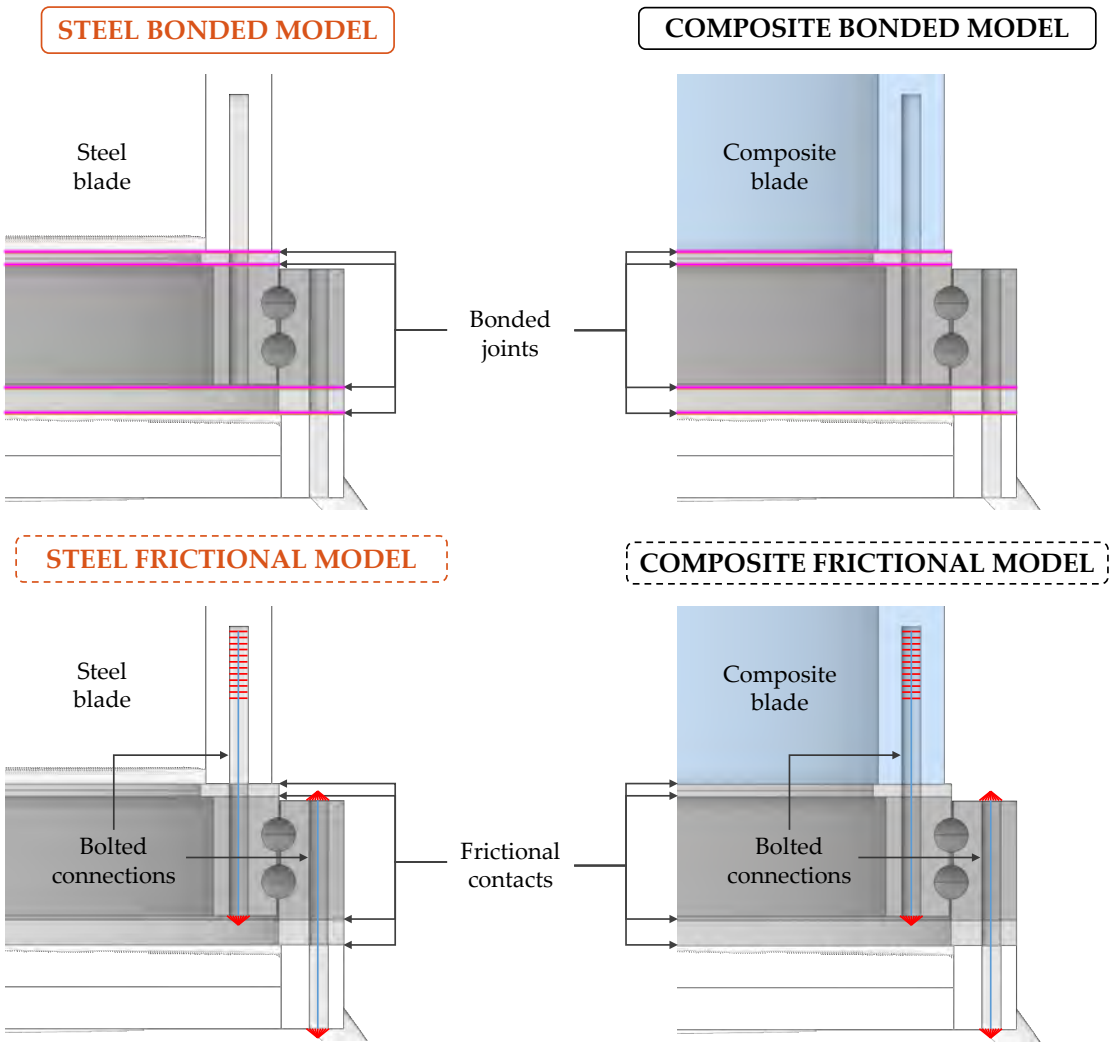

Figure 3.15. Representation of the final FE models after the blade material and bolted connection changes.

On top of that, after introducing the modelling method that replaces the bearing for three springs, two more variants are introduced. However, these results are only compared with the reference model (composite blade with bolted connection) and only the connection modelling technique between the elements is varied, resulting in the following models (see also Figure 3.16):

- **3 Springs MPC composite bonded**: the same model as the *composite bonded* model, but using the three springs to represent the bearing stiffness and joining them to the stiffener plate and extender with MPC elements.
- **3 Springs MPC composite frictional**: the same model as the *composite frictional* model, but using the three springs to represent the bearing stiffness and joining them to the stiffener plate and extender with MPC elements

- **3 Springs RBE3 composite bonded**: the same model as the *composite bonded* model, but using the three springs to represent the bearing stiffness and joining them to the stiffener plate and extender with RBE3 elements.
- **3 Springs RBE3 composite frictional**: the same model as the *composite frictional* model, but using the three springs to represent the bearing stiffness and joining them to the stiffener plate and extender with RBE3 elements.

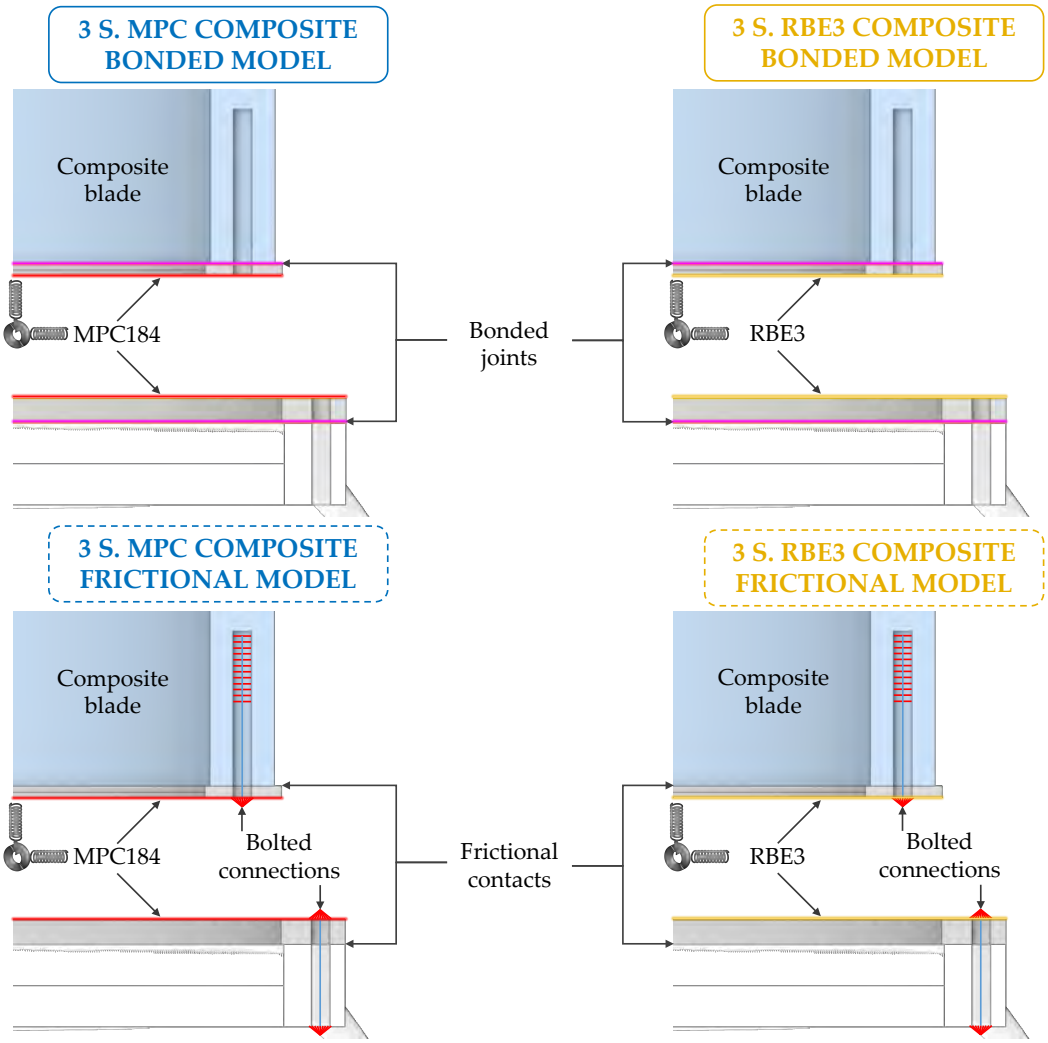

Figure 3.16. Assembly of the model components.

3.4 Simulation results

The obtained results for each of the simulations are presented and compared in this section. For this purpose, the deformation results are post-processed to analyse the effect of each of the proposed changes on the bearing rings and also on ball-raceway contact forces and contact angles.

Figure 3.17 shows the selected edges of the faces in contact with the bearing, the deformations of which are post-processed. Selecting these edges enables being able to obtain the shape of the deformations or, from another perspective, the shape of the load distribution reaching the bearing from the blade side (outer edge of the bearing and stiffener matching faces) and the hub side (inner edge of the bearing and extender matching faces). These circumferences are used as a reference without any deformation and are referred to as *Base Circumferences*.

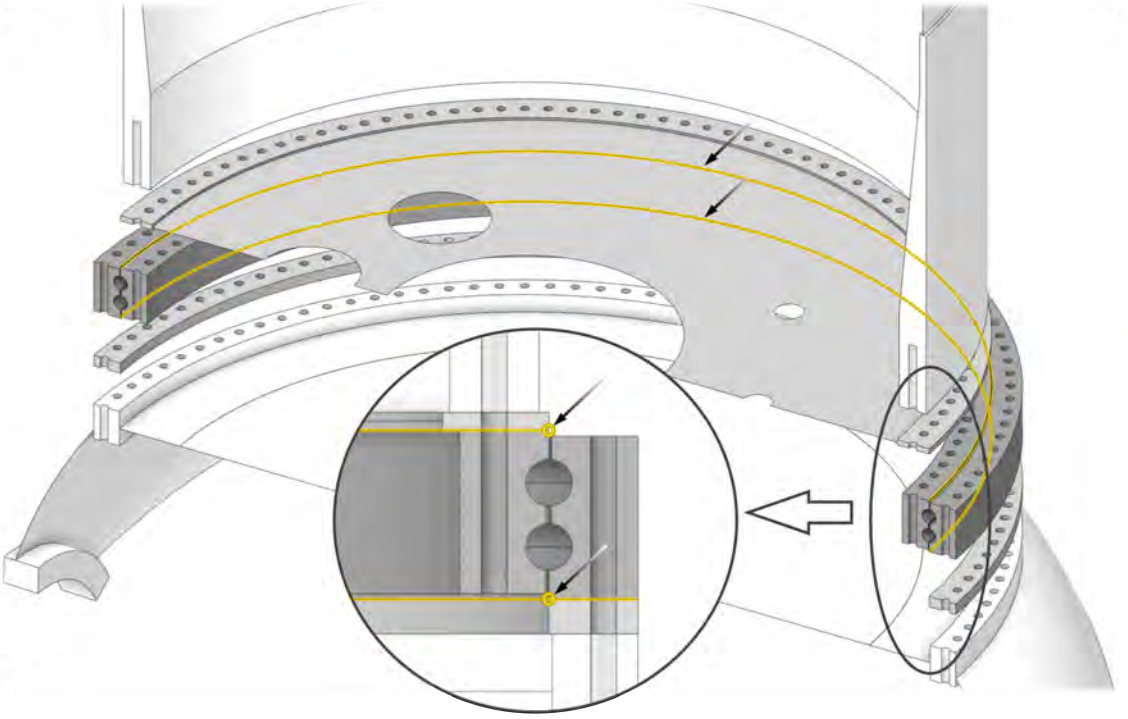

Figure 3.17. Selected bearing edges to be analysed and compared for each of the FE models.

3.4.1 Blade material and bolted connection

To analyse the local ring deformations, the global displacements of the rings must first be subtracted. After the FE analysis, a Matlab script is used to displace and rotate the *Base Circumferences* nodes (undeformed) to a final position that best fits the final location of the edge nodes (deformed). This retrieves the rotation (α)

in the XZ plane and the displacements (dO_X, dO_Y and dO_Z) of the centres, which are indicated in the following table:

Table 3.2. Displacements of the reference circumference centres after the blade material and bolted connection modelling technique changes for extreme loads.

		Composite Frictional	Composite Bonded	Steel Frictional	Steel Bonded
Blade side	dO_X *(mm)*	-1.613	-1.547 / -4.1%	-1.415 / -12.3%	-1.274 / -21.0%
	dO_Y *(mm)*	0.000	0.000	0.000	0.000
	dO_Z *(mm)*	0.458	0.500 / +9.2%	0.537 / +17.2%	0.513 / +12.0%
	α *(deg)*	0.067	0.066 / +1.5%	0.068 / +1.5%	0.064 / -4.5%
Hub side	dO_X *(mm)*	-1.286	-1.277 / -0.7%	-1.335 / +3.8%	-1.320 / +2.6%
	dO_Y *(mm)*	0.000	0.000	0.000	0.000
	dO_Z *(mm)*	0.306	0.270 / -11.8%	0.302 / -1.3%	0.278 / -9.2%
	α *(deg)*	0.025	0.023 / -8.0%	0.024 / -4.0%	0.023 / -8.0%

These results show more rigid behaviour of the ring for the steel and bonded models, as lower displacements are obtained in the X direction (dO_X) on the blade side, especially for the *Steel Bonded* model. On the hub side, the *bonded connection* implies more rigid behaviour, but the blade material change shows a small increase in the displacements in the X direction, although these are negligible. The same can be concluded regarding the Z direction displacements (dO_Z), where the differences are minimal.

The values from the previous table are shown in Figure 3.18 after magnifying the displacements by 100 and the angle variation by 5.

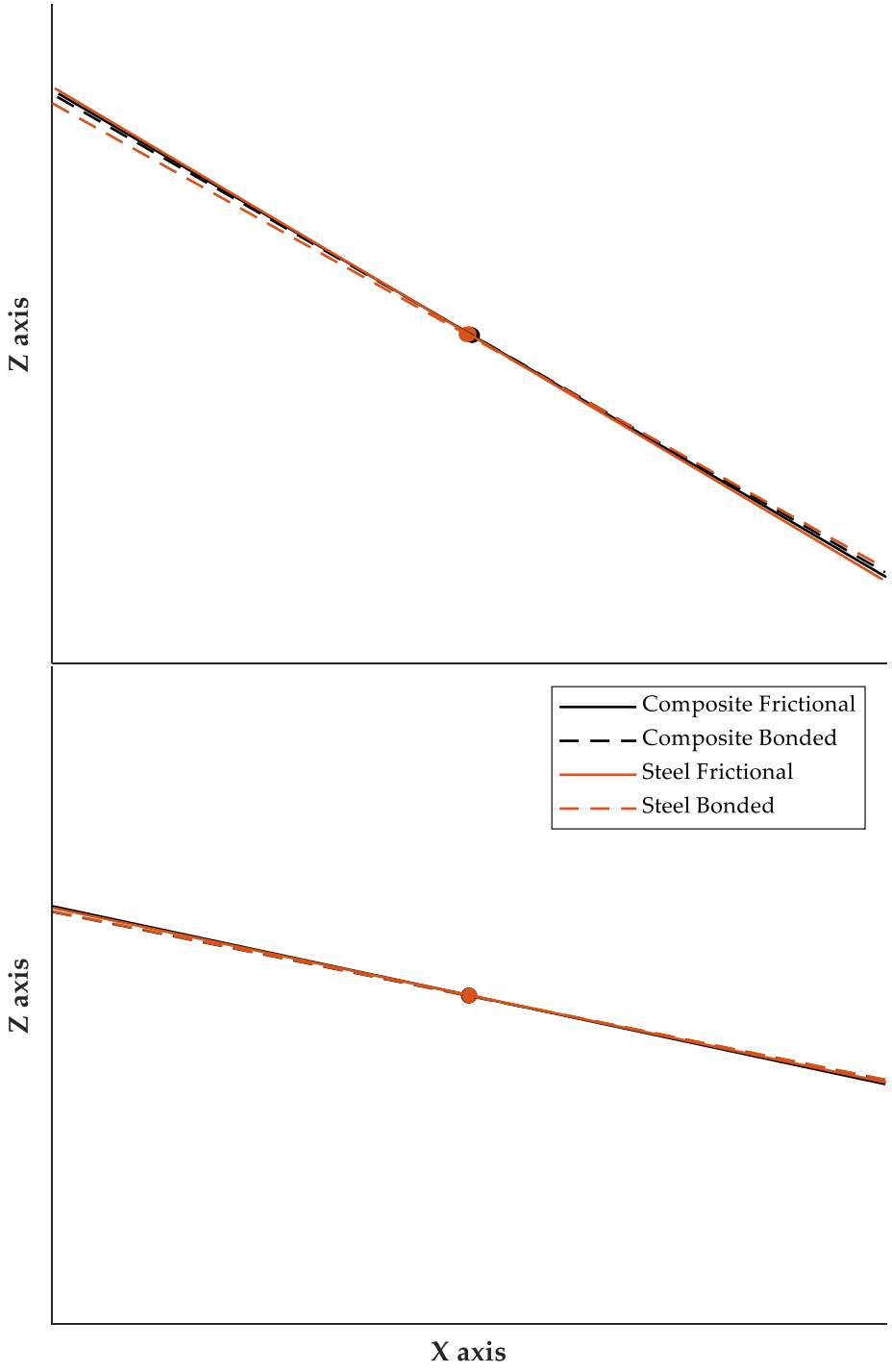

Figure 3.18. Magnified displacements and rotations of the selected cirumferences of the blade side (up) and hub side (down).

The deformations can be distinguished from the displacements with these results. The deformed shapes are plotted to compare and analyse how the rings are deformed in each case, before (blade side) and after (hub side) the bearing. Due to the small deformations compared to the displacements and the geometry

sizing, the deformed shapes in the following figures are magnified (10^3 times) and plotted together with the *Base Circumference* for each case.

Figure 3.19 shows the deformed shape of the bearing at the blade side from a top view of the plane obtained after adjusting the *Base Circumference* for each case. Figure 3.20 shows the same deformed shapes at the hub side. From both figures, it can be deduced that the effect of the bolt modelling or changing the blade material is negligible when it comes to in-plane deformations.

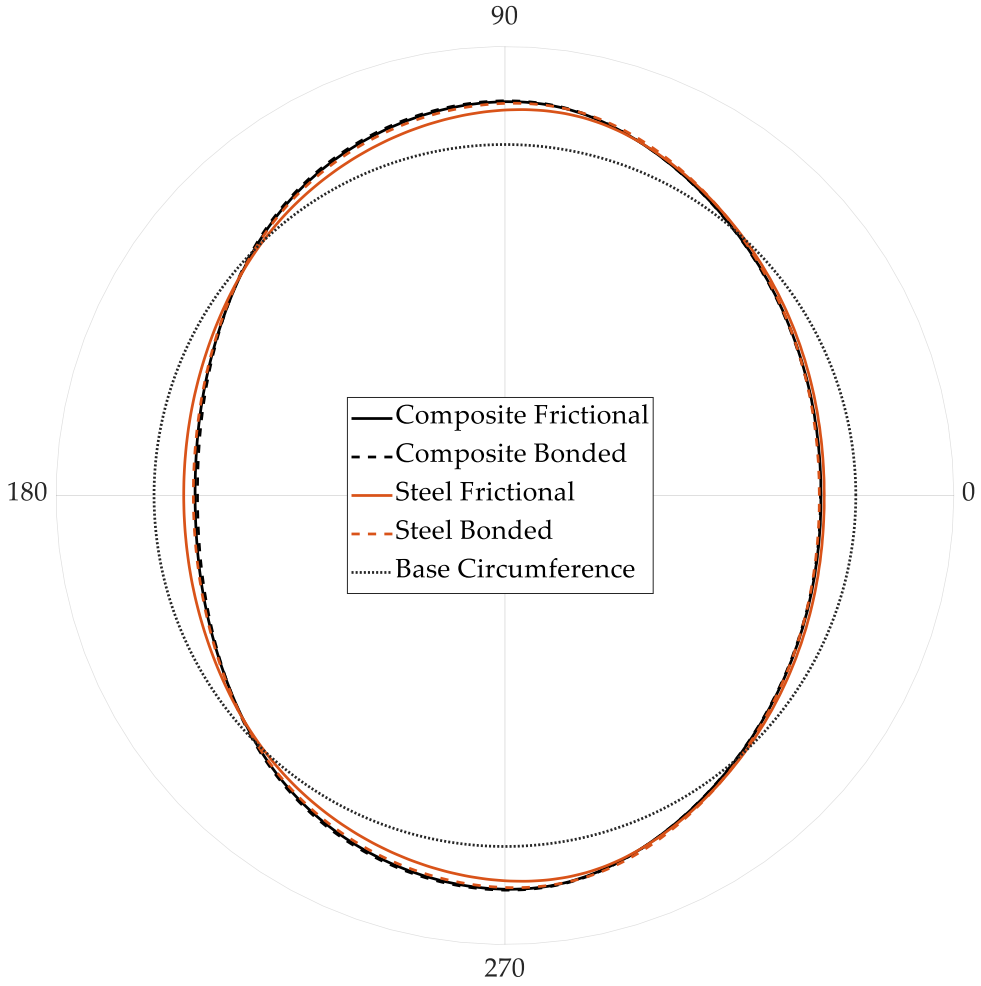

Figure 3.19. In-plane deformations of the blade side circumferences for extreme loads.

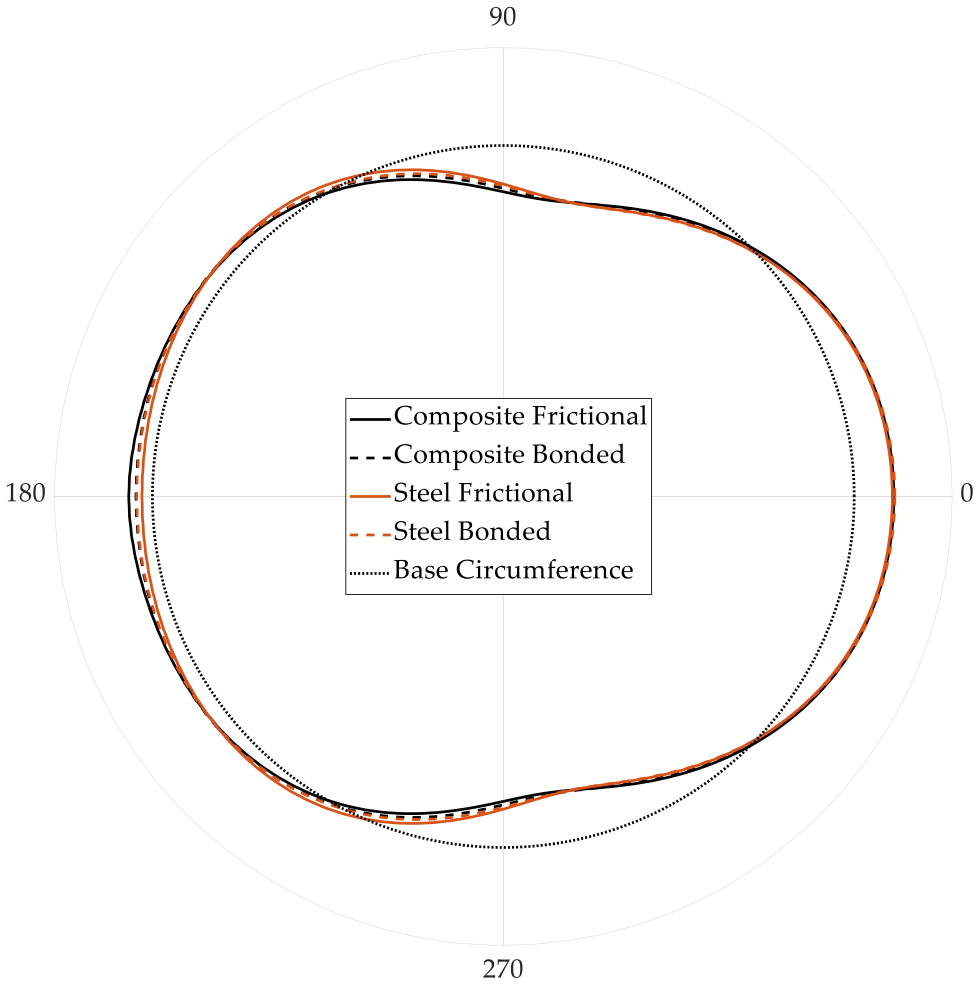

Figure 3.20. In-plane deformations of the hub side circumferences for extreme loads.

Figure 3.21 shows the out-of-plane deformations of the blade side circumference. The first conclusion is drawn from the significant discrepancy between the *Composite Frictional* reference model and the cases with the steel blade model (in orange). The *Composite Bonded* model, however, shows smaller differences from the reference model for half of the circumference. This is an indication of a possible cause, which is discussed below.

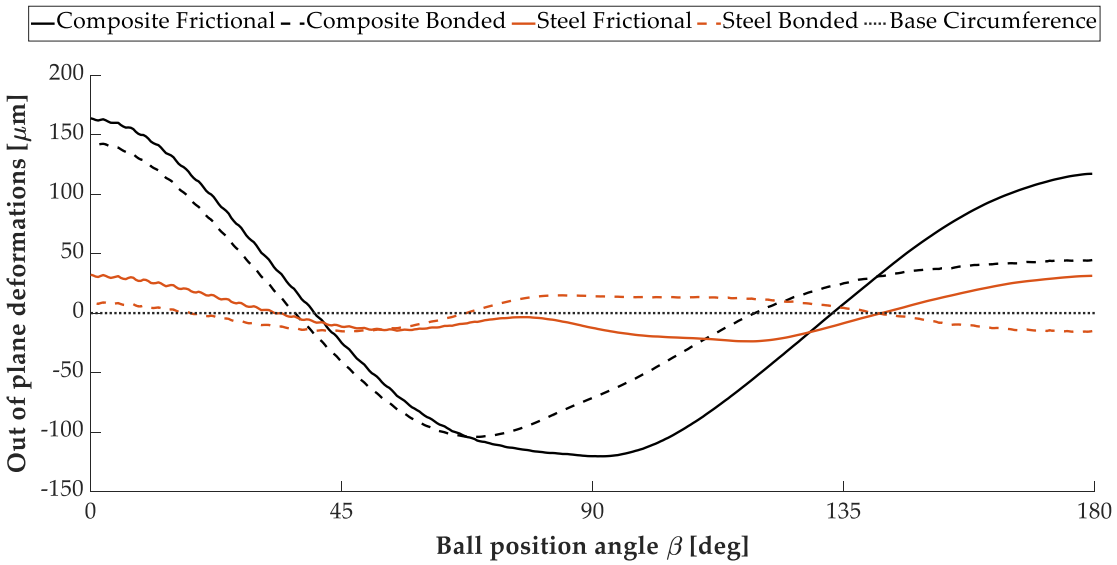

Figure 3.21. Out-of-plane deformations of the blade side circumferences for extreme loads.

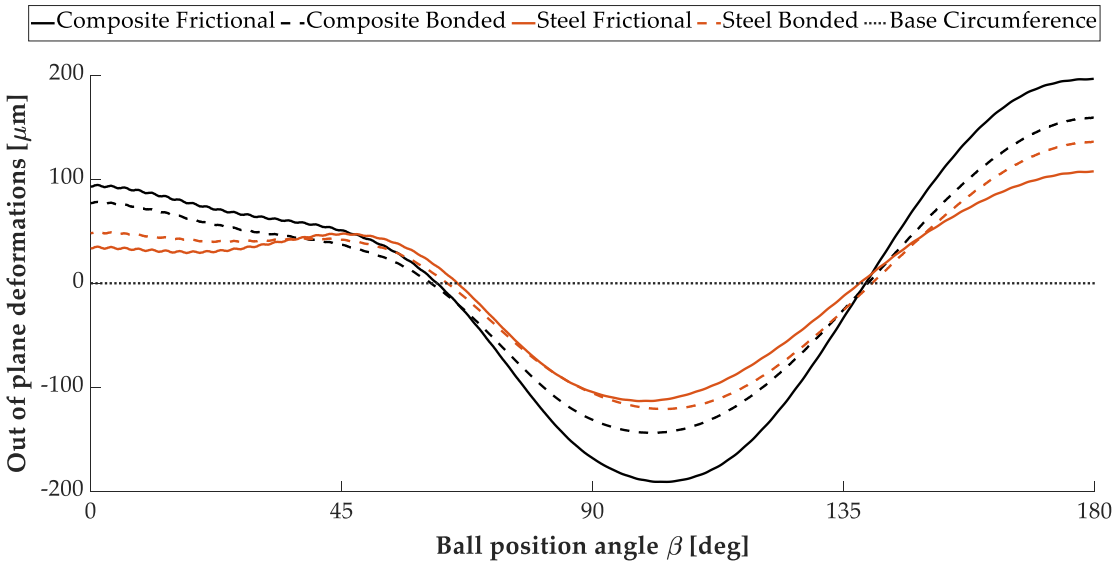

Figure 3.22. Out-of-plane deformations of the hub side circumferences for extreme loads.

Figure 3.22, on the other hand, shows the out-of-plane deformations of the hub side circumference, where in fact, the same conclusions can be drawn regarding the effect of the blade material and bolted connection modelling changes. However, the discrepancy on the hub side is not as high as on the blade side. Given that the hub is made of steel, more rigid boundaries imply a more uniform load distribution, similar to the *bonded connection*, reducing the impact of the bolted connection modelling technique used.

Regarding the high discrepancy seen in Figure 3.21, it was known that the joints between elements could show an opening in the tensioned areas (see Figure 3.27, extracted from the performed analyses to obtain the bearing stiffness as in [10]), and this could show more flexible behaviour than expected in the obtained results.

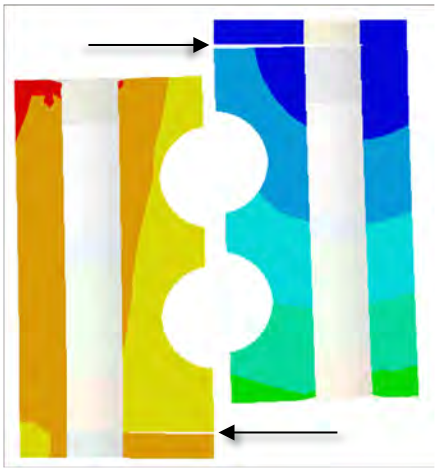

Figure 3.23. Deformations of an FE analysis showing an opening at the interfaces of the components when they are subjected to tension.

Taking account that the 0° ball is aligned with the X-axis of the assembly model (see Figure 3.3), Figure 3.27 is representative of the section located at 180° of the assembly model, a section where the observed mismatch between the circumferences is subjected to tension, implying that there could be an opening between the components. Figure 3.28 shows the contact status at each of the faces that contain the Base Circumferences. The yellow areas of the image indicate a gap, whereas the orange areas indicate sliding between components and the red areas indicate stick regions.

However, since FEM analyses are performed by applying the loads gradually (substeps), it was possible to analyse the load distribution and deformations for 50% of the extreme loads, where no sliding between components was appreciated.

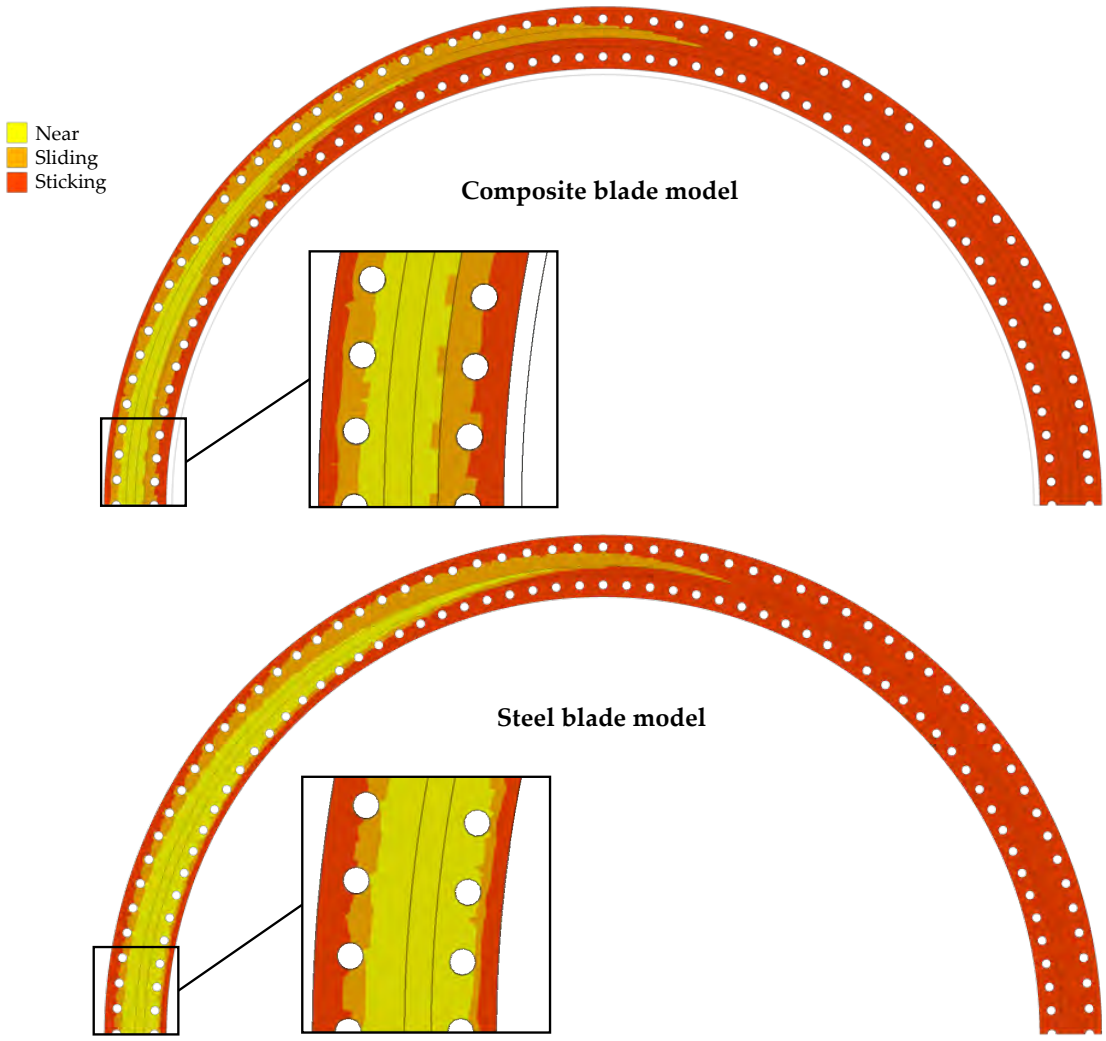

Figure 3.24. Stick (red), sliding (orange) and non-contact/sticking (yellow) status at the faces containing the *Base Circumferences* of the analysis under extreme loads for the composite blade model (up) and the steel blade model (down).

Figure 3.25 and Figure 3.26 show the out-of-plane deformations for these reduced acting loads. In this case, it can be said that for lower loads, the *Composite Bonded* and *Steel Bonded* models show similar deformations to their corresponding frictional models, concluding that the effect of the bolted connection is negligible on both the blade and hub side.

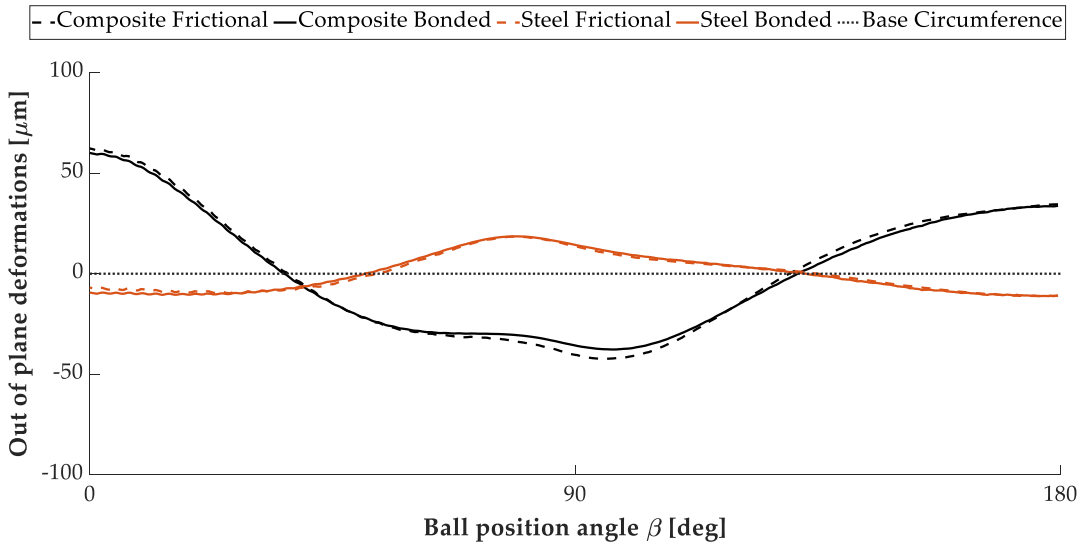

Figure 3.25. Out-of-plane deformations of the blade side circumferences for half of the extreme loads applied.

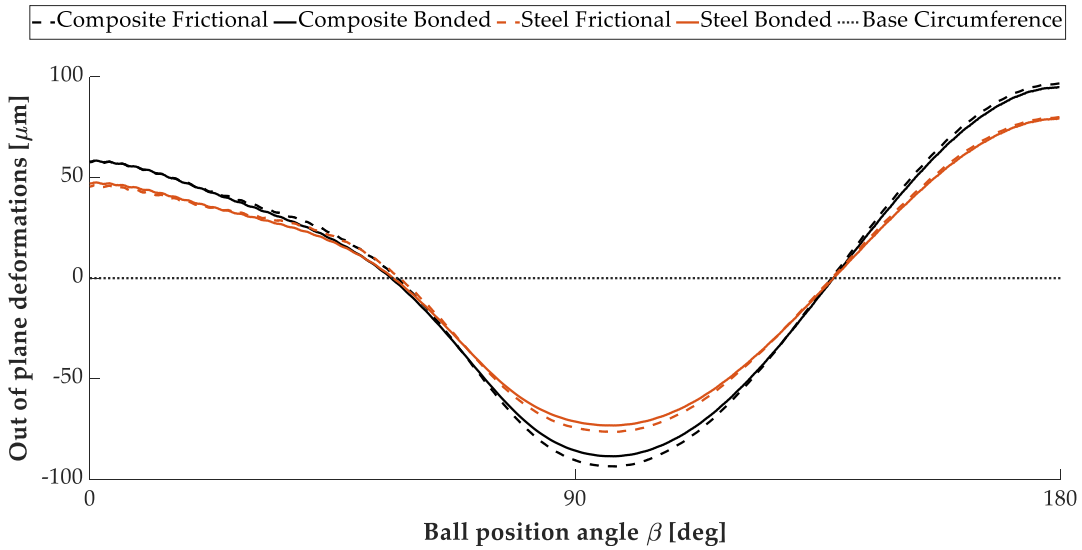

Figure 3.26. Out-of-plane deformations of the blade side circumferences for half of the extreme loads applied.

When it comes to analysing the obtained load distribution in the ball-raceway contacts, Figure 3.27 shows the results for both the upper and lower rows. The load distribution shows the most loaded diagonal for each ball position, for the extreme load case.

The load distribution results also indicate how the forces are distributed while passing from the inner ring to the outer ring (or from the blade to the hub), as well as the most loaded balls. In addition to this, Figure 3.28 shows the contact angles obtained for each of the most loaded contacts for the upper and lower races.

Both of these results emphasize the similarities between the *bonded* and *frictional contact* cases for both composite and steel blades. The observed minor discrepancies coincide again around 180° for being the tension side, as well as being further from the fixed support.

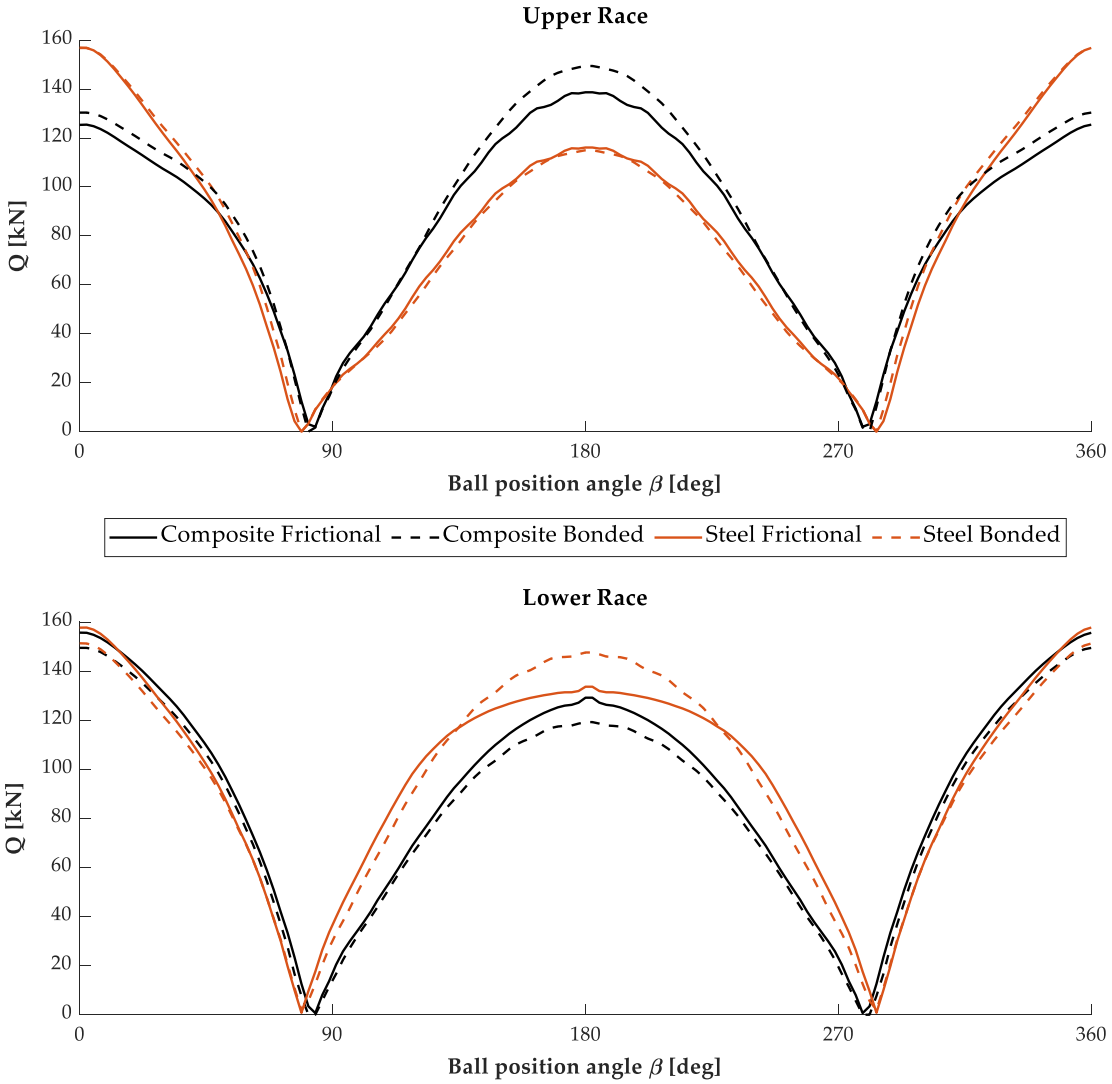

Figure 3.27. Load distribution (most loaded contact diagonal) for the upper and lower race of the bearing under extreme loads.

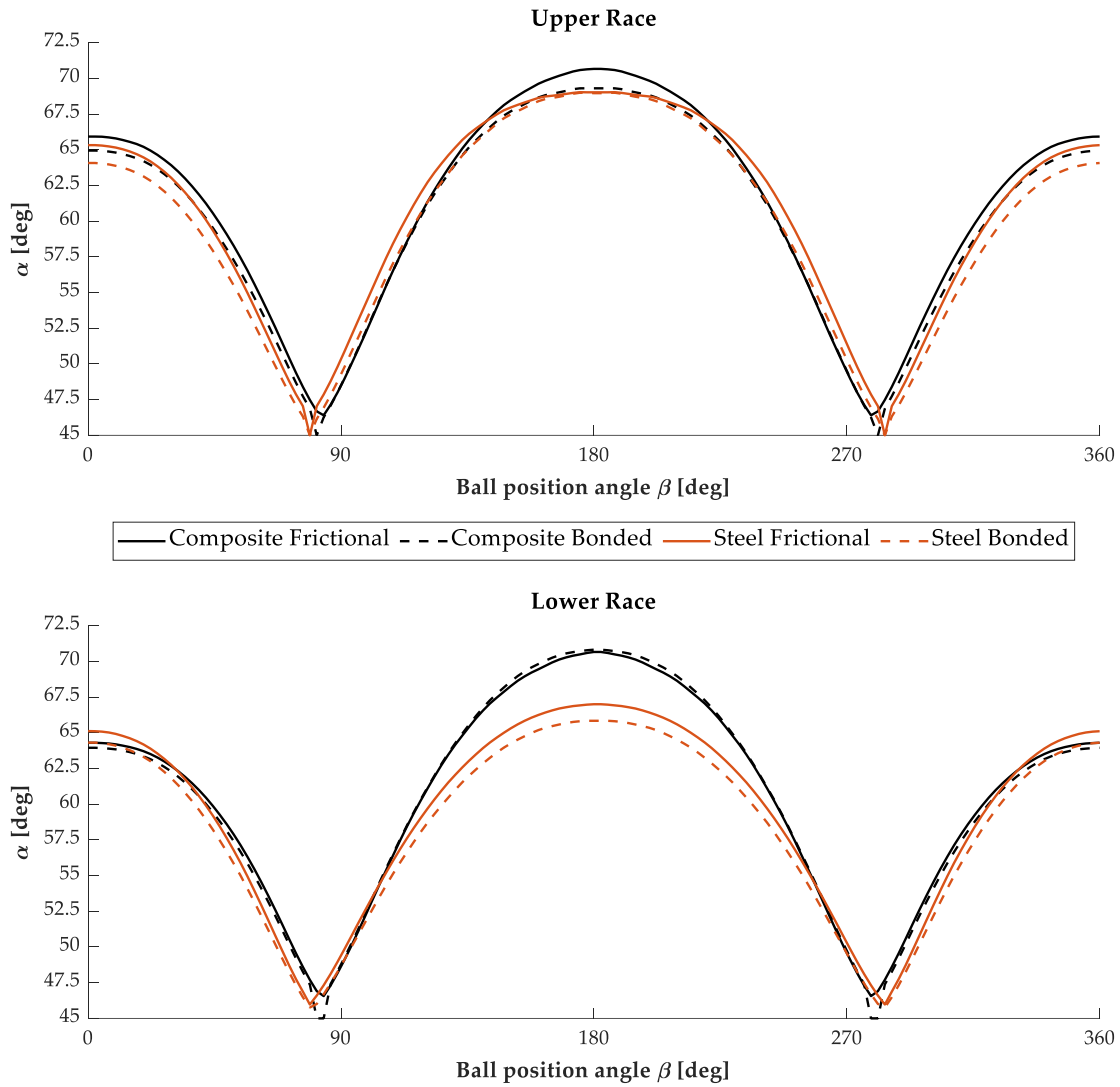

Figure 3.28. Contact angles at the most loaded contact diagonal, for the upper and lower race of the bearing under extreme loads.

Figure 3.29 and Figure 3.30 show the same results for the same load step analysed before, when 50% of the acting loads were applied. These results reaffirm that the difference between the frictional and bonded models is negligible as long as the bolted joints do not open or slide. As a result, it can be concluded that bolt modelling (and their preload) is not required under non extreme loading conditions, in the preliminary design stage analysis of slewing bearings. Yet, significant differences can be seen when comparing the results for the steel blade and composite blade.

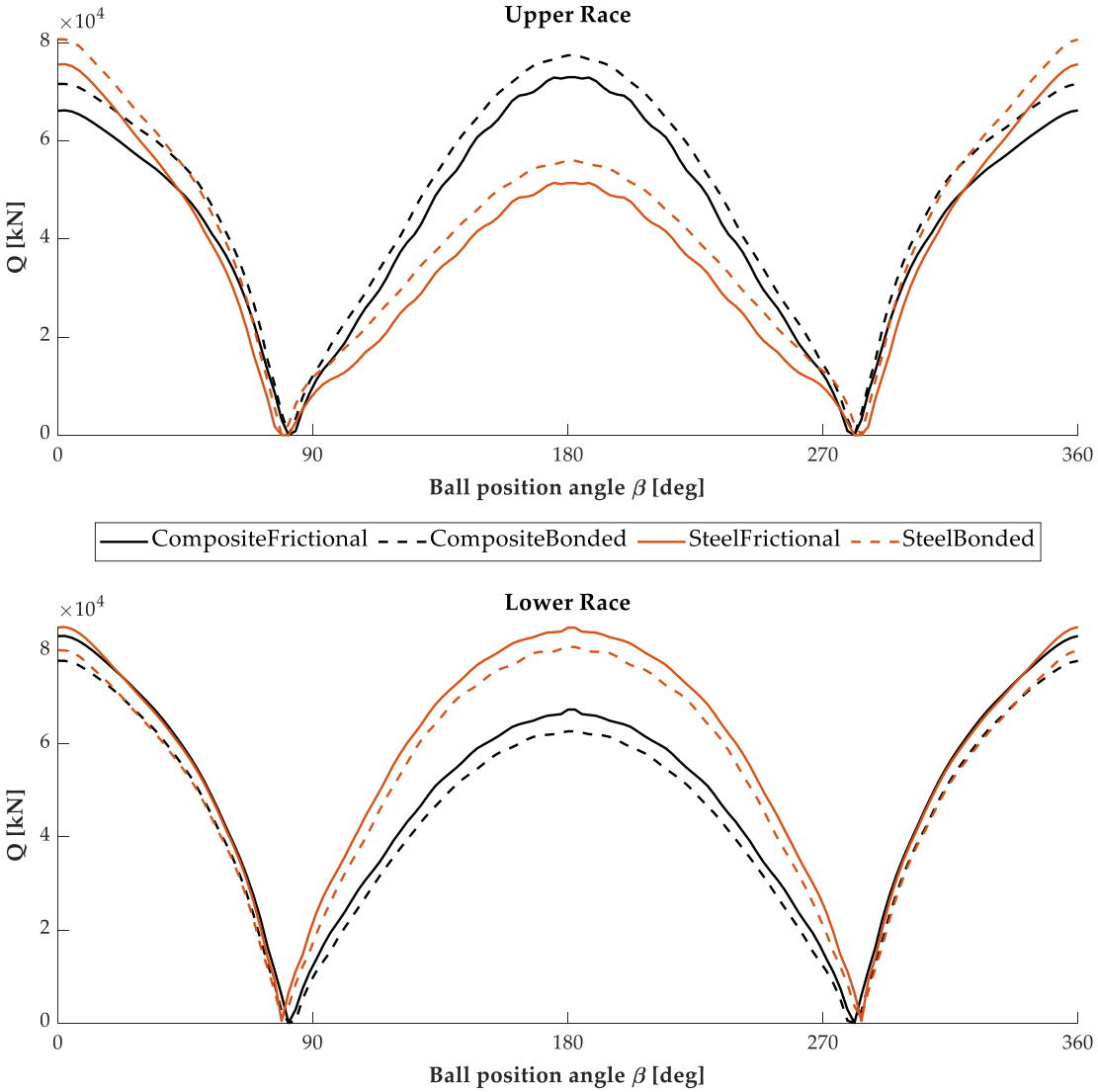

Figure 3.29. Load distribution (most loaded contact diagonal) for the upper and lower race of the bearing under non-extreme loads.

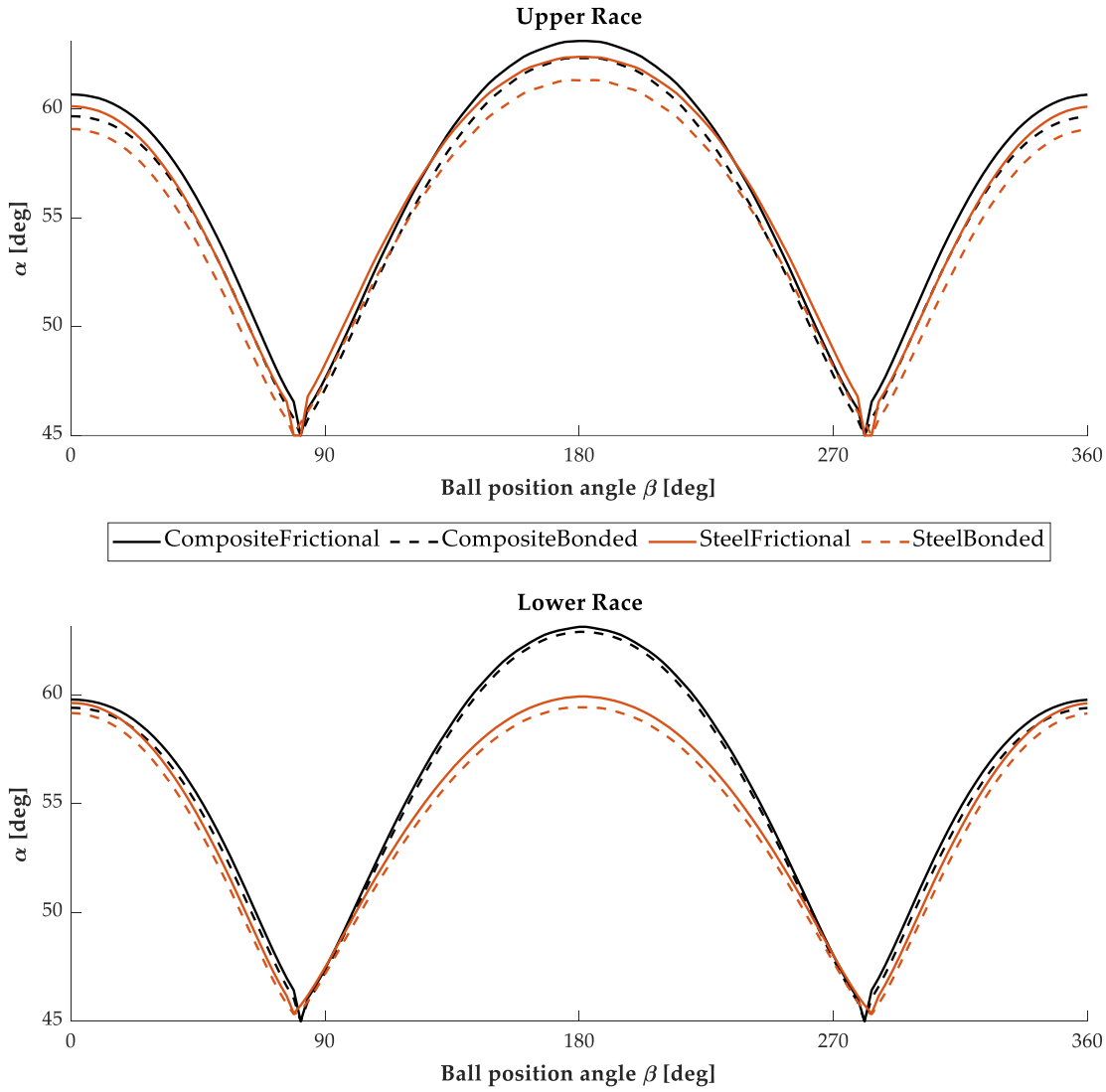

Figure 3.30. Contact angles at the most loaded contact diagonal, for the upper and lower race of the bearing under non-extreme loads.

The relationship between contact loads and contact angles could shed more light on the results. To properly analyse this relationship, the most loaded contacts on each race in both the traction and compression zones are chosen (see Figure 3.31).

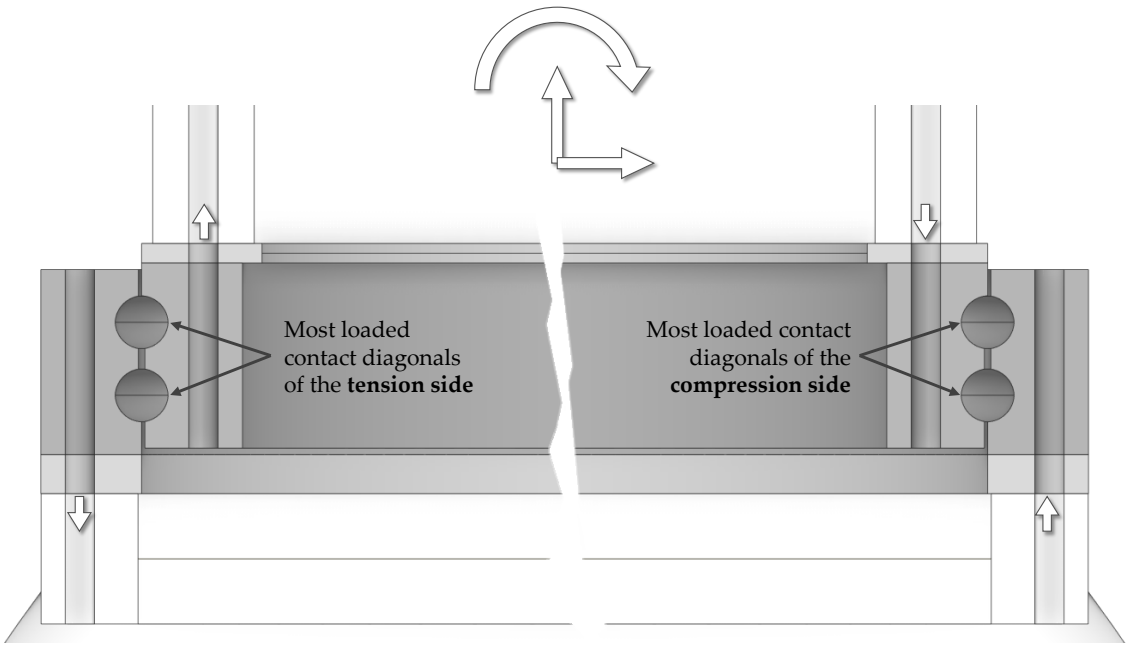

Figure 3.31. Most loaded ball-raceway contact location for each race on each of the tension/compression zones.

The top image in Figure 3.32 shows the ball-raceway contact load and contact angle relationship on the tension side for the upper row, where the frictional models present lower contact loads than their corresponding bonded models. With non-rigid contacts between components, the frictional models allow for more displacement and deformations, as was shown in previous results. This results in a deformed ring, which ends up with higher contact angles for the same contact loads. The same criteria can be applied when comparing the composite blade and steel blade modes, where in previous results the steel blade models shows less ring deformations. With stiffer rings, the lower race contact diagonal supports most of the transmitted loads, contrary to the composite model (see the lower image of Figure 3.32).

It must be noted that being the tension side area, it can be seen how the sliding affects the evolution of the contact loads and angles. The *Steel Frictional* results of the lower race clearly indicate where joint sliding is occurring, when compared with the *Steel Bonded* results, where a contact load evolution change can be seen. After losing part of the transmitted forces, the rings become more flexible, so the curve lowers the contact load increase, approaching the *Composite Frictional* results. Almost the beginning of this can be seen for the upper race of the *Composite Frictional* results, where a less slippage between components could be seen in Figure 3.24, so higher loads are required to begin changing its behaviour.

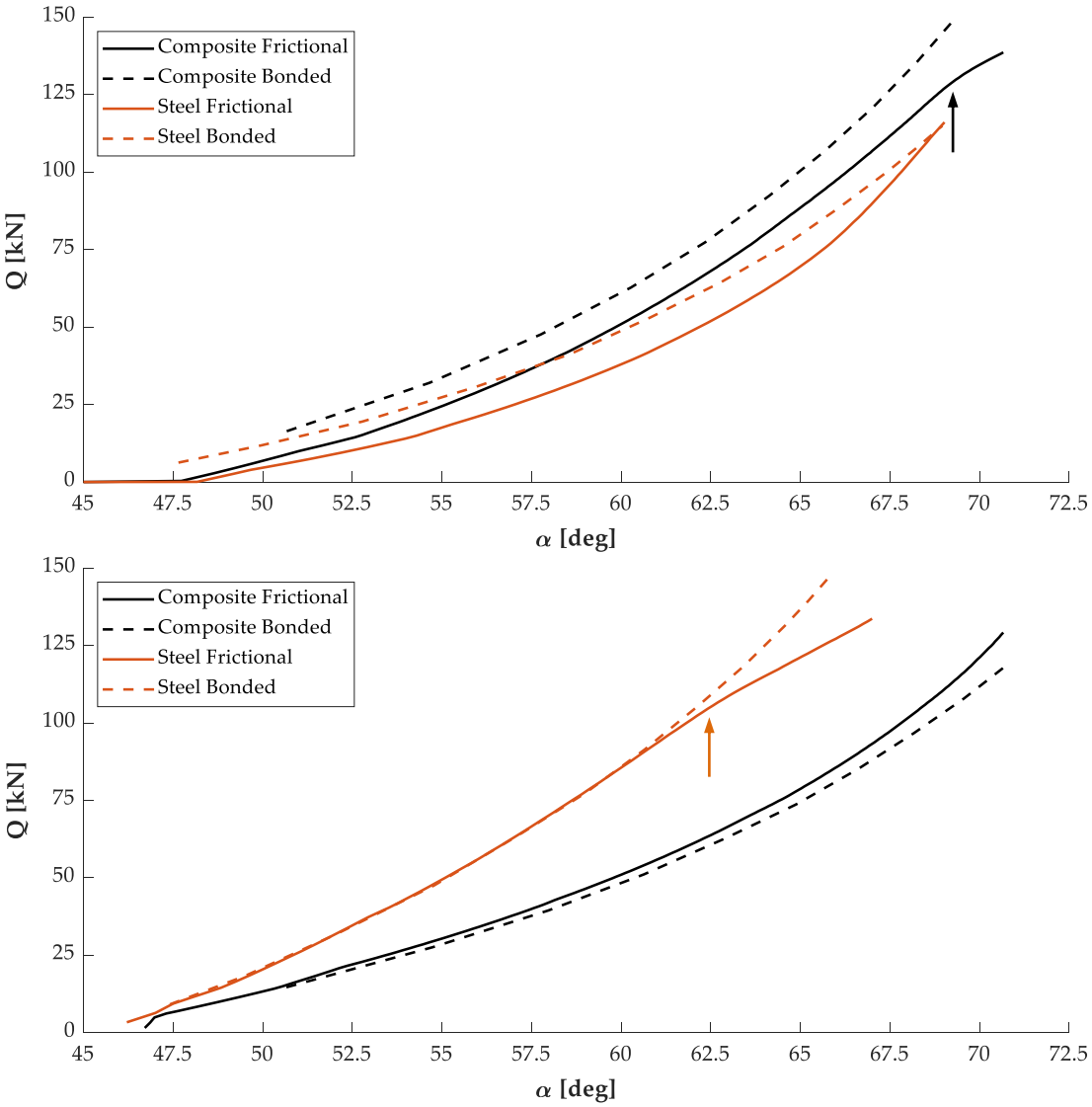

Figure 3.32. Ball-raceway contact load and contact angle relationship on the tension side for the upper row (up) and lower row (down).

Regarding the compression side results (Figure 3.33), there is no sliding between components in this region so no change in the evolution of the contact loads and contact angles is seen. Furthermore, the opposite of the tension side can be concluded.

On the upper race of the compression side, the steel blade models show the greatest contact loads compared to the composite blade models, as well as the bonded models compared to the frictional models. However, the major changes come from the material change, which varies the contact load and contact angle evolution. On the lower race, on the other hand, the behaviour between the models is very similar.

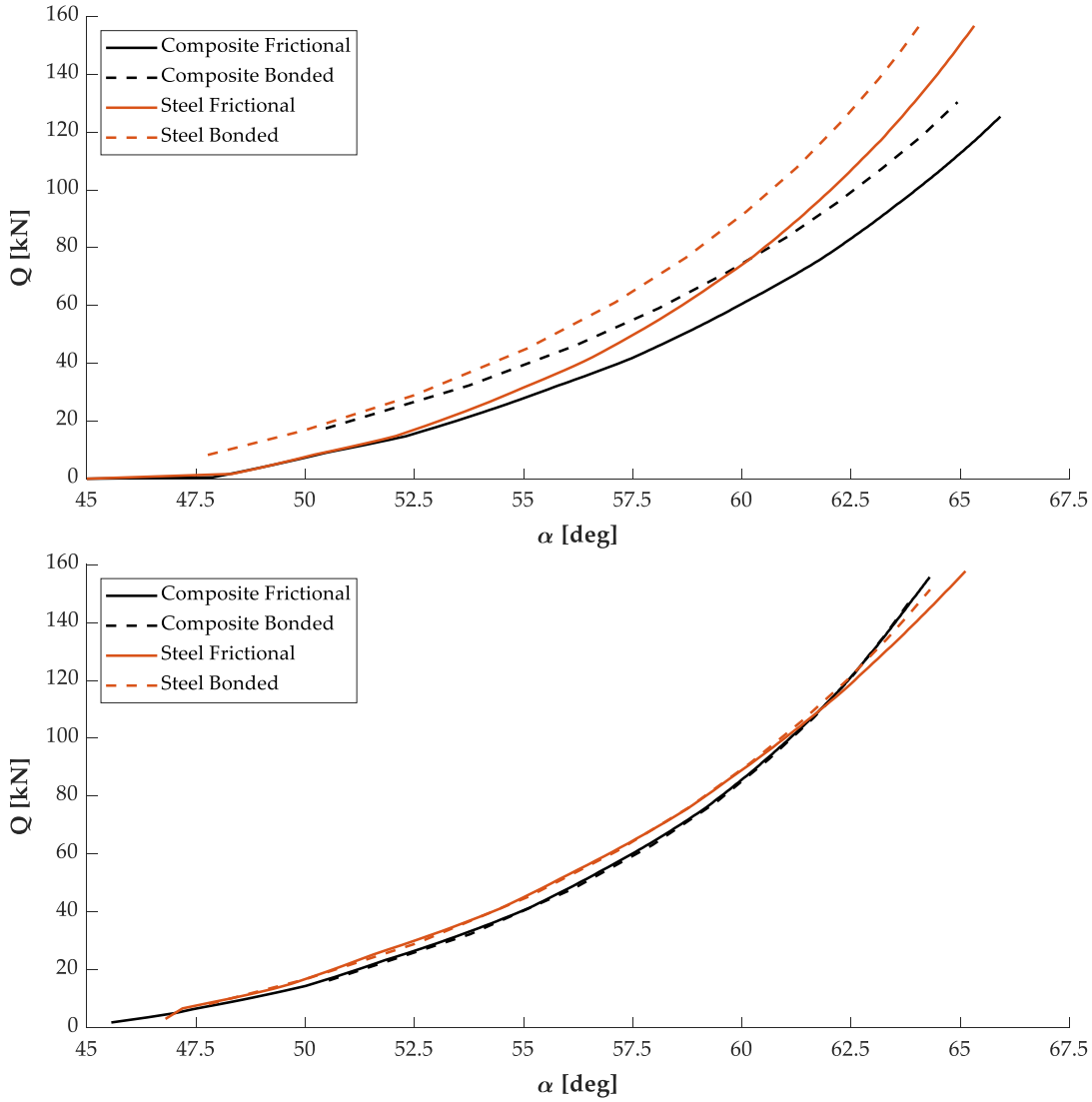

Figure 3.33. Ball-raceway contact load and contact angle relationship in the compression side for the upper race (up) and lower race (down).

Whatever the case, after reviewing all of these results, the conclusion can be drawn that the effect of the blade material is significant. Meanwhile, as long as no extreme loads are applied to the blade, the different bolted connections modelling techniques do not show a significant difference between the models. As a result, it can be concluded that these can be simplified by *bonded connections* in such cases in simulations for the early design stages, but bolted connections need to be modelled for precise results.

3.4.2 Three springs models

Again, to analyse the local ring deformations, the global displacements of the rings are subtracted for the models that replace the bearing with the three non-

linear springs. The rotation (α) and the displacements (dO_X, dO_Y and dO_Z) of the centres are indicated in Table 3.3. Additionally, the mean value of the results between the blade and the hub has been added this time, intended to represent the bearing centre displacements, for a better comparison between each of the models.

Table 3.3. Displacements of the reference circumference centres after the blade.

		Comp. Frictional	3 S. MPC Comp. Frictional	3 S. RBE3 Comp. Frictional	Comp. Bonded	3 S. MPC Comp. Bonded	3 S. RBE3 Comp. Bonded
Blade side	***dO**x (mm)*	-1.613	-0.355 -78.0%	-0.346 -78.5%	-1.547	-0.324 -79.0%	-0.310 -80.0%
	***dO**Y (mm)*	0.000	0.000	0.000	0.000	0.000	0.000
	***dO**z (mm)*	0.458	0.055 -88.0%	-0.133 -129.0%	0.500	0.064 -87.2%	0.067 -86.6%
	***α** (deg)*	0.067	0.038 -43.3%	0.041 -38.8%	0.066	0.037 -43.9%	0.060 -9.1%
Hub side	***dO**x (mm)*	-1.286	-0.578 -55.1%	-0.770 -40.1%	-1.277	-0.539 -57.8%	-0.597 -53.2%
	***dO**Y (mm)*	0.000	0.000	0.000	0.000	0.000	0.000
	***dO**z (mm)*	0.306	0.014 -95.4%	0.112 -63.4%	0.270	0.023 -91.5%	0.011 -95.9%
	***α** (deg)*	0.025	0.017 -32.0%	0.023 -8.0%	0.023	0.015 -34.8%	0.016 -30.4%

The values from the previous table are shown in Figure 3.34 after magnifying the displacements by 100 and the angle variation by 5.

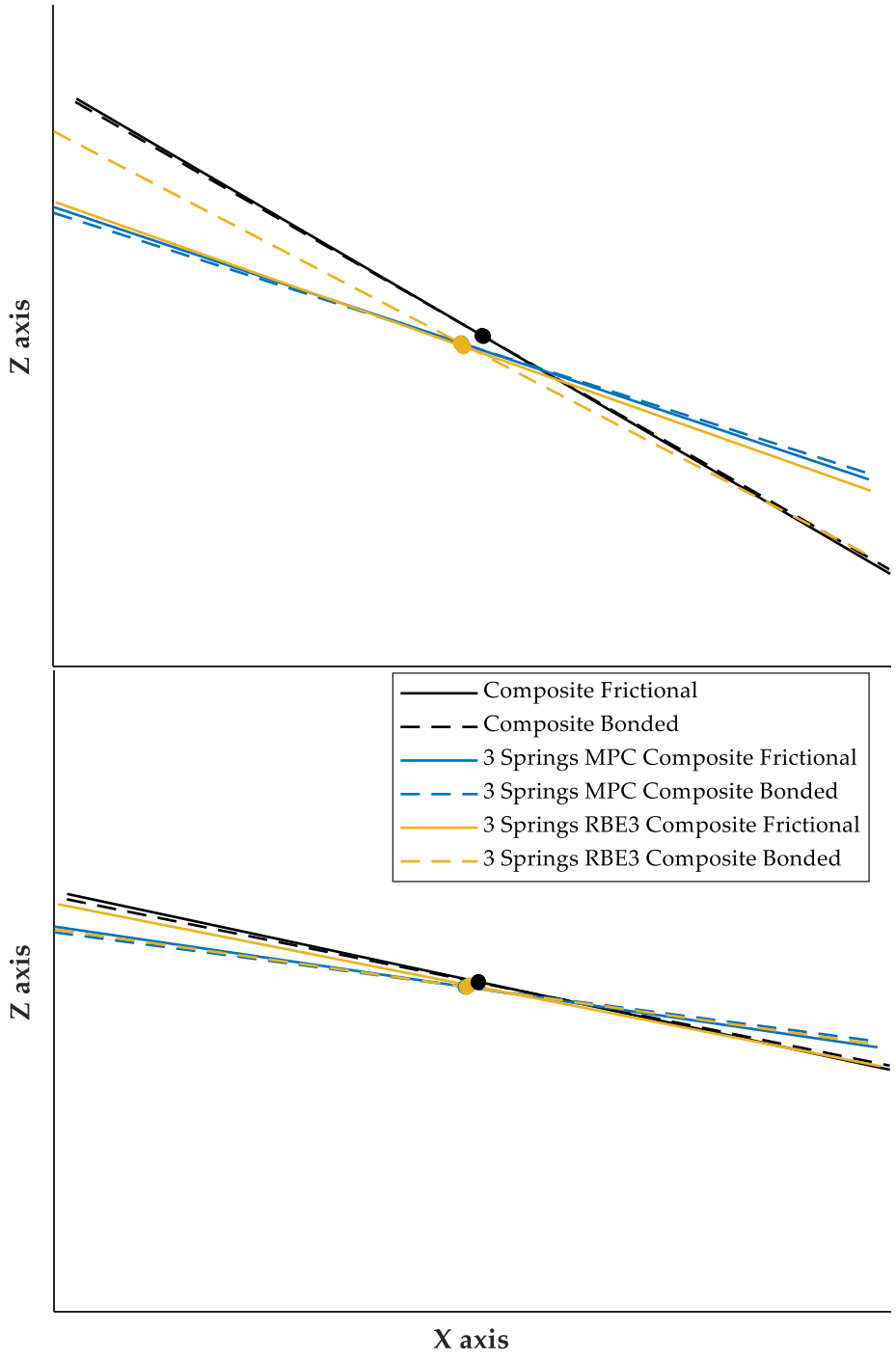

Figure 3.34. Magnified displacements and rotations of the selected circumferences of the blade side (up) and hub side (down) for the three springs assembly model.

These results show more rigid behaviour of the ring when the bearings are replaced, as lower displacements are obtained in the X direction (dO_X) on both the blade and hub side for all the models, compared to the reference models, *Composite Bonded* and *Composite Frictional*. The same can be concluded regarding the Z direction displacements (dO_Z) and angle variations (α).

Again, the deformed shapes are magnified (10^3 times) and plotted together with the *Base Circumference* for each case. Figure 3.35 shows the in-plane deformed shape of the bearing at the blade side from a top view of the obtained planes. Figure 3.36 shows the same deformed shapes at the hub side.

Analysing the results obtained for the in-plane deformations on the blade side, it can be said that replacing the bearing with three springs yields different results compared with the reference *Composite Frictional* model. Both MPC and RBE3 elements transmit the load uniformly, so it results in a circular deformed shape.

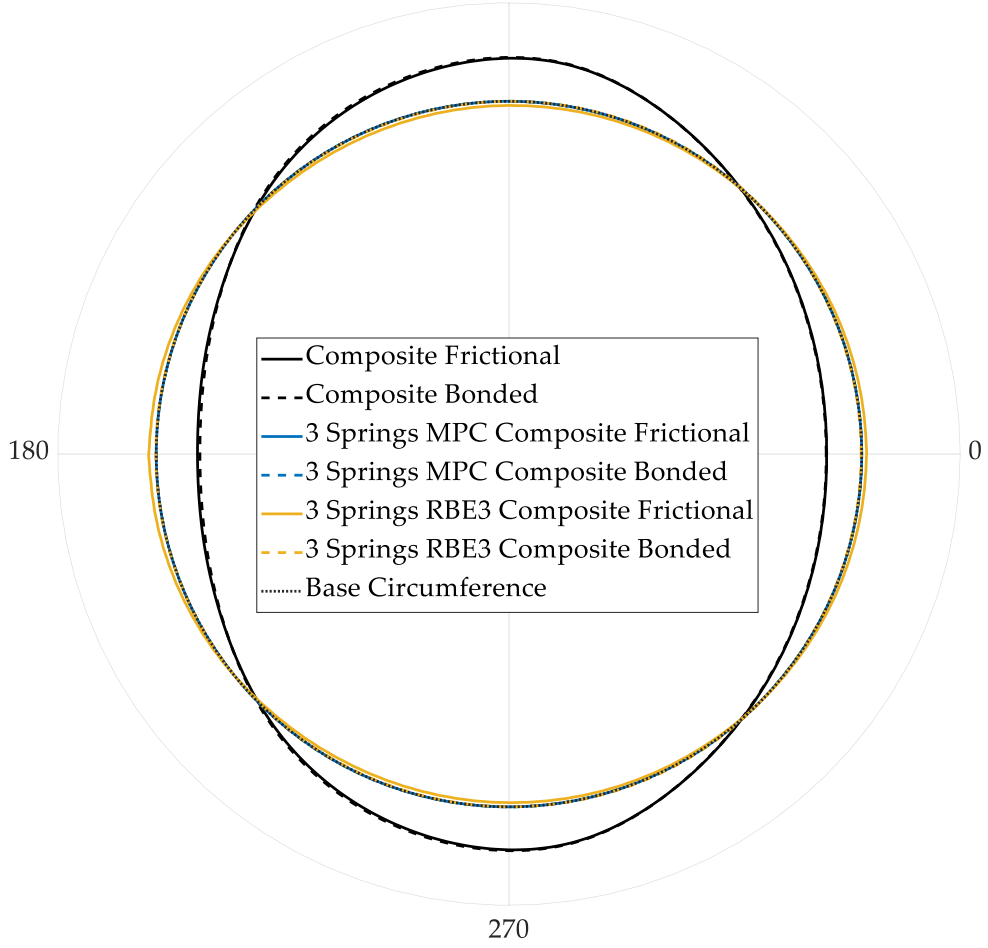

Figure 3.35. In-plane deformations of the blade side circumferences after replacing the bearing with three springs.

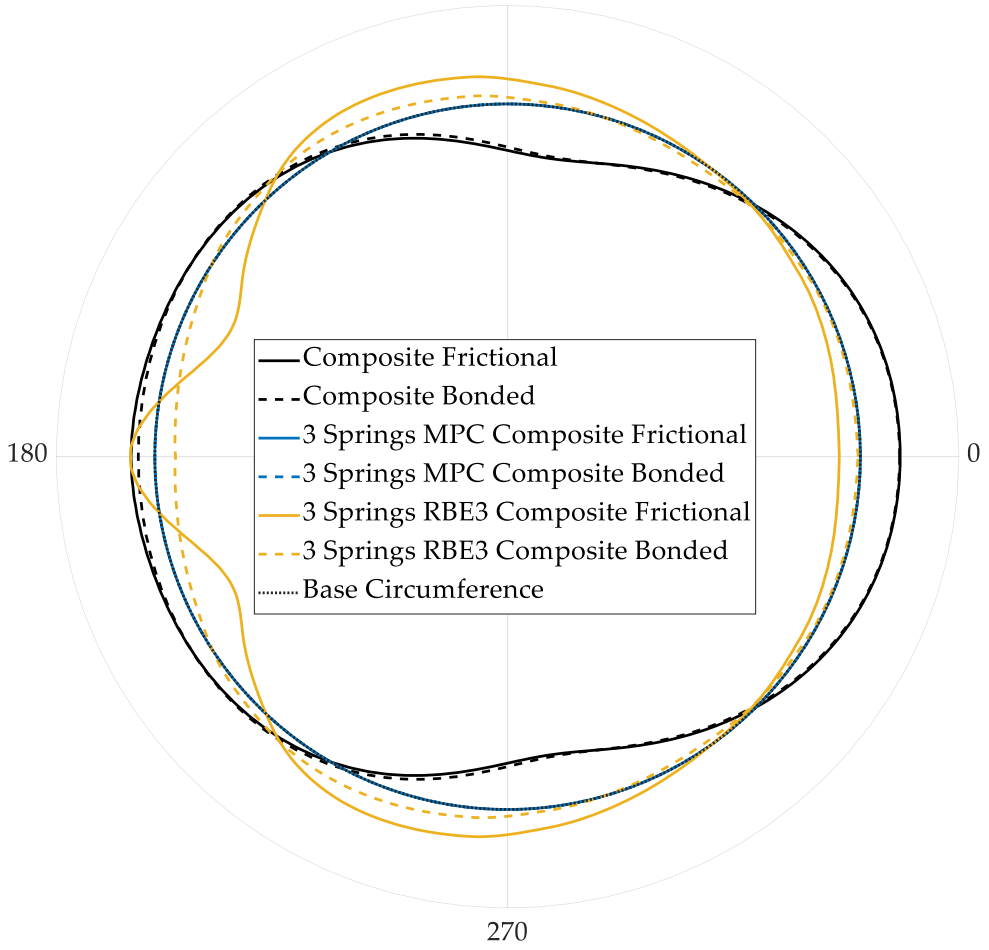

Figure 3.36. In-plane deformations of the hub side circumferences after replacing the bearing with three springs.

However, analysing the results obtained for the in-plane deformations on the hub side, Figure 3.36 shows that the in-plane deformations are related to the stiffness of the hub on each angular coordinate. Once more, it can be said that replacing the bearing with three springs yields different results compared with the reference *Composite Frictional* model for the same reason as before.

The out-of-plane deformations of both the blade side (Figure 3.37) and the hub side (Figure 3.38) confirm the previous statement. Clearer results are yielded this time, showing that the models that include MPC elements have no deformations on the selected circumferences, as these elements are infinitely rigid. All of these results also shed light on the impact of the shape of the deformations, where even if flexible elements are used to model the boundaries or the linkages between components, how the loads are transmitted through the components may affect more than their stiffness.

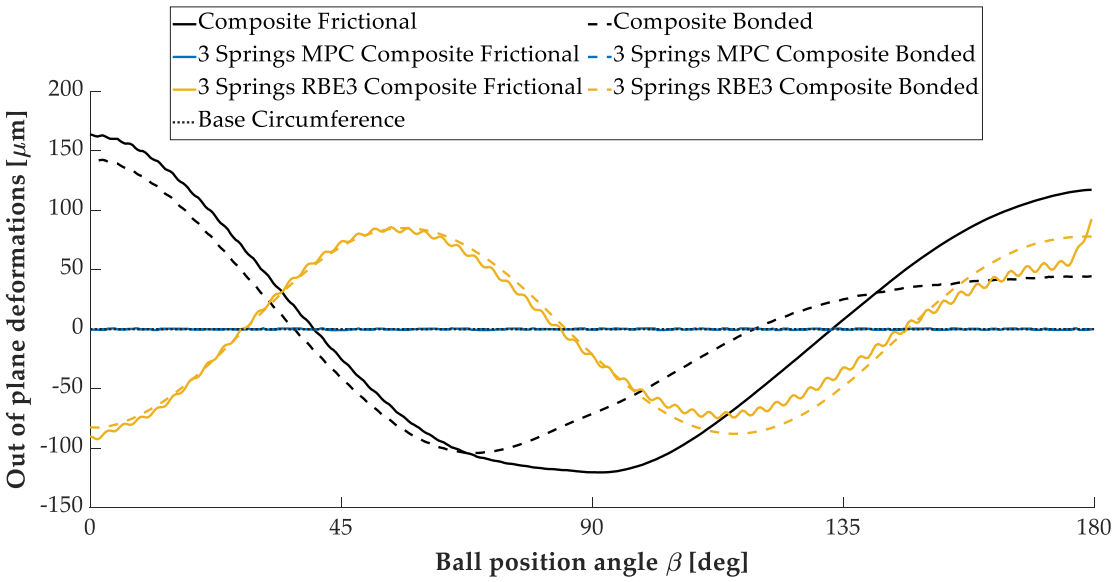

Figure 3.37. Out-of-plane deformations of the blade side circumferences.

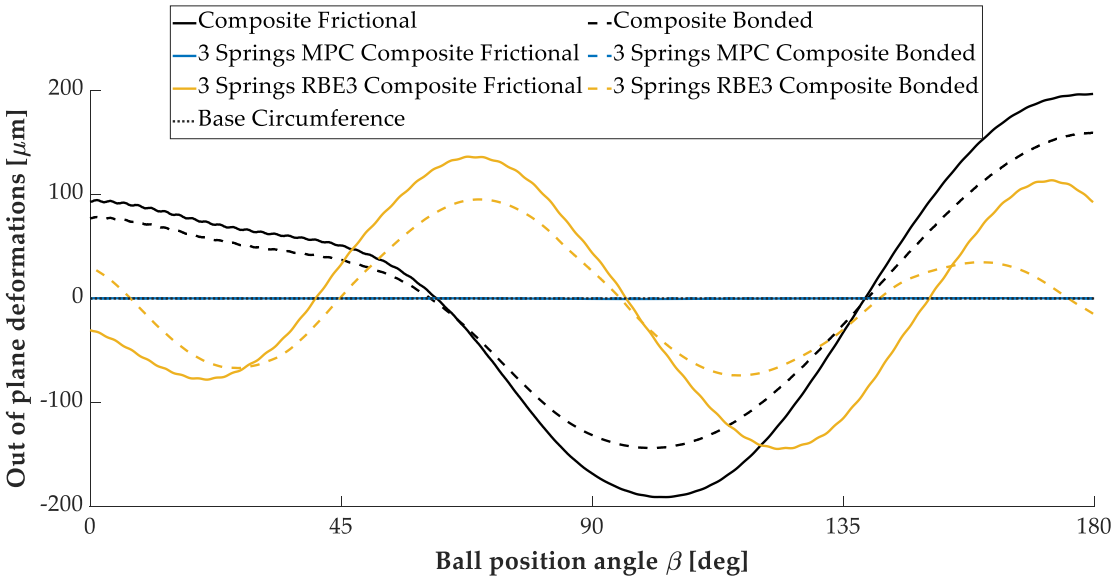

Figure 3.38. Out-of-plane deformations of the hub side circumferences.

3.5 Correct implementation of Daidié's mechanism to avoid undesired residual forces

As stated above, the flexibility of the rings significantly affects the load distribution and consequently affects the load-carrying capacity of the bearing [74][165]. Therefore, the high-precision simulations required to validate these components require the flexibility of the rings to be characterised. Accordingly, FEM is the primary tool currently used to simulate orientation guidance systems

with slewing bearings, which, however, can be expensive. Proper characterisation of the complete bearing usually requires models with a high number of degrees of freedom, required to faithfully simulate the behaviour of all the involved ball-raceway contacts.

The Daidié's mechanism used in the previous models allows for a drastic reduction in the total number of degrees of freedom of the model. The mechanism not only avoids the cost inherent in the meshing of the balls but also the refinement of the raceways, necessary for the correct characterization of the contacts [18,66]. Despite all these advantages, Daidié's mechanism is known to have limitations when the bearing experiences radial displacement, which has not been studied or quantified. The following section not only studies and quantifies these constraints, but also proposes strategies to effectively mitigate them.

3.5.1 Problem description

In a real bearing, the balls do not transmit any force outside the plane containing the ball-raceway contacts. However, when Daidié's mechanism is used for the simulation of these contacts, the mechanism elements may move out of their original radial plane. This involves transmitting the loads out of the plane, with a force component in the circumferential direction that does not represent reality.

Figure 3.39 shows the radial displacement of the inner ring modelled with Daidié's mechanism, showing how the springs are loaded (extended) after leaving their original radial plane, introducing the unwanted circumferential forces mentioned above. As a reminder, the compressed (shortened) springs do not transmit any load, as Daidié's mechanism uses tension-only springs.

These unwanted circumferential forces introduce some errors in load distribution and radial load-carrying capacity. The latter is defined based on the most loaded contact point. The residual forces introduced by Daidié's mechanism can reduce the load on the most loaded ball and, when simulating a case such as that shown in Figure 3.39, the maximum load obtained could be less than the real one. Incorrect load distribution would result in inaccurate stiffness results for the bearing. In particular, the bearing would show greater radial stiffness, as shown in Figure 3.39, as the springs align with the radial load.

Although this effect is already known [12], no research work in literature quantifies the inherent limitations.

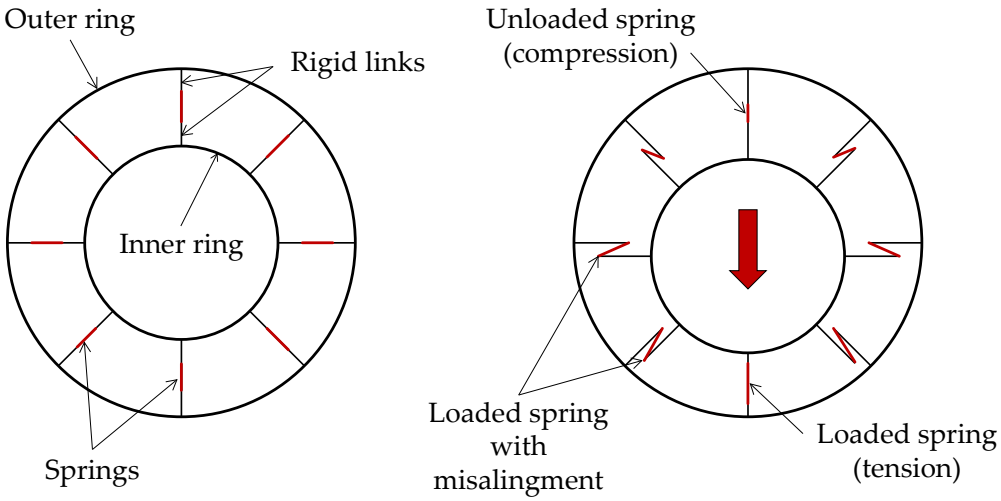

Figure 3.39. Graphical representation of the out-of-plane displacement of the springs of Daidié's mechanism.

To analyse the error introduced by Daidié's mechanism, the same as the one used for the blade-bearing-hub assembly has been used, modelled with FE and replacing the balls with the mechanism, as shown above in Figure 3.5, together with the model mesh. In this case, instead of modelling the whole assembly, two rigid flanges have been used to allow the opening or the sliding of the joint and make the results independent from the flexibility of the adjacent structures. These flanges are joined to the bearing rings using bolted connections, which are modelled with beams and pretension elements, and a rigidly connected remote point to apply the external displacement to the inner bearing. Thus, a fixed boundary condition is imposed on the opposing flange face that connects to the bearing outer ring. Just as in the previous assembly model, only half of the bearing has been modelled, taking advantage of the symmetry of the geometry, the boundary conditions and the loads.

The FE model described above has been used to study the load distribution for three pure displacement cases, i.e. axial, radial and tilting. The results confirm that Daidié's mechanism remains on the unaltered radial plane in the case of axial and tilting displacements. Hence, no forces are exerted on the springs in the circumferential direction in either case and it is confirmed that the mechanism operates flawlessly. Thus, no results for these cases are shown.

Figure 3.40 shows the results for the load distribution under pure radial displacement, which corresponds to a radial force significantly lower than the load rating of the bearing, which is common in normal operating conditions. Figure 3.40 shows that the maximum residual force occurs between 50° and 60° of the angular position of the balls, reaching a 7% of the maximum contact load. The maximum misalignment of the springs occurs at 90°, as anticipated in Figure 3.39. It causes a deviation of 7° with respect to the original plane containing the springs, which is approximately three times the contact angle variation obtained. Moreover, in the two graphs in Figure 3.40, it can be seen that some springs are loaded beyond 90°. This is not consistent with a real bearing under pure radial displacement, as these balls would have lost contact with the raceways.

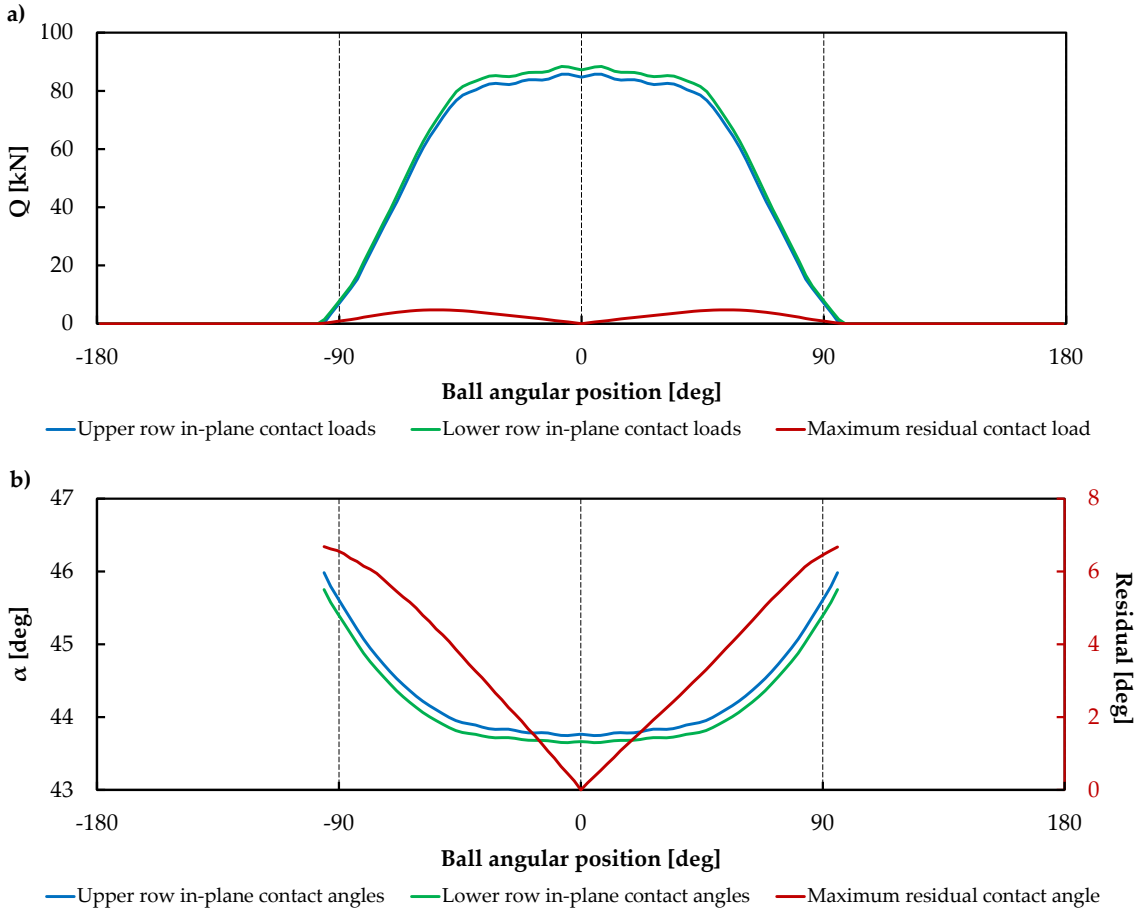

Figure 3.40. Load distribution and spring angles for radial load case of Daidié's mechanism.

All of this shows that Daidié's mechanism can yield inaccurate load distribution results. However, even if the residual forces and the misalignments of the springs have been quantified, this is not enough to assess the true impact on the load distribution or bearing stiffness. Accordingly, an improvement that

avoids the above limitations so that the results can be compared with those presented in this section is presented below.

3.5.2 Improvement on Daidié's mechanism implementation

Two methods are proposed below to correctly implement Daidié's mechanism and overcome the previous limitations:

- The first method prevents the mechanism from leaving the original radial plane, thereby avoiding the source of the problem. This method relies on not embedding the rigid beams of the mechanism in the contact surfaces (see Figure 3.5 and Figure 3.39). Instead, only the DoFs corresponding to the motion within the radial plane are coupled, which means the axial and radial displacements and the in-plane rotation. As a result, the model contains two overlapping nodes for each rigid link, one from the raceway and one from the beam. Each node has its own 6 DoF, and only the aforementioned DoF are coupled between them (see Figure 3.41). The remaining DoF related to the out-of-plane displacements and rotations are decoupled from the movement of the inner ring (displaced one) and instead are embedded in the outer ring (fixed one). This prevents the nodes from leaving the original plane, avoiding any rigid solid motion.

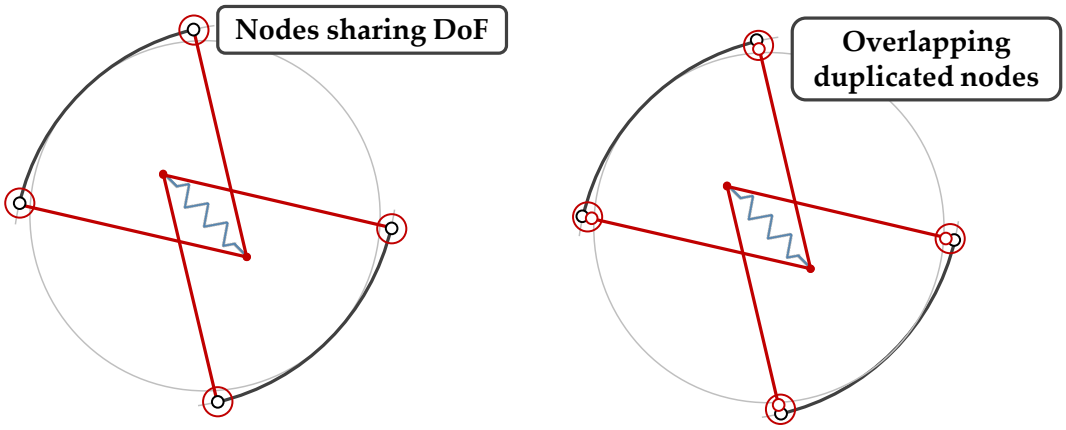

Figure 3.41. Implementation of Daidié's mechanism in FE model.

It could be argued that the implementation of the new mechanism transmits forces even if the contact faces are not directly opposed. This may result in errors, as the same ball cannot be in contact with both faces simultaneously once they are displaced. Note that the bearing is being studied under static load in a stationary condition and the relative misalignments between the rings are significantly smaller than the size of the rolling element.

Consequently, this hypothetical source of error can be disregarded, as indicated in the results section.

- Another approach to address the limitations of Daidié's mechanism limitations is implementing it in an analytical model. This way, the mechanism would define the elastic behaviour of the contact and the flexibility of the rings could be taken into account using stiffness matrices. Zupan and Prebil [165] proposed this procedure initially, with Olave et al [74] following it. Later, Heras et al. [12] would propose a similar method based on minimising potential energy. This work also mentioned the limitations of Daidié's mechanism. The analytical procedure only focuses on the DoF in the radial plane of each mechanism, therefore the out-of-plane motions are not considered. The latter work proposes to use the superelement technique with an FE model to compute the stiffness matrix of the rings, reducing the elastic behaviour of the rings to the centres of the raceways. While this second proposal does not introduce a new approach, it has been included to complete the analysis of the problem and available solutions, in addition to comparing this alternative to the first one.

The second approach allows for much faster simulations, even when the stiffness matrices are calculated using a sector FE model, as suggested in [12]. Despite this, the procedure has one main drawback: to calculate the stiffness matrices of the rings, linear elastic behaviour of the rings and the boundary conditions must be assumed. However, there are certain cases, as the one examined in previous sections involving a bolted joint with frictional contact, which cannot be modelled directly. Instead, these must be linearised by using simplifications such as *bonded connections*, but this may lead to inaccuracies.

Finally, this procedure is more challenging to formulate and code than an FE analysis, and while it is clearly advantageous in the long run, it is more expensive to implement in a standard design workflow.

3.5.3 Simulations results

Here the load distribution and radial stiffness results presented above are compared with those obtained using the method proposed in the previous section, to assess and quantify the limitations of the original Daidié's mechanism.

However, in this case, the second method proposed in the previous section is not applicable to this case of study, given that the bolted connection is not linear.

Figure 3.42 shows the results for the original implementation of the mechanism (Figure 3.41a) represented by dots, while those obtained from the proposed method (Figure 3.41b) are represented by lines. This figure shows how the springs of the new implementation are no longer loaded from 90° onwards.

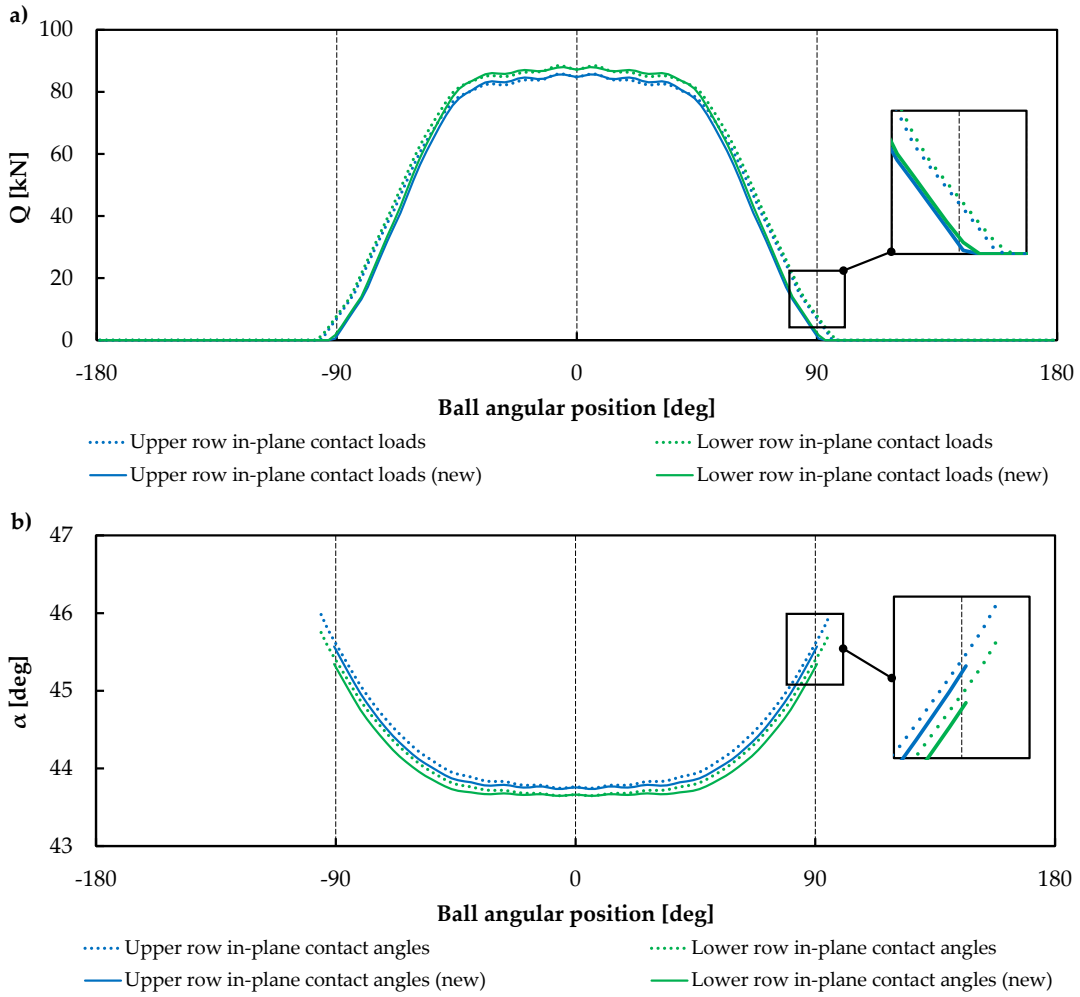

Figure 3.42. Load distribution under applied radial force with the corrected Daidié's mechanism (new).

Figure 3.42a shows how there is a discrepancy from 50° onwards between the old and new contact loads, with this difference increasing until it reaches its maximum at 90°. However, this corresponds to the least loaded balls, while the loads do not vary significantly for the most loaded ones (from 0° to 50°). Given that the load-carrying capacity of the bearing relies on the most loaded rolling element, the corrected implementation of Daidié's mechanism does not provide

any advantage in this respect. Moreover, focusing on the contact angle distribution results (Figure 3.42b), the identified differences are also minimal.

On the other hand, significant differences can be seen in the radial stiffness curves shown in Figure 3.43. As expected, the stiffness of the bearing with the original implementation of Daidié's mechanism is greater. In this case, the discrepancy is up to 5% before the flange slips (vertical dotted line), which increases up to 7% at higher radial displacements. It can be seen how from the point where the slippage occurs, the stiffness behaviour is no longer linear.

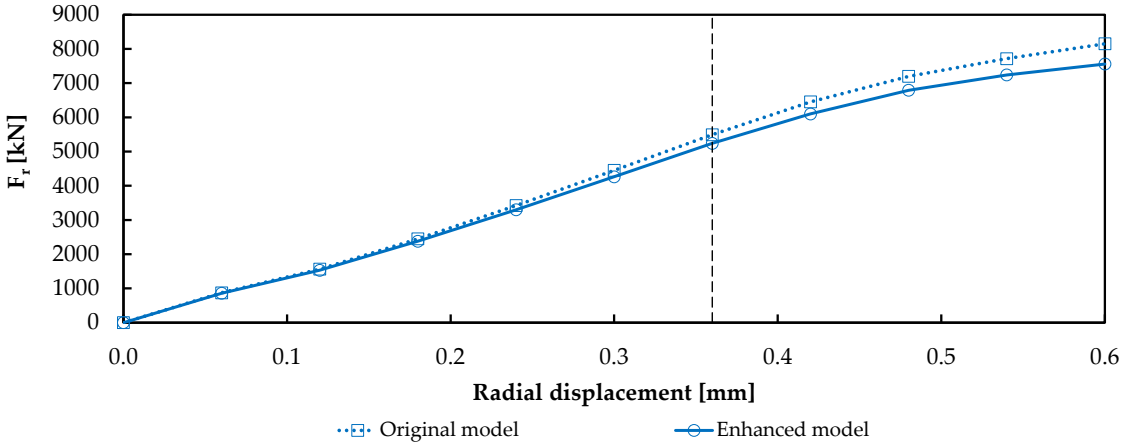

Figure 3.43. Radial stiffness curves.

3.6 Conclusions and additional remarks

After carrying out several studies to improve the modelling of slewing bearings, both on their own and for blade-bearing-hub assemblies, different aspects of the methodology to be followed have been clarified, allowing the structural analyst to select more accurate but slow, or faster but inaccurate modelling techniques, aware of the trade-offs involved. A summary of the conclusions obtained from the work are summarised below:

- It is concluded that, although using the Daidié mechanism results in some inaccuracies when calculating the load distribution in four-point contact bearings, it only affects the least loaded part of the bearing contacts. Therefore, its impact on the load-carrying capacity is negligible. However, its effect on the stiffness of the bearing is relevant, as it increases the radial stiffness. More specifically, for a wind turbine blade bearing, the study reveals that the radial stiffness can be increased by up to 5% before the

joint slides. In fact, this difference increases once the joint starts to slide. Consequently, it is found that the limitations of Daidié's mechanism are marginal to some extent; nevertheless, they cannot be neglected if a precise estimation of the radial stiffness is required. In addition, two alternatives for implementing the mechanism properly are presented, which avoid these limitations in both FE and analytical models.

- Since the friction torque is primarily influenced by the less loaded balls, the new Daidié's mechanism implementation provides a direct improvement to the friction torque calculation. To achieve this, an FE model combined with the new implementation is used to solve the load distribution problem. Subsequently, an analytical model, such as the one used in the current thesis, can be used to solve the friction torque problem.

- It is concluded that the effect of modelling the bolted joints and their corresponding preload with simplification techniques, such as using rigid joints between components, is negligible as far as displacements and deformations are concerned. However, the load distribution can be affected in cases where the bearing is being analysed under extreme loads. These conclusions are significant in that the modelling and calculation time is reduced during the early design stages, with these components not needing to be modelled until the more advanced stages for more precise analyses.

- It has been seen that replacing the blade material with steel affects both the load distribution and the displacements and deformations. Therefore, it has been verified that it is important to use real blade materials for the analyses and experimental tests.

- Bearing simplification techniques have been studied by replacing the bearing with three springs to represent its stiffness. This type of simplification does not represent the true effects of how loads are transmitted and the resulting global displacements and deformations. This is significant because, in dynamic analyses of bladed wind turbine models, it is common practice to replace the bearing for its stiffness matrices. For these analyses, this simplification may be required due to the large number of elements to be modelled and the computational cost involved. However, it has been shown that the manner in which the loads

are transmitted from the blade through the bearing does not represent reality with these types of modelling techniques, leading to results in the regions adjacent to the bearing that are not completely reliable. Although these techniques are appropriate for global models focusing on the dynamic analysis of the whole turbine, they are not suitable for more local analyses such as the blade-bearing-hub assembly studied in this thesis.

4 An engineering approach for the friction torque calculation

4.1 Introduction

Slewing bearings are commonly used for orientation purposes in many applications, like in tower cranes or wind turbine generators. In these cases, having a tool to predict the friction torque becomes essential for assessing bearing performance and reliability, as well as for correctly sizing the drive system. In addition, the friction torque can be used as a quality control indicator: a big difference from the reference value may indicate problems during manufacturing or the assembly process.

Therefore, as described in Chapter 1 and according to the aforementioned state-of-the-art approaches, complex models are required to obtain reliable results of the friction torque as a function of external loads. In Chapter 2, it was shown how these models can provide more accurate results than the NREL formula [49], i.e. implementing the preload scatter in the analytical model from Joshi et al. [124]. However, these require more effort when it comes to their practical implementation. In the literature, there are no methods by which to assess the friction torque for these bearings that is both accurate (as state-of-the-art methods) and practical (as simple formulae) for potential users. This chapter proposes a way to solve this issue, offering an easy-to-use tool in the form of friction torque maps. These maps can be useful either for bearing manufacturers to determine the manufacturing parameters in order to reach the desired frictional behavior and for applications engineers who intend to select the best bearing for their application.

The proposal consists of performing calculations with state-of-the-art models, covering all the design space, accordingly creating a sufficiently well populated database that could be used to calculate the friction torque for any geometry and

load condition by interpolation. Nonetheless, a major challenge arises with the first approach: the high number of parameters involved in the problem. In this regard, normalising the friction torque as was done for the external loads with respect to the load carrying capacity in [8,20] would allow friction torque results to be stored compactly. The more design parameters successfully included in the normalisation, the more compact the result set. In this sense, the friction torque should be normalised with respect to as many parameters as possible, without compromising accuracy.

According to the described approach, this work proposes a normalised expression for the friction torque so that it turns out to be independent of bearing macrogeometry (ball size, pitch diameter and number of balls) and a coefficient of friction adopted to represent the actual mixed lubrication regime, as originally assumed by Jones in [120] (which is fairly acceptable for low-speed applications). Thus, the normalised friction torque proposed in this work only depends on six variables. On the one hand, the bearing microgeometry, which is given by three parameters: the osculation ratio, the initial contact angle, and the preload of the balls (ball-raceway geometrical interference). On the other hand, an external load system, defined by the axial load, the radial load and a tilting moment aligned with the radial load, all of them normalised with respect to the axial load capacity, which makes the approach consistent with previous research works [8,20]. Many simulations are performed, considering multiple combinations of the microgeometrical parameters and normalised loads, defined on the basis of a well-founded Design of Experiments (DoE). Rigid rings are assumed for the simulations, since ring deformations depend on the flexibility of the surrounding structures, which varies from one application to another. The results of the DoE are interpolated along the aforementioned six variables and filtered to create normalised friction torque maps. These friction torque maps represent the main contribution of this research work along with the very definition of the normalised friction torque. The maps can serve as a practical tool to estimate the friction torque of any four-point contact slewing bearing in early design stages; something that is useful for both bearing customers and manufacturers. The practical focus of the approach also means that is can be implemented in standards or in design guidelines. Moreover, the database the friction torque maps are based on can be also used and specifically interpolated to develop computer applications, so that the friction torque calculation is automatic.

4.2 Methodology

The purpose of the work in this section is to obtain normalised friction torque maps and, in order to do so, a large number of simulations are required. In this work, the approach by Joshi et al. is used [124] as a reference to calculate the friction torque along with the modification of the initial kinematics proposed by Heras [25] to systematically ensure the convergence of the model. This allows the load distribution problem to be decoupled from the friction torque problem.

Accordingly, the first step is to solve the load distribution problem for all the combinations of the geometrical parameters and external loads. In order to do this, the analytical approach proposed by Aguirrebeitia et al. [8,20] is used, established on the basis of contact geometrical interferences, while rigid rings are assumed (see Section 4.2.1). This approach normalises external loads with respect to load-carrying capacity. The normalisation includes the ball size, the pitch diameter of the ball set and the number of balls. This way, the load distribution is assessed only for various combinations of three microgeometrical parameters (preload level, osculation ratio and initial contact angle).

Subsequently, the friction torque is computed for these load distributions. However, the purpose of this work is to provide a streamlined approach to estimate the friction torque under specific load combinations and for any bearing design. To this end, the possibility of normalising the friction torque with respect to the same normalising parameters used in the previous step is proposed and verified (see Section 4.2.2). Reducing geometrical parameters by means of normalisation considerably reduces the amount of simulations, and thus, the computational cost.

Finally, the procedure to validate the normalisation and the interpolated results together with the generation of the friction torque maps is further detailed in Section 4.2.3, where the authors aim to give the reader an overview of the workflow.

4.2.1 Load distribution problem

Aguirrebeitia et al. [8,20] presented a geometrical interference based ball-raceway load distribution model. In that model the external loads were normalised with respect to the axial load-carrying capacity (C_{0a}) of the bearing. This approach allowed for the removal of the ball diameter (D_w), the pitch

diameter of the bearing (D_{pw}) and the number of balls (Z) from the force equilibrium equations for the case in which $D_{pw} \gg D_w$. Thus, the bearing was defined by the initial contact angle (α_0), osculation ratio (s) and preload level (p). The preload level was defined as the ratio between the initial ball-raceway interference (δ_p) and the deformation limit (δ_{lim}) of the ball, set out as:

$$p = \delta_p / \delta_{lim} \tag{4.1}$$

$$\delta_{lim} = 0.005465\,(1 - s)^{-0.182}\,D_w \tag{4.2}$$

Where δ_{lim} is defined as the ball-raceway maximum contact deformation that depends on the ball size and the osculation ratio, to reach a maximum contact pressure of 4200 MPa [45]. This simplified expression was derived from by Houpert's work [60] for the case of balls and raceways made of steel (E = 200 GPa) and osculation ratios (s) ranging from 0.886 to 0.992. It should be noted that the ball-raceway contact deformation refers to the sum of the deformations in the two contact zones between the ball and the two raceways.

According to [8,20], the load distribution problem could be normalised via three macrogeometric "normalising parameters" (D_w, D_{pw} and Z), and remained dependent on another three microgeometric "non-normalising parameters" (p, s and α_0). In this work, the load distribution problem is solved using the model developed by Aguirrebeitia outlined in Figure 4.1, where the normalised axial (δ_a/δ_{lim}), radial (δ_r/δ_{lim}) and angular ($\delta_\theta/\delta_{lim}$) displacements, together with the non-normalising parameters, are inputs of the load distribution problem, as outlined in Table 4.1.

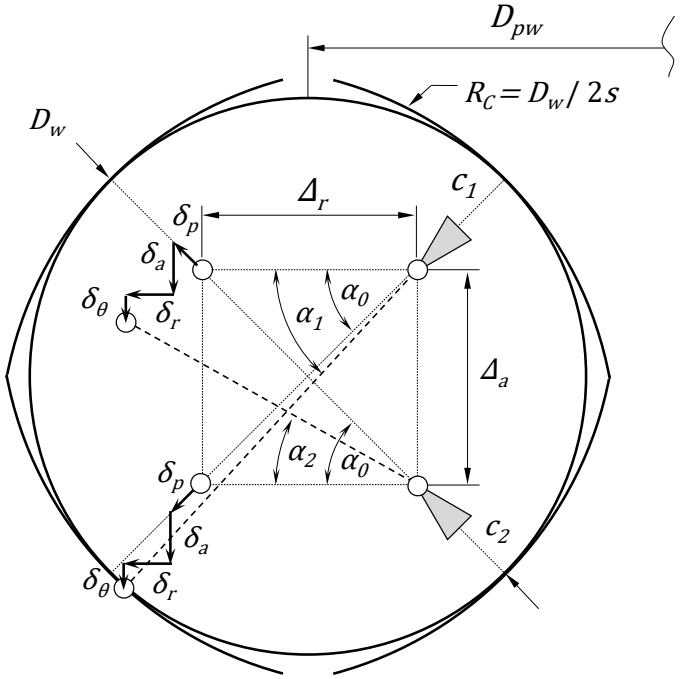

Figure 4.1. Geometrical interference model parameters [8].

Table 4.1. Inputs of the load distribution problem.

	Normalised displacements			**Non-normalising parameters**		
	Axial	***Radial***	***Angular***	***Preload level***	***Osculation ratio***	***Initial contact angle***
Symbol	$\delta_a^n = \frac{\delta_a}{\delta_{lim}}$	$\delta_r^n = \frac{\delta_r}{\delta_{lim}}$	$\delta_\theta^n = \frac{\delta_\theta}{\delta_{lim}}$	$p = \frac{\delta_p}{\delta_{lim}}$	s	α_0

This way, the interference model equations are as follows:

$$\Delta_a^n \equiv \frac{\Delta_a}{\delta_{lim}} = \left(182.98 \frac{(1-s)^{1.182}}{s}\right) sin\, \alpha_0 \tag{4.3}$$

$$\Delta_r^n \equiv \frac{\Delta_r}{\delta_{lim}} = \left(182.98 \frac{(1-s)^{1.182}}{s}\right) cos\, \alpha_0 \tag{4.4}$$

$$\frac{\delta_{1,\psi}}{\delta_{lim}} = \sqrt{\left(\Delta_a^n + p\, sin\, \alpha_0 + \delta_a^n + \delta_\theta^n\, cos\, \psi\right)^2 + \left(\Delta_r^n + p\, cos\, \alpha_0 + \delta_r^n\, cos\, \psi\right)^2} - \sqrt{\left(\Delta_a^n + \Delta_r^n\right)^2} \tag{4.5}$$

$$\frac{\delta_{2,\psi}}{\delta_{lim}} = \sqrt{\left(\Delta_a^n + p\,sin\,\alpha_0 - \delta_a^n - \delta_\theta^n\,cos\,\psi\right)^2 + \left(\Delta_r^n + p\,cos\,\alpha_0 + \delta_r^n\,cos\,\psi\right)^2} - \sqrt{\left(\Delta_a^n + \Delta_r^n\right)^2} \tag{4.6}$$

$$\alpha_{1,\psi} = atan\left(\frac{\Delta_a^n + p\,sin\,\alpha_0 + \delta_a^n + \delta_\theta^n\,cos\,\psi}{\Delta_r^n + p\,cos\,\alpha_0 + \delta_r^n\,cos\,\psi}\right) \tag{4.7}$$

$$\alpha_{2,\psi} = atan\left(\frac{\Delta_a^n + p\,sin\,\alpha_0 + \delta_a^n + \delta_\theta^n\,cos\,\psi}{\Delta_r^n + p\,cos\,\alpha_0 + \delta_r^n\,cos\,\psi}\right) \tag{4.8}$$

Where Δ_a and Δ_r are the initial axial and radial distances between raceway curvature centres, and $\delta_{i,\psi}$ and $\alpha_{2,\psi}$ are, the contact deformation and the contact angle, respectively, on contact diagonal i for a ball located in azimuthal position ψ, as shown in Figure 4.1. The axial load-carrying capacity used in the work performed by Aguirrebeitia was defined as the axial load for which the ball-raceway contact pressure reached 4200 MPa, considering that the contact angle varies with the external load. However, in this work, the axial load-carrying capacity is conveniently defined as in ISO-76 [45], for which the contact angle does not vary with axial load. This leads to equations similar to those presented by Aguirrebeitia in [8,20]:

$$K = \frac{31191.35\,D_w^{1/2}}{(1-s)^{0.3621}} \tag{4.9}$$

$$C_{0a} = ZK\delta_{lim}^{3/2}\,sin\,\alpha_0 \tag{4.10}$$

$$F_a^n \equiv \frac{F_a}{C_{0a}} = \frac{1}{2\pi\,sin\,\alpha_0}\left(\int_{\delta^+}\left(\frac{\delta_{1,\psi}}{\delta_{lim}}\right)^{\frac{3}{2}} sin\,\alpha_{1,\psi}\,d\psi - \int_{\delta^+}\left(\frac{\delta_{2,\psi}}{\delta_{lim}}\right)^{\frac{3}{2}} sin\,\alpha_{2,\psi}\,d\psi\right) \tag{4.11}$$

$$F_r^n \equiv \frac{F_r}{C_{0a}} = \frac{1}{2\pi\,sin\,\alpha_0}\left(\int_{\delta^+}\left(\frac{\delta_{1,\psi}}{\delta_{lim}}\right)^{\frac{3}{2}} cos\,\alpha_{1,\psi}\,cos\,\psi\,d\psi + \int_{\delta^+}\left(\frac{\delta_{2,\psi}}{\delta_{lim}}\right)^{\frac{3}{2}} cos\,\alpha_{2,\psi}\,cos\,\psi\,d\psi\right) \tag{4.12}$$

$$M^n \equiv \frac{M}{D_{pw}C_{0a}} = \frac{1}{4\pi \sin\alpha_0}\left(\begin{array}{l}\int_{\delta^+}\left(\frac{\delta_{1,\psi}}{\delta_{lim}}\right)^{\frac{3}{2}} \sin\alpha_{1,\psi}\cos\psi\, d\psi - \\ \int_{\delta^+}\left(\frac{\delta_{2,\psi}}{\delta_{lim}}\right)^{\frac{3}{2}} \sin\alpha_{2,\psi}\cos\psi\, d\psi\end{array}\right) \tag{4.13}$$

Where K in (4.9) is the coefficient that establishes the nonlinear relationship between the load and the contact deformation (again, for steel material properties and osculation ratios from 0.886 to 0.992). Table 4.2 shows the outputs of the normalised load distribution problem for ball-raceway contact diagonal i. The ball-raceway contact load is derived from these outputs, which is required to arrange the expression of the normalised torque in Section 4.2.2:

$$Q_{i,\psi} = K\left(\frac{\delta_{i,\psi}}{\delta_{lim}}\cdot\delta_{lim}\right)^{3/2} = K\delta_{i,\psi}^{3/2} \tag{4.14}$$

Table 4.2. Outputs of the load distribution problem.

			Normalised loads		
	Ball contact deformations	***Ball contact angles***	***Axial force***	***Radial force***	***Tilting moment***
Symbol	$\frac{\delta_{i,\psi}}{\delta_{lim}}$	$\alpha_{i,\psi}$	$F_a^n = \frac{F_a}{C_{0a}}$	$F_r^n = \frac{F_r}{C_{0a}}$	$M^n = \frac{M}{D_{pw}C_{0a}}$

At this point, the choice of the axial load-carrying capacity as a normalising factor needs to be adequately justified. The main reason is that it is easily obtained, since it is always provided in the catalogues, or can even be easily calculated by applying the standards [45]. Of course, the dynamic capacity (or even the fatigue limit) could also have been used for this purpose, for example, but considering the working regime of these components, the static capacity was deemed to be more suitable. The point is that, in either case, the approach would be equally valid, as long as all these normalising factors represent reasonable reference forces.

4.2.2 Friction torque problem: normalised torque

The friction torque of the bearing is computed as the sum of the contribution of each ball in contact with the raceways. The purpose of here is to normalise the

friction torque with at least the same parameters Aguirrebeitia used to normalise the load distribution. According to Heras [24], in the case of bearings with $D_{pw} \gg D_w$ working under quasi-static conditions, and considering full sliding in all the ball-raceway contacts, contribution T_i of a ball i to the total friction torque can be expressed as:

$$T_i = \frac{3\mu}{2\pi}\left(\begin{matrix} Q_{1,i}\int_0^{2\pi}\int_0^1 \rho\sqrt{1-\rho^2}\,cos\,\gamma_{1,i}\,r_{1,i}^{ap}\,d\rho d\theta + \\ Q_{2,i}\int_0^{2\pi}\int_0^1 \rho\sqrt{1-\rho^2}\,cos\,\gamma_{2,i}\,r_{2,i}^{ap}\,d\rho d\theta \end{matrix}\right) \tag{4.15}$$

Where ρ and θ are integration variables of the contact ellipses and, for ball i and contact point j in the outer ring (j = 1,2), $Q_{j,i}$ is the normal contact load, $\gamma_{j,i}$ is the angle which defines the direction of the shear stresses determined by the relative speeds as it was defined by Leblanc and Nelias [122,123], and $r_{j,i}^{ap}$ is the distance between the friction force differential application point and the axis of the bearing. Expression (4.15) depends on the coefficient of friction μ, the loads on the contact points, and the kinematics of the ball sandwiched between the raceways, which depends on parameters p, s, α_0, D_{pw} and D_w [24,25].

As far as the coefficient of friction μ is concerned, it can be easily demonstrated from [123] that the kinematics does not depend on μ under quasi-static motion and full sliding on all the contacts. This means that, under these assumptions, T_i is fully proportional to the coefficient of friction μ, and therefore the integrals in (4.15) do not depend on it.

For the studied case, where $D_{pw} \gg D_w$, the following approximation can be further assumed:

$$r_{j,i}^{ap} = \frac{D_{pw}}{2} \tag{4.16}$$

This simplification was not assumed in [24] but, for normalisation purposes, it is a very convenient approximation with no appreciable lack of accuracy. Thus, substituting this expression in (4.15):

$$T_i = \frac{3\mu D_{pw}}{4\pi}\begin{pmatrix} Q_{1,i}\int_0^{2\pi}\int_0^1 \rho\sqrt{1-\rho^2}\,cos\,\gamma_{1,i}\,d\rho d\theta + \\ Q_{2,i}\int_0^{2\pi}\int_0^1 \rho\sqrt{1-\rho^2}\,cos\,\gamma_{2,i}\,d\rho d\theta \end{pmatrix} \tag{4.17}$$

Next, the friction torque of the bearing is arranged by the sum of the contribution of each ball, which leads to the next expression:

$$T = \frac{3\mu D_{pw}}{4\pi}\sum_{i=1}^{Z}\left[\begin{pmatrix} Q_{1,i}\int_0^{2\pi}\int_0^1 \rho\sqrt{1-\rho^2}\,cos\,\gamma_{1,i}\,d\rho d\theta + \\ Q_{2,i}\int_0^{2\pi}\int_0^1 \rho\sqrt{1-\rho^2}\,cos\,\gamma_{2,i}\,d\rho d\theta \end{pmatrix}\right] \tag{4.18}$$

Substituting the loads with the ball-raceway contact deformations by using (4.14):

$$T = \frac{3\mu D_{pw}K}{4\pi}\sum_{i=1}^{Z}\left[\begin{pmatrix} \delta_{1,i}^{3/2}\int_0^{2\pi}\int_0^1 \rho\sqrt{1-\rho^2}\,cos\,\gamma_{1,i}\,d\rho d\theta + \\ \delta_{2,i}^{3/2}\int_0^{2\pi}\int_0^1 \rho\sqrt{1-\rho^2}\,cos\,\gamma_{2,i}\,d\rho d\theta \end{pmatrix}\right] \tag{4.19}$$

The same approach used in the load distribution model δ_{lim} is implemented. Also, transforming the summation into an integral dependent on the angular position of the balls, the expression becomes independent from the number of balls Z, as in [36] and [8,20] for the internal load distribution by using the concept of load distribution integral by Jones and Harris [36]. Thus, the expression becomes as follows:

$$T = \frac{3\mu D_{pw}KZ\delta_{lim}^{3/2}}{8\pi^2}\int_{\delta_+}\left[\begin{matrix} \left(\frac{\delta_{1,\psi}}{\delta_{lim}}\right)^{3/2}\int_0^{2\pi}\int_0^1 \rho\sqrt{1-\rho^2}\,cos\,\gamma_{1,\psi}\,d\rho d\theta + \\ \left(\frac{\delta_{2,\psi}}{\delta_{lim}}\right)^{3/2}\int_0^{2\pi}\int_0^1 \rho\sqrt{1-\rho^2}\,cos\,\gamma_{2,\psi}\,d\rho d\theta \end{matrix}\right] d\psi \tag{4.20}$$

Reordering the expression and introducing the axial load-carrying capacity (4.10):

$$T^n \equiv \frac{T}{\mu D_{pw} C_{0a}} =$$
$$= \frac{3}{8\pi^2 \sin\alpha_0} \int_{\delta_+} \left[\begin{matrix} \left(\frac{\delta_{1,\psi}}{\delta_{lim}}\right)^{3/2} \int_0^{2\pi} \int_0^1 \rho\sqrt{1-\rho^2}\cos\gamma_{1,\psi} d\rho d\theta + \\ \left(\frac{\delta_{2,\psi}}{\delta_{lim}}\right)^{3/2} \int_0^{2\pi} \int_0^1 \rho\sqrt{1-\rho^2}\cos\gamma_{2,\psi} d\rho d\theta \end{matrix} \right] d\psi \quad (4.21)$$

Where $\cos\gamma_{i,\psi}$ is still dependent on geometrical parameters that have been well defined in other works such as Leblanc and Nelias [122,123]:

$$\cos\gamma_{i,\psi} = f(D_w, D_{pw}, p, \alpha_0, s) \quad (4.22)$$

4.2.3 Procedure to obtain and validate the friction torque maps

Expression (4.21) can be understood as a dimensionless normalised friction torque, where the effects of some parameters have been completely removed (μ and Z), while the expression is still dependent on parameters p, s, α_0, D_{pw} and D_w apart from the external displacement space. In fact, successfully removing the effect of p, s and α_0 parameters is a very challenging task, since the term $\cos\gamma_{i,\psi}$ in expressions (4.21) and (4.22) is highly non-linearly dependent on them [25]. Nonetheless, a detailed analysis of expression (4.22) reveals that the effect of D_{pw} and D_w could be isolated under certain assumptions.

In this regard, in Section 4.3 the effect of parameters D_{pw} and D_w on the obtained normalised friction torque expression (4.21) is studied within the scope of slewing bearings. The purpose of this study is to check whether the effect of these two parameters is significant or, contrarily, it can be neglected. This is done by means of a DoE (defined in Section 4.3.1) that analyses the effect of the D_{pw}/D_w ratio (see Section 4.3.2). Should this effect be negligible, only the three microgeometrical parameters would affect the normalised friction torque, i.e. p, s and α_0; therefore D_{pw} and D_w would become normalising parameters.

Once the proposed expression of the friction torque is validated in Section 4.3, a second DoE is performed in Section 4.4 to obtain the sought friction torque maps. These maps will represent the effect of the non-normalising parameters and normalised external loads on the normalised friction torque. Prior to conducting this DoE (defined in Section 4.4.1), a study is performed to search for symmetries and patterns on the displacement space in order to perform a

computationally cost-effective analysis. The DoE results are interpolated in the load space and filtered for each non-normalising parameter combination (Section 4.4.2). Subsequently, the obtained interpolated results are compared to the calculation model presented by Joshi et al. [124] and the NREL formula [49] with validation purposes (Section 4.4.3). The interpolated results are then represented by heatmaps called "normalised friction torque maps", and their use is explained in Section 4.5.

4.3 Validating the normalisation

This section describes the procedure by which to validate the proposed normalisation of the friction torque and thus, the normalising parameters.

4.3.1 DoE to validate the normalisation

Hereafter, the effect of parameters D_{pw} and D_w on the normalised friction torque is quantified and Table 4.3 shows the selection of seven normalised displacement cases for this purpose. These cases are selected to cover different displacement combination scenarios.

Table 4.3. Displacement cases of the DoE to validate the normalisation.

	Displacement case						
	1	***2***	***3***	***4***	***5***	***6***	***7***
$\boldsymbol{\delta_a^n}$	1	0	0	½	½	0	⅓
$\boldsymbol{\delta_r^n}$	0	1	0	½	0	½	⅓
$\boldsymbol{\delta_\theta^n}$	0	0	1	0	½	½	⅓

The design space defined in [10] is used to evaluate the range of geometries for which the normalisation is valid (in terms of D_{pw} and D_w), which is based on catalogues from various slewing bearing manufacturers, with the upper and lower limits indicated in Figure 4.2. Several combinations of D_{pw} and D_w have been grouped around two reference bearings, selected based on their dimensions in various applications, such as robotics or medical equipment for small sizes, and cranes, wind turbines or space applications for large sizes.

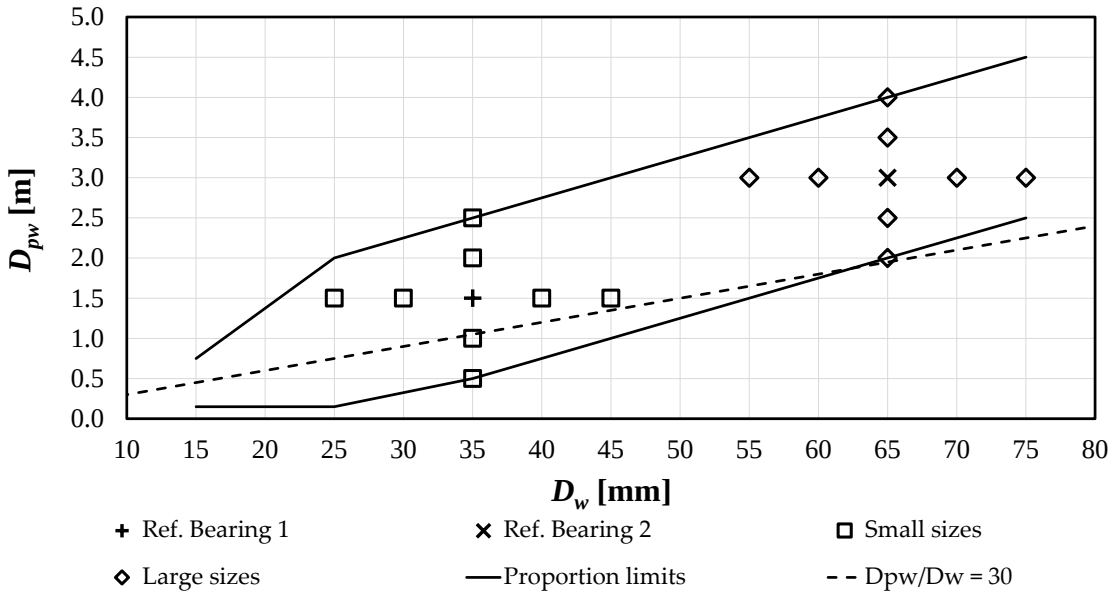

Figure 4.2. Selected D_{pw} and D_w combinations considering bearing size and ball size proportion limits.

For the calculated cases, reference values for the non-normalising parameters ($s = 0.94$, $p = 0$ and $\alpha_0 = 45°$) are set to calculate the normalised friction torque. Then, the relative error is calculated for each case with respect to the normalised friction torque of the reference bearings.

4.3.2 Application range of the normalisation

Figure 4.3 shows the results of the calculations for the validation described in Section 4.3.1. This figure represents the error introduced in the normalisation for each D_{pw} and D_w value. The results showed that the D_{pw}/D_w ratio was more significant to represent the error introduced during the normalisation, so this is how the results are represented in the plot.

It can be seen that the inaccuracy introduced by the normalisation with respect to D_w and D_{pw} is less than 2% in all cases, provided that the D_{pw}/D_w ratio is greater than 30 (see dashed line in Figure 4.2). In fact, the plotted data in Figure 4.2 shows that the majority of slewing bearings from catalogues have ratios greater than this value. Furthermore, the dotted data line in Figure 4.3, which represents an estimate of the upper bound of the committed error, shows how the error from normalisation falls as the value of this ratio increases.

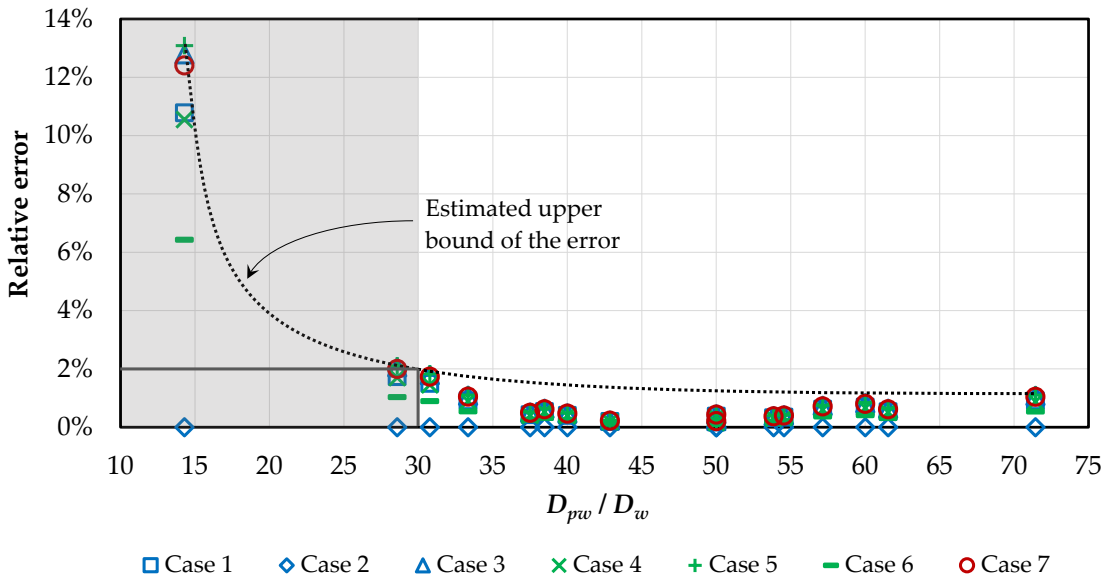

Figure 4.3. Relative error in the normalised friction torque as a function of the D_{pw}/D_w ratio.

Therefore, it can be assumed that the normalised friction torque is independent of these two parameters, provided that $D_w \ll D_{pw}$. This means that D_w and D_{pw} are normalising parameters of the normalised friction torque with minor limitations. Therefore, the following can be stated:

- The normalised friction torque depends on the same non-normalising parameters that affect the load distribution.
- It is sufficient for the normalising parameters D_{pw} and D_w to take a reference value for the normalised friction torque simulations.

4.4 Obtaining the friction torque maps

This section describes the steps followed to create the normalised friction torque maps. To do so, a detailed analysis of the design space is conducted and the DoE is defined in an initial (see Section 4.4.1). Then, the simulations planned in the DoE are performed and the obtained results are interpolated, obtaining the desired friction torque maps (see Section 4.4.2). Finally, the interpolated results are validated by comparing them with other friction torque calculation approaches (see Section 4.4.3). The friction torque maps for the whole design space are given in the Appendix.

4.4.1 DoE to obtain the friction torque maps

As stated above, the purpose of this work is to provide a friction torque calculation tool, in the form of a collection of friction torque maps. These maps will relate the normalised friction torque with the normalised external loads of a bearing. However, the analytical approach used to solve the load distribution problem (explained in Section 4.2.1) calculates bearing forces as a function of the bearing normalised displacements and the non-normalising parameters; this is indeed, the first step in the procedure to obtain the friction torque maps (Step 1 in Figure 4.4). Subsequently, the normalised friction torque is computed based on the displacement space (Step 2 in Figure 4.4). It must be recalled that, to solve the normalised friction torque problem, the normalising parameters must be set with some reference values. To this end, the following ones were adopted, coinciding with one of the reference bearings in Figure 4.2: $D_{pw} = D_{pw}^{ref} = 1500$ mm and $D_w = D_w^{ref} = 35$ mm. Finally, the normalised friction torque results obtained in Step 2 are related with the normalised external loads from Step 1, together with the non-normalising parameters. All this data is appropriately arranged and presented as friction torque maps (Step 3 in Figure 4.4).

To achieve the desired friction torque maps, a structured set of calculations must be performed. This is obtained by means of a DoE, in which the levels of the normalised displacements and non-normalising parameters are defined. Figure 4.4 shows the flowchart of the calculation sequence, detailing the inputs and outputs of each step. The whole procedure in Figure 4.4 outlines the problem that must be solved for each experiment (simulation) of the DoE.

To start with the definition of the DoE, the values for the normalised displacements must be defined, ensuring that the entire load space (normalised loads) for any bearing is obtained within the scope of the static load carrying capacity. This is possible since the expressions of the normalised loads with respect to the axial load capacity (4.11), (4.12) and (4.13) are available. Accordingly, a large displacement space can be defined and, later, the cases exceeding the static load capacity or incurring in ball truncation can be discarded.

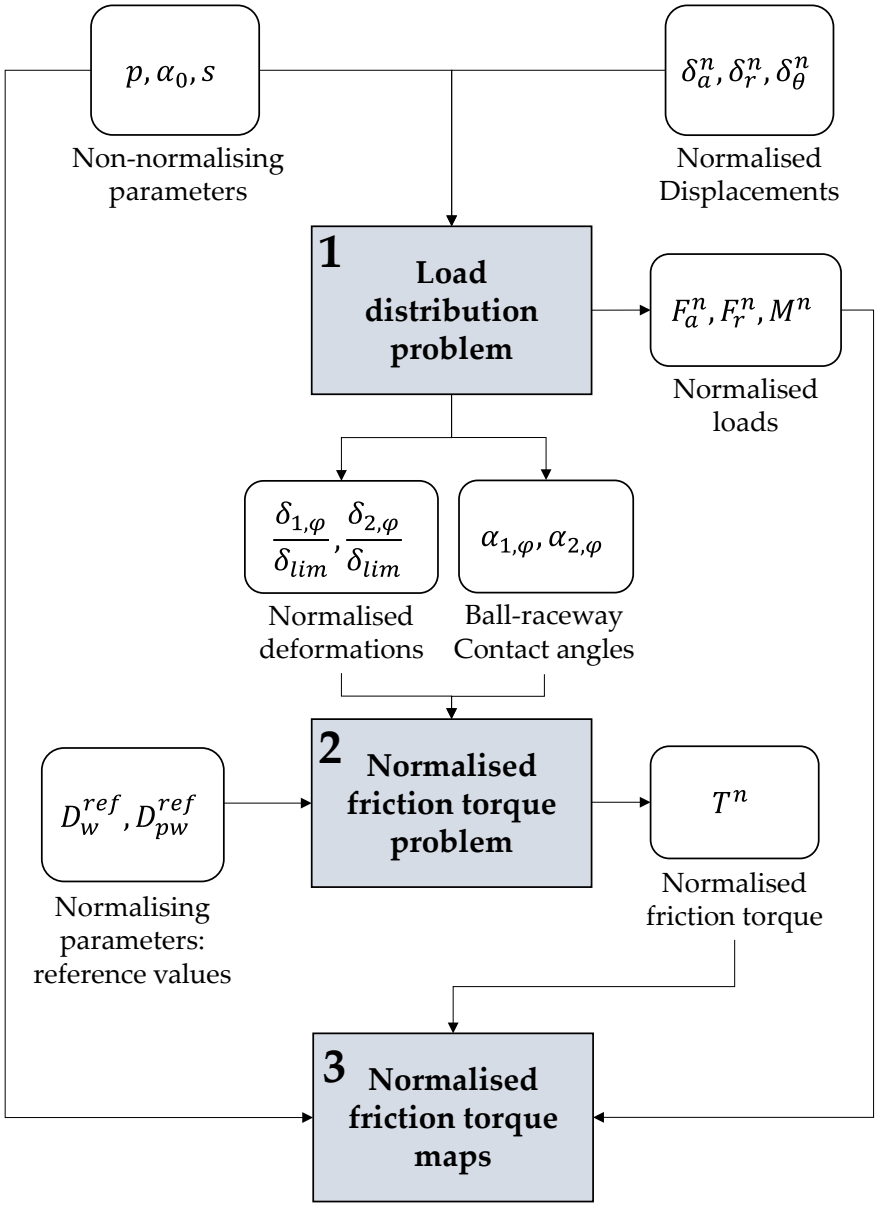

Figure 4.4. Calculation procedure of the analytical model for each experiment (simulation).

Nevertheless, considering the whole displacement space could be unfeasible depending on the computational capabilities, given the resulting large number of combinations to be analysed. Therefore, it is convenient to verify whether any symmetries or patterns apply in the displacement space, with the purpose of reducing the number of combinations to be computed. As the load distribution problem assumes rigid rings, it can be expected that different equidistant displacements within the displacement space can involve the same friction torque due to the cyclic symmetry of the bearing. To address this, eight equimodular normalised displacements are considered, covering all possible symmetries of the displacement space, as shown in Figure 4.5.

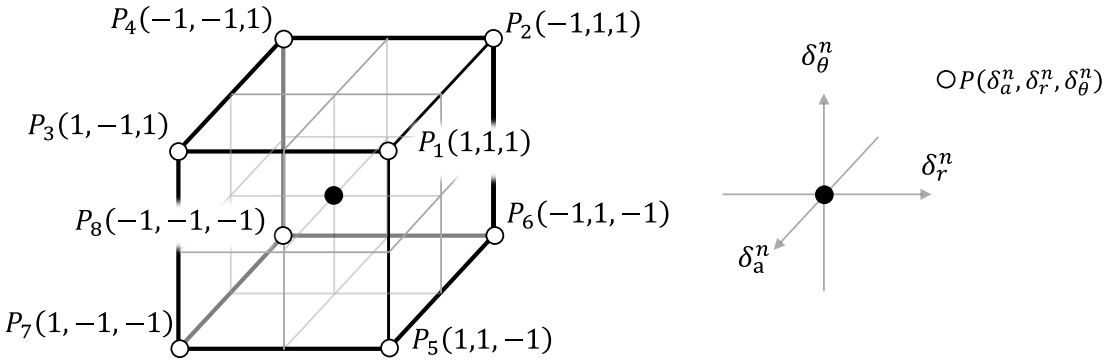

Figure 4.5. Displacement cases covering the design space.

These cases are computed for the same values of the non-normalising parameters as in the validation procedure in Section 4.3, namely: $s = 0.94$, $p = 0$ and $\alpha_0 = 45°$.

Table 4.4. Friction torque results for each octant of the design space.

	Normalised displacements			**Resulting external loads**			**Friction torque**		
Octant number	$\boldsymbol{\delta_a^n}$	$\boldsymbol{\delta_r^n}$	$\boldsymbol{\delta_\theta^n}$	$\boldsymbol{F_a}$	$\boldsymbol{F_a}$	$\boldsymbol{M_a}$	$\boldsymbol{T}$	$\boldsymbol{T^n}$	***Graph colour***
1	1	1	1	9871.37	5965.36	5289.40	32341.6	2.647E-2	Blue
2	-1	1	1	-5649.60	1003.85	1643.98	41538.8	3.399E-2	Red
3	1	-1	1	5649.66	-1003.82	1643.96	41553.0	3.400E-2	Red
4	-1	-1	1	-9871.41	-5965.34	5289.39	32341.6	2.647E-2	Blue
5	1	1	-1	5649.60	1003.85	-1643.98	41538.8	3.399E-2	Red
6	-1	1	-1	-9871.37	5965.36	-5289.40	32341.6	2.647E-2	Blue
7	1	-1	-1	9871.41	-5965.34	-5289.39	32341.6	2.647E-2	Blue
8	-1	-1	-1	-5649.66	-1003.82	-1643.96	41553.0	3.400E-2	Red

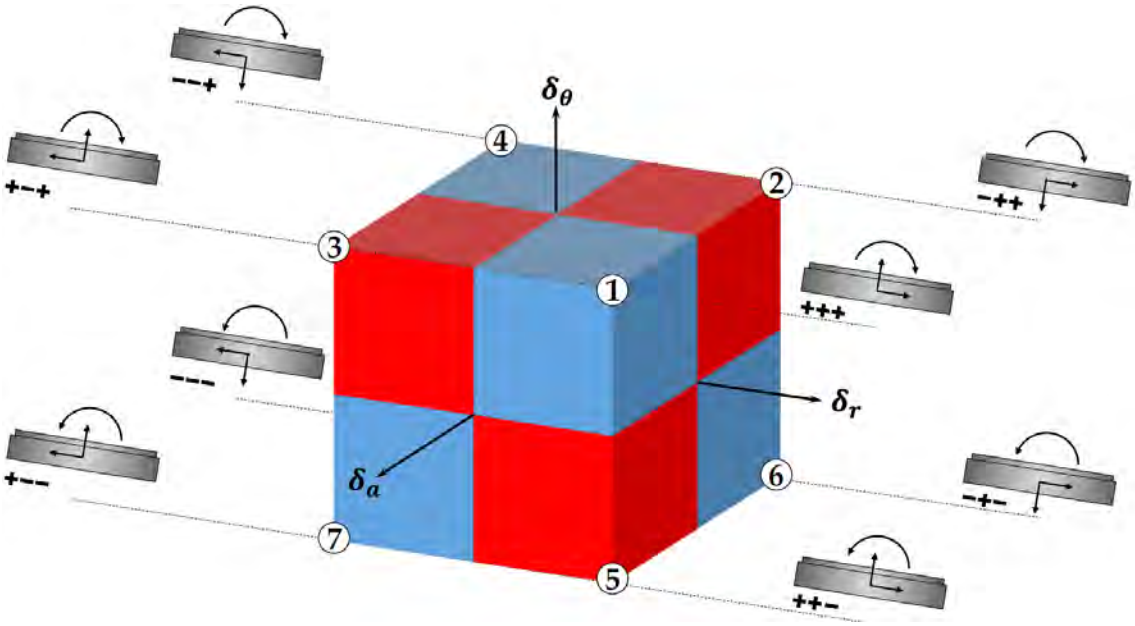

Figure 4.6. Obtained octant pattern: 1st octant in blue, 2nd octant in red.

The results show that only two octants of the displacement space need to be considered for simulations. In this regard, whenever the sign/direction of two of the three displacements is changed, the same values for loads (with their corresponding signs) and friction torque are obtained. Table 4.4 and Figure 4.6 show this results pattern. This conclusion could have been drawn without any calculations (with geometrical interference reasoning) but, for the sake of proof, it was deemed appropriate to include eight symmetrical points located on each of the eight octants (as defined in Figure 4.5).

The results of this study show that it is possible to reduce the number of analyses performed on the DoE. Therefore, a reduced design space is proposed where the normalised friction torque is computed for only two octants in the normalised displacement space.

Table 4.5. Normalised displacement value ranges.

	From	*To*	*Interval*	*Levels*
δ_a^n	-2	2	0.1	40 (20 per octant)
δ_r^n	0	2	0.2	10
δ_θ^n	0	2	0.2	10

Table 4.6. Non-normalising geometrical parameter values.

	Values (5 levels considered)				
$\boldsymbol{p}$	0	0.05	0.10	0.15	0.20
$\boldsymbol{s}$	0.910	0.925	0.94	0.95	0.96
$\boldsymbol{\alpha_0}$	35	40	45	50	55

In summary, the DoE considers six input variables: three normalised displacements and three non-normalising geometrical parameters. Table 4.5 shows the range of values for the normalised displacements and Table 4.6 shows the values of the non-normalising geometrical parameters. The ranges for each parameter have been selected considering available computational capabilities.

Again, the normalising parameters will take the same reference values as before: D_{pw}^{ref} = 1500 mm and D_{w}^{ref} = 35 mm. Computing all the combinations for each of the values of the six variables implies a set of $40\times10\times10\times5^3$ = 500 000 experiments (simulations) to be computed. However, and since the cases where contact truncation or the maximum contact deformation is reached for any ball will be later discarded, the number of results included in the friction torque maps will be less.

4.4.2 Normalised friction torque maps

After removing cases with truncation or exceeding the bearing capacity, the remaining cases calculated from the previously designed DoE resulted in 51 184 bearing friction torque results. Each case took about 3 minutes on average to solve (2x Intel Xeon E52697 v3 @2.6Ghz Windows 10 programmed in Matlab), which equated to about 3 months of computation time.

In Figure 4.7 and Figure 4.8 all the computed points of the DoE are expressed in the load space. To differentiate each octant of the displacement space (previously shown in Figure 4.6) represented in the load space, each region is coloured accordingly. The blue dots represent points of displacement octant number one, while the red ones relate to the points of displacement octant number two. It should be noted that the points of an octant in the displacement

space do not have to remain in the same octant of the load space. This can be seen in the 3D view of the data cloud in Figure 4.9.

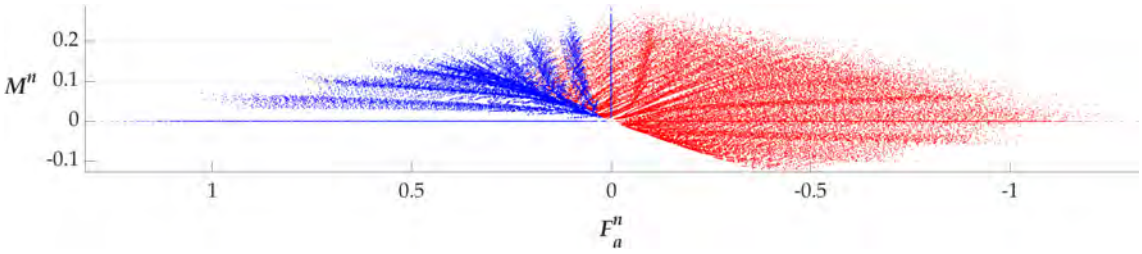

Figure 4.7. Front view of the calculated points (tilting moment vs axial force) of octants 1 and 2.

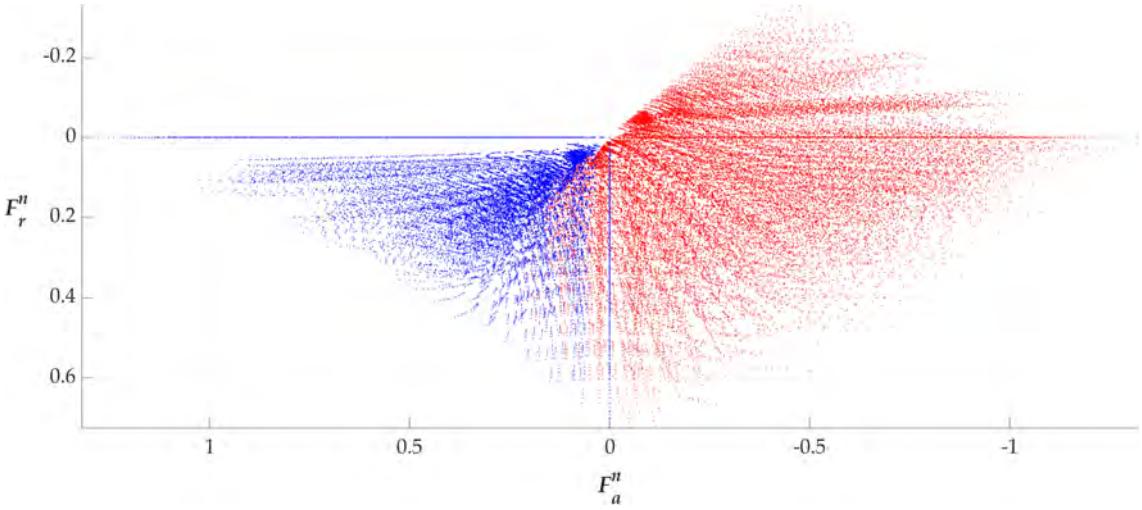

Figure 4.8. Side view of the calculated points (radial force vs axial force) of octants 1 and 2.

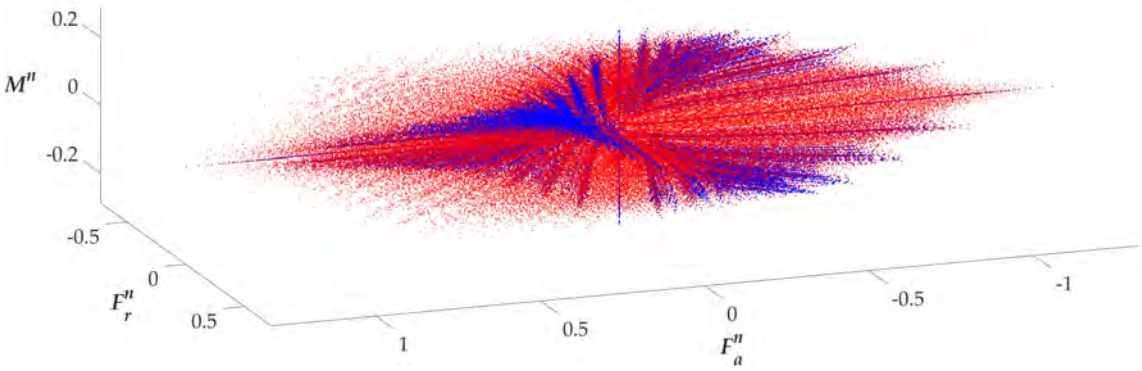

Figure 4.9. 3D view of the whole normalised load space of the calculated points.

The calculated results for the normalised friction torque must then be interpolated across the normalised load space (F_a^n, F_r^n and M^n) for each non-normalising geometrical parameter set (s, p and α_0) to create the friction torque maps. When creating the maps, the interpolation is not considered for the non-

normalising geometrical parameters, since representative values of these parameters were chosen based on the values used in the preliminary design stages. The interpolated results are therefore used to create the friction torque maps, grouped for each non-normalising geometrical parameter set (p, s and α_0) and classified by the normalised radial force (F_r^n), as shown in Figure 4.10.

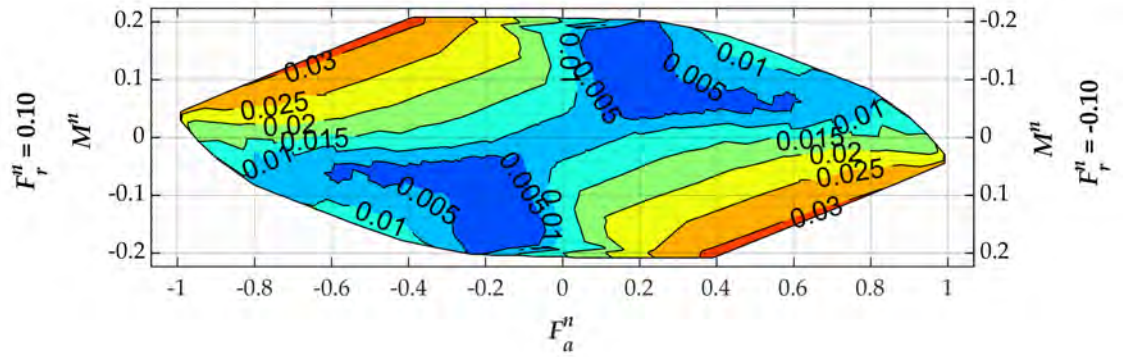

Figure 4.10. Normalised friction torque map sample for non-normalising parameters $p = 0$, $s = 0.94$ and $\alpha_0 = 45°$ and normalised radial force $F_r^n = \pm 0.10$.

A set of equispaced results are shown in the Appendix (see Figure 4.11) for different non-normalising microgeometrical parameter sets (s, p and α_0) and a given range within the normalised radial force. In addition, the raw database obtained from the DoE is available upon request from the corresponding author, so custom interpolation tools can be further programmed.

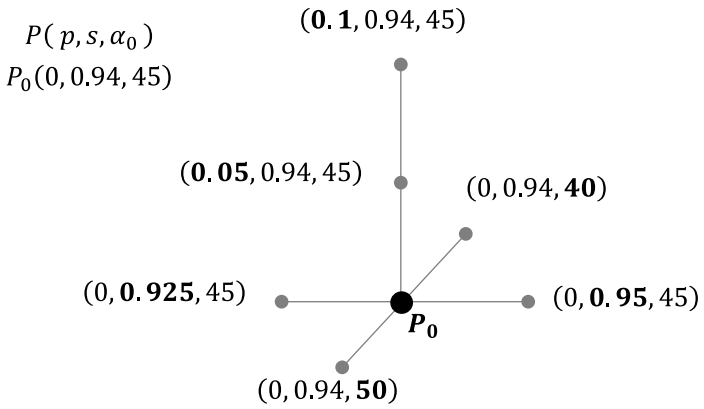

Figure 4.11. Set of equispaced results in the appendix.

4.4.3 Validation of the interpolated results

The results of the interpolation that created the friction torque maps need to be validated by means of a comparison with other approaches to determine the capabilities and limitations of the proposed approach. It is therefore necessary to

investigate the potential sources of error, which can be divided into two categories: the error related to the calculation of the normalised friction torque and the error committed during the creation of the interpolated point cloud.

On the one hand, the error related to the calculation of the normalised friction torque for each considered experiment (simulation) is expected to be negligible and may be originated from two sources:

- Friction torque normalisation error: as discussed in Section 3, the error introduced due to the proposed normalisation is less than 2% when the D_{pw}/D_w ratio is greater than 30.
- Integration error: different discretisation values may produce different results when solving the integral in equation (4.21). However, this error is completely assumable, as it is when the concept of load distribution integral applies [36]. In this sense, this error is zero if the discretization level matches the ball number for a given bearing.

On the other hand, besides these previous sources of error, there is a misestimate due to the interpolation, and this is expected to be the largest one. Moreover, of all the regions in the load space, the pure axial load case has been found to provide the worst misestimate for interpolated values. Figure 4.12 depicts the three pure load cases: axial load (a), tilting moment (b) and radial load (c). In this figure, the analytical model from Joshi et al. [124] is used as a reference to show the error introduced due to the interpolation. In addition, the friction torque calculated using the NREL formula [49] has been included to compare the accuracy of the results with a different approach. A sample of the interpolated data has been chosen and de-normalised to compare realistic friction torque values. The following data was chosen to this end: D_w = 35 mm, D_{pw} = 1500 mm, Z = 80, μ = 0.1, p = 0.1, s = 0.94 and α_0 = 45°.

With the exception of the load cases where the axial force is largely predominant, the results show that the error is negligible after interpolation. In fact, since the model assumes rigid rings and considers no manufacturing errors, all the balls have the same preload and they are uniformly loaded under axial load. This means that, under these assumptions, all the balls will experience a transition from four to two contact points for a given pure axial load, resulting in an abrupt drop in the friction torque [31], as shown in Figure 4.12a and according to the reference model by Joshi et al. [124]. Nonetheless, this drop does not

correspond to the behaviour shown in experimental results analysed in Chapter 2.

In practice, different bearings with exactly the same design may well show very different values of friction torque for low to moderate applied axial loads. The four to two point contact is indeed a hard phenomenon to predict, as was explained in Chapter 2, and it can be affected by very sensitive factors (like manufacturing errors). Despite the axial load case being the most sensitive to study, the interpolated data in Figure 4.12a shows an excellent agreement with the reference model by Joshi et al. [124]. Moreover, it provides more accurate results than the NREL formula, which provides conservative results for high loads, but is not conservative in low or medium loads.

The previous reasoning was focused on the axial load case, but it is important to point out that these bearings are mainly designed to withstand tilting moments. For this load case, it can be seen in Figure 4.12b that the interpolated results yield the same friction torque values than the reference analytical model. At the same time, it can be seen that, as occurred for the axial load case, the NREL formula underestimates the friction torque for low loading cases, while overestimating it for high loads.

Finally, for the radial force (Figure 4.12c), the NREL formula underestimates the friction torque for any case. Meanwhile, interpolated and analytical results show no difference at all.

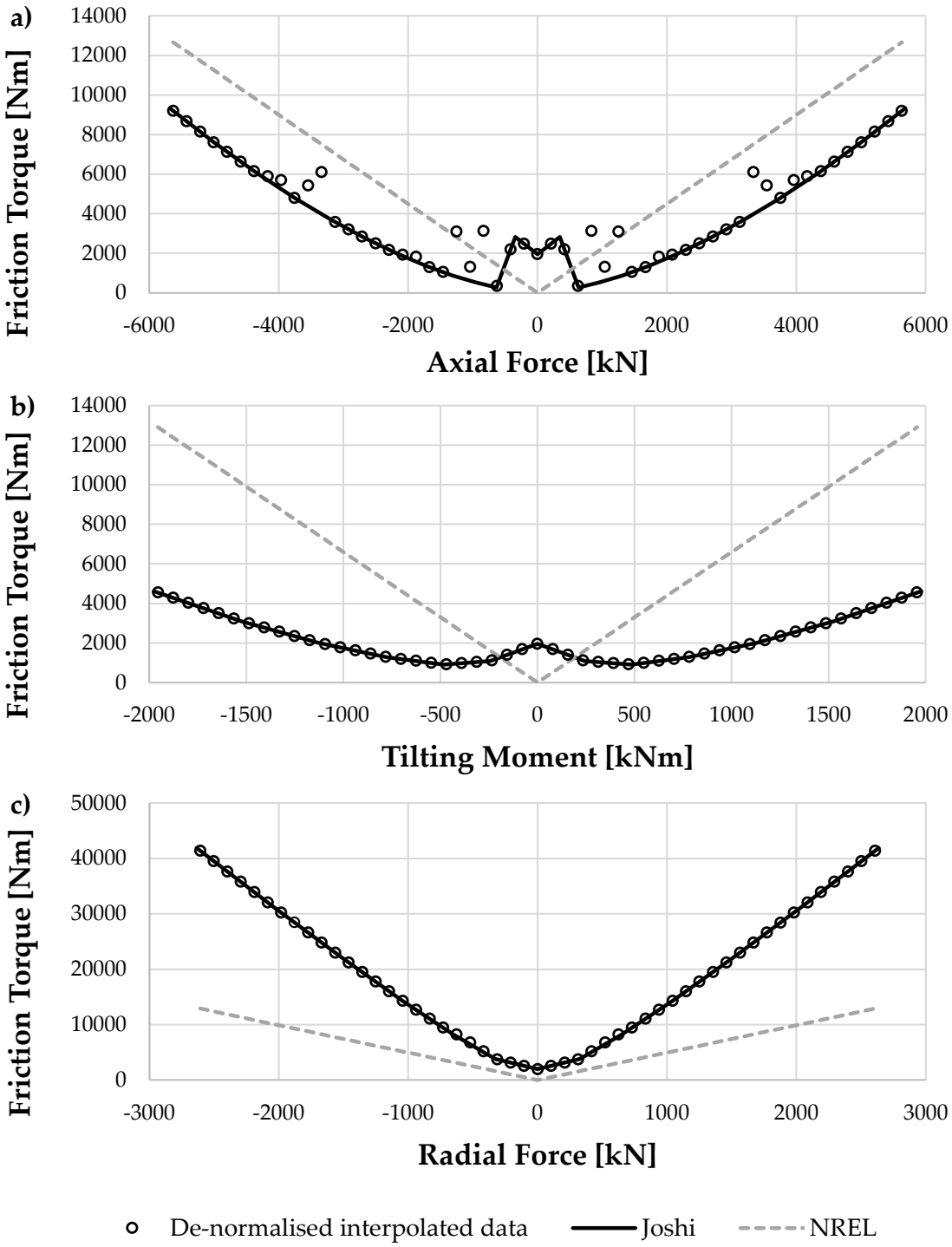

Figure 4.12. Comparative results between the interpolated data, the reference analytical model by Joshi et al. [124] and the NREL friction torque formula [49]. Friction torque for pure axial force (a), tilting moment (b) and radial force (c) for D_w = 35 mm, D_{pw} = 1500 mm, Z = 80, μ = 0.1, p = 0.1, s = 0.94 and α_0 = 45°.

4.5 Use of friction torque maps

Once the friction torque maps have been obtained, and considering that the purpose of this work is to develop a useful tool for bearing customers and designers, this section is focused on how they are used.

Firstly, the user needs to normalise the loads acting on the bearing based on the bearing geometry, according to equations (4.11), (4.12) and (4.13). Then, the proper friction torque map is selected attending to the non-normalising parameters and the normalised radial load. Then, the normalised friction torque is obtained from the map depending on the normalised axial load and moment. Finally, using the same normalising parameters, the normalised friction torque can be de-normalised (4.21).

Figure 4.13 contains a flowchart with the steps to follow to obtain the friction torque for a specific bearing subjected to any load. Besides, Figure 4.14 shows a normalised friction torque map and how to use it to calculate the normalised friction torque from the normalised external loads.

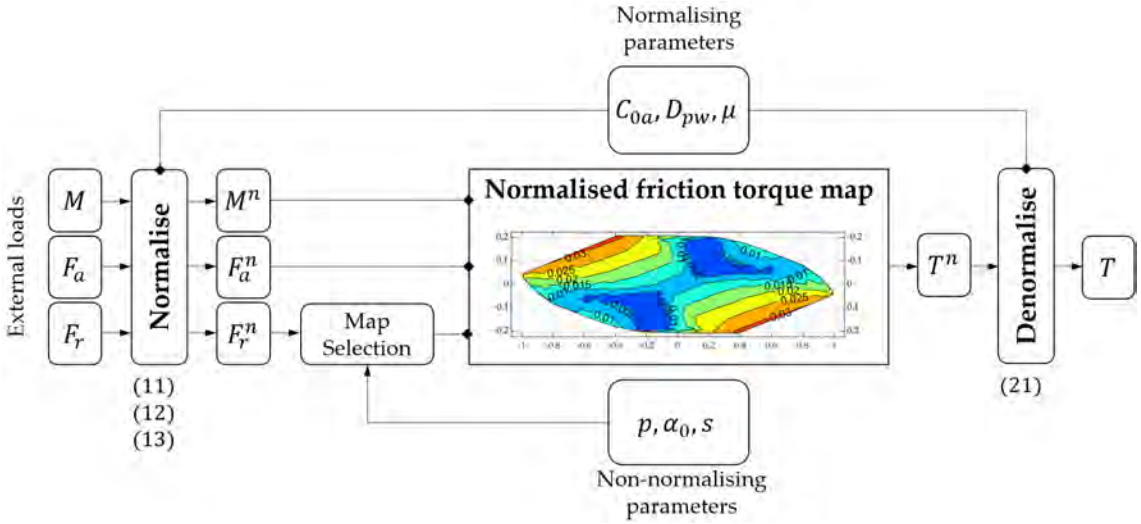

Figure 4.13. Steps to use the normalised friction torque maps.

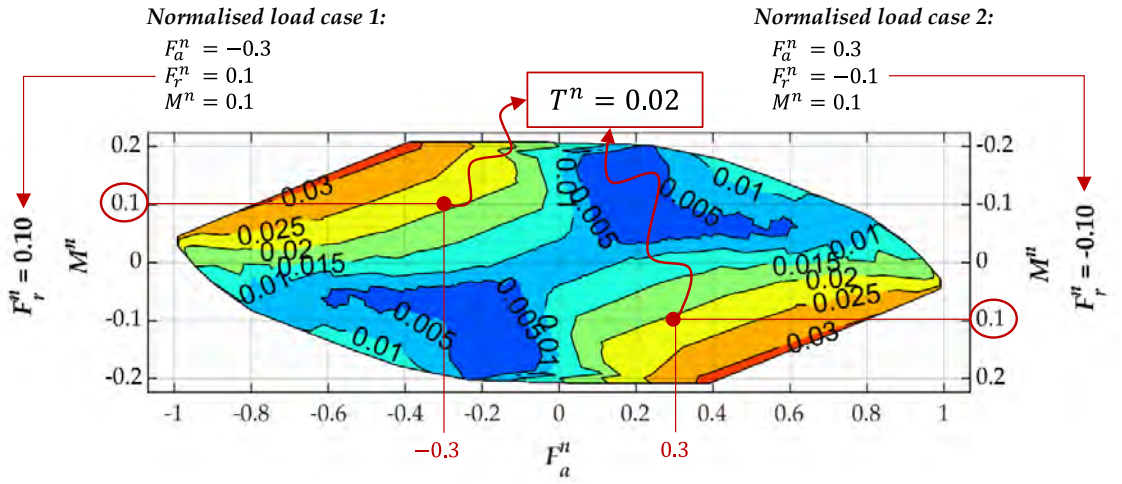

Figure 4.14. Example of the application of a torque map for a bearing with $p = 0.1$, $s = 0.94$ and $\alpha_0 = 45°$.

Note that the friction torque maps include two vertical axes, depending on whether the normalised radial force is positive or negative (see left and right axes in Figure 4.14), which also flips the sign of the normalised tilting moment on the corresponding axis. Due to the symmetries found in the displacement space, the friction torque results for two different load combinations can be displayed in a compact form on each friction torque map. This is also shown in Figure 4.14, together with two examples that show how to use the friction torque maps (the same values for the loads but with the axial and radial forces with opposite signs).

4.6 Conclusions and additional remarks

State-of-the-art approaches to calculate of the friction torque on four-point contact slewing bearings are either simple and practical but inaccurate, or accurate but difficult to use in a practical way. Thus, there are no methods or procedures in literature that allow reliable results to be obtained in a direct and simple way. This research work provides a solution in this respect. To this end, some simplifications are considered, such as adopting an overall sliding coefficient of friction for the lubricated contacts, assuming of rigid rings with no manufacturing errors and the omission of the effects of cages or spacers. On this basis, the contributions of this work are summarised in the next points:

- A normalised expression of the friction torque is presented. This normalised friction torque only depends on the external loads (axial force, radial force and tilting moment) and the microgeometry, namely the

osculation ratio, the initial contact angle and the preload of the balls. Therefore, it becomes independent of the macrogeomety of the bearing, defined by its mean diameter, the ball diameter and the number of balls, and also of the coefficient of friction. The expression is shown to report an error of less than 2%, provided the D_{pw}/D_w ratio is greater than 30, which is mostly the case for slewing bearings. The normalised expression of the friction torque is not only a convenient and useful way to simplify the the friction torque calculation, but is also consistent with previous works by the authors focused on the static load capacity of the bearings.

- Based on the presented normalised expression, friction torque maps are obtained and presented, intended to be used in early design stages. These maps serve as a powerful calculation tool, which is as accurate as complex state of the art simulation models, but at the same time almost as practical and easy-to-use as the NREL formula. Accordingly, these maps represent a useful tool either for bearing manufacturers, who strive for the most appropriate manufacturing parameters to optimise the frictional behaviour, and for applications engineers, who intend to select the best bearing for their application. This approach could also prove useful for future standards or design guidelines.

- The friction torque maps are established using a database, obtained from a large simulation campaign. The full database obtained from all the friction torque simulations carried out is available upon request from the corresponding author, so custom interpolation tools can be further programmed by future potential users (applications engineers).

Due to the considered assumptions, the friction torque maps provided in this research work may lose predictive capacity with some applications. It is already known that ring flexibility or manufacturing errors can significantly affect friction torque under certain circumstances, so future work should focus on developing practical approaches to address these phenomena.

5 Conclusions and Future Work

5.1 Conclusions

This section presents the main findings from the research conducted for the entire Doctoral Thesis. A detailed description of the relationship between the different chapters and their purpose is given in Section 1.5. Subsequently, the conclusions are listed below and presented in the same order as the previous chapters.

Chapter 2 proposes an improved methodology for calculating the friction torque by implementing a preload scatter:

- Implementing the preload scatter justifies the smooth transition of the friction torque under compression loads, especially for those loads where the balls experience a transition from four to two contact points (transition zone). This zone is, indeed, where current state-of-the-art analytical models show a sudden drop of the bearing friction torque, while the experimental results show a smooth evolution. Thus, implementing a preload scatter is an effective way to represent the real behaviour of the friction torque. Moreover, the presented analytical approach provides considerably more accurate results than the practical formula provided by NREL for these types of bearings, even though the latter can still be useful for rough estimations when only the macrogeometry of the bearing is known.

- Different tuning parameters have been established to adjust the proposed methodology of friction torque calculation. The proposed calculation methodology allows for adjusting the analytical model for each design or geometry, requiring a varying number of experimental test results based on the known bearing and desired accuracy.

- Satisfactory results were obtained by considering a constant contribution to the friction torque from the seals and separating elements for a given bearing, which correlated closely with experimental test results.

- Under an applied bending moment, it has been shown how the friction torque is driven by the less loaded balls, which have four points in contact, rather than the most loaded ones, which only have two. This indicates the high sensitivity of the friction torque to the preload and its scatter, even under high bending moments. The greater the preload, the more balls will be in the four-point contact state, thereby yielding a higher friction torque.

- The rigid ring assumption has been proven to yield inaccurate friction torque results when a bearing region is subjected to tension, such as a bearing under tension axial force or tilting moment. It has been proven that considering the flexibility of the rings and the surrounding structures is necessary to obtain more reliable friction torque results in such load cases. In this regard, the FEM has proven to be an effective but inefficient method to account for this flexibility, which shows a strong correlation with experimental results for high loads.

- Some guidelines for using and tuning the model are proposed, in order to obtain a reliable friction torque prediction tool, meant to be of use for users ranging from a bearing manufacturer with extensive knowledge about their product, to a user with more limited information.

The findings in the preceding chapter call for further research on the slewing bearing modelling techniques, which is covered in Chapter 3 by studying the effect on the flexibility of different modelling techniques on a blade-bearing-hub assembly using FEM:

- Ball-raceway contact modelling has been improved by modifying the implementation of Daidié's mechanism, which had some shortcomings when solving the load distribution problem under radial load. The proposed implementation of Daidié's mechanism reduces the errors in the less loaded sections. Although there is a minimal impact on static load-carrying capacity, radial stiffness is significantly affected. Moreover, since friction torque is primarily affected by the least loaded balls, this new implementation provides a direct improvement of the friction torque calculation. To achieve this, an FE model combined with the new Daidié's mechanism implementation is used to solve the load distribution problem.

Subsequently, an analytical model, such as the one used in this thesis, can be used to solve the friction torque problem.

- A blade-bearing-hub assembly with two different blade materials has been modelled. The conclusion has been drawn that replacing a composite blade with a steel blade is not feasible as the differences in the obtained bearing load distribution and deformations are significant. Therefore, it is established that using a steel blade leads to unreliable results when studying the structural behaviour of a blade-bearing hub assembly, discarding the possibility of using a steel blade for both FE calculations and experimental tests.

- It has been observed how the modelling of the bolts on a blade-bearing-hub assembly can be simplified with *bonded connections* as long as it is not under extreme working loads. Therefore, the bearing results will be accurate enough for early design stages, with more accurate bolted joint models required in the final design stages for validation purposes.

- Using the same approach as in wind turbine global structural analyses, where simple models are used to simulate bearing stiffness, the possibility of replacing the bearing with three non-linear springs representing the bearing stiffness in a blade-bearing-hub is studied. It is concluded that this type of modelling cannot provide a correct representation of load distribution and the deformations of the surrounding structures next to the bearing. Therefore, although using these techniques is appropriate in global models focused on the dynamic analysis of the whole turbine, they are not viable in more local analyses such as the blade-bearing-hub assembly analysed in this work.

After focusing on improving the accuracy of the friction torque models in the previous chapters, Chapter 4 proposes two main novelties to improve the calculation speed: a normalised frictional torque expression and a torque estimation tool in the form of heatmaps.

- A normalised friction torque expression has been presented, allowing for a simpler calculation process. This expression depends on the external loads (in the form of normalised displacements) and the bearing microgeometry. For D_{pw} / D_w ratios greater than 30, the proposed expression for the normalised friction torque is shown to be almost independent of the macrogeometry, with an error of less than 2%.

- Based on the previous normalised friction torque expression, a campaign of simulations has been conducted and established based on a DoE. The obtained database relates the bearing displacements to the external forces and friction torque for each microgeometry combination, which allows it to be implemented in external calculation tools for fast estimations of the friction torque. The assumption of rigid rings limits the applicability of the friction torque results, but it can be useful for early design stages.

Based on the database, a series of heatmaps have been created by interpolating the data. These heatmaps directly relate the normalised external loads applied to a bearing with the normalised friction torque for a series of typical values of the microgeometrical parameters. These normalised friction torque maps are a tool that, whilst being less accurate than analytical methods, are as straightforward as the expressions provided in the guidelines (DG03), but offer greater accuracy than the latter. Therefore, they are not only useful for quick torque estimations, but can also be integrated into standards or design guidelines. The normalised friction torque database and heatmaps are the simplified counterpart to the more demanding solution presented in Chapter 2.

5.2 Future work

Possible future studies resulting from this Doctoral Thesis are proposed in the following points:

- Implementing the preload scatter into an FE model and adjusting the parameters defining this scatter, to obtain new load distribution results that would be a better fit with the experimental friction torque results, particularly in the case of applied tilting moments.

- Considering the preload scatter with SE based models to generate stiffness matrices that could be implemented into analytical models to efficiently solve the load distribution problem. This approach would consider the flexibility of the rings analytically and would yield fast and precise friction torque results.

- Fit the friction torque results considering different probability distributions for the preload scatter. For more precise results, proper sensorisation of a bearing within a test bench or real assembly would be

required, which would allow for estimating the final preload value after the assembly process and fitting the preload scatter model.

- Developing an engineering formulation that would characterise the load distribution for different boundary conditions, such as different turbine blade sizes, configurations and materials.
- Developing an alternative model or procedure that would allow for the substitution of the bearing in blade-bearing-hub assemblies that represent the bearing stiffness and distribution of the forces to the surrounding structures more accurately.
- Mapping the friction torque of rolling elements in the same way as done for the whole bearing. This would allow for the quick calculation of the friction torque once the load distribution has been solved separately. Combining an FE model with considering a preload scatter to solve the load distribution, with a ball-raceway friction torque database would improve the accuracy and efficiency of friction torque calculations. Thus, the accuracy of the load distribution would dictate the accuracy of the friction torque
- Applying the above procedures to other bearings, such as crossed-roller slewing bearings or angular contact ball bearings.

5.3 Research work dissemination

Part of the research work presented in this Doctoral Thesis was published in high-impact factor scientific journals in the following manuscripts:

- Iñigo Escanciano, Iker Heras, Luis María Macareno, Josu Aguirrebeitia, An engineering approach to assess friction torque in generally loaded four-point contact slewing bearings, Mechanism and Machine Theory, Volume 192, 2024, 105542, ISSN 0094-114X. DOI: 10.1016/j.mechmachtheory.2023.105542

- Iñigo Escanciano, Iker Heras, F. Schleich, Josu Aguirrebeitia, Methodology for the assessment of the friction torque of ball slewing bearings considering preload scatter, FRICTION, 2024, ISSN 2223-7704 (Accepted for publication 18-Dec-2023)

Furthermore, the different progress made in the field of slewing-bearings was presented in national and international congresses:

- Iñigo Escanciano, Iker Heras, Josu Aguirrebeitia, Iñigo Martín, Effect of the material of the blade and the joint simulation strategy in the pitch bearing of a wind turbine, International Conference on Machine Design 2021, Porto, Portugal, 9-10 September, 2021, www.md-conferences.com

- Iker Heras, Iñigo Escanciano, Ibai Coria, Josu Aguirrebeitia, Limitaciones del mecanismo de Daidié para la simulación de rodamientos: análisis y alternativas, XXIII Congreso Nacional de Ingeniería Mecánica, Jaen, Spain, 20-22 October, 2016, ISSN 0212-5072

- Iñigo Escanciano, Iker Heras, Josu Aguirrebeitia, Luis María, Influencia de los errores de fabricación en el par de fricción en rodamientos de bolas de cuatro puntos de contacto. Modelización analítica y correlación experimental bajo carga axial, Congreso Iberoamericano de Ingeniería Mecánica – CIBIM22, Madrid, Spain, 22-24 November, 2022, ISSN 1137-2729. DOI: 10.5944/bicim2022.107

- Iñigo Escanciano, Iker Heras, Josu Aguirrebeitia, Normalización y mapeo del par de fricción de rodamientos de vuelco de cuatro puntos de contacto, XXIV Congreso Nacional de Ingeniería Mecánica, Las Palmas de Gran Canaria, Spain, 25-27 October, 2023, ISSN 0212-5072

References

[1] I. International Energy Agency, Renewables 2022, (2022). https://www.iea.org/reports/renewables-2022 (accessed April 27, 2023).

[2] IEA, Total renewable electricity capacity additions, 2001-2027 – Charts – Data & Statistics , (n.d.). https://www.iea.org/data-and-statistics/charts/total-renewable-electricity-capacity-additions-2001-2027 (accessed May 2, 2023).

[3] I. - International Energy Agency, Renewable Energy Market Update - June 2023, (2023). www.iea.org/t&c/ (accessed December 19, 2023).

[4] Global Wind Energy Council, Global Wind Report 2023, (n.d.). https://gwec.net/globalwindreport2023/ (accessed May 2, 2023).

[5] Member States agree new ambition for expanding offshore renewable energy, (n.d.). https://energy.ec.europa.eu/news/member-states-agree-new-ambition-expanding-offshore-renewable-energy-2023-01-19_en (accessed May 2, 2023).

[6] I. International Energy Agency, Share of cumulative power capacity by technology, 2010-2027 – Charts – Data & Statistics, (n.d.). https://www.iea.org/data-and-statistics/charts/share-of-cumulative-power-capacity-by-technology-2010-2027 (accessed May 2, 2023).

[7] ADM - Grupo de Análisis y Diseño Mecánico - Escuela de Ingeniería de Bilbao - UPV/EHU, (n.d.). https://www.ehu.eus/es/web/bilboko-ingeniaritza-eskola/adm.

[8] J. Aguirrebeitia, R. Avilés, I.F. De Bustos, M. Abasolo, Calculation of general static load-carrying capacity for the design of four-contact-point slewing bearings, J. Mech. Des. Trans. ASME. 132 (2010) 0645011–0645016. doi:10.1115/1.4001600.

[9] J. Aguirrebeitia, M. Abasolo, R. Avilés, I. Fernández De Bustos, Theoretical calculation of general static load-carrying capacity for the design and selection of three row roller slewing bearings, Mech. Mach. Theory. 48

(2012) 52–61. doi:10.1016/J.MECHMACHTHEORY.2011.09.003.

[10] I. Heras, J. Aguirrebeitia, M. Abasolo, I. Coria, An engineering approach for the estimation of slewing bearing stiffness in wind turbine generators, Wind Energy. 22 (2019) 376–391. doi:10.1002/WE.2292.

[11] I. Martín, I. Heras, J. Aguirrebeitia, M. Abasolo, I. Coria, Static structural behaviour of wire bearings under axial load: Comparison with conventional bearings and study of design and operational parameters, Mech. Mach. Theory. 132 (2019) 98–107. doi:10.1016/J.MECHMACHTHEORY.2018.10.016.

[12] I. Heras, J. Aguirrebeitia, M. Abasolo, I. Coria, I. Escanciano, Load distribution and friction torque in four-point contact slewing bearings considering manufacturing errors and ring flexibility, Mech. Mach. Theory. 137 (2019) 23–36. doi:10.1016/J.MECHMACHTHEORY.2019.03.008.

[13] J. Aguirrebeitia, I. Martín, I. Heras, M. Abasolo, I. Coria, Wire twisting stiffness modelling with application in wire race ball bearings. Derivation of analytical formula and finite element validation, Mech. Mach. Theory. 140 (2019) 1–9. doi:10.1016/J.MECHMACHTHEORY.2019.05.012.

[14] I. Martín, I. Heras, I. Coria, M. Abasolo, J. Aguirrebeitia, Structural modeling of crossed roller wire race bearings: Analytical submodel for the roller-wire-ring set, Tribol. Int. 151 (2020) 106420. doi:10.1016/J.TRIBOINT.2020.106420.

[15] I. Martín, I. Heras, J. Aguirrebeitia, L.M. Macareno, Influence of the geometrical design on ball and crossed roller wire race bearing behavior under axial load, Tribol. Int. 156 (2021) 106817. doi:10.1016/J.TRIBOINT.2020.106817.

[16] I. Martín, J. Aguirrebeitia, I. Heras, M. Abasolo, Efficient Finite Element modelling of crossed roller wire race slewing bearings, Tribol. Int. 161 (2021) 107098. doi:10.1016/J.TRIBOINT.2021.107098.

[17] I. Martín, Study of the structural behaviour and analytical characterization of wire-race slewing bearings, UPV/EHU, 2022. http://hdl.handle.net/10810/56169.

[18] J. Aguirrebeitia, M. Abasolo, R. Avilés, I. Fernández De Bustos, General static load-carrying capacity for the design and selection of four contact point slewing bearings: Finite element calculations and theoretical model validation, Finite Elem. Anal. Des. 55 (2012) 23–30. doi:10.1016/J.FINEL.2012.02.002.

[19] J. Aguirrebeitia, J. Plaza, M. Abasolo, J. Vallejo, General static load-carrying

capacity of four-contact-point slewing bearings for wind turbine generator actuation systems, Wind Energy. 16 (2013) 759–774. doi:10.1002/WE.1530.

[20] J. Aguirrebeitia, J. Plaza, M. Abasolo, J. Vallejo, Effect of the preload in the general static load-carrying capacity of four-contact-point slewing bearings for wind turbine generators: theoretical model and finite element calculations, Wind Energy. 17 (2014) 1605–1621. doi:10.1002/WE.1656.

[21] J. Plaza, M. Abasolo, I. Coria, J. Aguirrebeitia, I.F. de Bustos, A new finite element approach for the analysis of slewing bearings in wind turbine generators using superelement techniques, Meccanica. 50 (2015) 1623–1633. doi:10.1007/S11012-015-0110-7/.

[22] M. Abasolo, I. Coria, J. Plaza, J. Aguirrebeitia, New selection curves for four contact point slewing bearings, Proc. Inst. Mech. Eng. Part C J. Mech. Eng. Sci. 230 (2016) 1715–1725. doi:10.1177/0954406215583522/ASSET/IMAGES/LARGE/10.1177_0954406215583522-FIG14.JPEG.

[23] I. Heras, J. Aguirrebeitia, M. Abasolo, Friction torque in four contact point slewing bearings: Effect of manufacturing errors and ring stiffness, Mech. Mach. Theory. 112 (2017) 145–154. doi:10.1016/J.MECHMACHTHEORY.2017.02.009.

[24] I. Heras, J. Aguirrebeitia, M. Abasolo, J. Plaza, Friction torque in four-point contact slewing bearings: Applicability and limitations of current analytical formulations, Tribol. Int. 115 (2017) 59–69. doi:10.1016/J.TRIBOINT.2017.05.011.

[25] I. Heras, Four-point contact slewing bearings for wind turbines: advances in structural modelling and friction torque calculation, University of the Basque Country (UPV/EHU), 2018.

[26] J. Aguirrebeitia, R. Avilés, I.F. De Bustos, M. Abasolo, General Static Load Capacity In Four Contact Point Slewing Bearings, WIT Trans. Eng. Sci. 66 (2010) 17–23. doi:10.2495/TD100021.

[27] J. Aguirrebeitia, M. Abasolo, R. Aviles, I. Fernández de Bustos, General Static Load Capacity in Slewing Bearings. Unified Theoretical Approach for Crossed Roller Bearings and Four Contact Point Angular Ball Bearings ., in: 13th World Congr. Mech. Mach. Sci. 19-25 June, Guanajuato, México, 2011.

[28] J. Aguirrebeitia, M. Abasolo, R. Avilés, I.F. De Bustos, R. Ansola, Static Load Carrying Capacity in Four Contact Point Slewing Bearings: Theoretical and Preliminary Finite Element Calculations, ASME Int. Mech.

Eng. Congr. Expo. Proc. 3 (2012) 763–768. doi:10.1115/IMECE2010-38542.

[29] M. Abasolo, I. Coria, J. Plaza, I. Aguirrebeitia, Josu, Fernández de Bustos, Estudio de la respuesta estática de rodamientos de 4 puntos de contacto angular mediante métodos de condensación estática, An. Ing. Mecánica. (2014).

[30] I. Heras, J. Aguirrebeitia, M. Abasolo, Calculation of the ball raceway interferences due to manufacturing errors and their influence on the friction moment in four-contact-point slewing bearings, Mech. Mach. Sci. 43 (2017) 3–11. doi:10.1007/978-3-319-44156-6_1/TABLES/2.

[31] I. Heras, I. Coria, J. Aguirrebeitia, M. Abasolo, I. Martín, Par de fricción en rodamientos de vuelco de cuatro puntos de contacto: procedimiento de cálculo y resultados experimentales, XXII Congr. Nac. Ing. Mecánica. (2018).

[32] I. Heras, I. Coria, J. Aguirrebeitia, M. Abasolo, I. Martín, Limitaciones en la aplicación de procedimientos de cálculo y selección de rodamientos con pista de rodadura alámbrica, XXII Congr. Nac. Ing. Mecánica. (2018).

[33] I. Martín, I. Heras, J. Aguirrebeitia, M. Abasolo, I. Coria, Analytical Model for the Estimation of Axial Stiffness and Contact Results in Wire Race Ball Bearings, Mech. Mach. Sci. 73 (2019) 3873–3882. doi:10.1007/978-3-030-20131-9_384/COVER.

[34] I. Heras, J. Aguirrebeitia, M. Abasolo, I. Coria, Load distribution in four-point contact slewing bearings considering manufacturing errors and ring flexibility, Mech. Mach. Sci. 59 (2019) 267–274. doi:10.1007/978-3-319-98020-1_31.

[35] Kaydon, Catalog 390, (2011).

[36] T.A. Harris, M.N. Kotzalas, Essential Concepts of Bearing Technology, 2006.

[37] H. Basener, Race wire bearing, 4568205, 1986.

[38] Rotis, Large slewing bearings catalogue, (2022).

[39] Liebherr, Web catalogue slewing bearings, (n.d.). https://www.liebherr.com/en/int/products/components/large-diameter-bearing/product-portfolio-large-diameter-bearing/product-portfolio-large-diameter-bearing.html (accessed June 7, 2023).

[40] IMO, Official website, (n.d.). http://www.goimo.eu.

[41] Franke GmbH, Wälzlager Produktübersicht | Rotativ bewegen, (n.d.).

https://www.franke-gmbh.de/drahtwaelzlager/standardprogramm/ (accessed June 7, 2023).

[42] ISO 15243:2017 Rolling bearings — Damage and failures — Terms, characteristics and causes, 2017.

[43] B. Corey D., Extend wind turbine life with pitch bearing upgrades, n.d. https://www.kaydonbearings.com/white_papers_16.htm (accessed June 19, 2023).

[44] F. Schwack, F. Prigge, G. Poll, Finite element simulation and experimental analysis of false brinelling and fretting corrosion, Tribol. Int. 126 (2018) 352–362. doi:https://doi.org/10.1016/j.triboint.2018.05.013.

[45] ISO 76:2006. Rolling bearings - Static load ratings, 2006.

[46] ISO/TR 10657:1991. Explanatory notes on ISO 76, 1991.

[47] J. Lai, P. Ovize, H. Kuijpers, A. Bacchettto, S. Ioannides, J. Beswick, S.W. Dean, Case Depth and Static Capacity of Surface Induction-Hardened Rings, J. ASTM Int. 6 (2009) 102630. doi:10.1520/JAI102630.

[48] P. Göncz, M. Ulbin, S. Glodež, Computational assessment of the allowable static contact loading of a roller-slewing bearing's case-hardened raceway, Int. J. Mech. Sci. 94–95 (2015) 174–184. doi:10.1016/j.ijmecsci.2015.03.006.

[49] T.A. Harris, J.H. Rumbarger, C.P. Butterfield, Wind Turbine Design Guideline DG03: Yaw and Pitch Rolling Bearing Life. Technical Report: NREL/TP-500-42362, Golden, Colorado, 2009. https://doi.org/10.2172/969722.

[50] ISO 281: 2007. Rolling bearings - Dynamic load ratings and rating life, 2007.

[51] ISO/TS 16281:2008. Rolling bearings - Methods for calculating the modified reference rating life for universally loaded bearings, 2008.

[52] L. Houpert, O. Menck, Bearing Life Calculations in Rotating and Oscillating Applications, J. Tribol. 144 (2022). doi:10.1115/1.4052962/1124886.

[53] ISO - 21.100.20 - Rolling bearings, (n.d.). https://www.iso.org/ics/21.100.20/x/ (accessed June 16, 2023).

[54] T.A. Harris, M.N. Kotzalas, Advanced Concepts of Bearing Technology,: Rolling Bearing Analysis, CRC Press, 2006.

[55] M. Stammler, O. Menck, Y. Guo, J. Keller, The DG03: An Outline of Suggested Changes, (2023).

[56] P.M. Stammler, O. Menck, Y. Guo, J. Keller, The Wind Turbine Design Guideline DG03: Yaw and Pitch Rolling Bearing Life Revisited - An Outline of Suggested Changes: Preprint, (2023). www.nrel.gov/publications. (accessed December 11, 2023).

[57] H. Hertz, On the Contact of Elastic Solids, Misc. Pap. (1896) 146–162.

[58] H. Hertz, On the Contact of Rigid Elastic Solids and on Hardness, Micellaneous Pap. (1896) 163–183.

[59] D.E. Brewe, B.J. Hamrock, Simplified Solution for Elliptical-Contact Deformation Between Two Elastic Solids, J. Lubr. Technol. 99 (1977) 485–487. doi:10.1115/1.3453245.

[60] L. Houpert, An Engineering Approach to Hertzian Contact Elasticity — Part I, Trans. ASME. 123 (2001). doi:10.1115/1.1308043.

[61] L. Houpert, An Engineering Approach to Non-Hertzian Contact Elasticity - Part II, Trans. ASME. 123 (2001) 589–594. doi:10.1115/1.1308042.

[62] R. Pandiyarajan, M.S. Starvin, K.C. Ganesh, Contact Stress Distribution of Large Diameter Ball Bearing Using Hertzian Elliptical Contact Theory, Procedia Eng. 38 (2012) 264–269. doi:10.1016/j.proeng.2012.06.034.

[63] R. Stribeck, Kugellager für beliebige belastungen, Zeitschrift Des Vereines Dtsch. Ingenieure. (1901) 45(3): 73--9 (pt I) & 45(4): 118--125 (pt II).

[64] R. Stribeck, Die wesentlischen eigenschaften der gleit- un rollenlager, Zeitschrift Des Vereines Dtsch. Ingenieure. (1902) 46(37):1341--1348 (pt I) & 46(38): 1432--1438 (pt.

[65] R. Stribeck, Ball bearings for various loads, Trans. ASME. 29 (1907) 420–463.

[66] S. Śpiewak, Methodology for calculating the complete static carrying capacity of twin slewing bearing, Mech. Mach. Theory. 101 (2016) 181–194. doi:10.1016/j.mechmachtheory.2016.03.017.

[67] H. Sjoväll, The load distribution within ball and roller bearings under given external radial and axial load, Tek. Tidskr. Mek. (1933) h.9.

[68] A.B. Jones, New departure engineering data: analysis of stresses and deflections., New Depart. Eng. Data. 2 (1946).

[69] A.B. Jones, A General Theory for Elastically Constrained Ball and Radial Roller Bearings Under Arbitrary Load and Speed Conditions, J. Basic Eng. 82 (1960) 309–320. doi:10.1115/1.3662587.

[70] J. Rumbarger, Thrust bearing with eccentric loads, Mach. Des. (1962).

[71] L. Houpert, A Uniform Analytical Approach for Ball and Roller Bearings Calculations, J. Tribol. (1997).

[72] J.I. Amasorrain, X. Sagartzazu, J. Damián, Load distribution in a four contact-point slewing bearing, Mech. Mach. Theory. 38 (2003) 479–496. doi:10.1016/S0094-114X(03)00003-X.

[73] R. Potočnik, P. Göncz, S. Glodež, Static capacity of a large double row slewing ball bearing with predefined irregular geometry, Mech. Mach. Theory. 64 (2013) 67–79. doi:10.1016/j.mechmachtheory.2013.01.010.

[74] M. Olave, X. Sagartzazu, J. Damian, A. Serna, Design of Four Contact-Point Slewing Bearing With a New Load Distribution Procedure to Account for Structural Stiffness, J. Mech. Des. 132 (2010) 21006. doi:10.1115/1.4000834.

[75] S. M S, M. K, The effect of manufacturing tolerances on the load carrying capacity of large diameter bearings, Sadhana. 40 (2015) 1899–1911. doi:10.1007/s12046-015-0427-x.

[76] S. Aithal, N. Siva Prasad, M. Shunmugam, P. Chellapandi, Effect of manufacturing errors on load distribution in large diameter slewing bearings of fast breeder reactor rotatable plugs, Proc. Inst. Mech. Eng. Part C J. Mech. Eng. Sci. 230 (2016) 1449–1460. doi:10.1177/0954406215579947.

[77] G. Chen, J. Wen, Load performance of large-scale rolling bearings with supporting structure in wind turbines, J. Tribol. 134 (2012). doi:10.1115/1.4007349/436432.

[78] G. Chen, P. Jia, J. He, Effects of geometric parameters on static load capacity of a double-row four-point contact ball bearing, J. Mech. Sci. Technol. 27 (2013) 1053–1061. doi:10.1007/s12206-013-0228-2.

[79] A. Daidié, Z. Chaib, A. Ghosn, 3D Simplified Finite Elements Analysis of Load and Contact Angle in a Slewing Ball Bearing, J. Mech. Des. 130 (2008) 82601. doi:10.1115/1.2918915.

[80] D.H. Golbach, Integrated Non-linear FE Module for Rolling Bearing Analysis, Proceeding NAFEMS World Congr. 2 (1999).

[81] T. Smolnicki, E. Rusiński, Superelement-Based Modeling of Load Distribution in Large-Size Slewing Bearings, J. Mech. Des. 129 (2007) 459–463. doi:10.1115/1.2437784.

[82] T. Smolnicki, D. Derlukiewicz, M. Stańco, Evaluation of load distribution in the superstructure rotation joint of single-bucket caterpillar excavators,

Autom. Constr. 17 (2008) 218–223. doi:10.1016/j.autcon.2007.05.003.

[83] S. Leupold, R. Schelenz, G. Jacobs, Investigation of the individual load distribution of a blade bearing test rig by means of finite element simulation, J Phys Conf Ser. 1618 (2020) 52056. doi:10.1088/1742-6596/1618/5/052056.

[84] J. Seok Nam, J. Woo Han, Y. Jun Park, Y. Yun Nam, G. Ho Lee, Development of highly reproducible test rig for pitch and yaw bearings of wind turbine †, J. Mech. Sci. Technol. 28 (2014) 705–712. doi:10.1007/s12206-013-1134-3.

[85] R. Liu, H. Wang, B.T. Pang, X.H. Gao, H.Y. Zong, Load distribution calculation of a four-point-contact slewing bearing and its experimental verification, Exp Tech. 42 (2018) 243–252. doi:10.1007/s40799-018-0237-2.

[86] S. Zupan, I. Prebil, R. Kunc, M. Češarek, Internal load distribution in large sized axial rolling bearing mounted on elastic structures, VDI. Ber. 1706 (2002) 639–656.

[87] S. Zupan, R. Kunc, I. Prebil, EXPERIMENTAL DETERMINATION OF DAMAGE TO BEARING RACEWAYS IN ROLLING ROTATIONAL CONNECTIONS, Exp. Tech. 30 (2006) 31–36. doi:10.1111/J.1747-1567.2006.00019.X.

[88] S. Lacroix, D. Nelias, A. Leblanc, Four-Point Contact Ball Bearing Model With Deformable Rings, J. Tribol. 135 (2013) 1–8. doi:10.1115/1.4024103.

[89] A. Palmgren, Neue Untersuchungen über Energieverluste in Wälzlagern - , VDI. Ber. (1957). https://books.google.es/books/about/Neue_Untersuchungen_über_Energieverlust.html?id=O4oJPwAACAAJ&redir_esc=y.

[90] M. Stammler, F. Schwack, N. Bader, A. Reuter, G. Poll, Friction torque of wind-turbine pitch bearings – comparison of experimental results with available models, Wind Energy Sci. 3 (2018) 97–105. doi:10.5194/wes-3-97-2018.

[91] Rothe Erde, Product catalogue, (2016).

[92] Rollix, Official website, (n.d.). http://www.rollix.com.

[93] SKF Group, Rolling bearings catalogue, PUB BU/P1 17000/1 EN. (2018) 1152.

[94] M.J. Todd, K.L. Johnson, A model for coulomb torque hysteresis in ball bearings, Int. J. Mech. Sci. 29 (1987) 339–354.

[95] L. Houpert, P. Leenders, A theoretical and experimental investigation into Rolling Bearing Friction, in: Proc. Eurotrib Conf., Lyon, 1985.

[96] L. Houpert, Numerical and analytical calculations in ball bearings, in: 8th Eur. Sp. Mech. Tribol. Symp. Vol. 438, Toulouse, France, 1999: p. 283. https://ui.adsabs.harvard.edu/abs/1999ESASP.438..283H.

[97] L. Houpert, Ball bearing and tapered roller bearing torque: Analytical , numerical and experimental results, Tribol. Trans. (2002).

[98] D. Olaru, G.C. Puiu, L.C. Balan, V. Puiu, A new model to estimate friction torque in a ball screw system, Prod. Eng. Eco-Design, Technol. Green Energy. (2004) 333–346. doi:10.1007/1-4020-2933-0_20.

[99] M.R.D. Bălan, V.C. Stamate, L. Houpert, D.N. Olaru, The influence of the lubricant viscosity on the rolling friction torque, Tribol. Int. 72 (2013) 1–12. doi:10.1016/j.triboint.2013.11.017.

[100] M.R.D. Bălan, L. Houpert, A. Tufescu, D.N. Olaru, Rolling Friction Torque in Ball-Race Contacts Operating in Mixed Lubrication Conditions, Lubricants. 3 (2015) 222–243. doi:10.3390/lubricants3020222.

[101] C. Zhang, L. Gu, Y. Mao, L. Wang, Modeling the frictional torque of a dry-lubricated tapered roller bearing considering the roller skewing, Friction. 7 (2019) 551–563. doi:10.1007/S40544-018-0232-8/METRICS.

[102] F.W. Carter, On the action of a locomotive driving wheel, Proc. R. Soc. London. Ser. A. 112 (1926) 151–157. doi:10.1098/rspa.1926.0100.

[103] H. Fromm, Berechnung des Schlupfes beim Rollen deformierbarer Scheiben, ZAMM - J. Appl. Math. Mech. / Zeitschrift Für Angew. Math. Und Mech. 7 (1927) 27–58. doi:10.1002/zamm.19270070106.

[104] J.J. Kalker, A Strip Theory for Rolling with Slip and Spin, 1964.

[105] J.J. Kalker, On the rolling contact of two elastic bodies in presence of dry friction, Technische Universiteit Delft, Nederland, 1967.

[106] D.J. Haines, E. Ollerton, Contact Stress Distribution on Elliptical Contact Surfaces Subjected to Radial and Tangential Forces, Proc. Inst. Mech. Eng. (1963) 95–114.

[107] J.J. Kalker, The Tangential Force Transmitted by Two Elastic Bodies Rolling Over Each Other with Pure Creepage, Wear. (1968) 421–430.

[108] J.J. Kalker, Simplified theory of rolling contact, Delft Prog. Report, Ser. C Mech. Aeronaut. Eng. Shipbuild. 1 (1973) 1–10.

[109] J.J. Kalker, A Fast Algorithm for the Simplified Theory of Rolling Contact, Veh. Syst. Dyn. 11 (1982) 1–13. doi:10.1080/00423118208968684.

[110] J.J. Kalker, Three-Dimensional Elastic Bodies in Rolling Contact, Springer Netherlands, 1990. doi:10.1007/978-94-015-7889-9.

[111] L. Baeza, Desarrollo de modelos para el estudio de la dinámica de vehículos ferroviarios, Universidad Politécnica de Valencia, 1999.

[112] R.D. Mindlin, Compliance Of Elastic Bodies In Contact.pdf, ASME Trans. (1949).

[113] H. Poritsky, Stresses and Deflections of Cylindrical Bodies in Contact With Application to Contact of Gears and of Locomotive Wheels, J. Appl. Mech. 17 (1950) 191–201. doi:10.1115/1.4010099.

[114] J.O. Smith, C.K. Liu, Stresses Due to Tangential and Normal Loads on an Elastic Solid With Application to Some Contact Stress Problems, J. Appl. Mech. 20 (1953) 157–166. doi:10.1115/1.4010643.

[115] K.L. Johnson, Surface interaction between elastically loaded bodies under tangential forces, Proc. R. Soc. London. Ser. A. Math. Phys. Sci. 230 (1955) 531–548. doi:10.1098/RSPA.1955.0149.

[116] K.L. Johnson, Energy Dissipation at Spherical Surfaces in Contact Transmitting Oscillating Forces, Http://Dx.Doi.Org/10.1243/JMES_JOUR_1961_003_048_02. 3 (1961) 362–368. doi:10.1243/JMES_JOUR_1961_003_048_02.

[117] K.L. Johnson, Rolling Contact Phenomena, in: Elsevier, 1962.

[118] K.L. Johnson, An Analysis of Plastic Deformation in Rolling Contact, Http://Dx.Doi.Org/10.1243/PIME_PROC_1963_177_052_02. 177 (1963) 676–690. doi:10.1243/PIME_PROC_1963_177_052_02.

[119] K.L. Johnson, A shakedown limit in rolling contact, Proc. U.S. Nat. Congr. Appl. Mech. (1962).

[120] A.B. Jones, Ball Motion and Sliding Friction in Ball Bearings, J. Basic Eng. 81 (1959) 1–12. doi:10.1115/1.4008346.

[121] B.J. Hamrock, Ball motion and sliding friction in an arched outer-race ball bearing, 1974.

[122] A. Leblanc, D. Nelias, Ball Motion and Sliding Friction in a Four-Contact-Point Ball Bearing, J. Tribol. 129 (2007) 801–808. doi:10.1115/1.2768079.

[123] A. Leblanc, D. Nelias, Analysis of Ball Bearings with 2, 3 or 4 Contact

Points, Tribol. Trans. 51 (2008) 372–380. doi:10.1080/10402000801888887.

[124] A. Joshi, B. Kachhia, H. Kikkari, M. Sridhar, D. Nelias, Running Torque of Slow Speed Two-Point and Four-Point Contact Bearings, Lubricants. 3 (2015) 181–196. doi:10.3390/lubricants3020181.

[125] B. Bhushan, Friction, in: Princ. Appl. Tribol., John Wiley & Sons, Ltd, 2013: pp. 321–401. doi:10.1002/9781118403020.ch6.

[126] B.J. Hamrock, W.J. Anderson, Rolling-Element Bearings, NASA Ref. Publ. 1105. (1983).

[127] O. Menck, K. Behnke, M. Stammler, A. Bartschat, F. Schleich, M. Graßmann, Measurements and modeling of friction torque of wind turbine blade bearings, J. Phys. Conf. Ser. 2265 (2022) 022087. doi:10.1088/1742-6596/2265/2/022087.

[128] Rolling bearings, (n.d.). https://www.iwes.fraunhofer.de/en/test-centers-and-measurements/drive-train-components.html (accessed June 20, 2023).

[129] V. Paleu, S. Cretu, B. Dragan, R. Balan, Test Rig for Friction Torque Measurement in Rolling Bearings, Mach. Des. (2004) 85–91. http://www.scopus.com/inward/record.url?eid=2-s2.0-84922483418&partnerID=tZOtx3y1.

[130] J. Woo Han, J. Seok Nam, Y. Jun Park, G. Ho Lee, Y. Yun Nam, An experimental study on the performance and fatigue life of pitch bearing for wind turbine, J. Mech. Sci. Technol. 29 (2015) 1963–1971. doi:10.1007/s12206-015-0417-2.

[131] BANCO DE ENSAYOS DE RODAMIENTO DE PALA Y BUJE - WINDBOX, (n.d.). http://www.clusterenergia.com/windbox-banco-rodamiento-pala-y-buje (accessed June 20, 2023).

[132] Großlagerprüfstand ASTRAIOS | Mediathek | Schaeffler Gruppe, (n.d.). https://www.schaeffler.com/de/medien/mediathek/downloadcenter-detail-seite.jsp?id=3521600 (accessed June 20, 2023).

[133] Slewing bearings for tunnelling | Liebherr, (n.d.). https://www.liebherr.com/en/gbr/products/components/large-diameter-bearing/slewing-bearings-for-tunnelling-machines/slewing-bearings-for-tunnelling-machines.html (accessed June 20, 2023).

[134] Lippstadt: It's all about testing, (n.d.). https://www.thyssenkrupp-rotheerde.com/en/newsroom/stories/lippstadt-its-all-about-testing (accessed June 20, 2023).

[135] T. Lim, R. Singh, Vibration transmission through rolling element bearings, part I: Bearing stiffness formulation, J. Sound Vib. 139 (1990) 179–199.

[136] X. Hernot, M. Sartor, J. Guillot, Calculation of the Stiffness Matrix of Angular Contact Ball Bearings by Using the Analytical Approach, J. Mech. Des. 122 (2000) 83–90.

[137] H.-V. Liew, T. Lim, Analysis of time-varying rolling element bearing characteristics, J. Sound Vib. 283 (2005) 1163–1179.

[138] D. Noel, S. Le Loch, M. Ritou, B. Furet, Complete Analytical Expression of the Stiffness Matrix of Angular Contact Ball Bearings, J. Tribol. 135 (2013) 1–8.

[139] A.B. Jones, T.A. Harris, Analysis of a Rolling-Element Idler Gear Bearing Having a Deformable Outer-Race Structure, J. Basic Eng. 85 (1963) 273–278. http://dx.doi.org/10.1115/1.3656576.

[140] T.A. Harris, J.L. Broschard, Analysis of an Improved Planetary Gear-Transmission Bearing, J. Basic Eng. 86 (1964) 457–461. http://dx.doi.org/10.1115/1.3653139.

[141] L. Mignot, L. Bonnard, V. Abousleiman, Analysis of Load Distribution in Planet-Gear Bearings, AGMA Tech. Pap. 10FTM16. (2010).

[142] Y. Guo, R. Parker, Stiffness matrix calculation of rolling element bearings using a finite element/contact mechanics model, Mech. Mach. Theory. 51 (2012) 32–45.

[143] J.T. Sawicki, S. a. Johansson, J.H. Rumbarger, R.B. Sharpless, Fatigue Life Prediction for Large-Diameter Elastically Constrained Ball Bearings, J. Eng. Gas Turbines Power. 130 (2008) 22506. doi:10.1115/1.2772632.

[144] R. Potočnik, P. Göncz, J. Flašker, S. Glodež, Fatigue life of double row slewing ball bearing with irregular geometry, Procedia Eng. 2 (2010) 1877–1886. doi:10.1016/j.proeng.2010.03.202.

[145] I. Portugal, M. Olave, A. Zurutuza, A. López, M. Muñiz-Calvente, A. Fernández-Canteli, Methodology to evaluate fatigue damage under multiaxial random loading, Eng. Fract. Mech. (2017). doi:10.1016/j.engfracmech.2017.04.012.

[146] J. V. Poplawski, S.M. Peters, E. V. Zaretsky, Effect Of Roller Profile On Cylindrical Roller Bearing Life Prediction—Part I: Comparison of Bearing Life Theories, Http://Dx.Doi.Org/10.1080/10402000108982466. 44 (2008) 339–350. doi:10.1080/10402000108982466.

[147] P. Göncz, S. Glodež, Rolling Contact Fatigue Life Assessment of Induction Hardened Raceway, Procedia Eng. 74 (2014) 392–396. doi:10.1016/j.proeng.2014.06.286.

[148] F. Schwack, M. Stammler, G. Poll, A. Reuter, Comparison of Life Calculations for Oscillating Bearings Considering Individual Pitch Control in Wind Turbines, in: J. Phys. Conf. Ser., 2016. doi:10.1088/1742-6596/753/11/112013.

[149] N.D. Londhe, N.K. Arakere, G. Subhash, Extended Hertz Theory of Contact Mechanics for Case-Hardened Steels With Implications for Bearing Fatigue Life, J. Tribol. 140 (2017) 21401. doi:10.1115/1.4037359.

[150] P. He, R. Liu, R. Hong, H. Wang, G. Yang, C. Lu, Hardened raceway calculation analysis of a three-row roller slewing bearing, Int. J. Mech. Sci. 137 (2018) 133–144. doi:10.1016/j.ijmecsci.2018.01.021.

[151] P. He, R. Hong, H. Wang, X. Ji, C. Lu, Calculation analysis of yaw bearings with a hardened raceway, Int. J. Mech. Sci. 144 (2018) 540–552. doi:10.1016/J.IJMECSCI.2018.06.016.

[152] M.U. Abdullah, Z.A. Khan, W. Kruhoeffer, Evaluation of Dark Etching Regions for Standard Bearing Steel under Accelerated Rolling Contact Fatigue, Tribol. Int. 152 (2020) 106579. doi:10.1016/J.TRIBOINT.2020.106579.

[153] D. Godfrey, Fretting corrosion or false brinelling?, Tribol. Lubr. Technol. 12 (2003) 28–29.

[154] M.H. Zhu, Z.R. Zhou, On the mechanisms of various fretting wear modes, Tribol. Int. 44 (2011) 1378–1388. doi:10.1016/J.TRIBOINT.2011.02.010.

[155] M. Grebe, False brinelling - standstill marks at roller bearings, (2012).

[156] X. Li, F. Guo, G. Poll, Y. Fei, P. Yang, Grease film evolution in rolling elastohydrodynamic lubrication contacts, Friction. 9 (2021) 179–190. doi:10.1007/S40544-020-0381-4/METRICS.

[157] S. Wandel, N. Bader, J. Glodowski, B. Lehnhardt, J. Leckner, F. Schwack, G. Poll, Starvation and Re-lubrication in Oscillating Bearings: Influence of Grease Parameters, Tribol. Lett. 70 (2022) 1–14. doi:10.1007/S11249-022-01655-7/FIGURES/9.

[158] X. Bai, H. Xiao, L. Zhang, The Condition Monitoring of Large Slewing Bearing Based on Oil Analysis Method, Key Eng. Mater. 474–476 (2011) 716–719. doi:10.4028/WWW.SCIENTIFIC.NET/KEM.474-476.716.

[159] C. Lu, J. Chen, R. Hong, Y. Feng, Y. Li, Degradation trend estimation of slewing bearing based on LSSVM model, Mech. Syst. Signal Process. 76–77 (2016) 353–366. doi:10.1016/J.YMSSP.2016.02.031.

[160] Y. Feng, X. diao Huang, R. jing Hong, J. Chen, Online residual useful life prediction of large-size slewing bearings—A data fusion method, J. Cent. South Univ. 24 (2017) 114–126. doi:10.1007/S11771-017-3414-Z/METRICS.

[161] M. Žvokelj, S. Zupan, I. Prebil, EEMD-based multiscale ICA method for slewing bearing fault detection and diagnosis, J. Sound Vib. 370 (2016) 394–423. doi:10.1016/j.jsv.2016.01.046.

[162] M. Žvokelj, S. Zupan, I. Prebil, Multivariate and multiscale monitoring of large-size low-speed bearings using Ensemble Empirical Mode Decomposition method combined with Principal Component Analysis, Mech. Syst. Signal Process. 24 (2010) 1049–1067. doi:10.1016/j.ymssp.2009.09.002.

[163] R. Liu, Condition monitoring of low-speed and heavily loaded rolling element bearing, Ind. Lubr. Tribol. 59 (2007) 297–300. doi:10.1108/00368790710820892/FULL/PDF.

[164] E. V Zaretsky, Rolling Bearing Life Prediction, Theory, and Application, in its entirety, (2016). http://www.sti.nasa.gov (accessed June 20, 2023).

[165] S. Zupan, I. Prebil, Carrying angle and carrying capacity of a large single row ball bearing as a function of geometry parameters of the rolling contact and the supporting structure stiffness, Mech. Mach. Theory. 36 (2001) 1087–1103. doi:10.1016/S0094-114X(01)00044-1.

[166] M. Graßmann, F. Schleich, M. Stammler, Validation of a finite-element model of a wind turbine blade bearing, Finite Elem. Anal. Des. 221 (2023) 103957. doi:10.1016/J.FINEL.2023.103957.

[167] G. Lundberg, A. Palmgren, Dynamic Capacity of Rolling Bearings, ACTA, Polytech. Mech. Eng. Ser. 1 (1947) 7.

[168] G. Lundberg, A. Palmgren, Dynamic Capacity of Roller Bearings, 1952.

[169] Timken, Timken Engineering Manual, 150 11-22 Order No. 10424. (2022).

[170] Y. Zhao, Z. Ma, Y. Zi, Skidding and spinning investigation for dry-lubricated angular contact ball bearing under combined loads, Frict. 2022. (2023) 1–21. doi:10.1007/S40544-022-0703-9.

[171] M. Krynke, R. Ulewicz, Analysis of the influence of slewing bearing mounting on their static load capacity, (2019).

doi:10.1016/j.trpro.2019.07.105.

[172] S. Leupold, R. Schelenz, G. Jacobs, Method to determine the local load cycles of a blade bearing using flexible multi-body simulation, Forsch. Im Ingenieurwesen/Engineering Res. 85 (2021) 211–218. doi:10.1007/S10010-021-00457-Y.

[173] D. Becker, D. Billenstein, T. Handreck, P. Müller, M. Neidnicht, G. Volmer, D. Schlüter, T. Netz, B. Lüneburg, J. Rollmann, Design and calculation process for large-sized multi-MW blade bearing applications based on advanced multi-bearing FE-analyses, Bear. World Int. Conf. (2022) 280–284.

[174] M. Buescher, R. Schelenz, G. Jacobs, V. Schneider, G. Poll, Contact Analysis of Wind Turbine Blade Bearings by Means of Finite Element Method and Alternative Slicing Technique Contact Load Modeling, Bear. World Int. Conf. (2022) 286–294.

[175] M.R. Lovell, M.M. Khonsari, R.D. Marangoni, Low-Speed Friction Torque on Balls Undergoing Rolling Motion, Tribol. Trans. (1993) 290–296.

[176] T. Cousseau, B. Grac -A A, A. Campos, J. Seabra, Friction torque in grease lubricated thrust ball bearings, (2010). doi:10.1016/j.triboint.2010.06.013.

[177] D. Gonçalves, S. Pinho, B. Graça, A. V Campos, J.H.O. Seabra, Friction torque in thrust ball bearings lubricated with polymer greases of different thickener content, Tribol. Int. 96 (2016) 87–96. doi:10.1016/j.triboint.2015.12.017.

[178] C. Long, X. Xintao, Z. Haotian, Q. Ming, Friction Torque Behavior as a Function of Actual Contact Angle in Four-point-contact Ball Bearing, Appl. Math. Nonlinear Sci. 1 (2016) 53–64. doi:10.21042/AMNS.2016.1.00005.

[179] N. De Laurentis, A. Kadiric, P. Lugt, P. Cann, The influence of bearing grease composition on friction in rolling/sliding concentrated contacts, Tribol. Int. 94 (2016) 624–632. doi:10.1016/J.TRIBOINT.2015.10.012.

[180] J. Guegan, A. Kadiric, A. Gabelli, H. Spikes, The Relationship Between Friction and Film Thickness in EHD Point Contacts in the Presence of Longitudinal Roughness, Tribol. Lett. 64 (2016) 1–15. doi:10.1007/S11249-016-0768-6.

[181] L. Yang, W. Xue, S. Gao, H. Liu, Y. Cao, D. Duan, D. Li, S. Li, Study on sliding friction and wear behavior of M50 bearing steel with rare earth addition, Tribol. Int. 174 (2022) 107725. doi:10.1016/J.TRIBOINT.2022.107725.

[182] O. Menck, M. Stammler, F. Schleich, Fatigue lifetime calculation of wind turbine blade bearings considering blade-dependent load distribution, Wind Energy Sci. 5 (2020) 1743–1754. doi:10.5194/WES-5-1743-2020.

[183] W. Popko, P. Thomas, A. Sevinc, M. Rosemeier, M. Bätge, R. Braun, F. Meng, D. Horte, C. Balzani, O. Bleich, E. Daniele, B. Stoevesandt, M. Wentingmann, J.D. Polman, M. Leimeister, B. Schümann, A. Reuter, IWES Wind Turbine IWT-7.5-164. Rev 4, (2018). doi:10.24406/IWES-N-518562.

[184] M. Stammler, P. Thomas, A. Reuter, F. Schwack, G. Poll, Effect of load reduction mechanisms on loads and blade bearing movements of wind turbines, Wind Energy. 23 (2020) 274–290. doi:10.1002/we.2428.

Appendix: normalised friction torque maps

This appendix contains the normalised friction torque maps referenced in Chapter 4.

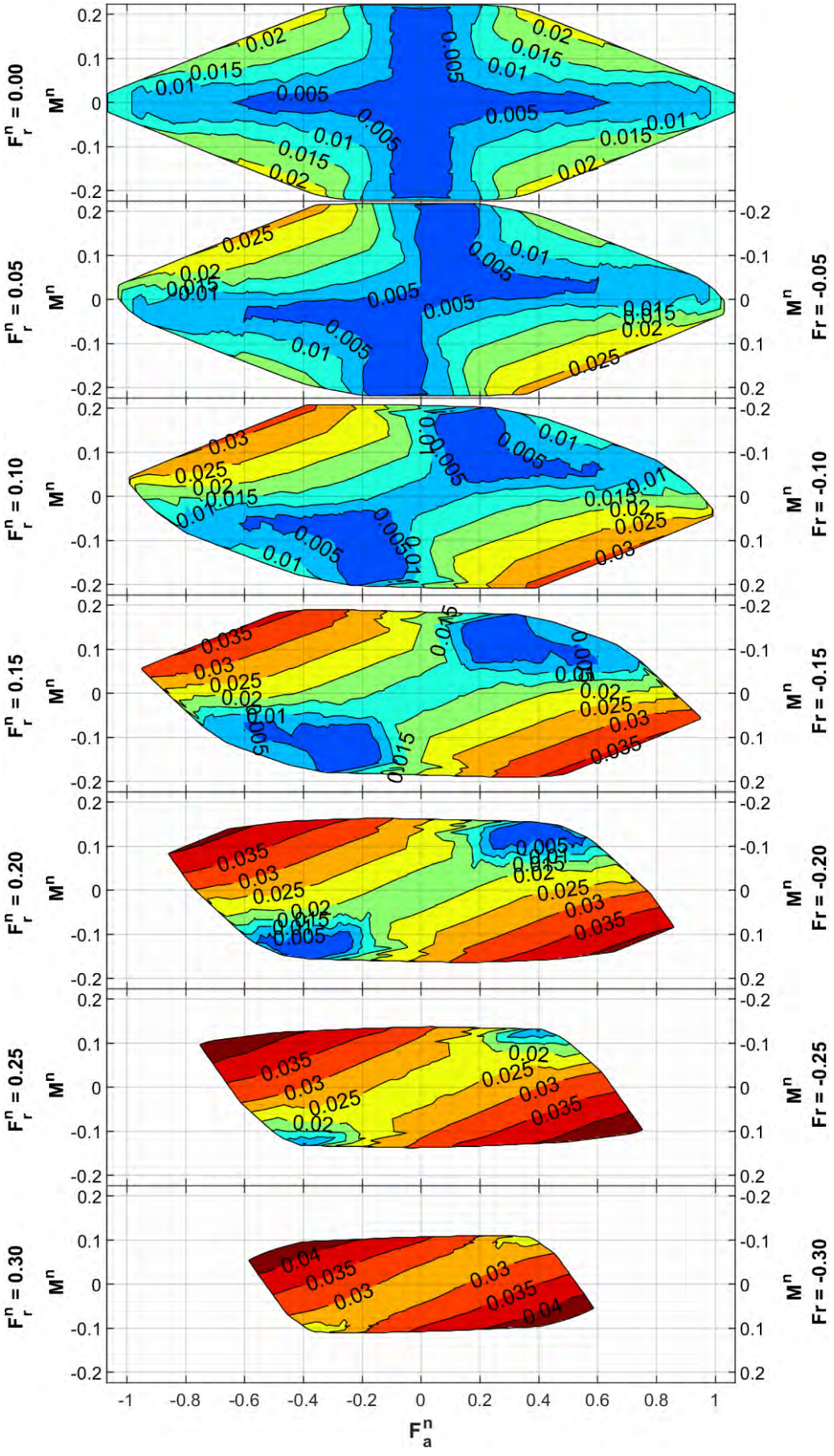

Figure A.1. Friction torque map: $p = 0.00$, $s = 0.940$ and $\alpha_0 = 45°$.

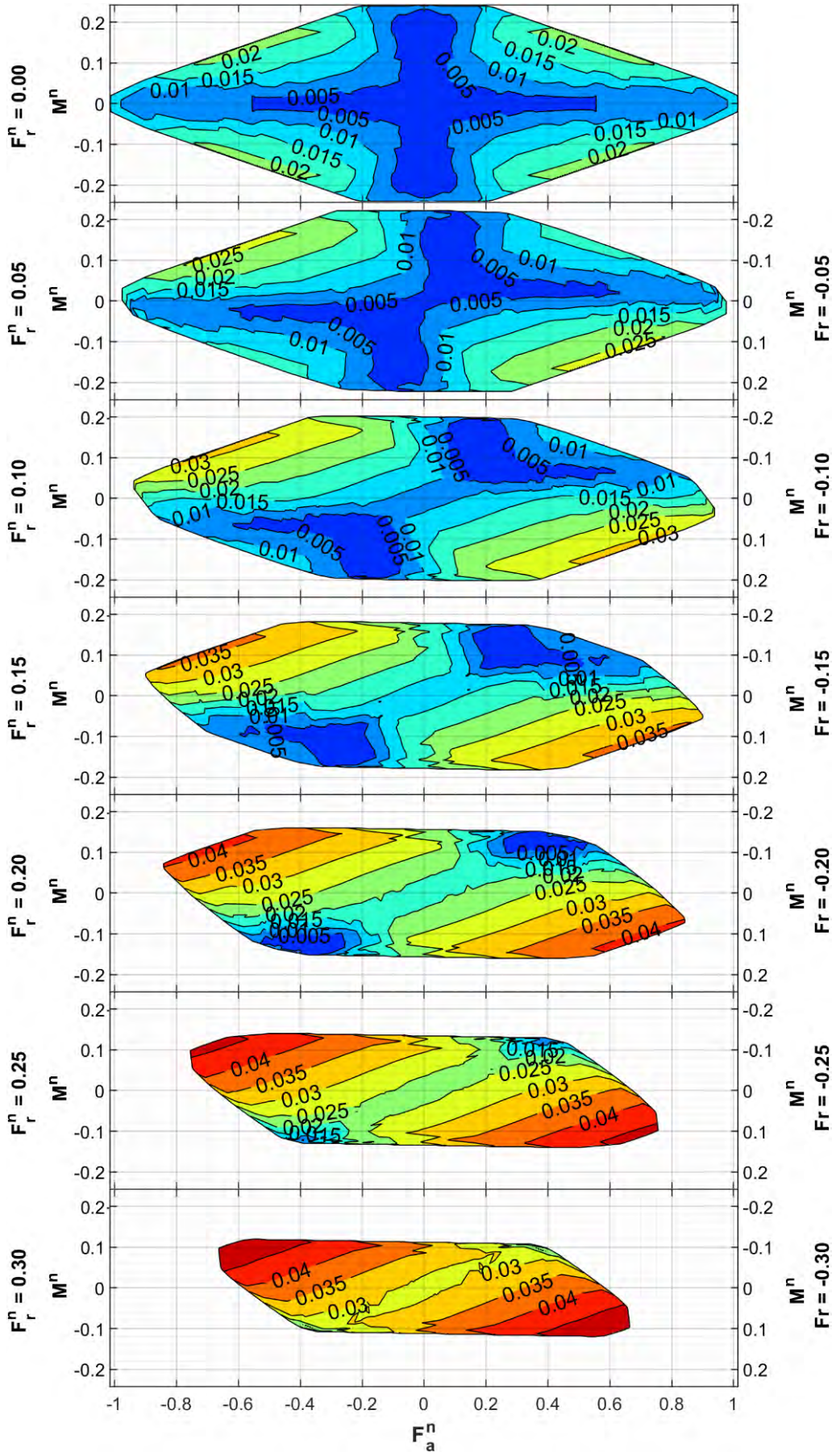

Figure A.2. Friction torque map: $p = 0.05$, $s = 0.940$ and $\alpha_0 = 45°$.

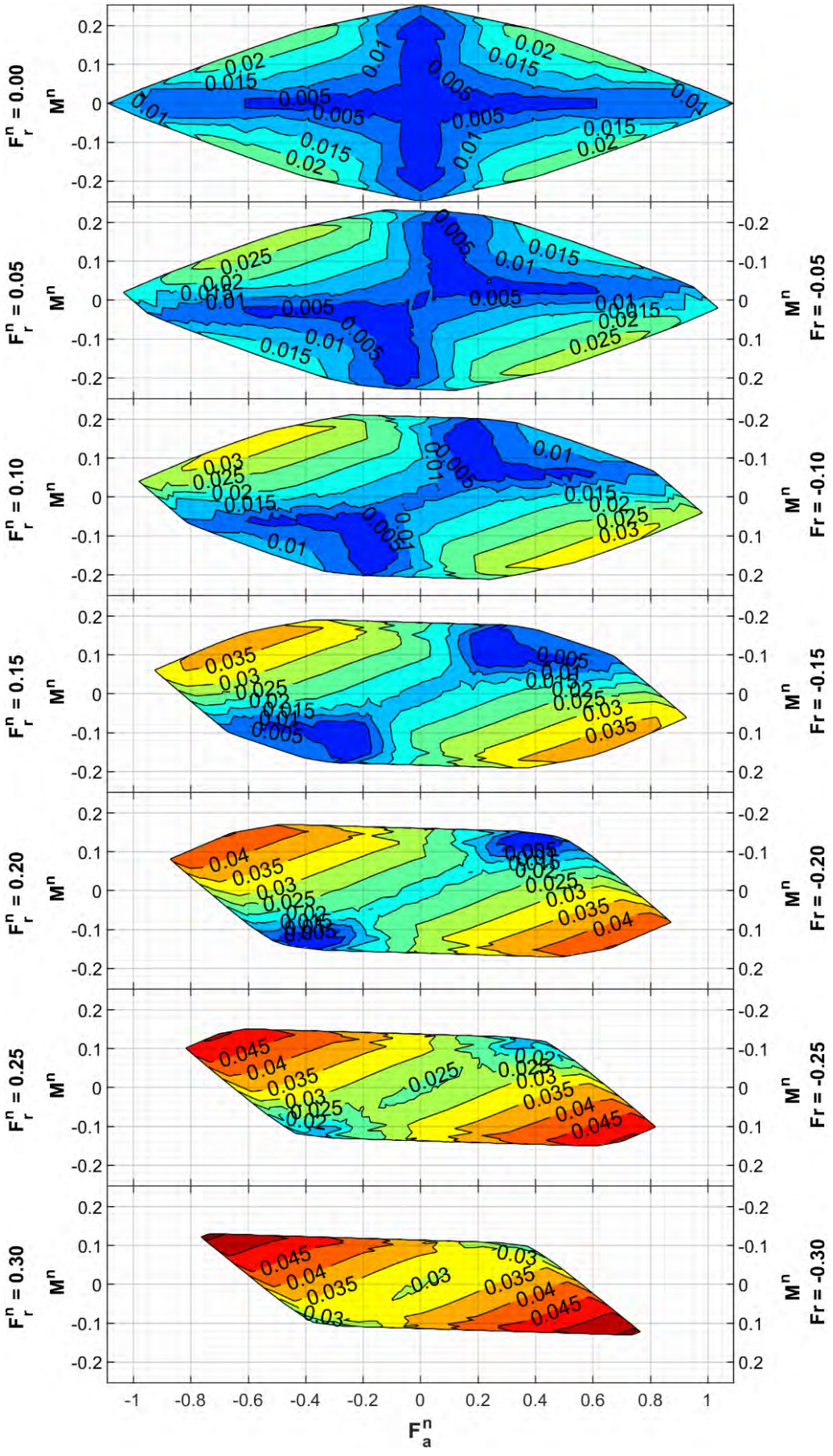

Figure A.3. Friction torque map: $p = 0.10$, $s = 0.940$ and $\alpha_0 = 45°$.

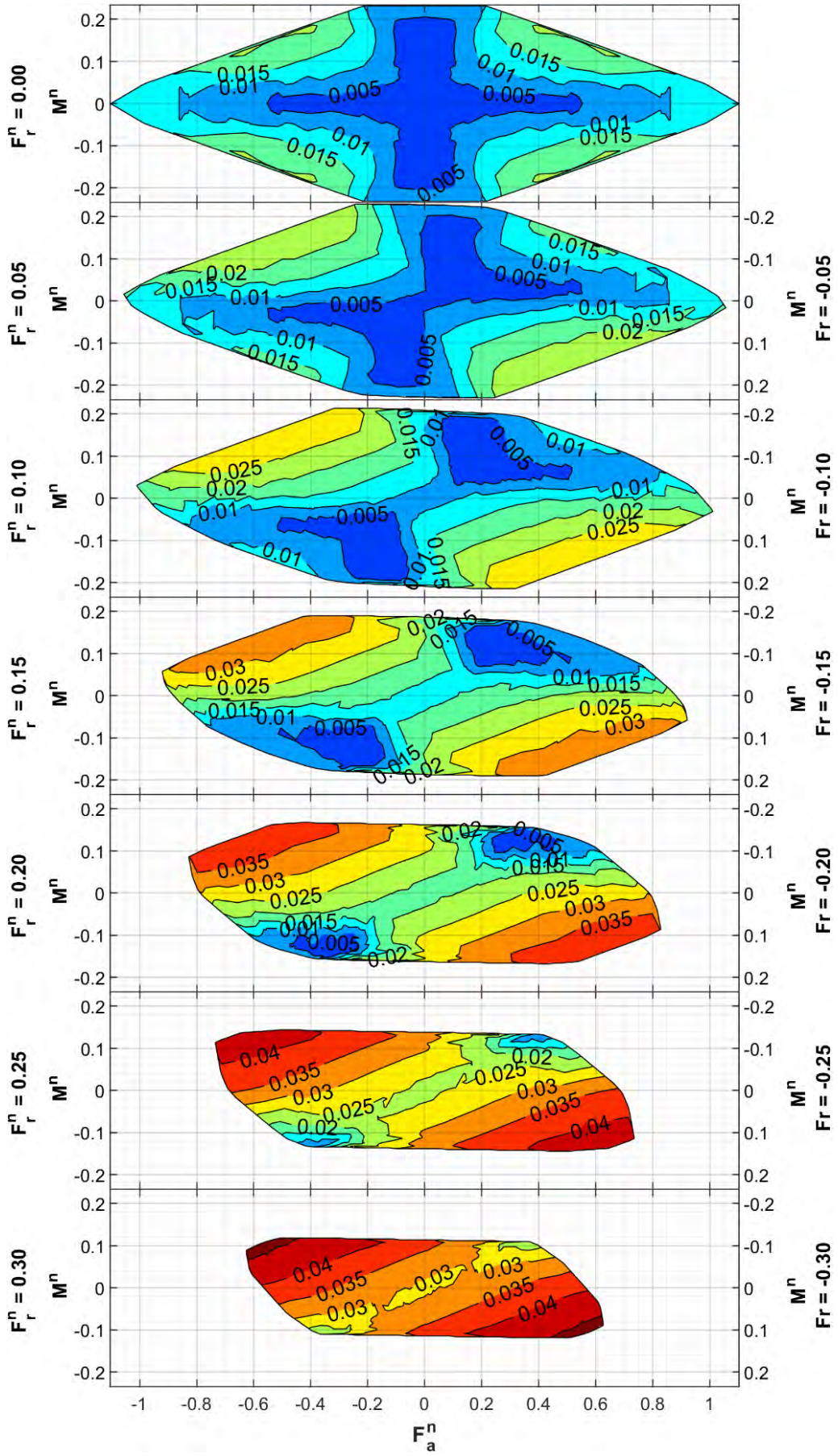

Figure A.4. Friction torque map: $p = 0.00$, $s = 0.950$ and $\alpha_0 = 45°$.

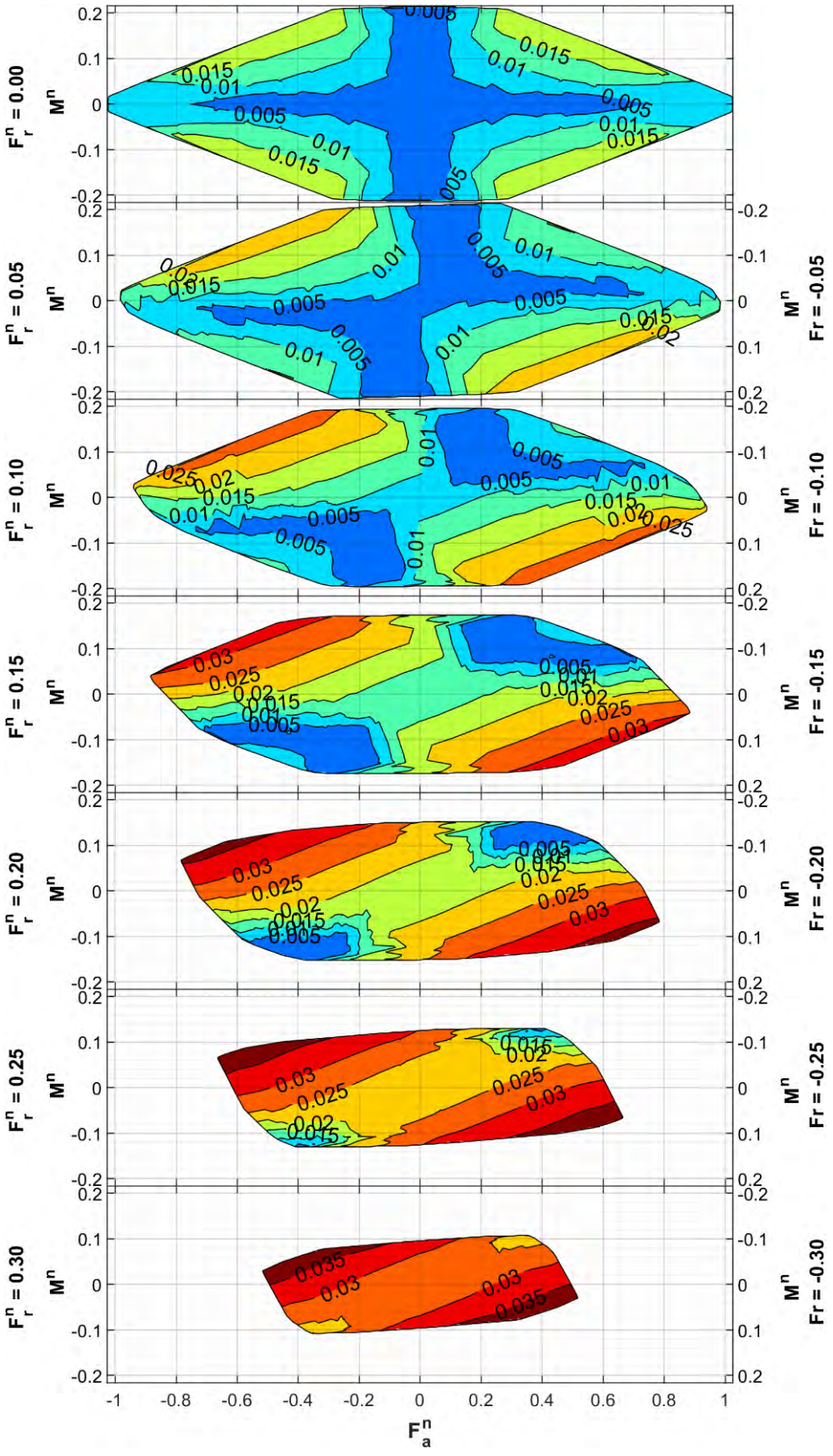

Figure A.5. Friction torque map: $p = 0.00$, $s = 0.925$ and $\alpha_0 = 45°$.

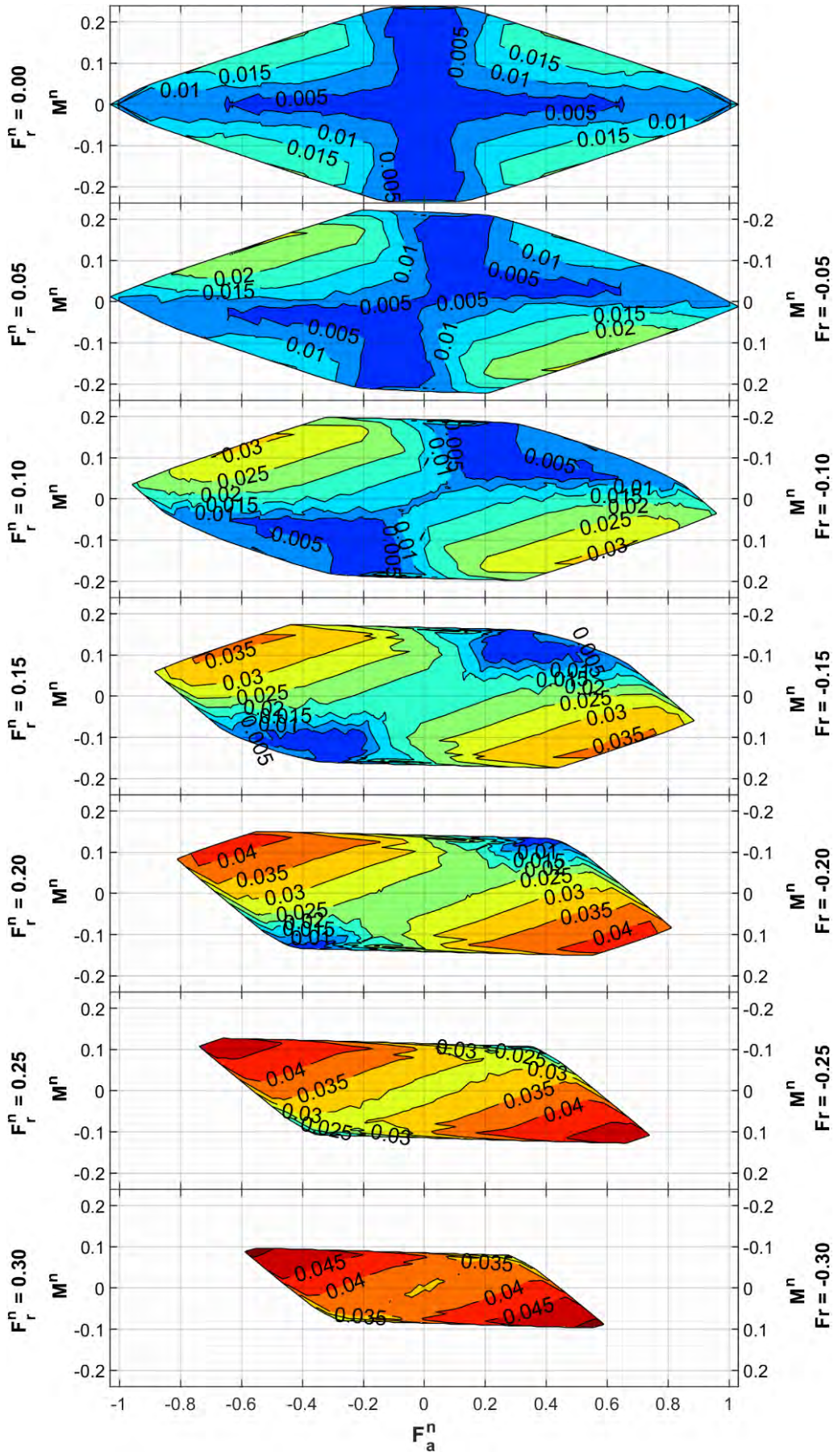

Figure A.6. Friction torque map: $p = 0.00$, $s = 0.940$ and $\alpha_0 = 50°$.

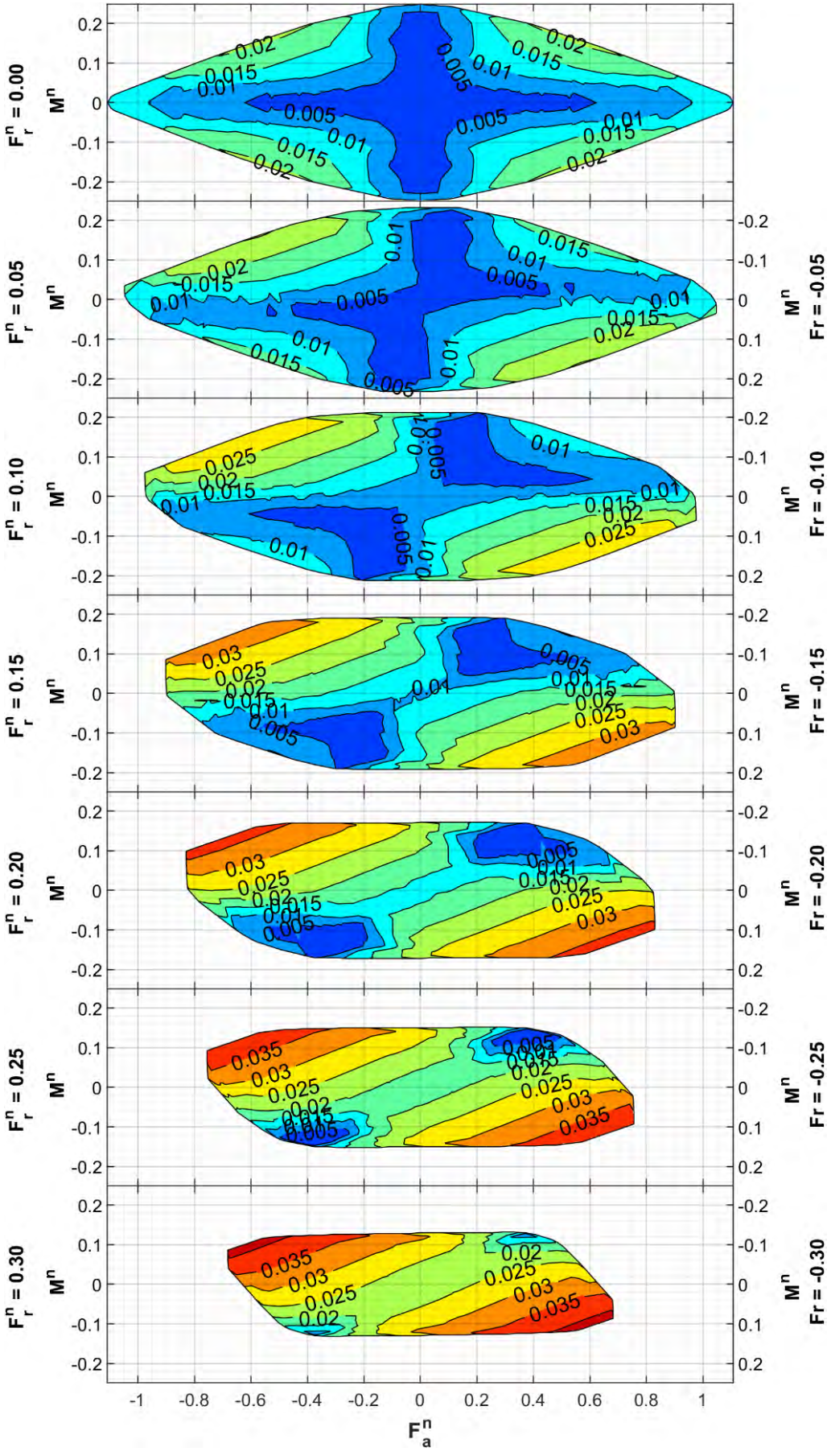

Figure A.7. Friction torque map: $p = 0.00$, $s = 0.940$ and $\alpha_0 = 40°$.